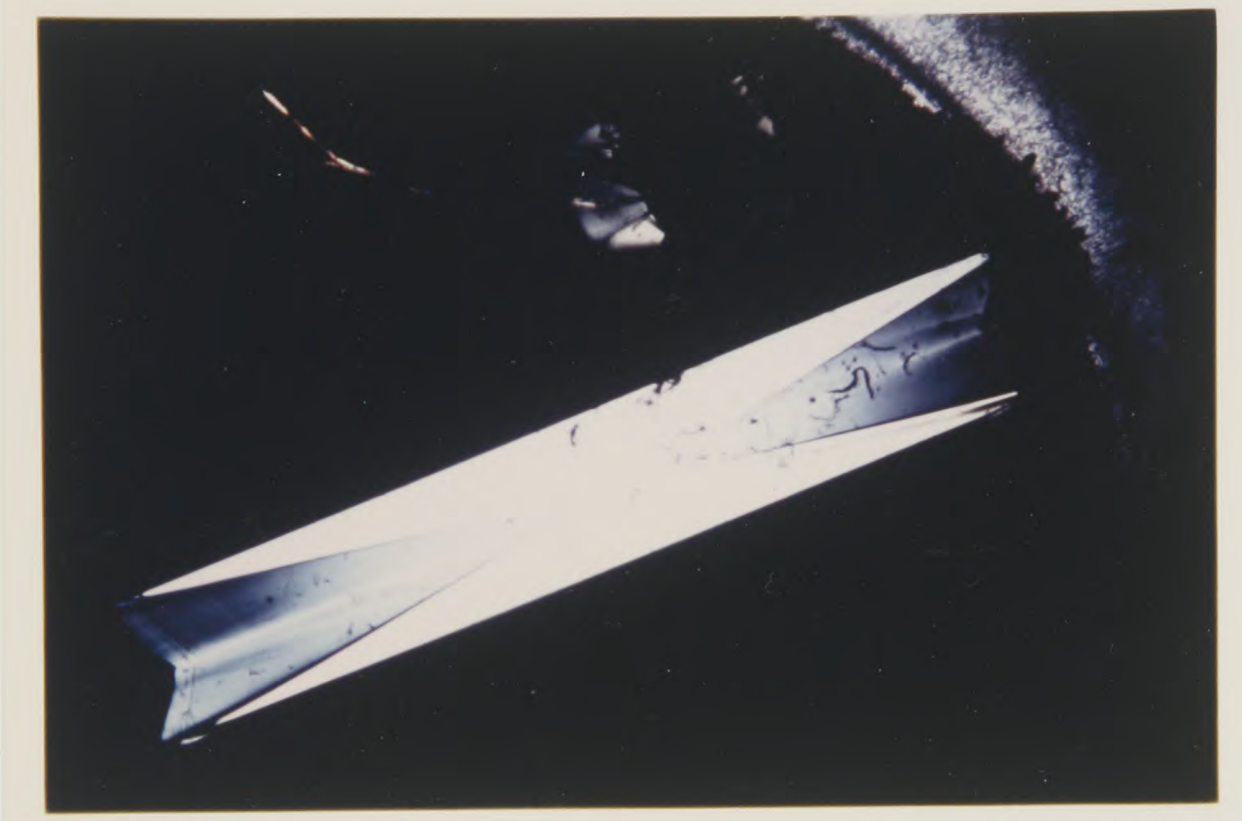
FRONTSPIECE



A tetragonal native phosphorylase b crystal viewed in the (olo) direction between crossed polarisers. The dimensions of the crystal are approximately 6.0 mm. by 1.0 mm.

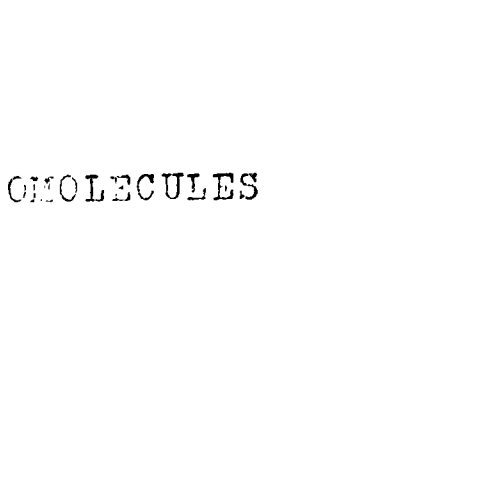
X-RAY ANALYSIS OF BIOLOGICAL MACROMOLECULES

A thesis submitted for the degree of

Doctor of Philosophy

in the University of Oxford

James Mosley



December 1973

Laboratory of Molecular Biophysics

St. Edmund Hall

ABSTRACT

The work described in this thesis relates to two topics: the crystallography of the enzyme α-glucan phosphorylase extracted from rabbit muscle, and the development of a photographic data collection system using a rotation camera.

Crystals of phosphorylase in the a and b forms were obtained with the spacegroup $P2_1$. These crystals have the phosphorylase tetramer, molecular weight 400,000 daltons, as the asymmetric unit and, therefore, the structure determination using them presents a considerable crystallographic problem. The crystals were also grown in the presence of methyl mercury chloride thereby producing a potential heavy atom derivative. A small amount of work was carried out on these crystals before another crystal form of phosphorylase b was discovered.

This second crystal form has the space group $P4_12_12$ (or $P4_32_12$) and has the phosphorylase monomer, molecular weight 100,000 daltons, as the asymmetric unit. Although the unit cell volume of these tetragonal crystals is slightly larger than that of the monoclinic crystals, the spacegroup symmetry reduces the number of unique reflections by a factor of approximately 4; hence these crystals are potentially more useful for a structure determination. The tetragonal crystals grow most readily in the presence of inosine monophosphate, and will not grow at all in the presence of adenosine monophosphate.

A search for isomorphous heavy atom derivatives of these tetragonal crystals has been conducted with a limited amount of success. Diffusion of platinum, in the form of the platinum diamino-dichloride ion, into the native crystals yields a

single site derivative of high occupancy. Various methods of data collection were considered before 6Å data sets were collected on the four circle diffractometer for the native and 4 potential heavy atom derivatives. The method of data collection and data processing are discussed in this thesis and the results given.

A rotation camera had been built in the laboratory by Mr. M. Pickford and Mr. J. Marsh to a design by Dr. D.I.Brown. The camera was intended for use with crystals which had large unit cells. Testing and further development of this camera was carried out, and is described in this thesis. The films from the rotation camera are processed using a Photoscan P1000 Microdensitometer which produces digital images of the films on magnetic tapes. The development of computer programmes to predict the positions of reflections on rotation films and to calculate their integrated intensities using the microdensitometer output tapes is described. An outline of rotation camera geometry is also given.

A series of rotation photographs was taken with a crystal of lysozyme on the camera in order to check the computer programmes. The first results of these checks were very encouraging. Some initial experiments using a tetragonal phosphorylase b crystal on the camera were carried out with encouraging results.

LIST OF CONTENTS

Page

ACKNOWLEDGEMENTS

LIST OF ABBREVIATIONS

I. INTRODUCTION

1.1 Phosphorylase a and b 1
1.2 Catalytic Reaction 2
1.3 Physical and Chemical Properties 3
1.4 Binding sites on the Molecule 5
1.5 Mechanism of Action 7
1.6 Control of Enzymic Activity 8
1.7 Mechanism of Action 12
1.8 Summary 12

II. PROTEIN CRYSTALLOGRAPHY

2.1 Crystals and Lattices 14
2.2 X-ray Diffraction 15
2.3 The Electron Density 18
2.4 The Ewald Sphere 19
2.5 The Energy of a Diffracted Beam 21
2.6 Measurement of Reflection Intensities 22
2.7 The Phase Problem 27
2.8 Location of Heavy Atom Positions 29
2.9 The Quality of Heavy Atom Derivatives 32
2.10 Scaling Derivative to Native Structure Amplitudes 37
2.11 Refinement of Heavy Atom Parameters 38
2.12 Calculation of Phase Angles 40
2.13 Anomalous Scattering Information 43

III. CRYSTALLOGRAPHIC INVESTIGATION OF PHOSPHORYLASE

3.1 Monoclinic crystals 45
3.1.1 Practical details 46
3.1.2 Difference Patterson 47
3.1.3 Discussion 49
3.2 Tetragonal crystals 50
3.2.1 The role of IMP 52
3.2.2 The mode of growth 54
3.2.3 Heavy atom derivatives 56
3.2.4 Strategy of data collection 59
3.2.5 Setting up the diffractometer 61
3.2.6 Absorption correction 63
3.2.7 Radiation damage 64
3.2.8 Diffractometer practical details 64
3.2.9 Data processing 65

Page

III (Cont.)

3.2.10 Initial attempts at data collection 70
3.2.11 The 6Å Resolution data 70
a) Native data 71
b) Platinum derivative data 73
c) Co-crystallised methyl mercury data 83
d) Uranyl acetate derivative data 89
e) Pipsyl derivative data 94
3.2.12 Conclusion 98

IV. THE DEVELOPMENT OF A ROTATION CAMERA 100

4.1 Introduction 100
4.2 The Camera 102
4.3 Outline of Reflection Geometry 105
4.4 Spot Sizes and Resolution 109
4.5 Crystal Alignment 112
4.6 Lysozyme Photographs 115
4.7 Film Processing
a) Coordinate generation 120
b) Film orientation 127
c) Reflection integration 134
d) Subsequent processing 135
4.8 First Results 138

V. CONCLUDING REMARKS 140

APPENDIX 145

REFERENCES 154

ACKNOWLEDGEMENTS

The research described in this thesis was supervised by Dr. L.N. Johnson; I am greatly indebted to her for her kindness, encouragement and advice during the last three years. The work on phosphorylase was carried out in collaboration with Keith Wilson and Dr. Niel Madsen; I owe much to them both, and have been greatly stimulated by them. I wish them and Dr. Johnson every success in their future studies on the enzyme. Mr. M. Pickford and Mr. J. Marsh have given invaluable technical help with the rotation camera; I wish to thank them both very much. I am very grateful to other members of this laboratory and Professor Hodgkin's group for the use of computer programmes written by them, and for many helpful discussions with them.

This Thesis was typed by Mrs. Ross Carlisle and Barbara Coysh, and the photographs were prepared by Mr. J. Heywood; I thank them very much, and also my wife who has been of great help especially during the preparation of the thesis.

I am grateful to the Science Research Council for the support of an Oxford Enzyme Group Studentship for the period 1970 to 1973.

LIST OF ABBREVIATIONS

$\underline{a}$, $\underline{b}$, $\underline{c}$	Unit cell vectors in Å
$\underline{a}^*$, $\underline{b}^*$, $\underline{c}^*$	Reciprocal lattice vectors in reciprocal lattice units
a,b,c, a*,b*,c*	Moduli of lattice vectors
α	Protein structure factor phase angle
ADP	Adenosine di-phosphate
AMP	Adenosine mono-phosphate
ATP	Adenosine tri-phosphate
BES	N, N - bis [2-hydroxyethyl] - 2 - aminoethane sulphonic acid
EDTA	Ethylenediamine tetracetic acid
f_c	Calculated heavy atom contribution to derivative structure factor
f_H	Observed heavy atom contribution
F_p	Native structure amplitude
$\underline{F_p}$	Native structure factor
F_{pH}	Derivative structure amplitude
$\underline{F_{pH}}$	Derivative structure factor
G-1-P	Glucose, 1-phosphate
G-6-P	Glucose, 6-phosphate
hkl	Reflection indices
IMP	Inosine mono-phosphate
λ	X-ray wavelength in Å
LP	Lorentz and polarization factors
Pp$\underline{a}$	Phosphorylase $\underline{a}$
Pp$\underline{b}$	Phosphorylase $\underline{b}$
$\tilde{P}_i$	Inorganic phosphate (PO_3^{2-})

PLP	Pyridoxal phosphate
ϕ	Heavy atom contribution phase angle, or rotation angle (the meaning is clear from the context)
θ	Bragg angle
TRIS	Tris - (hydroxymethyl) aminomethane
u,v,w	Co-ordinates in Patterson space
ξ, ζ, ϕ	Cylindrical polar co-ordinates in reciprocal space.

I INTRODUCTION

The Glycolytic Pathway

Glycolysis is the primary method of energy production in cells. It is found in most forms of life from unicellular organisms through to higher plants and animals. It appears that the glycolytic system evolved early in the history of life, possibly as much as 3000 million years ago, since it is a system of energy production well suited to the reducing atmosphere of the earth during that epoch.

The overall effect of glycolysis is the degradation of glycogen into pyruvate under anaerobic conditions. During the process two molecules of ATP, the energy transporting medium of the cell, are produced. The whole system involves some eleven chemical steps each catalysed by a separate enzyme.

Glycogen phosphorylase (E.C.2.4.1.1) catalyses the first step in the sequence, and as such exerts an important controlling effect over glycolysis.

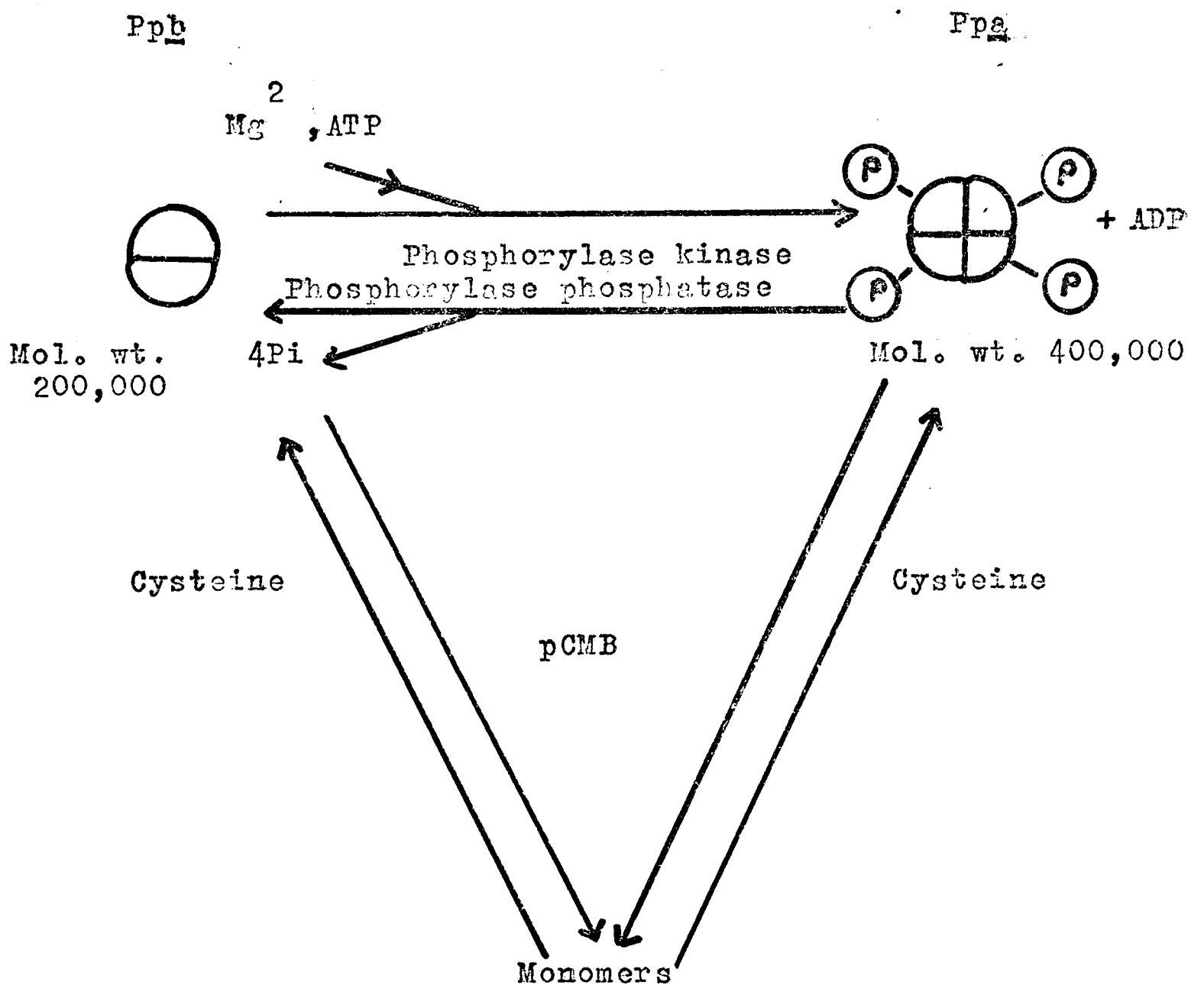
1.1 Phosphorylase a and b

Phosphorylase has been extracted from a large variety of organisms; the most extensively studied is that from rabbit skeletal muscle, which is the form discussed in this thesis.

The enzyme exists in two forms (Green and Cori (1943)):

1. Phosphorylase b which requires the nucleotide, AMP, for activity; in this form the enzyme is normally a dimer.
2. Phosphorylase a which is active in the absence of AMP; in this form the enzyme is normally a tetramer.

FIGURE 1.1



The association and dissociation of phosphorylase

The only difference so far discovered between these two forms of the enzyme is that in Ppa one serine residue on each of the subunits has been phosphorylated (Krebs and Fischer (1956)). Conversion of Ppb to Ppa occurs through phosphorylation of the protein by Mg^{2+} and ATP in a reaction catalyzed by the enzyme, phosphorylase kinase. The reverse conversion is catalyzed by phosphorylase phosphatase.

Both a and b forms may be reversibly dissociated into monomeric subunits on treatment with sulphydryl reagents such as para-chloromercuribenzoate (pCMB) (Madsen and Cori (1956)) or 5,5'-dithiobis-(2-nitrobenzoic acid) (DTNB), or "deforming agents" such as imidazole citrate. The subunits re-associate if the dissociating agent is removed; e.g. by addition of cysteine in excess in the case of pCMB or dialysis. (Fischer et al (1970)). Figure 1.1 indicates the scheme of reactions.

Each monomer appears to be a single polypeptide chain (Fischer et al (1970)) of molecular weight approximately 100,000.

Similar types of interconversion between a and b forms have been observed in phosphorylases from other species; e.g. insects and yeast; but they have not been demonstrated in potato or in bacterial phosphorylases (Graves and Wang (1972)) p. 436).

1.2 Catalytic Reaction

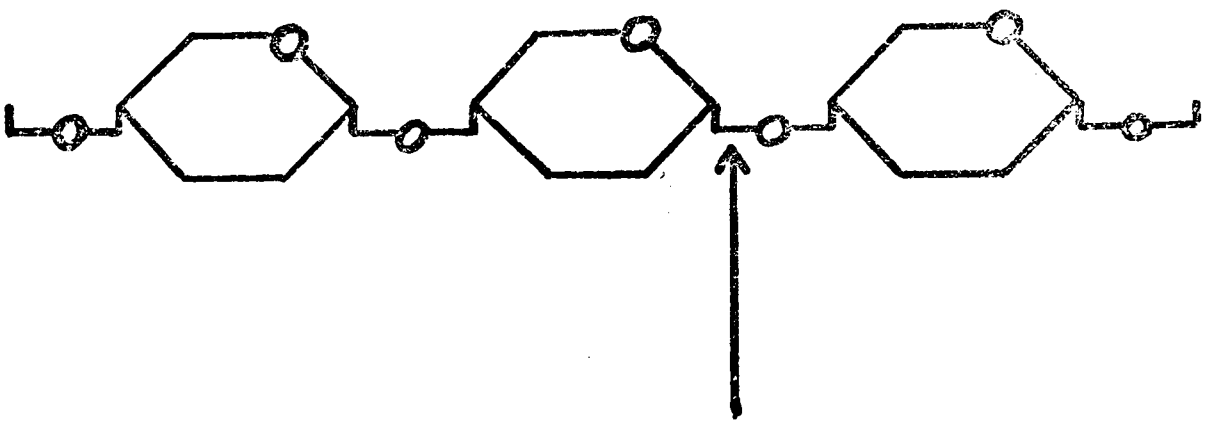
The reaction catalyzed by phosphorylase is:

$$G_n + P_i \rightleftharpoons G_{n-1} + G\text{-}1\text{-}P$$

where G_n and G_{n-1} represent polysaccharides of α-1,4-glucosides with n and (n-1) glucosyl units respectively. Figure 1.2 shows

FIGURE 1.2

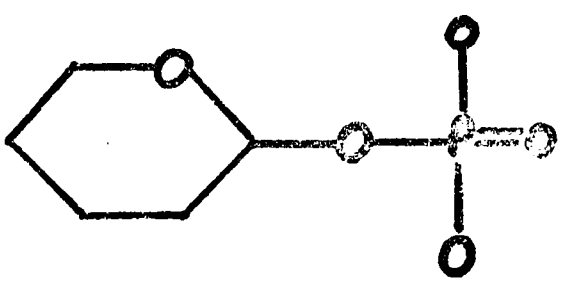
3 α-1,4-glycosyl residues:



Cleavage point

The point of cleavage in the degradation of glycogen

Glucose-1-phosphate



the point of clevage in the glucoside chain. The muscle enzyme reacts optimally with the branched polysaccharides glycogen and amylopectin (Brown and Cori (1961)).

The equilibrium constant of the reaction is determined by the ratio $[P_i]/[G\text{-}1\text{-}P]$ (Hestrin (1949); it is pH dependent and at pH 6.8 the ratio is 3.6 (Hanes and Maskell (1942)). However, in vivo the main function of the enzyme is to degrade polysaccharide; i.e. the equilibrium lies on the other side (Larner et al. (1960)). Turnover rates at pH 6.8 are typically of the order of 8000μ mole of substrate converted per min per μ mole of enzyme protomer.

1.3 Physical and Chemical Properties

There have been numerous determinations of the molecular weight of the enzyme by various means. These experiments give a molecular weight for the monomer in the range 9.25×10^4 to 9.8×10^4 for the rabbit muscle enzyme. Phosphorylases from several species and tissues have molecular weights similar to that of the rabbit muscle enzyme (Graves and Wang (1972)).

An electron microscopic investigation (Chignell et al. (1968)) indicated that the dimer of Ppb consists of two ellipsoidal units with overall measurements 55 Å x 65 Å x 110 Å. The tetramer was thought to be a symmetrical association of dimers giving an overall rhombic shape. This result lead these workers to suggest that the monomeric units were not precisely identical. However a more recent investigation using an electron microscope (Eagles and

TABLE 1.1

AMINO ACID COMPOSITION OF MUSCLE GLYCOGEN PHOSPHORYLASES

RESIDUES PER 92500 G OF PROTEIN

	Rat	Rabbit	Human	Frog	Lobster
Lysine	43	43	47	42	49
Histidine	19	19	23	20	21
Arginine	60	59	63	53	51
Aspartic acid	95	91	94	90	93
Threonine	31	32	32	34	39
Serine	28	27	24	34	37
Glutamic acid	91	94	88	84	91
Proline	36	39	33	43	31
Glycine	45	46	46	47	48
Alanine	59	60	62	55	57
Cystine	8	8	8	11	11
Valine	53	57	56	57	46
Methionine	22	20	21	20	20
Isoleucine	48	45	46	43	61
Leucine	74	75	75	70	73
Tyrosine	34	34	33	34	34
Phenylalanine	35	36	39	35	32
Tryptophan	13	12	11	12	13
Total	794	797	801	784	807

Johnson (1972)) shows that the tetramer is a square planar array of subunits. There is no evidence from this work that the subunits are not identical.

Low angle X-ray scattering from phosphorylase in solution gives the dimensions of the dimer to be 55.3Å x 61.6Å x 109.4Å (Puchwein et al (1970)).

Optical rotary dispersion and circular dichroism experiments (Johnson and Graves (1966); Hedrick (1966)) indicate that α-helical structure is present in phosphorylase. The action of AMP on Ppb and the phosphorylation of Ppb both cause an 8 to 9 per cent change in the helix content.

The amino acid compositions of rat, rabbit, human, frog and lobster muscle phosphorylases are shown in Table 1.1 (Graves and Wang (1972)). The complete sequence is not yet known for any phosphorylase, however evidence (Graves and Wang (1972), p. 448) suggests that each monomer is only one polypeptide chain. The similarities in composition between the phosphorylases of different species are probably indicative of homology in sequence. The sections of polypeptide chain around the pyridoxal phosphate site (see below), the phosphorylated seryl residue and at the N-terminus have been sequenced for both the rabbit muscle enzyme and the dogfish enzyme. These sections are homologous to almost 90% thus showing a high degree of conservation since dogfish separated from the evolutionary line leading to mammals approximately 450 million years ago (Fischer et al (1971)).

Modification of phosphorylase with various thiol reagents results in loss of enzymic activity. On the basis

of the reactivity of the sulphydryl groups towards iodoacetamide the eight -SH groups per monomer (molecular weight 92500) may be classified into three types (Battell et al (1968); Auramoic-Zikie et al (1970)):

(a) 2 -SH groups react at a similar rate to those in model compounds suggesting surface exposure. Alkalation has little effect on the structure and activity of the enzyme.

(b) 2 -SH groups react several hundredfold more slowly than (a) with resultant inactivation and dissociation of the enzyme.

(c) The remaining -SH groups are not reactive towards iodoacetamide unless the protein is first denatured; these groups are probably buried in hydrophobic regions within the protein.

There is evidence that irradiation with X-rays of phosphorylase in solution results in the loss of enzymic activity and the destruction of the -SH groups. (Damjanovich et al (1967)).

1.4 Binding Sites on the molecule

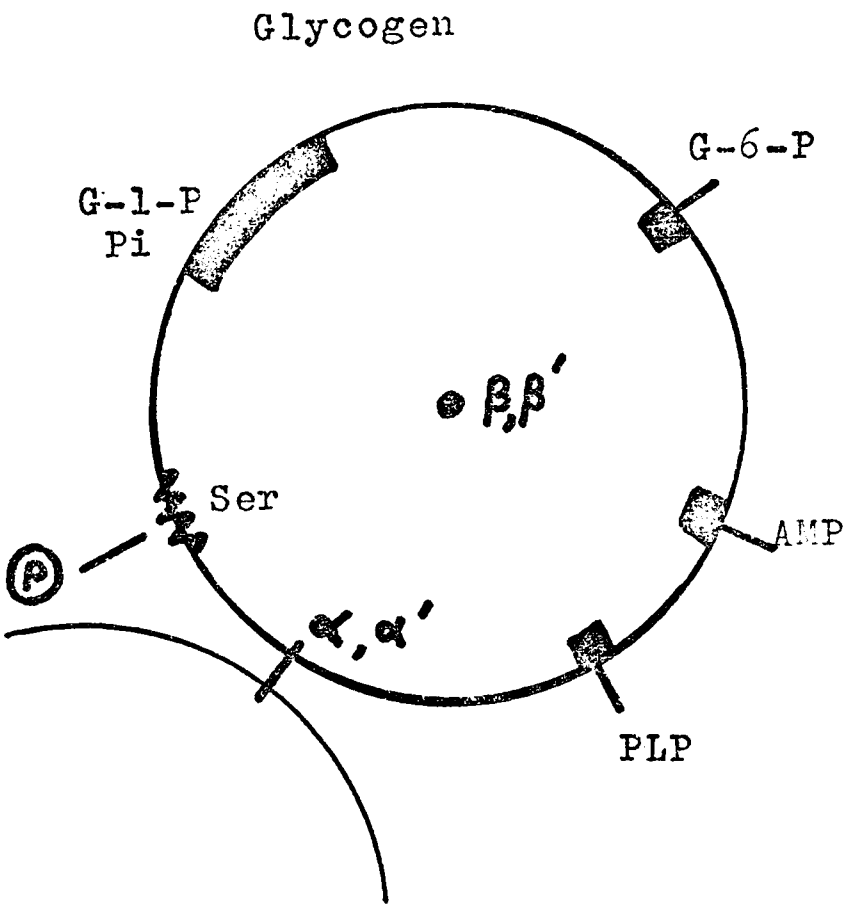
The monomer appears to have binding sites for several different metabolites. These sites are:

1. Mg^{2+} site This site is involved in the conversion from Ppb to Ppa.

2. Glucose-6-Phosphate site G-6-P is an inhibitor of the enzyme.

3. Substrate binding sites These are sites which bind glycogen, glucose-1-phosphate and inorganic phosphate.

FIGURE 1.3



α, α is the monomer-monomer interaction site

β, β is the dimer-dimer interaction site

The binding sites on the phosphorylase moner

4. AMP binding site. Ppb is inactive in the absence of AMP, though Ppa is active in the absence of this effector. IMP, is also found to activate Ppb though not to the same degree as AMP unless a number of the ions are added as well; e.g. protamine, polyamines and F^-, or the concentration of the substrate G-1-P is increased (Graves and Wang (1972)). ATP is a competitive inhibitor of Ppb and probably binds at the AMP site.

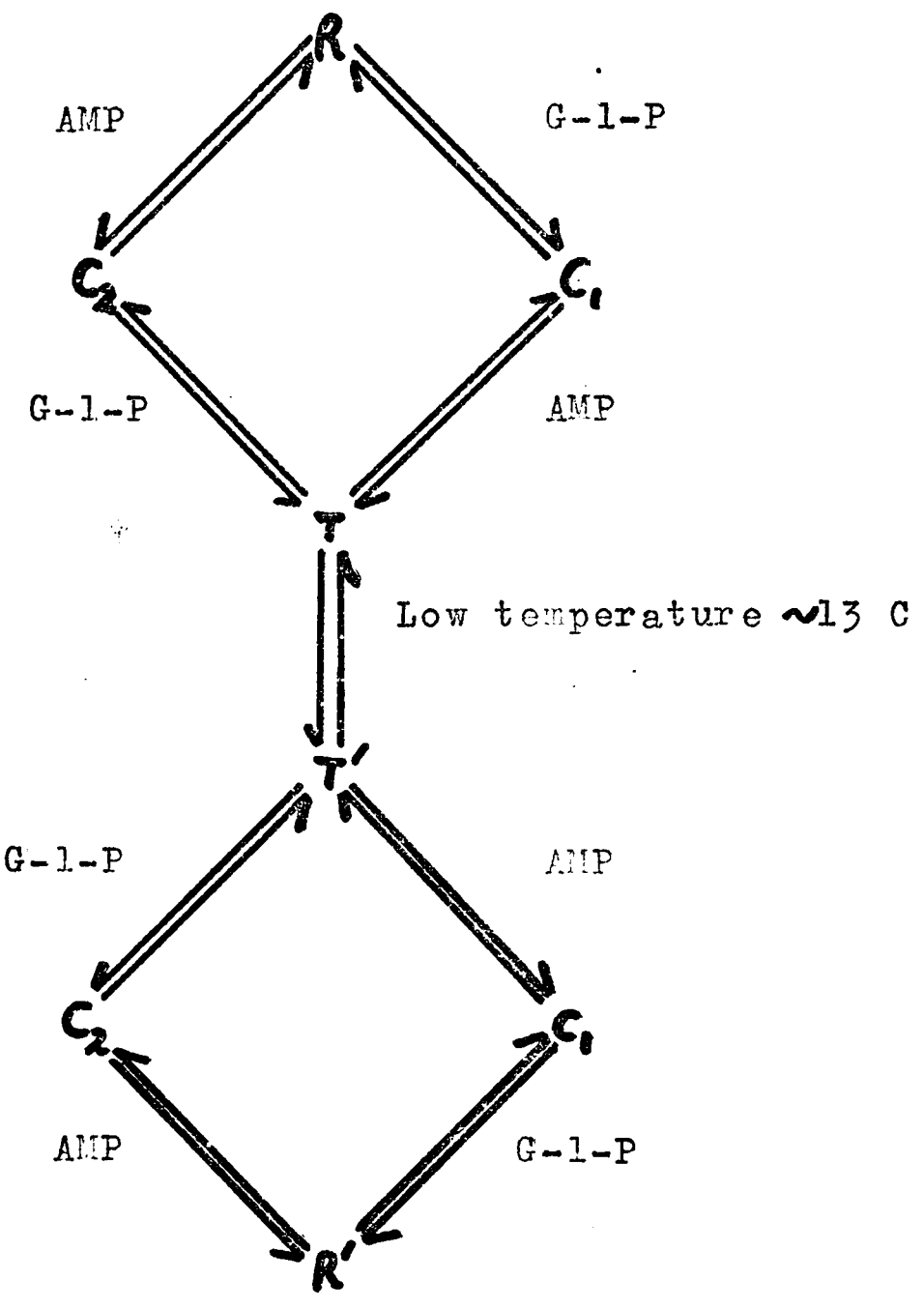
5. Pyridoxal phosphate site. Phosphorylase requires this coenzyme for activity, but its function is not yet known. If PLP is removed the enzyme becomes completely inactive (Illingworth et al (1958)). The apo-enzyme has the same helix content as the native enzyme, but a slightly less ordered overall structure as measured by optical rotary dispersion experiments (Hedrick (1966)). All the α-glucan phosphorylases so far studied which catalyse the phosphorylation of α-1,4-polyglucose chains with retention of configuration contain PLP and are inactive without it.

6. Serine site. This is the serine, the -OH group of which, is phosphorylated during the conversion from Ppb to Ppa. This phosphorylation is responsible for the covalent control of enzymic activity (Krebs and Fischer (1950)). It appears that the serine must occupy an exposed site on the enzyme's surface because:

(i) it is acted on by both phosphorylase kinase and phosphorylase phosphatase and so must be structurally capable of this interaction.

(ii) it is readily attacked by several proteolytic

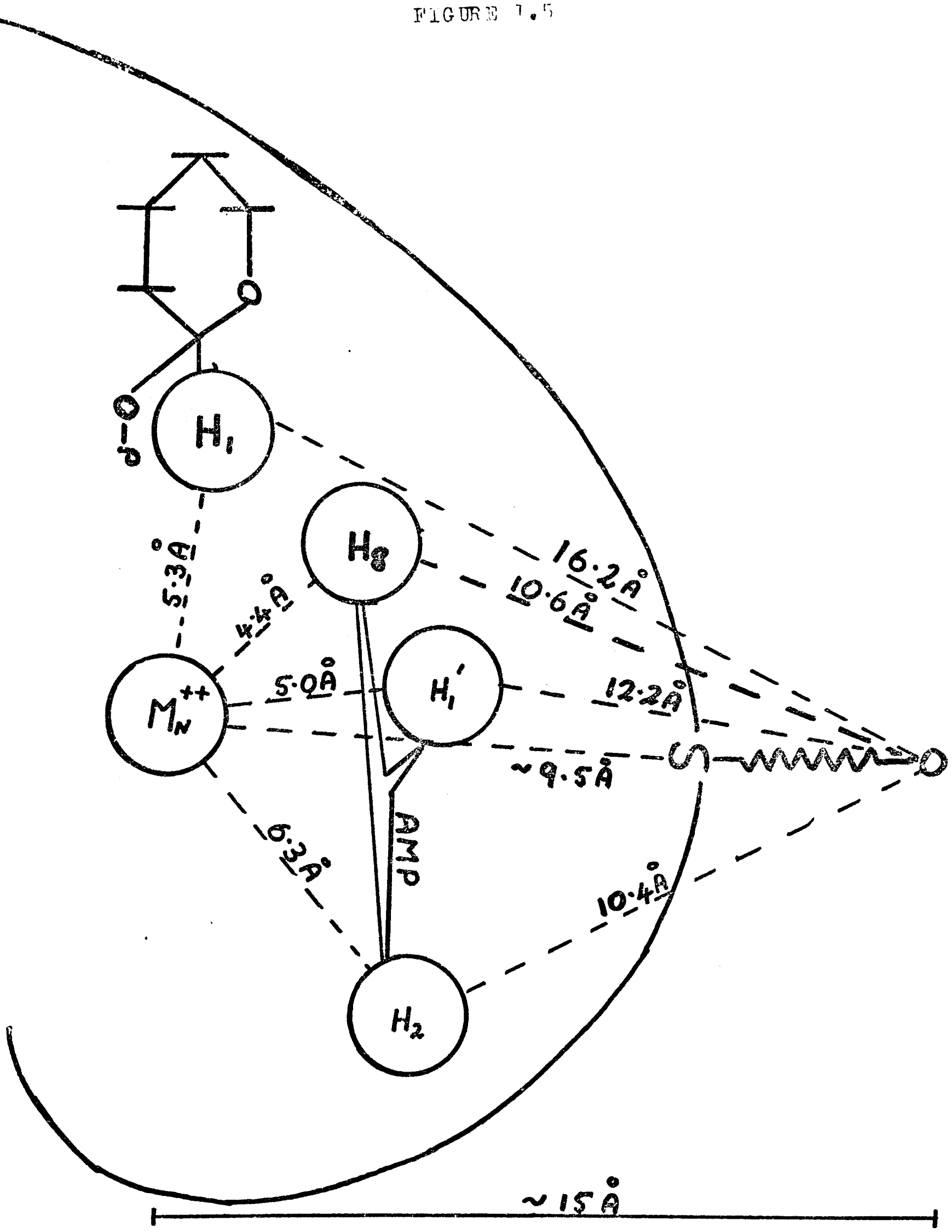
FIGURE 1.4



R, R', C_1, C_2, T&T' are conformational states of the enzyme

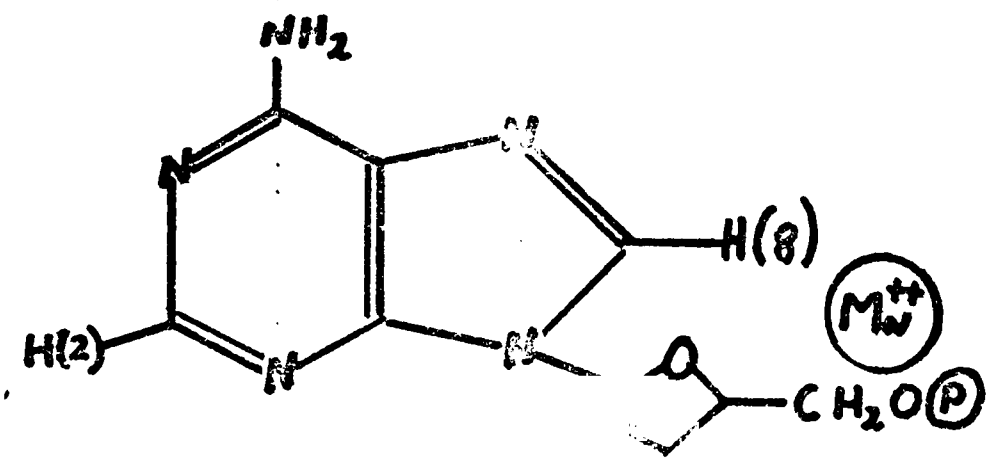
The conformational states of Phosphorylase b

FIGURE 7.5



The positions of the groups on the enzyme surface

The AMP hydrogen atoms are:



enzymes. (Fischer et al (1970) p. 37)

In addition to these sites there must be monomer-monomer, and dimer-dimer interaction sites. Figure 1.3 shows a schematic representation of the monomer with some of these sites indicated.

Phosphorylase b has been investigated using the techniques of nuclear magnetic resonance, electron spin resonance, and fluorescence quenching (Bennick et al (1971)); Dwek and Radda (1972)). These studies indicated four conformational states of the enzyme in the presence and absence of the effectors, G-1-P and AMP. A temperature dependent transition at 13°C was also observed which lead to a further four conformational states. These results are represented schematically in Figure 1.4.

Using an Mn^{2+} paramagnetic probe bound to the enzyme, these workers were also able to suggest the relative orientation of the G-1-P, AMP, Mn^{2+} sites and one of the -SH groups on the enzyme's surface, and derive values for the distances between these sites. The resultant map of the enzyme's surface is shown in Figure 1.5.

1.5 Mechanism of Action

The fact that Ppb requires AMP for activity lead to the prediction (Monod et al (1963)) that phosphorylase should be analogous to other allosteric enzymes and exhibit co-operative kinetics. Two models have been suggested to explain this:

1. The concerted model (Monod et al (1965)). The basis of this model is that equilibrium is maintained between the two conformation states of an oligomeric enzyme; these

states differ in their affinities towards substrates and effectors. Symmetry is conserved and, therefore, conformational changes within the subunits of any one molecule occur in concert. Preferential binding of a ligand to one of the states displaces the equilibrium, and the resulting statistical increase in the number of binding sites generates apparent cooperative ligand binding; i.e. homotrophic interaction. Heterotrophic interaction is also possible with this model.

2. The Sequential Model (Koshland et al (1966))

The basis of this model is a ligand induced conformational change in the subunit. This can result in heterotrophic interactions within the subunit, and, if the subunits are tightly coupled so that a change in one induces a similar change in the other, homotrophic cooperativity.

With the experimental data so far obtained it has not been possible to decide which model best explains the mode of action of phosphorylase. The allosteric properties of phosphorylase are still poorly understood.

The monomer of phosphorylase appears to have no intrinsic enzymic activity (Feldman et al (1972)).

1.6 Control of Enzymic Activity

Interconversion between the a and b forms of phosphorylase constitutes an important mode of control of energy metabolism. In resting muscle the enzyme exists predominantly in the inactive b form (Krebs and Fischer (1955)). Activation occurs via non-covalent changes in conformation due to effectors such as AMP, or covalent modification to the a form.

Activation by AMP depends on the nature and concentration of the substrates, the type and concentration of divalent metal ions present, and the pH and the temperature of the environment of the enzyme. In muscle, the concentration of AMP is sufficiently high that Ppb should always be active. Such activity is not observed probably because of the relatively high concentrations of the inhibitors ATP and G-6-P in the cell.

It has been suggested that the AMP induced allosteric transition of Ppb consists of two stages (Black and Wang (1968)):

1. enhancement of the enzyme's affinity towards the substrate, G-1-P.

2. Enhancement of the catalytic efficiency of the enzyme.

The binding of IMP to the enzyme may affect only the second stage, and, therefore, the binding and cooperativity of G-1-P are independent of IMP concentration. This would imply an additional conformational state of the enzyme, induced by IMP binding, which is active, but has a poor affinity for G-1-P.

In vivo AMP activation of phosphosylase appears to be less important than the covalent conversion from the b to the a form. b to a conversion requires Mg^{2+} and ATP and is catalysed by phosphorylase kinase; the reverse reaction is catalysed by phosphorylase phosphatase. When both these enzymes react simultaneously the overall effect is that of an ATP-ase:

$$Ppb + 4ATP \xrightarrow{\text{Phos. kinase}} Ppa + 4ADP$$

$$Ppa + 4H_2O \xrightarrow{\text{Phos. phosphatase}} Ppb + 4P_i$$

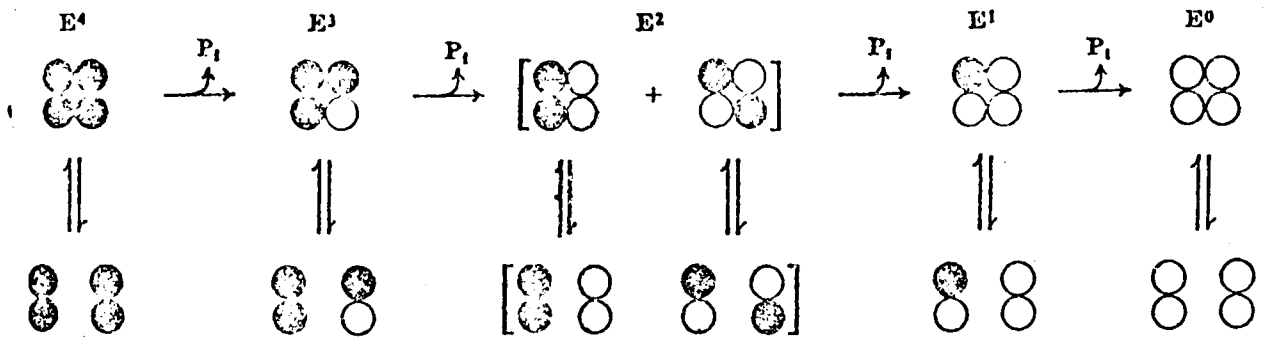
$$\text{Sum: } 4\ ATP + 4H_2O \longrightarrow 4ADP + 4P_i$$

Phosphorylase kinase and phosphorylase phosphatase are strictly specific with respect to phosphorylase. No other proteins have been observed to act as substrates for them, nor have other kinases or phosphatases been shown to act on them (Graves et al (1960)). However, the converting enzymes do not posess rigid species specificity; e.g. the kinase and phosphatase from rabbit muscle act on Ppb and Ppa from a variety of tissues and species (Childress and Sacktor (1970)). This indicates a high degree of conservation of the sequence surrounding the seryl residue which is phosphorylated and de-phosphorylated during the conversions.

The interconversion reactions are affected by metabolites; e.g. the phosphorylase phosphatase reaction is strongly inhibited by AMP (Nolan et al (1964)) and activated by G-6-P. This action of AMP apparently results from its binding to Ppa, since it does not affect the rate of dephosphorylation of phosphopeptides. The activation of phosphorylase phosphatase by glucose is mediated through a conformational change in the structure of Ppa

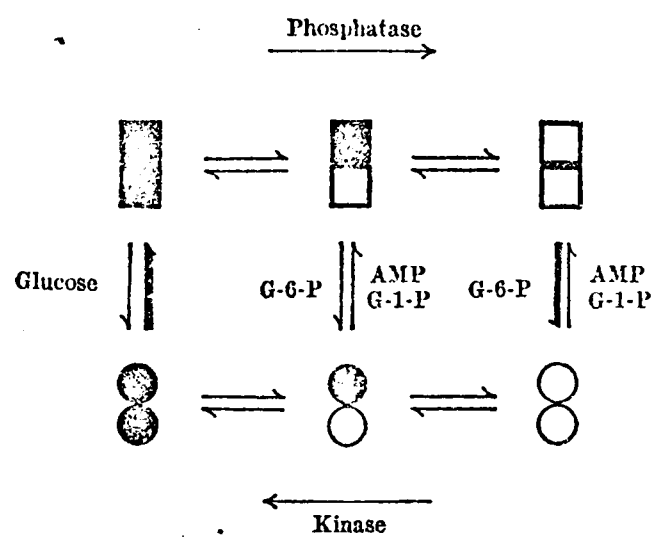
It is possible that some of the specific sites on phosphorylase may have two roles in the control of activity. Firstly, they may affect the activity directly, and secondly, they may regulate the covalent modification of the enzyme.

FIGURE 1.6



A model for the formation of phospho-dephospho hybrids during the phosphorylase a to b conversion.

FIGURE 1.7



A model for the structure and conformation of phospho-dephospho hybrids.

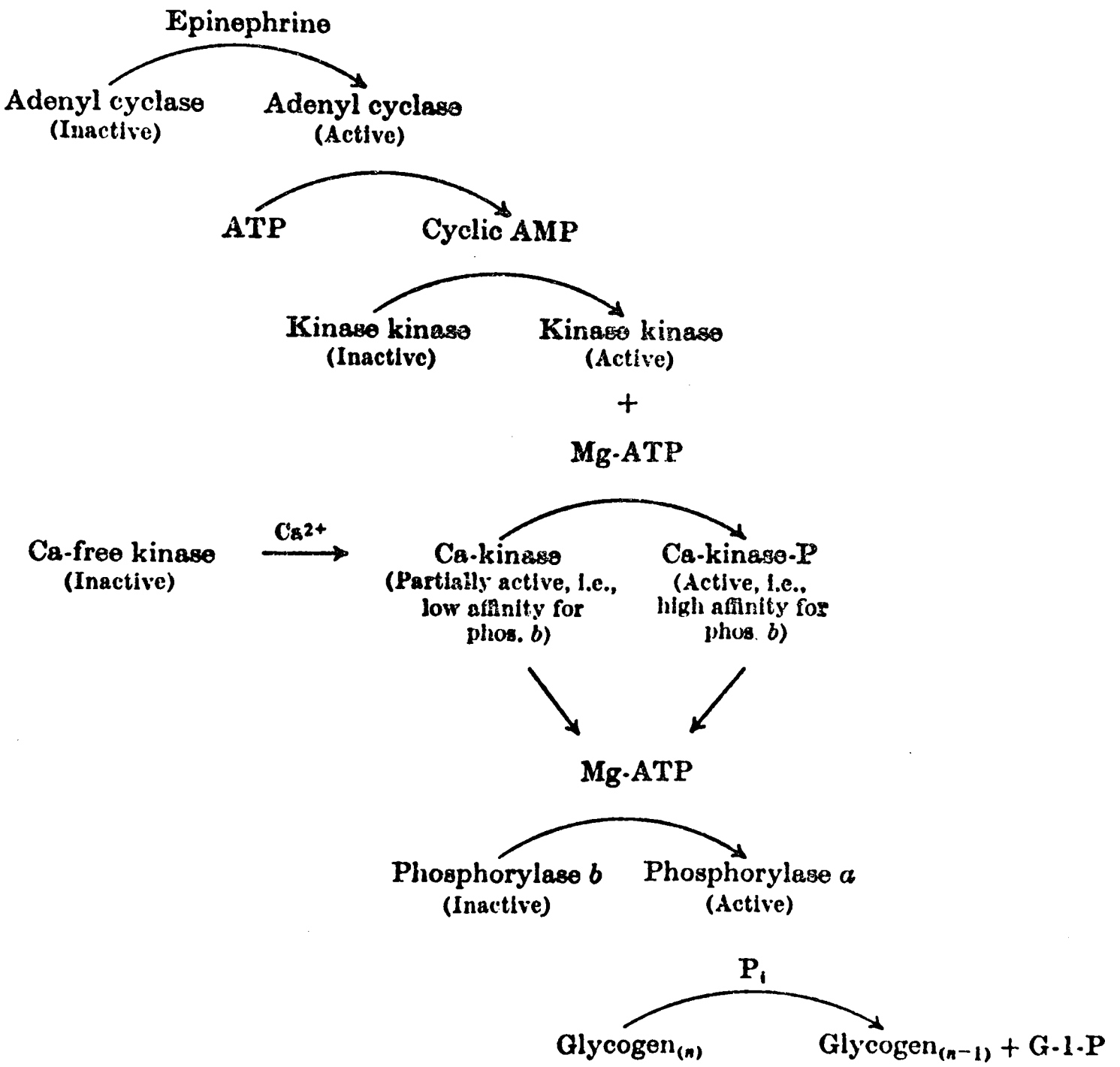
In both figures circles represent inactive conformations and squares active ones. Open and filled symbols represent non-phosphorylated and phosphorylated subunits respectively.

Phosphorylase kinase has 12 subunits and an overall molecular weight of approximately 1.2×10^6. The subunits are of three different types designated α β and γ: the α type is of molecular weight 132,000, the β type is of molecular weight 118,000, while the γ type has a molecular weight of 41,000. The α β and γ types associate into trimers, four of which associate to form the complete molecule (Cohen (1972)). Phosphorylase kinase depends for its activity on Ca^{2+} ions which in the muscle cell are released from the sarcoplasmic reticulum after electrical exitation. The enzyme is converted into a form 20 to 30 fold more active by a protein kinase which in turn depends on cyclic AMP for its activity.

The reactions from the fully phosphorylated a form of phosphorylase to the completely de-phosphorylated b form of the enzyme (and vice-versa) proceed in a step by step fashion so that partially phosphorylated intermediates are produced. The type of reaction scheme is shown in Figure 1.6 (Fischer et al (1970)).

It has further been suggested (Fischer et al (1970)) that phosphorylase may exist in both active and inactive forms which are in equilibrium with each other (Figure 1.7). In Ppb the inactive conformation is favoured unless effectors such as AMP, or high concentrations of inorganic phosphate are present; G-6-P favours the inactive state. The reverse is true for Ppa where the active conformation is favoured unless glucose is present. In each case the active conformation has a strong tendency to aggregate, and so Ppa, and Ppb in the presence of AMP are normally found in

FIGURE 1.8



A schematic representation of the sequence of reactions leading to phosphorylase activation.

the tetrameric state. The formation of tetramers follows activation, the dimer being the active species (Dwek and Radda (1972)).

1.7 Mechanism of Activation

Despite the relatively high concentrations of Mg^{2+} (approx.10mM) and ATP (approx.7mM) in resting muscle (Fischer et al (1970)), phosphorylase remains inactive in the b form. This appears to be due to phosphorylase kinase which is inactive at physiological pH (approx. 6.8); the activity can be increased by raising the pH to 8.2-8.6 (Krebs et al (1959)); (Krebs et al (1966)); (Krebs et al (1964)). In the cell phosphorylase kinase is converted into a form which is active at pH 6.8 in a reaction which requires Ca^{2+} ions and is catalysed by the enzyme, kinase kinase. Kinase kinase is dependent on the presence of cyclic AMP for activity. Cyclic AMP is produced from ATP by the enzyme, adenyl cyclase, which is stimulated by the hormone, epinephrine. (Bitensky and German (1973)).

Thus the steps leading to the activation of phosphorylase and consequent degradation of glycogen form a very elaborate control mechanism which is stimulated initially by a hormone. A schematic representation of the sequence of reactions is shown in Figure 1.8.

1.8 Summary

From this review it is clear that phosphorylase is a very important enzyme from several respects:

1. It is one of the controlling enzymes in the glycolytic system.

2. It is a good model system for the study of phosphorylation.

3. It can help us to a better understanding of the structural basis of control states.

4. It is a good model of allosteric systems.

Many of the questions about this enzyme will not be answered until its three dimensional structure has been determined to a high resolution. X-ray crystallography is the only technique, in use at the present time, by which we can hope to find this structure. However, the very large molecular weight of the enzyme and, consequently, large unit cells of its crystals make the structure determination a daunting problem.

Until recently the only crystals which had been obtained of a suitable size for X-ray structure determination were of phosphorylase in the tetrameric state (Madsen et al (1971)), and therefore presented a considerable crystallographic problem since the assymmetric unit had a molecular weight of approximately 400,000. However, recently, large single crystals with the monomer as the assymetric unit have been obtained (Eagles et al (1973)). These crystals are very suitable for X-ray analysis and so the three dimensional structure determination has been started using them. Part of this thesis describes this work.

II PROTEIN CRYSTALLOGRAPHY

In this chapter an outline of the crystallographic theory relevant to the structural studies on phosphorylase, discussed in Chapter 3, and the rotation camera work, discussed in Chapter 4, is given.

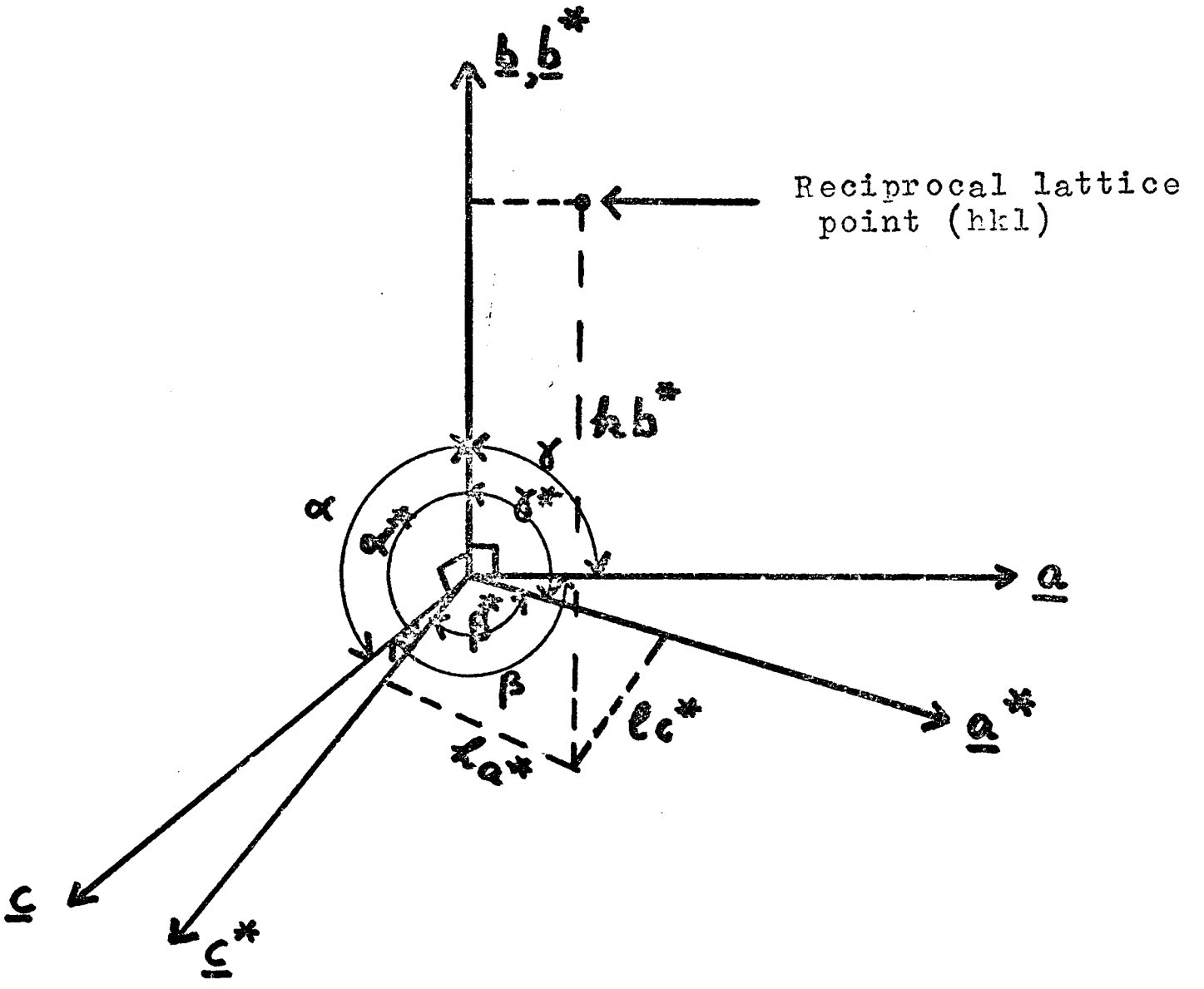
2.1 Crystals and Lattices

The basis of a crystal is an atom, or group of atoms, which is repeated in three dimensional space to form a lattice. The repeat units, or assymmetric units, are related to each other by various symmetry operations, for example, two fold rotation axes, and mirror planes. The number and type of symmetry operations which relate the assymmetric units in a crystal determine the space group of the crystal. By considering the combination of the various symmetry operations it can be shown that there are a possible 230 space groups into which atom and molecules may crystallise.

Proteins are composed of linear polymers of l-amino-acids and, as a result, have a definite "hand". This "handedness" prevents proteins from crystallising into crystal forms which have mirror or glide planes amongst their symmetry elements. As a result, the number of spacegroups for protein crystals is greatly reduced from the 230 possible space groups to the 65 enantiomorphic space groups.

A crystal may be considered to be built up from small parallelepiped-shaped volumes each of which contain one or more assymmetric units. Theparallelepiped which displays the highest possible symmetry, i.e. the space group symmetry,

FIGURE 2.1



The angles are:

$$\left.\begin{aligned}\alpha = \gamma &= 90^\circ \\ \beta &> 90^\circ\end{aligned}\right\}$$ Real space

$$\left.\begin{aligned}\alpha^* = \gamma^* &= 90^\circ \\ \beta^* &< 90^\circ\end{aligned}\right\}$$ Reciprocal space

The relationship between real and reciprocal space vectors for a typical arrangement of unit cell axes.

is called the unit cell, and by convention its three sides are denoted by the vectors $\underline{a}$, $\underline{b}$ and $\underline{c}$.

2.2 X-Ray Diffraction

When a crystal is placed in an X-ray beam the radiation is diffracted because the repeat distances in the crystal are of a size comparable to the wavelength of the X-rays. Typically X-rays with wavelengths in the range 0.5Å to 3Å are used; the most common choice of radiation being Copper Kα of wavelength 1.54182Å.

The X-ray diffraction pattern from a crystal is the fourier transform of the crystal lattice convoluted with the fourier transform of the contents of the unit cell. The fourier transform of the lattice is itself a lattice of discrete points with defining vectors $\underline{a}^*$, $\underline{b}^*$ and $\underline{c}^*$, and is called the reciprocal lattice. $\underline{a}^*$ $\underline{b}^*$ and $\underline{c}^*$ are related to the real space vectors $\underline{a}$, $\underline{b}$ and $\underline{c}$ by the equations:

$$\underline{a}^* = \lambda \frac{\underline{b} \times \underline{c}}{v}$$

$$\underline{b}^* = \lambda \frac{\underline{c} \times \underline{a}}{v}$$

$$\underline{c}^* = \lambda \frac{\underline{a} \times \underline{b}}{v}$$

where v is the volume of the unit cell (= $\underline{a}.\underline{b} \times \underline{c}$), and λ is the wavelength of the X-rays used. a*, b* and c* are measured in dimensionless quantities called reciprocal lattice units (r.l.u.). The geometrical relationship between the real and reciprocal space vectors is shown in Figure 2.1. Any point in the reciprocal lattice can be described exactly by three integers, hkl, called the indices of the point,

which refer to the vectors $\underline{a}^*$, $\underline{b}^*$ and $\underline{c}^*$ respectively (see Figure 2.1). This concept of the reciprocal lattice results from the theory of diffraction originally proposed by von Laue who showed that the conditions necessary for a diffracted beam to be produced in a given direction by a crystal are:

$$\underline{a}.\underline{s} = h$$
$$\underline{b}.\underline{s} = k$$
$$\underline{c}.\underline{s} = l$$

where $\underline{s}$ is the scattering vector defined by the equation:

$$\underline{s} = \frac{1}{\lambda}(\underline{s}_p - \underline{s}_o)$$

where $\underline{s}_p$ is a unit vector in the direction of the diffracted beam, and $\underline{s}_o$ is a unit vector in the direction of the incident X-ray beam. From the above it may be seen that $\underline{s}$ is also given by:

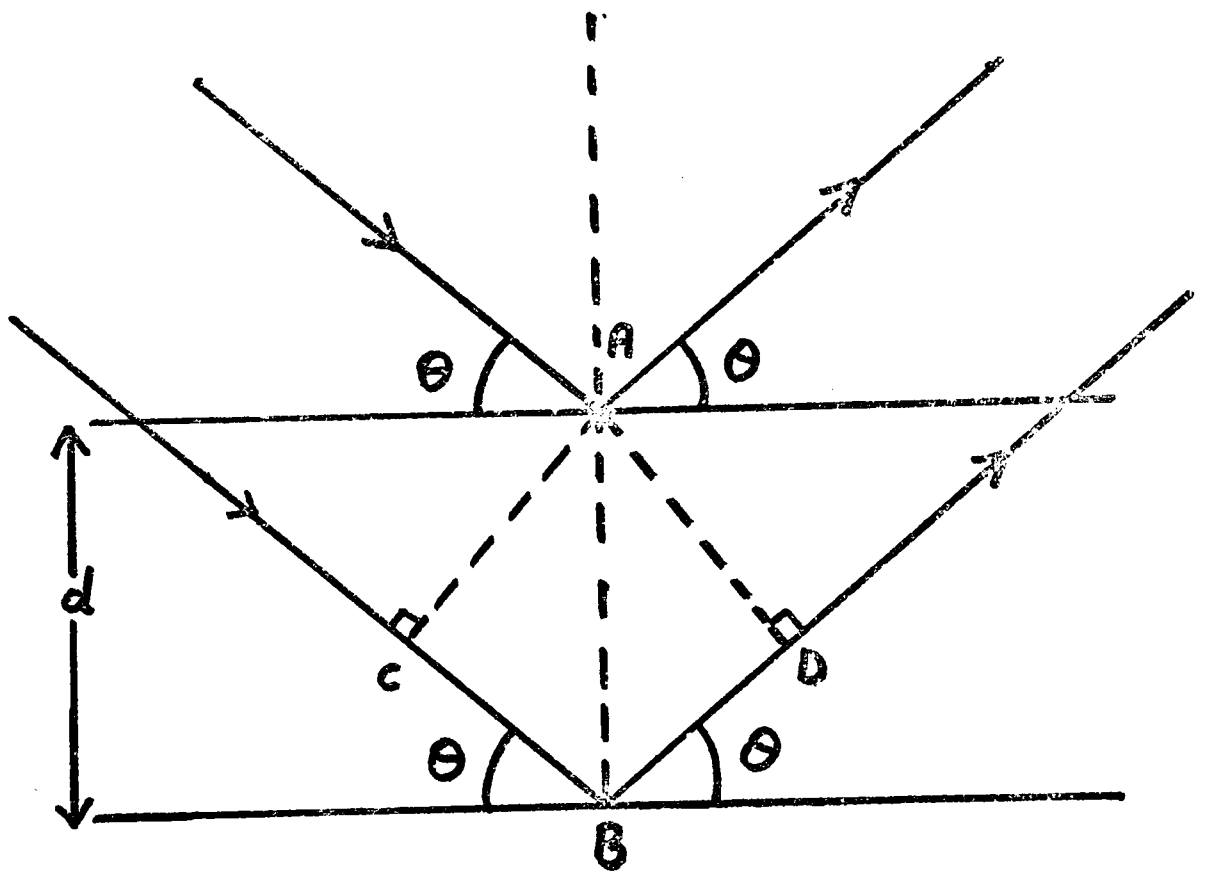
$$\underline{s} = \frac{1}{\lambda}(h\underline{a}^* + k\,\underline{b}^* + l\underline{c}^*)$$

Since the reciprocal lattice is composed of discrete points, the total diffraction pattern of the crystal is the set of points which describe the reciprocal lattice. Each reciprocal lattice point gives rise to a reflection from the crystal which has a precise direction relative to the primary X-ray beam. Each reflection has associated with it a structure factor, $\underline{F}(hkl)$, which is a complex quantity having both an amplitude, $F(hkl)$, and a phase, $\alpha(hkl)$; i.e.:

$$\underline{F}(hkl) = F(hkl) \exp i\alpha(hkl) \qquad 2.1$$

The structure factor arises from the fourier transform of the electron density in the cell according to an equation which is usually expressed as:

FIGURE 2.2



The path difference between X-rays reflected at A and those reflected at b is given by:

$$BC + BD = 2.d.\sin\theta$$

Bragg reflection from crystal planes

$$\underline{F}(hkl) = \sum_{j=1}^{N} f_j(hkl)\exp[2\pi i(hx_j + ky_j + lz_j)] \qquad 2.2$$

where the summation is over the N atoms in the unit cell $f_j(hkl)$ is the atomic scattering factor of the $j^{\underline{th}}$ atom, i.e. the ratio of the amplitude of X-rays scattered by the atom j in the direction of the (hkl) reflection to the amplitude of the beam scattered in that direction by a single electron at the same position $(x_j\ y_j\ z_j)$ in the unit cell. Equation 2.2 shows that each atom in the unit cell contributes to each structure factor through the vector sum of the individual atomic scattering factors.

An alternative view of the geometry of diffraction is due to Bragg (1913). The Bragg and Laue approaches are entirely complementary. In the Bragg approach the planes of atoms in the crystal are considered to be planes of electron density which reflect X-rays in a specular fashion. The situation for two such planes is shown in Figure 2.2. If the primary X-ray beam is at an angle θ to the crystal planes, the path difference between beams reflected by neighbouring planes is $2d\sin\theta$, where d is the separation of the planes. A reflection will occur only when the two reflected beams are in phase, i.e. their path difference is an integral number of wavelengths. The condition for a reflection is then:

$$n\lambda = 2d\ \sin\theta \qquad 2.3$$

where n is an integer and λ is the wavelength of the X-rays. Equation 2.3 is known as Bragg's Law. For a given reflection with indices hkl, the interplanar spacing, d, in the Bragg

equation is related to the distance, d*, of the reciprocal lattice point from the origin of the reciprocal lattice by the equation:

$$d = \frac{\lambda}{d^*}$$

where $d^* = |h\underline{a}^* + k\underline{b}^* + l\underline{c}^*|$

Equation 2.3 with n=1 then gives:

$$d^* = 2 \sin\theta \qquad 2.4$$

Figure 2.2 shows that for a Bragg angle, θ, the diffracted X-ray beam is at an angle 2θ to the incident beam. Equation 2.4 then shows that reflections with higher indices will be diffracted through larger angles than those with lower indices.

2.3 The Electron Density

The aim of X-ray crystallography is to find the electron density, $\rho(xyz)$, at each point in the unit cell. The electron density is related to the structure factors by the inverse fourier transform of equation 2.2; the equation is normally written as:

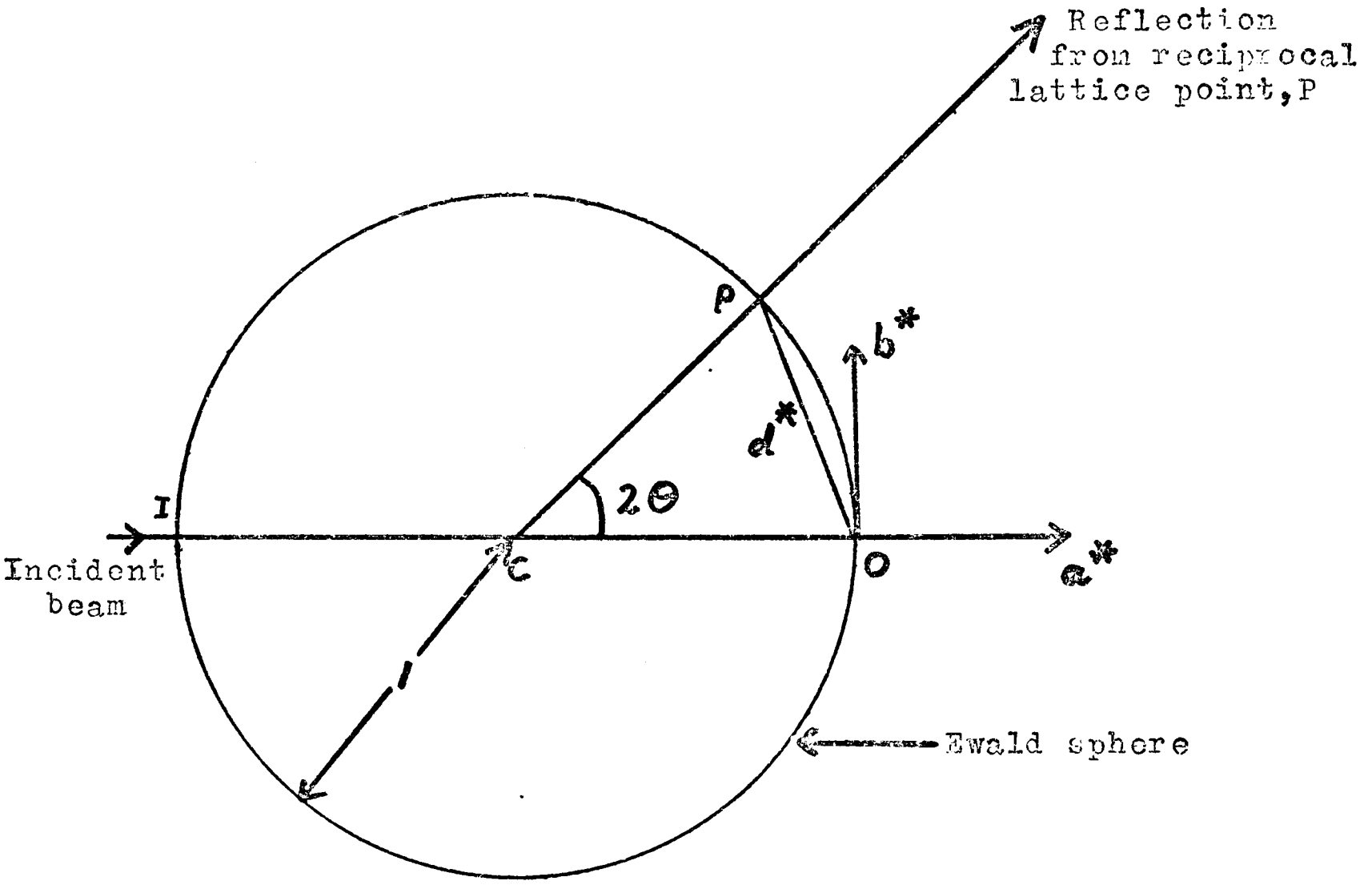
$$\rho(xyz) = \frac{1}{v}\sum_{hkl}\sum\sum F(hkl) \exp i[-2\pi(hx+ky+lz)+\alpha(hkl)] \qquad 2.5$$

where v is the volume of the unit cell.

The quantities F(hkl) and α(hkl) must thus be measured by experiment before a solution of equation 2.5 can be found.

Bragg's Law gives a useful indication of the resolution of this image. If only reflections which correspond to large values of d (equation 2.3) are included in equation 2.5 the image will reveal only the gross structure in the unit

FIGURE 2.3



C represents the position of the crystal
O is the origin of the reciprocal lattice

d^* is the distance from P to the origin of the reciprocal lattice.

The Ewald Construction

cell. As more reflections which correspond to lower values of d are included the finer detail in the structure will become more apparent. In practice the resolution of the image is defined in terms of the minimum value of d for which reflections are included in equation 2.5. Thus a structure determined to a resolution of 6Å is one for which only terms with θ values not greater than $\sin^{-1}(\lambda/2.6)$ are included in equation 2.5.

James (1948) has shown that if dm is the minimum interplanar spacing for which terms are included in equation 2.5, then detail on a smaller scale than about 0.71.dm cannot be resolved in the electron density image. This assumes that the full set of data is included out to the value of dm.

2.4 The Ewald Sphere

The conditions under which reflections occur for a given orientation of a crystal are best understood through a construction due to Ewald. If we consider a circle of unit radius centered on the crystal with the incident X-ray beam forming a diameter of the circle, the origin of the reciprocal lattice is then at the edge of the circle (Figure 2.3) A reflection will occur from a reciprocal lattice point, P, if this point lies on the circle in the given orientation of the crystal. Bragg's law shows that a reflection is deviated by an angle, 2θ, from the incident X-ray beam, and so the angle, $P\hat{C}O$, in Figure 2.3 has a value 2θ. Simple geometry will show that:

$$d^* = 2 \sin \theta$$

which is an alternative formulation of Bragg's Law.

If the crystal is moved, the reciprocal lattice is considered to move in a corresponding manner. Thus, for example, if the crystal is rotated by 5^{o} about a vertical axis, the reciprocal lattice also rotates 5^{o} about a parallel vertical axis. During such a rotation several reciprocal lattice points will cut the circle and give rise to corresponding reflections.

This two dimensional representation of diffraction geometry can readily be extended to three dimensions. The circle of unit radius becomes a sphere of unit radius called the sphere of reflection, or the Ewald Sphere. In such a situation, the points I C and O (Figure 2.3) all lie in the same plane, but the point P may be out of that plane.

In order to measure a reflection the crystal is moved in such a manner that the reciprocal lattice point corresponding to the reflection cuts the reflecting sphere during the motion. The path of the reflection can then be predicted, and a measurement made of the intensity. In practice a crystal is made up of small crystallites all slightly mis-orientated with respect to each other; this mis-orientation is known as the mosaic spread. As a result of the mosaic spread the reciprocal lattice points have a finite size, and so to collect a given diffracted beam the crystal must be moved slowly through a small angular range about the reflecting position so that the whole of the reciprocal lattice point cuts through the sphere of reflection.

2.5 The Energy of a Diffracted Beam

The energy, E, of a diffracted beam arising from the reciprocal lattice point with indices hkl is given by an equation, due originally to Darwin, of the form: · (Woolfson (1970), p 183)

$$E = \frac{\lambda^3}{\omega} I_o K. A. L.p. \frac{V_c}{V^2} |\underline{F}(hkl)|^2 \qquad 2.6$$

where ω is the angular velocity of the crystal as it is moved through the reflecting position.

I_o is the intensity of the primary X-ray beam.

K is a universal constant

A is an absorption factor to account for absorption of the diffracted beam.

L is the Lorentz factor which depends on the reflection geometry.

p is the polarization factor; for a completely unpolarised primary beam this factor is $\frac{1}{2}(1+\cos^2 2\theta)$

V_c is the crystal volume.

V is the unit cell volume.

With any given crystal I_o and ω remain constant while reflection data is being collected and so equation 2.6 reduces to:

$$E \alpha A.L..p. |\underline{F}(hkl)|^2$$

The integrated intensity, I, of a reflection is proportional to the energy of the reflection (Woolfson(1970) P. 168) with the result that:

$$I \alpha A.L.p. |\underline{F}(hkl)|^2$$

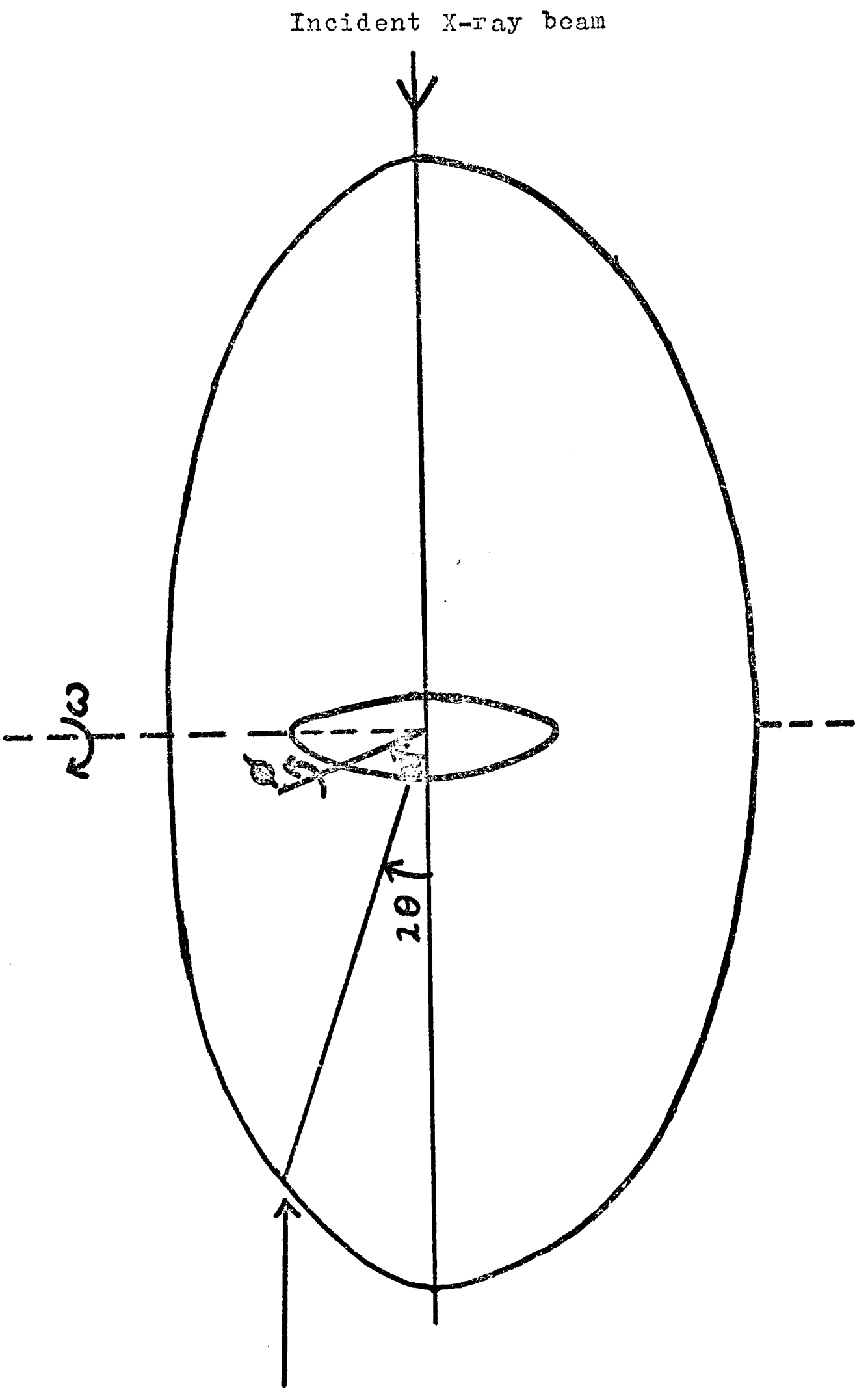
$$\therefore |\underline{F}(hkl)|^2 \alpha \frac{1}{A.L.p.} I \qquad 2.7$$

Equation 2.7 is the form of equation 2.6 which is normally used in X-ray crystallography. An experimental measurement of the integrated intensity of a reflection can be readily made by counting number of X-ray quanta in the reflected beam for a given time using a proportional counter or a scintillation counter, or by estimating the degree of blackening in a photographic emulsion caused by the reflection. The structure amplitude may then be calculated from equation 2.7. However, equation 2.7 carries no information about the phase of the structure factor, and so simply measuring the intensities of the reflections does not yield sufficient information to solve the electron density equation (equation 2.5). As yet there is no experimental method for measuring the reflection phases directly; these quantities must be estimated using techniques which will be discussed later.

2.6 Measurement of Reflection Intensities

The x-radiation used in protein crystallography is normally produced by bombarding a metal target with high energy electrons thus exciting the radiation characteristic of the target as well as white "Bremstrallung" radiation. Copper targets are normally used, the characteristic radiation being the Kα doublet and Kβ lines. Nickel has an absorption edge in a position such that it absorbs relatively more CuKβ than CuKα radiation and so this metal is used as a filter in order to produce relatively monochromatic CuKα radiation of wavelength 1.54182Å. Monochromatic radiation may also be produced by reflecting the radiation from the

FIGURE 2.4



A schematic representation of a 4-circle diffractometer

target off a crystal of known lattice spacing; e.g. a highly ordered graphite crystal; and choosing only that reflection with a Bragg angle corresponding to the required wavelength.

The reflection data from the protein crystal are then measured using either a camera with a photographic film, or a diffractometer with one or more scintillation or proportional counters. The essential difference between the two methods is that a photographic film acts as an area detector; i.e. it collects a large number of reflections without needing to be re-positioned; whereas a scintillation or proportional counter must be re-positioned in order to collect each reflection.

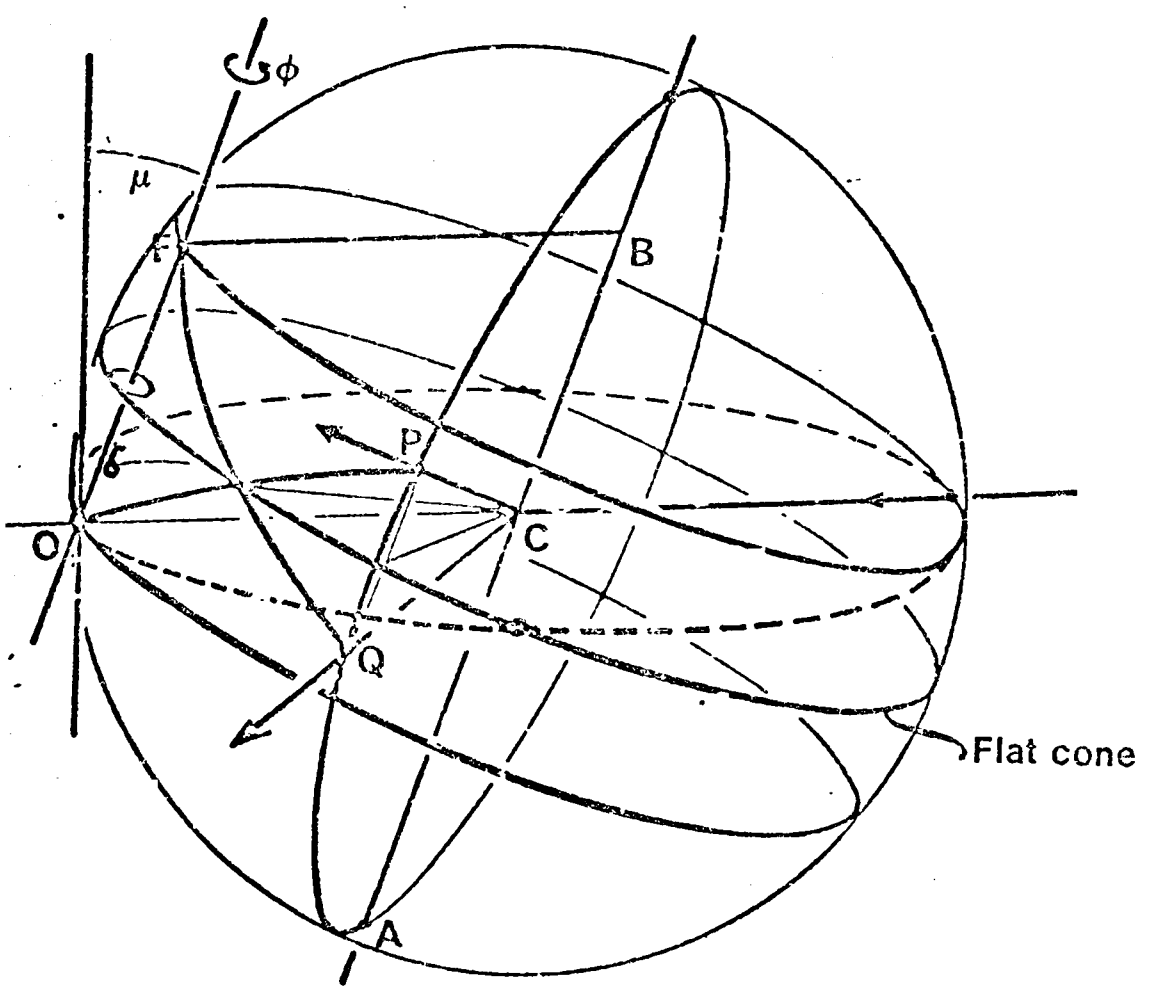
Diffractometers The single counter, four circle diffractometer (Arndt and Willis (1966)), based on Eulerean geometry is currently the most widely used type of diffractometer. The arrangement of the four circles is shown in Figure 2.4. This type of diffractometer is typically controlled by a small digital computer. Once the crystal has been aligned and its unit cell dimensions measured, the computer is programmed to position the diffractometer in the correct orientation relative to the incident beam to measure each reflection sequentially between specified resolution limits. In this manner approximately 30 to 80 reflections per hour may be measured depending on the precision required. With the 4-circle diffractometer the normal setting used is the equi-inclination setting in which the θ and ω angles are equal. In this setting every reflec-

tion within the copper sphere is accessible. There are many examples of protein structures which have been solved using 4-circle diffractometers, e.g. the structure of Phosphoglycerate Kinase to 6Å resolution (Blake et al (1972)).

In contrast to the 4-circle diffractometer, the linear diffractometer uses an analogue computer to control the positions of the crystal and counter relative to each other and the primary X-ray beam. (Arndt and Phillips (1961)); Arndt and Willis (1966)). Two slide arms, which are mechanically linked to the crystal rotation axis and the counter, model the reciprocal lattice within one level up the mounting axis. The diffractometer will measure reflections within one level automatically, but must be reset by the operator for each level.

The principal disadvantage of the diffractometers so far described is that only one reflection can be measured at once. This disadvantage may be overcome by equiping the diffractometer with several counters, and by careful choice of reflection geometry (Phillips (1964)). In the flat cone setting (Buerger (1942)) reflections in levels symmetrically related by the flat cone level will diffract simultaneously in pairs. Also the equivalent reflection in the flat cone level, and any other level within 0.05 rlu. will diffract quasi-simultaneously over a small oscillation range of approximately 1^{o}. A linear diffractometer modified to measure three reflections quasi-simultaneously has been described by Arndt et al (1964). This machine was used to collect the diffraction data from hen egg-white lysozyme

FIGURE 2.5



The flat cone setting.

P and Q are reciprocal lattice points in levels symmetrically related by the flat-cone setting.

crystals (Blake et al (1965)). A more advanced 5 counter diffractometer based on a standard 4-circle machine, but with an extra circle to enable the counters to be rotated about a horizontal axis, has been built in this laboratory (Banner (1972); Evans (1973)).

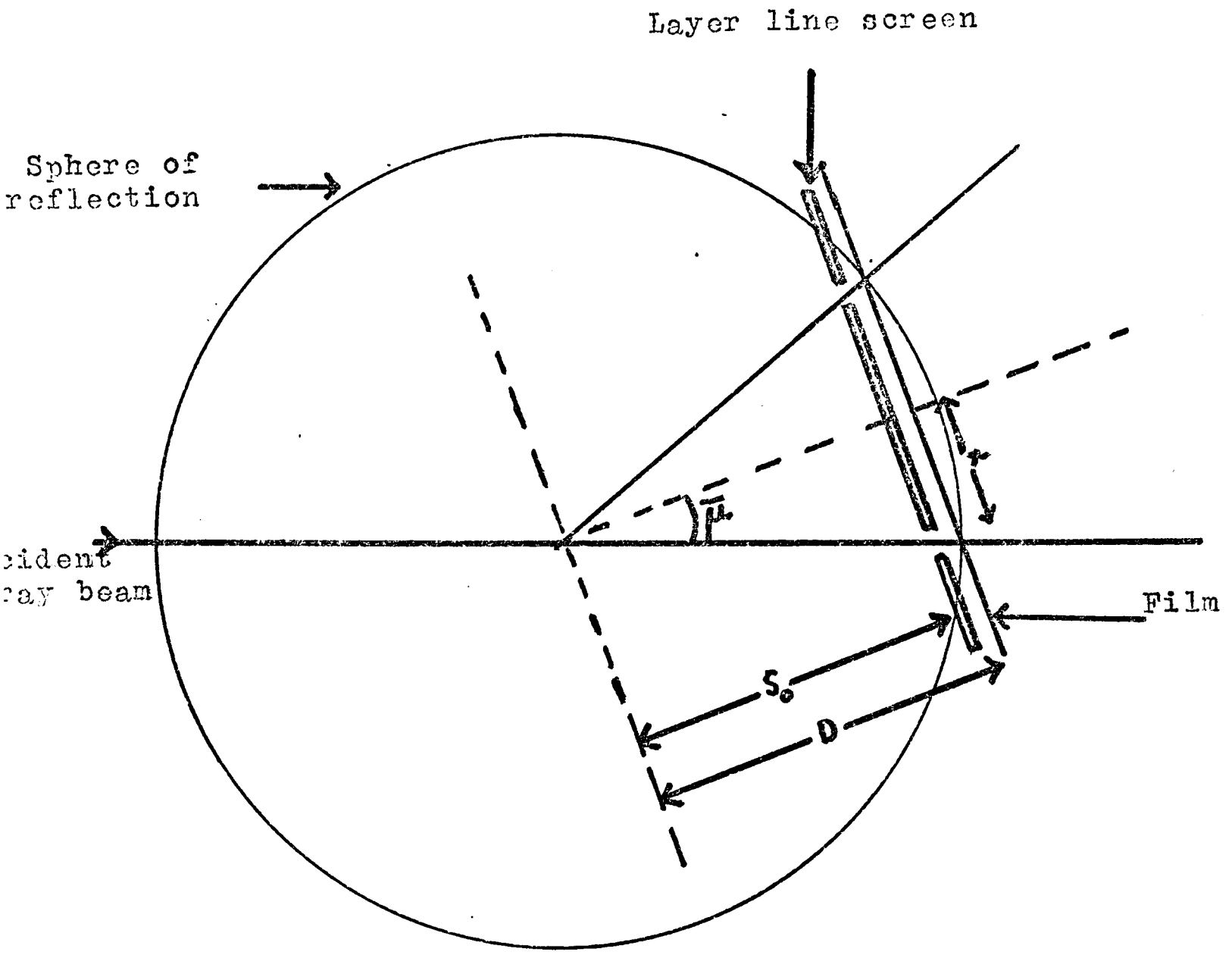
Figure 2.5 shows the flat-cone geometry. The main disadvantage of this setting is that there is a region near the crystal mounting axis on which reflections are inaccessible. The radius, r, or this blind-region is given by:

$$r = (1 - z^2)^{\frac{1}{2}} - (1 - \tfrac{1}{4}\delta^2)^{\frac{1}{2}}$$

where δ is the distance of the flat-cone level from the zero level, and z is the distance from the flat cone level at which r is to be evaluated. The reflections in this blind region may be measured either by putting the diffractometer into the equi-inclination setting, and using only one counter, or by mounting the crystal about a different axis and continuing in the flat cone setting.

Photographic Methods The Buerger precession camera is the traditional tool of protein crystallographers. The crystal and film perform a complex precessional motion about the incident X-ray beam with the result that a time average of a zone of reflections is obtained. In normal use these cameras are used to obtain photographs of given levels within the reciprocal lattice; annular screens are used to prevent reflections from other levels from reaching the film. The photographs so obtained are direct projections of the reciprocal lattice and are, therefore, very easy to

FIGURE 2.6



$\bar{\mu}$ is the precession angle
D is the crystal to film distance
r is the radius of the screen annulus
S is the crystal to screen distance

The precession geometry for measuring a zero level projection photograph.

index. Figure 2.6 shows the orientation of the crystal, screen and film when photographing a zero level projection. Used in this manner, the precession camera is very valuable in the initial stages of a structure determination.

Three dimensional data may be collected by taking screened precession photographs of upper levels; the diffraction data from sperm whale myoglobin crystals (Kendrew et al (1960)) were collected in this way. However, this method is inefficient since many reflections are lost due to the layer-line screen. Xong and Freer (1971) have described a method of collecting data using the screenless precession method with small precession angles. The photographs so obtained are very complicated and can be indexed only with the aid of computer programmes. The main disadvantage of this method is that the Lorentz correction factors become large, and vary rapidly even, in some cases, over the area of a diffraction spot. (Bühner (1972)). Some of the diffraction data from chymotoypsinogen crystals were collected using the screenless precession technique (Freer et al (1970)).

A simpler photographic method of three dimensional data collection is to be found in the rotation camera. In this method the crystal is simply rotated through a small angular range thus bringing various reciprocal lattice points into their reflecting positions. No screens are used, and, therefore, all the reflections which occur within any given partial rotation range are recorded. Since all the reciprocal lattice points move through the sphere along

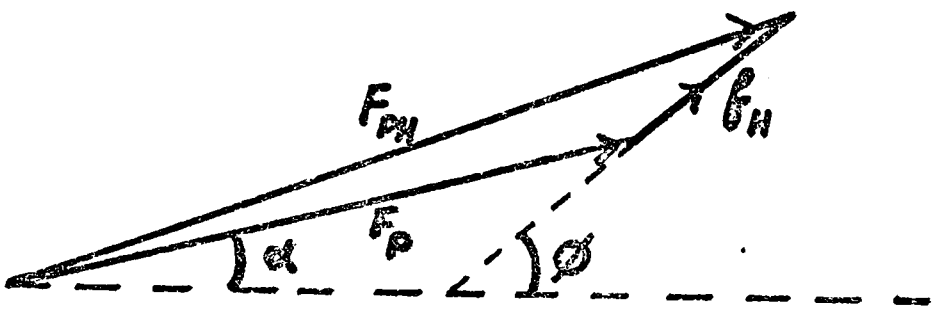
a direction almost normal to its surface, the Lorentz factor changes only slowly over a film. As for screenless precession, rotation photographs of protein crystals are difficult to index without the aid of computer programmes. A rotation camera, and the development of computer programmes to process the films from it, will be described in Chapter 4 of this thesis. No protein structure has yet been solved using diffraction data collected on a rotation camera, however, it is interesting to note that some of the first X-ray diffraction photographs of a crystalline protein were taken on a rotation camera (Bernal and Crowfoot (1934)).

It has been shown (Arndt (1968); Xong et al (1968)) that unscreened photography becomes a more efficient means of data collection compared to diffractometry and screened precession photography as the unit cell of the protein increases in size. A trend towards photographic data collection is inevitable as the structure determination of larger proteins (i.e. with molecular weights greater than approximately 50,000 daltons per assymmetric unit) are attempted. The development of digital microdensitometers (Abrahamsson (1966); Arndt et al (1968); Nockolds and Kretsinger (1970)) and high speed computers has made photographic data collection from crystals of large proteins a viable proposition.

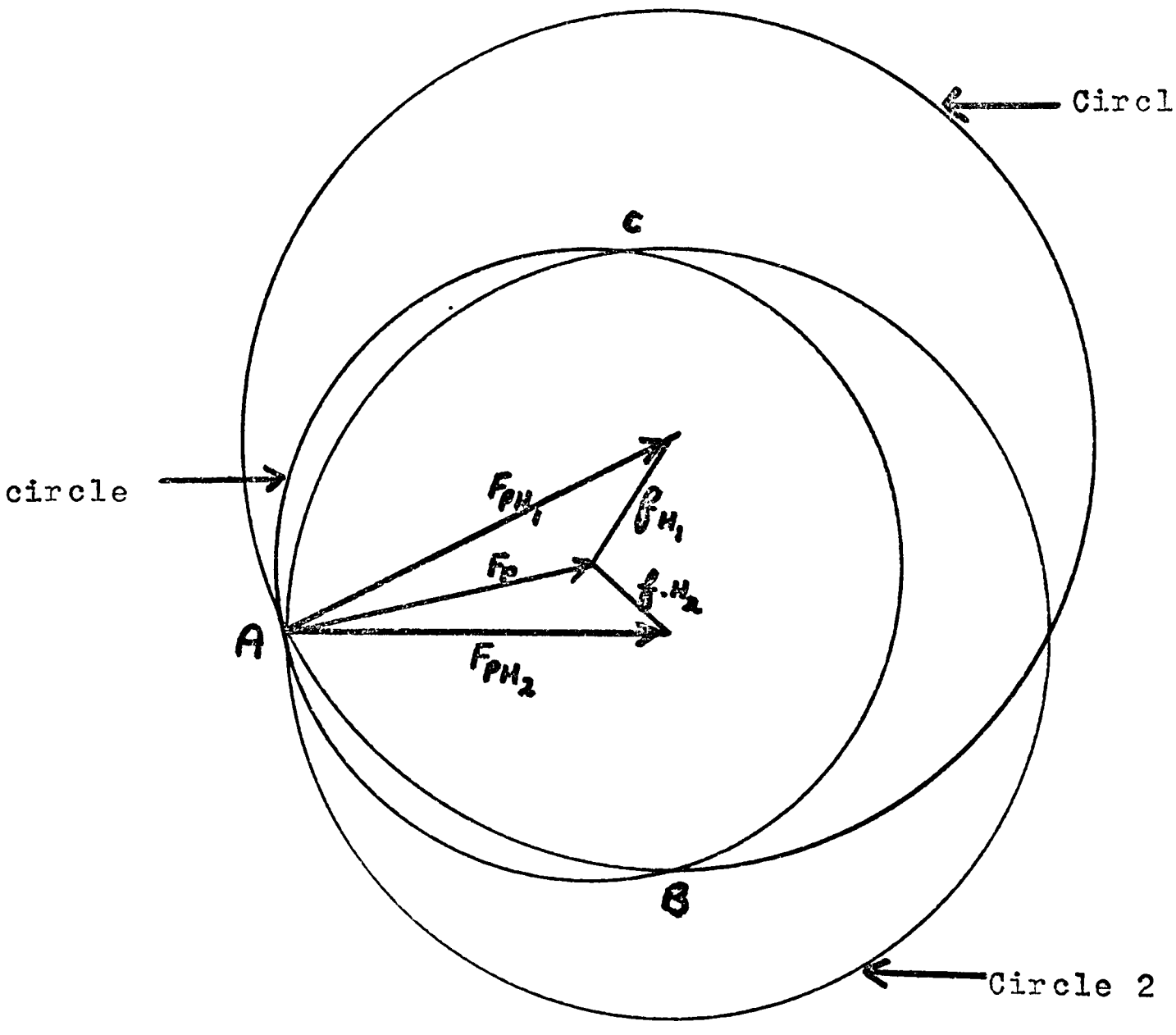
2.7 The Phase Problem

As stated earlier the phase angles of the diffracted beams cannot be measured directly. In all the protein structure determinations to date the method of isomorphous

FIGURE 2.7



a) The effect of addition of heavy atom on a structure factor



b) The Harker Construction

replacement has been used to determine the phases. This method involves replacing one or more light atoms in the native structure by much heavier atoms, normally heavy metal atoms. This replacement must be accomplished without affecting the conformation of the molecule or the lattice spacing in the crystal to any marked degree; that is, the native crystal and its heavy atom derivatives must be isomorphous. Figure 2.7(a) shows the effect on a typical structure factor of introducing a heavy atom into a crystal structure. $\underline{Fp}$ is the structure factor of the native protein with phase, α, and $\underline{f_H}$ is the contribution of the extra heavy atom with phase ϕ. These two quantities add vectorially as shown to give the structure factor $\underline{F_{pH}}$, of the derivative.

The quantities F_p and F_{pH} can be measured experimentally and the heavy atom contribution, f_H, with its phase, ϕ, may be calculated if the positions of the heavy atoms in the unit cell are known. Harker (1956) has given a geometrical construction which allows the estimation of the protein phase angle, α. (Figure 2.7(b)). The vector $\underline{f_{H1}}$ is drawn to scale and circles of radii F_p and F_{pH1} are drawn one centered at each end of $\underline{f_{H1}}$. These circles intersect at two points, B and A, thus giving two possible values for the protein phase, α. This ambiguity can be resolved if a second isomorphous derivative (with the heavy atoms occupying different positions from the first) is introduced with a contribution due to these extra atoms of $\underline{f_{H2}}$. This second derivative will again give two possible phase angles for the protein structure factor, corresponding to the points, A and C. Since the point A is common to both solutions the phase

ambiguity is resolved and the vector representing the protein structure factor, $\underline{F_p}$ will pass through the point A. This of course is an idealised case where the phase circles intersect exactly; the method of phase calculation used in practice is discussed below.

Green et al (1954) first demonstrated with their work on haemoglobin that the method of isomorphous replacement could be used to estimate the native protein phases.

2.8 Location of Heavy Atom Positions

The heavy atom positions must be known in order to calculate the heavy atom contribution, $\underline{f_H}$. These positions are normally found by calculating a difference Patterson synthesis; that is a fourier summation with coefficients:

$$\Delta F^2 = (F_{pH} - F_p)^2 \qquad 2.8$$

This synthesis reveals the vectors between the heavy atoms in the cell, thus allowing the determination of the coordinates of the heavy atoms if the number of binding sites in the assymmetric unit is small. If there is a large number of binding sites with approximately the same heavy atom occupancy at each one, the difference Patterson map becomes extremely complicated and very difficult, if not impossible, to solve.

Once the difference Patterson map of one heavy atom derivative has been solved an initial set of protein phases can be calculated. These phases may then be used to determine the heavy atom positions in another derivative by calculating a fourier summation with coefficients:

$$(F^1_{pH} - F_p)e^{i\alpha_p}$$

where F_{pH}^{1} refers to the second heavy atom derivative (North and Phillips (1969) P. 25). This type of synthesis is also used to refer heavy atom coordinates from different derivatives to the same coordinate system.

If the heavy atoms introduced into the crystal structure scatter anomalously (see below), their positionsmay be determined by a Patterson synthesis with coefficients:

$$(\Delta F_{an})^2 = (F_{pH}^{+} - F_{pH}^{-})^2 \qquad 2.9$$

where $F_{pH}^{+} \equiv F_{pH}(hkl)$ and $F_{pH}^{-} \equiv F_{pH}(\bar{h}\bar{k}\bar{l})$

(Rossmann (1961)). In this type of map the peaks represent the interatomic vectors between the anomalously scattering atoms. Unfortunately the anomalous difference, $(F_{pH}^{+} - F_{pH}^{-})$, is relatively small, and, in many cases, is of the same order of magnitude as the errors in the measurements of F_{pH}^{+} and F_{pH}^{-}. As a result an anomalous difference Patterson map normally has a low signal to noise ratio thus making the heavy atom positions more difficult to find. However, this type of synthesis sometimes provides a useful check of a solution obtained from an isomorphous difference Patterson map.

ΔF in equation 2.8 is a reliable estimate of the heavy atom contribution f_H only for centric reflections where $\underline{F_p}$, $\underline{F_{pH}}$ and $\underline{f_H}$ are colinear, and then only for those reflections where $\underline{f_H}$ has the same phase as $\underline{F_p}$ or where f_H is less than $|F_p|$. Matthews (1966b) has suggested a means of calculating a more reliable estimate of f_H using an equation of the form:

$$F_H^2 = F_p^2 + F_{pH}^2 \pm 2F_pF_{pH}\left(\frac{1-[wk(F_{pH}^{+}-F_{pH}^{-})]^2}{2F_p}\right)^{\frac{1}{2}} \qquad 2.10$$

where k is the ratio of the real to the anomalous scattering factors of the heavy atom; i.e. k = f'/f", and w is a weighting factor, which is an estimate of the relative reliability of the measurement of $(F_{pH}^{+}-F_{pH}^{-})$ compared with $(F_{pH}-F_p)$. The isomorphous differences, $(F_{pH} - F_p)$, are in general larger than the anomalous differences, $(F_{pH}^{+}-F_{pH}^{-})$, and can therefore be measured with greater relative accuracy. However, isomorphous differences are subject to errors due to lack of isomorphism, native to derivative scaling, and absorption corrections (North (1965)), whereas in favourable cases the anomalous differences are free from such errors and, therefore, have greater intrinsic accuracy. The value of w is chosen empirically to give the best signal to noise ratio in the Patterson synthesis; Matthews suggests a value of 0.75.

Equation 2.10 gives two values for F_H, one corresponding to the positive and the other to the negative signs; these are known as upper and lower estimates respectively, and are given the symbols F_{HUE} and F_{HLE} (Dodson and Vijayan (1971)). In practice F_{HLE} is used, but the value of F_{HUE} may be used to select only those reflections for which F_{HLE} is a reliable estimate of f_H. F_{HUE} is a reliable estimate of f_H only when $|\alpha_p - \alpha_{pH}|$ is greater than 90°. Dodson and Vijayanshow that this condition is true for very few reflections which may be easily selected out.

At first sight the value of k in equation 2.10 should be

equal to the theoretical ratio of the real to the anomalous form factors for the heavy atom in question. However (Matthews (1966 b)) the "heavy atoms" which are bound to protein molecules in the isomorphous replacement technique frequently take the form of large groups of atoms, e.g. $(PtCl_4)^{2-}$. The anomalous scattering from heavy atoms results from the tightly bound K, L and M shell electrons which, in general, are unaffected by chemical binding, whereas the real scattering component arises from the outer shell electrons which themselves take part in chemical binding. As a result the theoretical value of k for a particular heavy metal will not correspond to the observed value for that metal in a complex. In this situation it is better to use an empirical value for k determined from the equation:

$$k = 2 \frac{\sum |F_{pH} - F_p|}{\sum |F_{pH}^{+} - F_{pH}^{-}|} \qquad 2.11$$

where the sum is taken over reflections in a particular range of $\sin^2\theta/\lambda^2$. Using equation 2.11 values of k for various ranges of $\sin^2\theta/\lambda^2$ are obtained, and therefore a plot of k versus $\sin^2\theta/\lambda^2$ may be constructed. Such a plot is, in general, linear, and may be used to interpolate the value of k for a particular reflection. (Dodson and Vijayan(1971)). This empirical value of k is normally less than the theoretical value.

2.9 The Quality of Heavy Atom Derivatives

The thermal vibration of an atom in a crystal structure has the effect of reducing its contribution to the set of structure factors. Equation 2.2 may be amended to take account of this, giving an equation of the form:

$$\underline{F}'(hkl) = \sum_{j=1}^{N} f_j(\theta)\exp[2\pi i(hx_j+ky_j+lz_j)].\ \exp(-B_j\sin^2\theta/\lambda^2) \qquad 2.12$$

where B_j is a parameter known as the temperature factor of the atom j.

Wilson (1942),(1949) showed that if the asymmetric unit of the crystal contained a relatively large number of atoms of approximately the same scattering factor, f_j, then the mean intensity of the reflections in a given range of $\sin^2\theta/\lambda^2$ is given by:

$$\langle I\rangle_\theta \quad \alpha \quad \sum_{j=1}^{N} f_j^{\,2}(\theta)$$

where N is the number of atoms in the unit cell. Using equation 2.12, the mean intensity in a given range of $\sin^2\theta/\lambda^2$ can be expressed as:

$$\langle I\rangle_\theta = K\left(\sum_{j=1}^{N} f_j^{\,2}(\theta)\right)\exp(-2B\sin^2\theta/\lambda^2)$$

which may be re-arranged to:

$$\ln\left(\frac{\langle I\rangle_\theta}{\sum f_j^{\,2}(\theta)}\right) = -2B\frac{\sin^2\theta}{\lambda^2} + \ln K \qquad 2.13$$

Equation 2.13 thus shows that a plot of $\ln\left(\frac{\langle I\rangle_\theta}{\sum f_j^{\,2}(\theta)}\right)$ versus $\sin^2\theta/\lambda^2$ should be a straight line with a slope of -2B and an intercept lnK. K is the scale factor required to put the intensities on to an absolute scale. A plot such as this is known as a Wilson plot. The assumptions behind the theory have been shown to be valid experimentally (Howells et al. (1950)) provided that:

1. very low resolution data are excluded; i.e. reflections for which $\sin\theta \leqslant \lambda/a$, where a is the shortest cell

dimension, are excluded.

2. there is a large number of atoms in the unit cell all occupying general positions such that one, or a few, atoms do not dominate the intensity distribution.
3. a sufficiently large number (more than 100) of reflections should be used in calculating the averages.

Strictly speaking protein crystals do not obey Wilson statistics (Luzatti (1955)), but the plots tend to linearity at high resolution.

Wilson plots are used mainly for the initial estimation of the temperature factor of the heavy atom in an isomorphous derivative, and also to give an estimate of the absolute scale factor of the derivative which leads to an approximate value for the occupancy of the heavy atom. The general quality of a derivative may also be judged from the shape of its Wilson Plot. For such a 'heavy atom Wilson Plot" equation 2.13 takes the form:

$$\ln \frac{\langle | F_{pH}^2 - F_p^2 | \rangle_\theta}{\sum_{j=1}^{N} f_{H_j}^2(\theta)} = -2B_H \frac{\sin^2\theta}{\lambda^2} + \ln K \qquad 2.14$$

where N refers to the N heavy atoms in the unit cell. The relative temperature and scale factors between native and derivative crystals, or two derivative crystals, may also be estimated using a "Comparative Wilson Plot" (Adams 1968,p.40); here equation 2.13 takes the form:

$$\ln\left(\frac{\langle F_1^2 \rangle}{\sum_{j=1}^{N} f_{1_j}^2}\right) - \ln\left(\frac{\langle F_2^2 \rangle}{\sum_{j=1}^{N} f_{2_j}^2}\right) = -2(B_1 - B_2)\frac{\sin^2\theta}{\lambda^2} + \ln K' \qquad 2.15$$

where the subscripts 1 and 2 refer to the two crystal forms.

The average change in the intensities due to the addition of a heavy atom to a crystal may be estimated theoretically. Crick and Magdoff (1956) define the fractional change in intensity, $\phi\Delta I$, to be:

$$\phi\Delta I = \frac{[\langle(\Delta I)^2\rangle]^{\frac{1}{2}}}{\langle I_p\rangle} = \frac{[\langle(F_{pH}^2 - F_p^2)^2\rangle]^{\frac{1}{2}}}{\langle F_p^2\rangle} \qquad 2.16$$

and show that provided Wilson statistics are obeyed:

$$\phi\Delta I \simeq 2\left(\frac{N_H}{N_p}\right)^{\frac{1}{2}} \frac{f_H}{f_p} \qquad \text{for centric terms}$$

$$\phi\Delta I \simeq \sqrt{2}\left(\frac{N_H}{N_p}\right)^{\frac{1}{2}} \frac{f_H}{f_p} \qquad \text{for acentric terms.}$$

therefore:

$$\frac{(\phi\Delta I)\ \text{centric}}{(\phi\Delta I)\ \text{acentric}} \simeq \sqrt{2}$$

In practice the fractional change in intensity is calculated in various ranges of $\sin^2\theta/\lambda^2$, and a plot of $\phi\Delta I$ versus $\sin^2\theta/\lambda^2$ constructed. The equivalent theoretical plot may also be constructed and so comparison of the two plots will give an approximate value of N_H, the number of heavy atoms in the unit cell. This type of plot can also give a qualitative measure of the quality of a derivative by showing, for example, any discontinuities in $\phi\Delta I$.

For protein crystals the main difficulty in constructing Wilson and Crick-Magdoff plots lies in finding a reliable estimate of N_p, the number of protein atoms in the unit cell, and f_p, the form factor of the atoms in the protein. Ideally, N_p should also take into account the number of water molecules bound to the protein. Since proteins comprise mainly carbon, oxygen

and nitrogen atoms (excluding hydrogen atoms), an approximate value of N_p may be derived by dividing the molecular weight of the protein in the cell by 14 which is the mean mass number of carbon, oxygen and nitrogen. The scattering factor of nitrogen may be used for f_p since this is a reasonable average of the three scattering factors. This approach will obviously give only approximate values for N_p and f_p, and so the values derivated from Wilson and Crick-Magdoff plots will themselves be only very approximate. Despite this, these two types of plot are useful guides to the quality of heavy atom derivatives.

2.10 Scaling Derivative to Native Structure Amplitudes

Native and derivative data sets must, of course, be on the same scale in order to calculate isomorphous differences. An initial scale factor may be derived by considering the ratio:

$$\frac{\sum F_{pH}^{\ 2}}{\sum F_p^{\ 2}}$$

where the summation is taken either over the full data set, or over ranges within the data set, e.g. ranges of $\sin^2\theta/\lambda^2$ or ranges of a particular index. The $F_{pH}^{\ 2}$ are then multiplied by a scale factor to make this ratio unity, or, sometimes, approximately 1.02 to take into account the extra scattering power in the derivative crystals.

A slightly more sophisticated scaling procedure is possible if F_{HLE} coefficients are available. This is based on the assumption that:

$$k\langle F_{pH}^{\ 2}\rangle = \langle F_p^{\ 2}\rangle + \langle F_{HLE}^{\ 2}\rangle \qquad 2.17$$

where k is the scale factor to be calculated. Alternate cycles

of F_{HLE} calculation and scale factor calculation rapidly lead to convergence of the scale factor.

If the heavy atom contributions to the derivative structure factors are known approximately, the Kraut scaling procedure (Arnone et al (1971)) may be used. In this procedure the scale factor, k, is calculated from the equation:

$$k\langle F_{pH}^2\rangle = \langle F_p^2\rangle + \langle F_H^2\rangle$$

This is the most accurate method of calculating scale factors, but obviously can be used only at a fairly advanced stage in a structure determination.

2.11 Refinement of Heavy Atom Parameters

Refinement of the parameters (position, occupancy, temperature factor, and sometimes native/derivative scale factor) is achieved by first assuming a model for the heavy atoms; this model is normally the heavy atom solution obtained from a difference Patterson synthesis, or a difference fourier synthesis. The heavy atom contributions arising from this model are then calculated and compared with the experimental measurements. The heavy atom parameters are then adjusted in such a manner as to improve the agreement between calculated and observed quantities Refinement thus proceeds through a series of cycles until the best agreement is obtained. Heavy atom refinement will be successful only if the initial model is approximately correct; i.e. the heavy atom positions must be within approximately 1Å of their correct positions (Lipson and Cochran (1966) p.348).

In any particular case the type of refinement used depends on the type of data and the computing facilities available.

Hart's method (1961) is very useful if the data set contains a large number of centric terms. Only centric terms are used and the quantity minimised is:

$$E = \sum_{hkl} [k F_{pH} - |F_p \pm F_c|]^2$$

where k is the native to derivative scale factor. The minimisation is carried out through a trial-and-error method coupled with a steepest descents procedure.

A more powerful method used with both centric and acentric data involves the F_{HLE} coefficients. In this method the quantity minimised is:

$$E = \sum_{hkl} (F_{HLE} - F_c)^2$$

The refinement proceeds by a full matrix least squares method which minimises the quantity E. The main drawback of this method is that the native to derivative scale factor cannot be refined. The progress of the refinement is followed by monitoring the value of E and also the value of the R factor defined by:

$$R = \frac{\sum_{hkl} |F_{HLE} - F_c|}{\sum_{hkl} F_{HLE}} \qquad 2.18$$

Wilson (1950) showed that for a completely incorrect model structure R takes the values 0.828 for centric terms and 0.586 for acentric terms.

During the course of the refinement minor heavy atom sites may be found by calculating a fourier synthesis with coefficients

(Phillips (1966)):

$$(F_{HLE} - F_C)\, e^{i\alpha_H}$$

When protein phase angles are available, the so called phased refinement procedure may be used (Dickerson et al (1961)). In this method the quantity minimised, by a least squares method, is:

$$E = \sum_{hkl} \omega[k\, F_{pH} - |F_{\underline{p}} + F_{\underline{C}}|]^2$$

where ω is a weighting factor which is normally the square of the figure of merit (see below). The method normally proceeds by several cycles of refinement followed by a cycle of phasing. In its most sophisticated form it involves refining the N^{th} derivative using the phases calculated from the other (N-1) derivatives. The R factor normally used in phased refinement is the Kraut R (Kraut et al (1962)) which is defined by:

$$R_K = \frac{\sum_{hkl} |k\, F_{pH} - |F_{\underline{p}} + F_{\underline{C}}||}{\sum_{hkl} k\, F_{pH}} \qquad 2.19$$

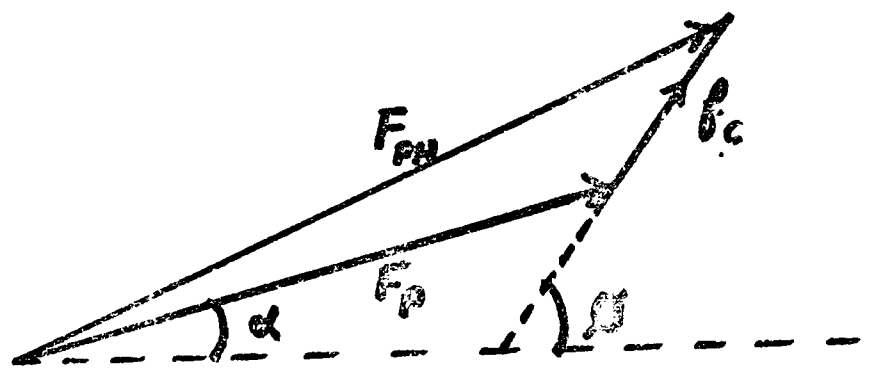
Unfortunately this R factor is relatively insensitive to the progress of the refinement; an overall fall of a few per cent during a series of refinement cycles would be considered significant.

F_{HLE} and phased refinements obviously require much more powerful computing facilities than does Hart's method. However, they are far more powerful methods and are therefore preferable.

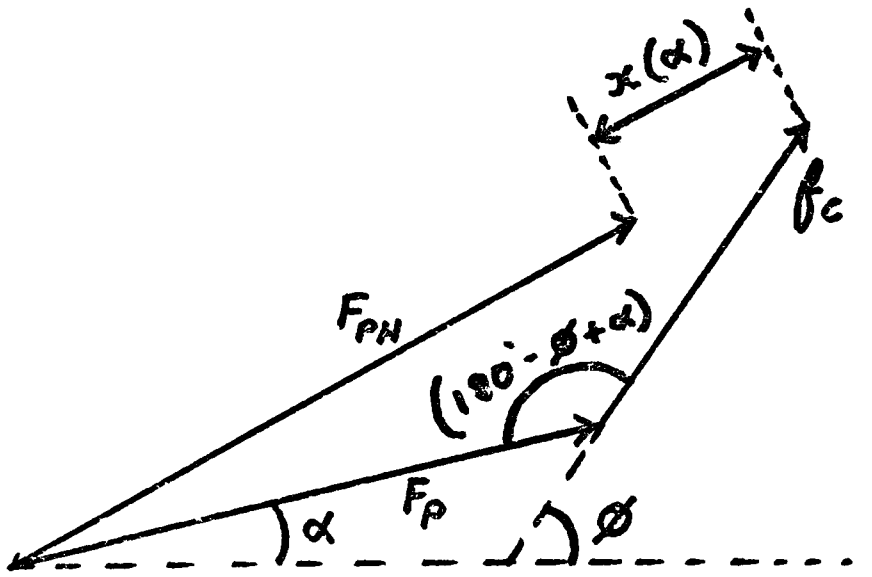
2.12 Calculation of Phase Angles

As has been stated earlier, ideally two isomorphous derivatives

FIGURE 2.8



a) The ideal case



b) The normal case

Phase triangles

are sufficient to determine the phase angles of the native structure factors. However, in practice, due to unavoidable errors the situation is not as clear cut as this, and so the phase probability distribution must be calculated for each reflection. Blow and Crick (1959) suggested a method for calculating this probability distribution.

In the ideal case:

$$\underline{F_{pH}} = \underline{F_p} + \underline{f_C}$$

where $\underline{f_C}$ is the calculated heavy atom contribution. However in general, this vector relationship will not be satisfied and a small error, $x(\alpha)$, must be added to F_{pH} in order to close the triangle. (See Figure 2.8). $x(\alpha)$ is known as the lack of closure error of the phase triangle, and may be considered to arise from two sources:

1) a contribution, ε, due to incorrect modelling of the heavy atoms, lack of isomorphism, and in some cases introduction of lighter atoms into the structure which have not been accounted for.

2) a component, δ, due to experimental errors in measuring the structure amplitudes, F_p and F_{pH}. The total error, E, is then given by:

$$E^2 = \langle x(\alpha) \rangle^2 = \langle \delta \rangle^2 + \langle \varepsilon \rangle^2$$

E may be estimated from centric reflections where:

$$E^2 = \langle [(F_{pH} \pm F_p) - F_H]^2 \rangle$$

and $\langle \delta \rangle^2$ by comparing measurements of the same reflections from different crystals; thus $\langle \varepsilon \rangle^2$ may be estimated.

Blow and Crick suggested that all the errors could be assumed to lie in the value of F_{pH}, and that they had a Gaussian

distribution. The probability, $P(\alpha)$, of a phase, α, being correct is then given by:

$$P(\alpha) = \exp(-x(\alpha)^2/2E^2) \qquad 2.20$$

for one derivative. The joint probability for more than one derivative is given by the product of the separate probability functions.

The lack of closure error for each derivative is calculated by applying the cosine rule to Figure 2.8(b):

$$(F_{pH} + x(\alpha))^2 = F_p^2 + f_c^2 + 2F_p f_c \cos(\phi-\alpha) \qquad 2.21.$$

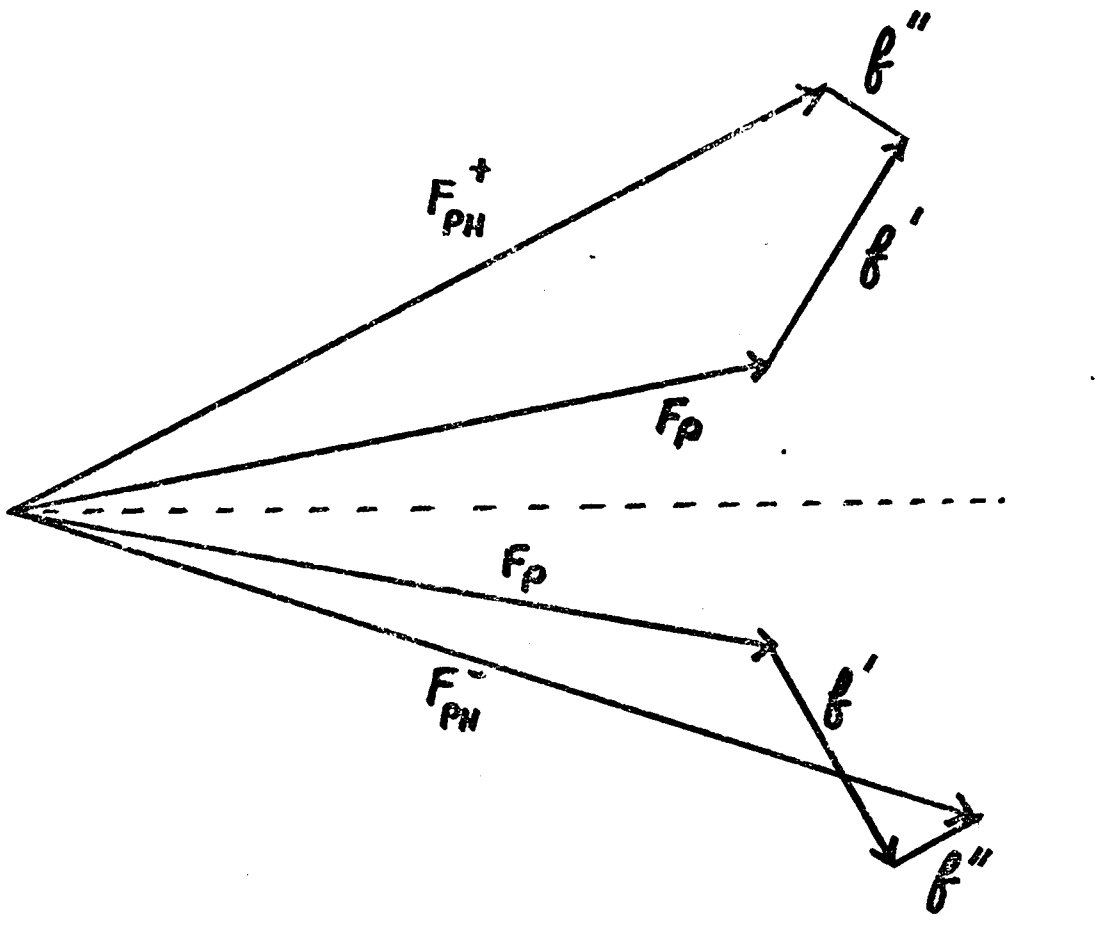
With any given phase distribution, the most obvious phase to use for a fourier summation is the one with the highest probability. However, Blow and Crick showed that the electron density map with the lowest mean square error was the one calculated using the phase angles of the centroids of the phase distributions, with terms weighted by the radii of gyration of the distributions. This type of fourier is called the "best fourier". Dickerson et al (1961) showed that this weight is the mean value of the cosine of the error in the phase angle for a given reflection; it is called the figure of merit, m. If α_B is the best phase angle, α_B and m are given by:

$$m \cdot \cos\alpha_B = \sum_i P_i \cos\alpha_i / \sum_i P_i$$

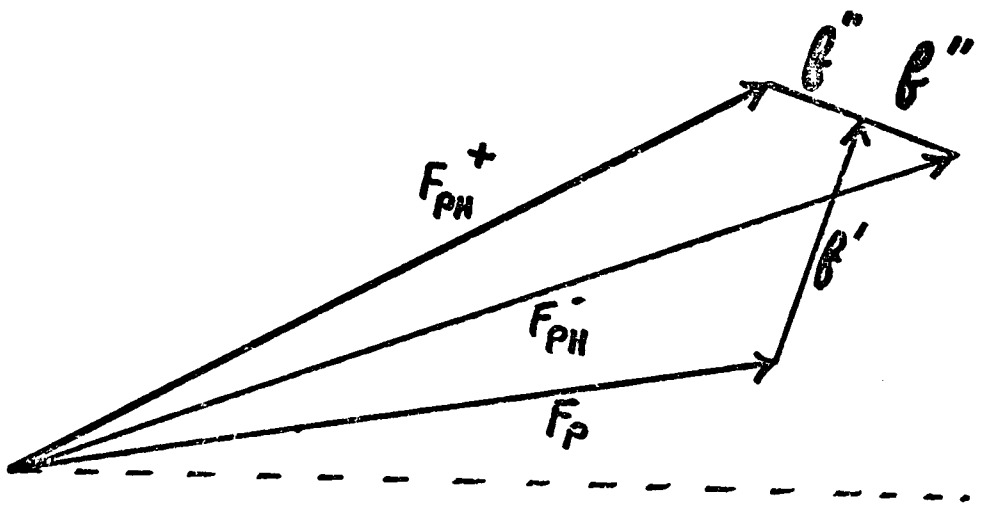
$$m \cdot \sin\alpha_B = \sum_i P_i \sin\alpha_i / \sum_i P_i$$

Where P_i is the probability at the i^{th} point around the phase circle.

FIGURE 2.9



a) Anomalous scattering resulting in different intensities for (hkℓ) and ($\bar{h}\bar{k}\bar{\ell}$) reflections.



b) The same situation as in (a) but reflected through the origin.

f' is the real scattering component

f" is the anomalous scattering component

Anomalous scattering

TABLE 2.1

The real and anomalous scattering factors (at $\sin\theta/\lambda = 0$), and absorption edges for some elements. The values of f' and f'' are for CuKα radiation.

Element	Z	f'	f''	K absorption edge	L absorption edge
N	7	7	0.0	30.99	-
O	8	8	0.1	23.32	-
S	16	16	0.6	5.0182	~76.05
I	53	53	7.2	0.373	2.719
Pt	78	78	8	0.15816	1.07239
Hg	80	80	9	0.14923	1.0089
Pb	82	81	10	0.14077	0.95029
U	92	91	16	0.10680	0.72226

The values of f' and f'' are in electrons, and those for the absorption edges are in Å. The figures are taken from the International Tables of Crystallography Volume III.

Electrons in a given shell will scatter anomalously if the energy of the absorption edge of the shell is less than, or comparable with the energy of the incident radiation. e.g. with CuKα radiation the electrons in the K and L shells of Pt scatter anomalously.

Dickerson et al also showed that the mean square error in the electron density of the best Fourier synthesis is given by:

$$\langle \Delta\rho^2 \rangle = \frac{2}{V^2} \sum_{hkl} F_p^{\,2}(hkl)(1-m_{hkl}^{\,2}) \qquad 2.21$$

The Blow and Crick phasing method has been used in the work reported in this thesis.

2.13 Anomalous Scattering Information

The energy of the x-rays used in crystallography is normally much higher than the energy of the electrons in the atoms of the crystals which diffract the radiation. These electrons then behave as classical free electrons and so scatter the radiation with a phase change of π. However, the inner shell (K, L and in some cases M) electrons of the heavier elements have transition energies close to the radiation energy (see Table 2.1). These electrons no longer behave as free electrons, but instead they scatter the radiation with a phase change of $\pi/2$ (Woolfson (1970)); that is they scatter anomalously. The ratio of the degree of anomalous scattering, f'', to real scattering, f', may be calculated for each element (see Table 2.1).

Bijvoet (1954) showed that anomalous scattering results in a difference in intensity between the Friedel pairs of acentric reflections. Figure 2.9 shows this situation for an isomorphous derivative of a protein crystal where the substituted atom displays anomalous scattering; the protein atoms are assumed to have negligible anomalous scattering. The difference between F_{pH}^{+} and F_{pH}^{-} is, in most cases, very small, and normally of the same order of magnitude as the errors in their measurements. Bijvoet suggested that anomalous scattering could be used to

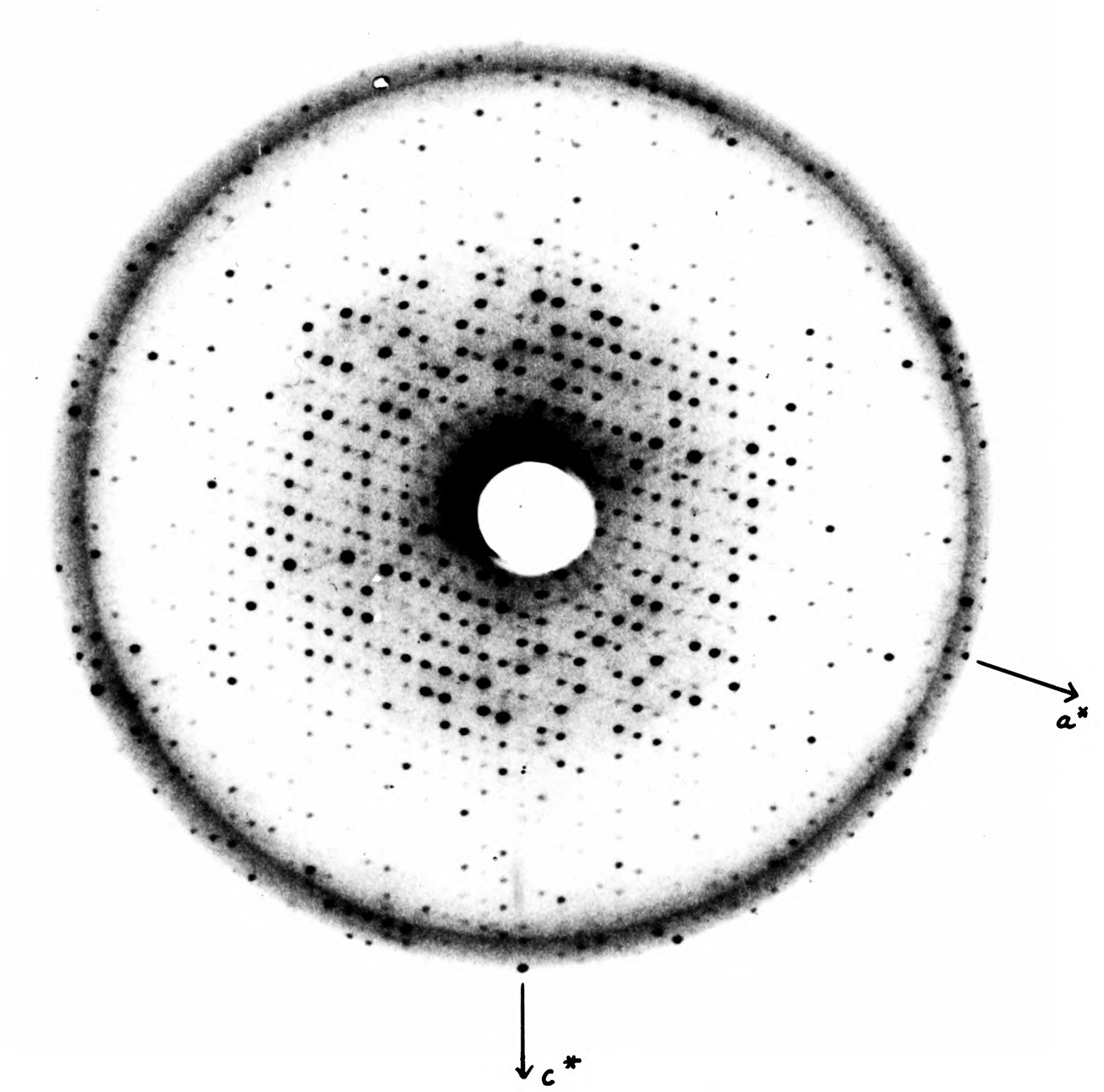
determine the phase angle by choosing between the two alternatives presented by a single isomorphous derivative.

North (1965) and Matthews (1966a) have shown how anomalous scattering information may be incorporated into isomorphous phase determination by the Blow and Crick method. This method makes use of the greater intrinsic accuracy of the anomalous differences, and in effect treats the anomalous differences as a second isomorphous derivative. An anomalous lack of closure error, $x'(\alpha)$ is calculated, and the combined isomorphous and anomalous phase probability, $P(\alpha)$,is given by:

$$P(\alpha) = \exp\left[- \left(\frac{x(\alpha)^2}{2E^2} + \frac{x'(\alpha)^2}{2E'^2}\right)\right] \qquad 2.22$$

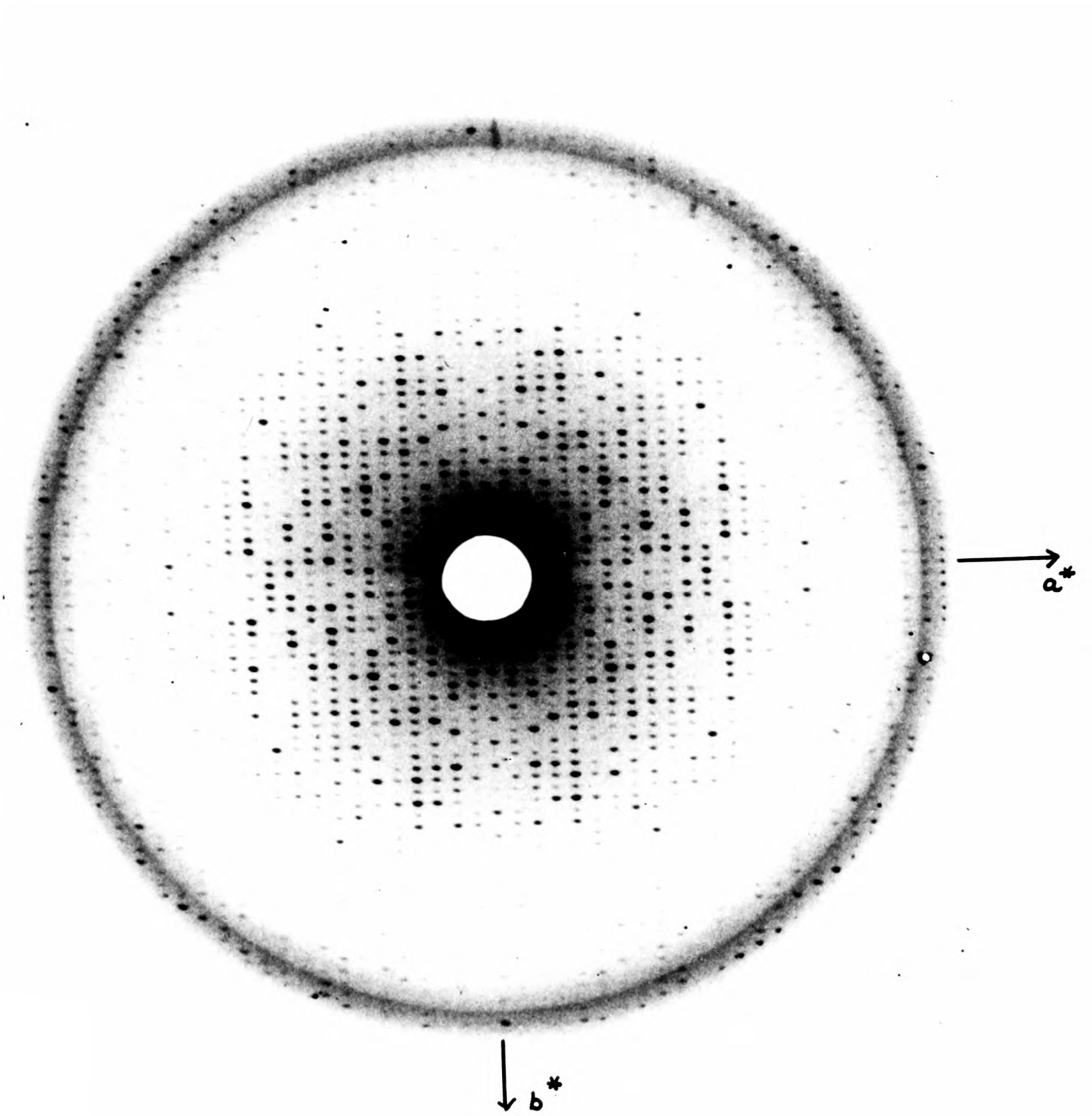
E' is estimated from Friedel equivalents in centric zones, or from native data; in practice E' is of the order of $\frac{1}{3}$ E.

FIGURE 3.1



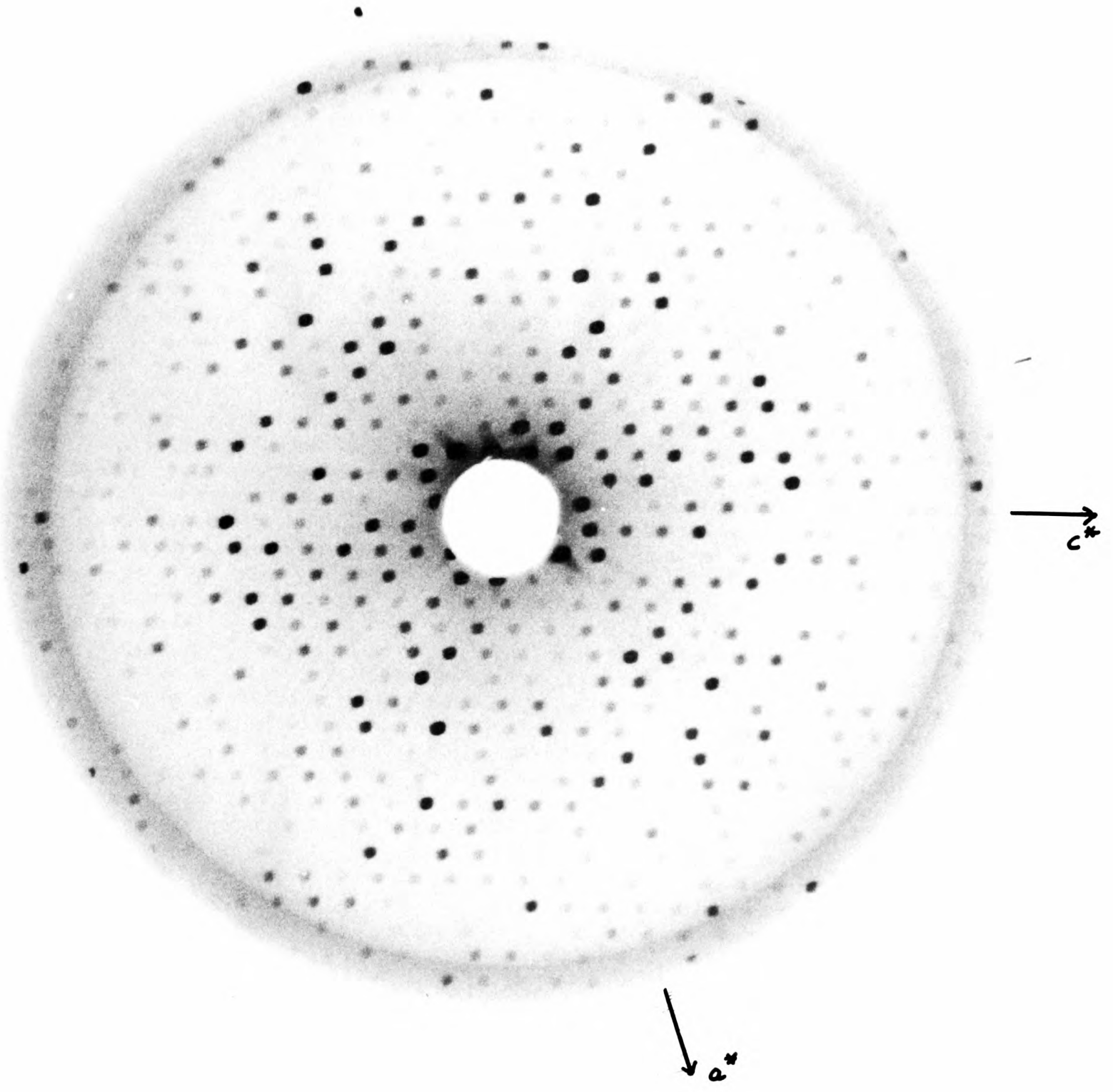
9° precession photograph of the (hol) zone of a native Ppa monoclinic crystal.

FIGURE 3.2



9° precession photograph of the (hko) zone of a native Pna monoclinic crystal.

FIGURE 3.3



7° precession photograph of the (hol) zone
of a Ppa methyl mercury chloride derivative crystal.

III CRYSTALLOGRAPHIC INVESTIGATION OF PHOSPHORYLASE

The crystallographic investigation of phosphorylase in this laboratory is being conducted in collaboration with Drs. N.B. Madsen and M.N.W. James of the University of Edmonton, Canada.

3.1 Monoclinic Crystals

Monoclinic crystals of phosphorylase in the a and b forms were obtained in 1971 by Dr. Madsen from a solution containing:

10 mM	glycerophosphate
0.5 mM	EDTA
5 mM	dithiothreitol
1.2 M	ammonium sulphate

with a pH of 7.5. The Ppb crystals were grown both in the presence, and absence, of 10 mM AMP. These crystals were investigated initially by Dr. James and were found to have the space group $P2_1$ with unit cell dimensions:
$a = 118.6\text{Å}$, $b = 188.6\text{Å}$, $c = 87.9\text{Å}$, $\beta = 108.6^{\circ}$, $V = 1.86 \times 10^6 \text{Å}^3$ (Madsen et al (1971)). The asymmetric unit of this crystal form is the phosphorylase tetramer with a molecular weight of approximately 400,000 daltons. Figure 3.1 shows the h0l zone of the diffraction pattern of this crystal form, and Figure 3.2 the hk0 zone. The diffraction patterns from the Ppa and Ppb crystals were identical as judged from photographs, suggesting that the conformation of the molecule in the two different crystals was the same. Crystals of phosphorylase b in the absence of AMP had the same space group and cell dimensions.

The diffraction pattern from these crystals was very similar to the patterns from crystals of Ppa and Ppb in the presence of AMP, which suggests that there is no gross conformational change when the molecule is activated with AMP.

A potential heavy atom derivative was obtained when isomorphous crystals were grown from a solution which contained eight equivalents of methyl mercury chloride per mole of enzyme; the crystallising solution contained no dithiothreitol. It was hoped that the mercury atoms had bound specifically to the two reactive sulphydryl groups on the surface of each monomer. Crystals were obtained of methyl mercury chloride co-crystallised with both Ppa and Ppb. The diffraction pattern (Figure 3.3) of this potential derivative showed small intensity changes when compared with the native diffraction pattern. These derivative crystals were more susceptible to radiation damage than the native crystals; after 20 hours exposure in the beam from an Elliott Rotating Anode X-ray generator operating at 40 kV anode potential and 40 mA filament current, the native crystals still showed an appreciable diffraction pattern, whereas the methyl mercury chloride crystals showed no pattern.

3.1.1 Practical Details

X-ray diffraction photographs of the crystals were obtained using Supper precession cameras mounted on Elliott Rotating Anode X-ray generators with copper anodes. The normal operating conditions were an anode potential of 40 kV and a filament current of 40 or 50 mA. The radiation was filtered through a 0.022 mm nickel foil in order to remove most of the white radiation and the copper Kβ line, thus leaving predominantly copper

Kα radiation of wavelength 1.54182Å. Exposure times of approximately 20 hours were used, and the photographs recorded on Ilford Industrial G X-ray film. A two film pack was used for each exposure so that any reflections which were too strong to measure on the front film would have measurable intensities on the rear film.

The crystals were mounted in small quartz capillary tubes of internal diameter 1.0 mm or 1.5 mm.depending on the size of the particular crystal. Typically a crystal was placed in a capillary tube using a teat pipette. The excess moisture was removed from the tube using small pieces of filter paper, and the crystal orientated by gently touching it with a fine bristle. A drop of the mother liquor was introduced into each end of the tube from a syringe, before the ends were sealed with wax. The capillary tube was then mounted on a goniometer head using "Plasticene".

The crystals were aligned on precession cameras using a series of still and small angle precession photographs as described by Henry, Lipson and Wooster (1960) Chapter 10.

3.1.2 Difference Patterson.

9° precession photographs of h0l zone of the native crystals and 7° precession photographs of the h0l zone of the methyl mercury chloride crystals were obtained as described above. These photographs were scanned on an Optronics P1000 Microdensitometer which produced digital images of the films on magnetic tapes. The densitometer will be described in greater detail later. The magnetic tape data were then processed on the Ferranti Argus 500 computer in the laboratory using programmes written by

P.R. Evans and Dr. S.H. Banyard. The output from this set of programmes was the native and derivative structure factors scaled together so that:

$$\frac{\sum F^2(\text{derivative})}{\sum F^2(\text{native})} = 1$$

where the summations were taken over all measured pairs of native and derivative reflections. The data extended to a lattice spacing of approximately 7Å. A difference patterson synthesis was computed using a programme written by Dr. S.D. Dover; however, the mercury sites could not be found from this. The fact that the difference Patterson yielded no solution was not surprising for two reasons:

1. If there were two mercury atoms bound per monomer, there would be 8 independent sites in the unit cell. 8 sites would give rise to a very complicated difference patterson with 56 peaks (8 x (8-1)). $\frac{n(n-1)}{2}$

2. The hOl zone of these crystals is projected down the longest axis in the unit cell (188.6Å), thus errors will tend to build up to further complicate the projection difference patterson.

It was decided that three dimensional data would be required in order to find the mercury binding sites. Potentially three methods of data collection were at our disposal:

1. 4 circle diffractiometer
2. Screened precession photography.
3. Use of a rotation camera which was being developed in the laboratory.

At the time when this data collection was under consideration, the Optronics Microdensitometer, which would be required for

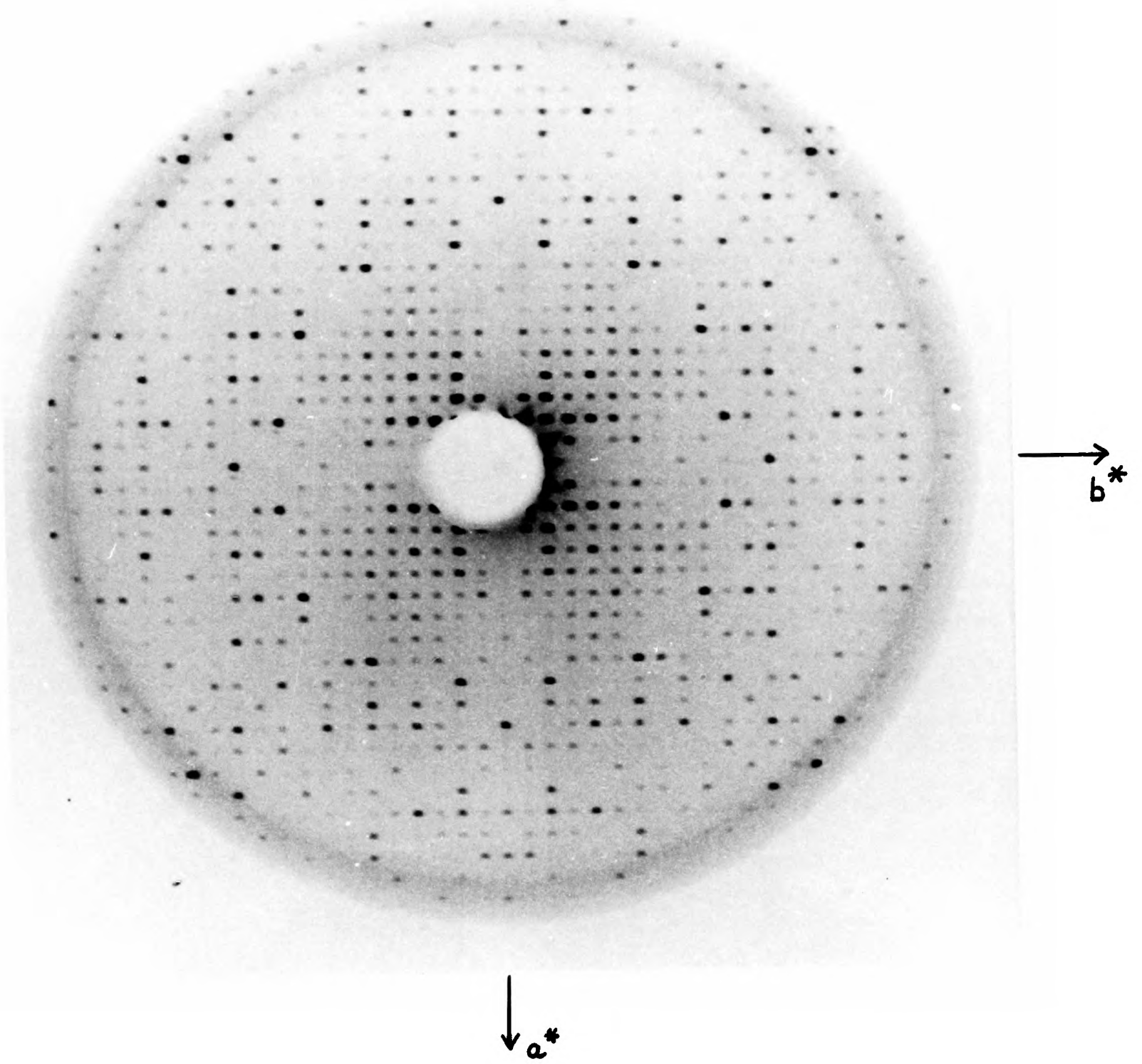
processing either precession or rotation photographs, developed a fault and remained inoperative because of this for the next two years. We were thus forced to turn to the Hilger and Watts Four Circle Y130 Diffractometer controlled by a Digital Equipment Corporation PDP8 computer. Tests to determine if reflections could be resolved on this instrument proved to be satisfactory, but before much serious data collection could be undertaken, a crystal form of phosphorylase more suitable for the structure determination was discovered, and so work on the monoclinic crystal form was suspended.

3.1.3 Discussion

The size of the asymmetric unit of these monoclinic crystals would make the determination of the molecular structure by conventional means a formidable problem. However, a knowledge of the Ppa structure would be of great interest because it would shed light on the dimer-dimer interaction in phosphorylase.

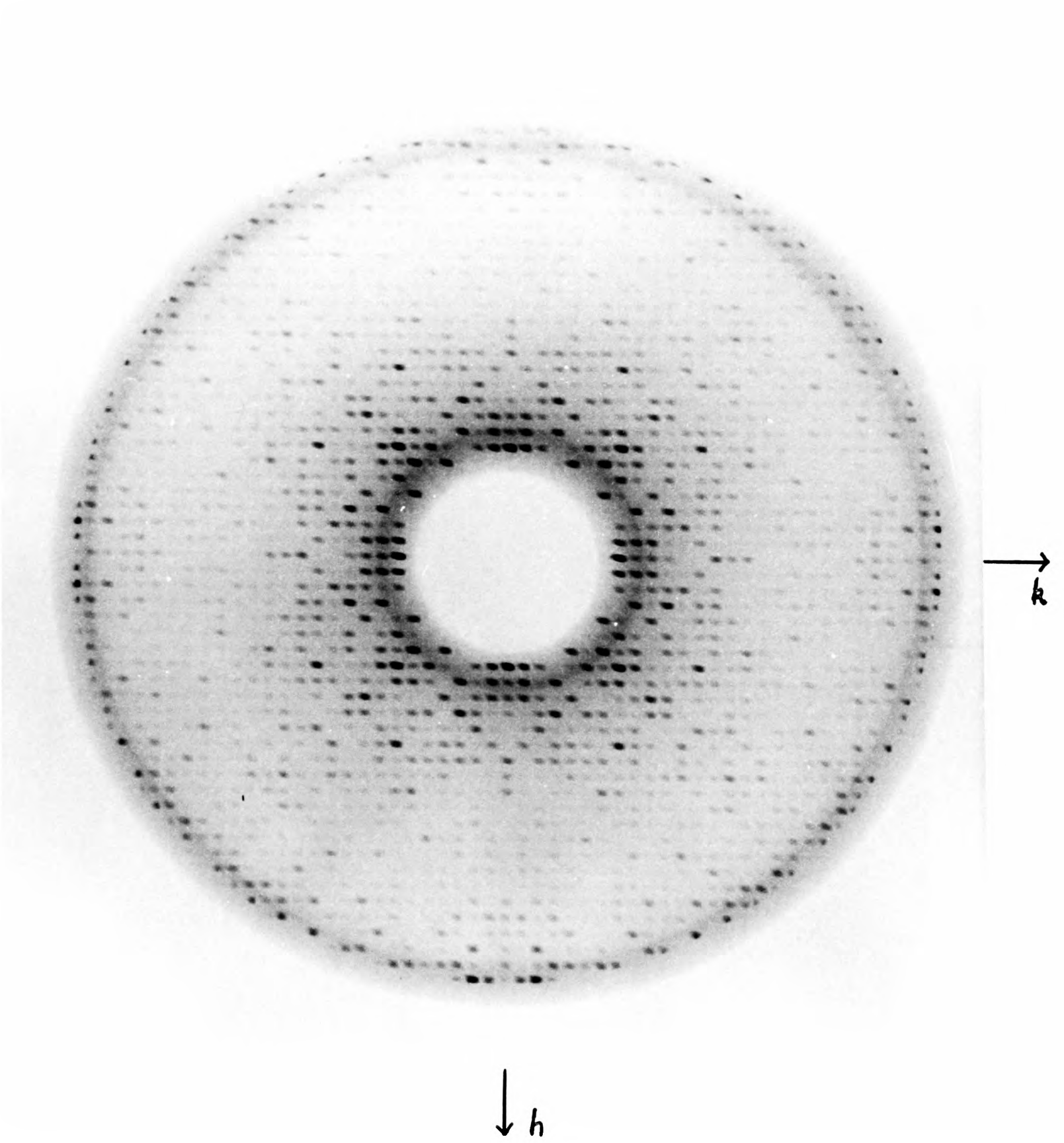
Since the asymmetric unit of this crystal form is a tetramer, and, presumably, has local symmetry axes, it may be possible to use the approach of Buehner et al (1973) to the structure determination of lobster D-glyceraldehyde-3-phosphate dehydrogenase. Here the molecular centre was found using rotation functions (Rossmann and Blow (1962)), and then the molecular symmetry used to solve the heavy atom difference pattersons. The phases were calculated to 6Å resolution using 3 derivatives, in the 6Å to 4Å shell using 2 derivatives, and from 4Å to 3Å using 1 derivative The subunits in the electron density map were then averaged to produce a clearer image with very encouraging results. Such a technique should be possible for Ppa, though, of course, any

FIGURE 3.4a



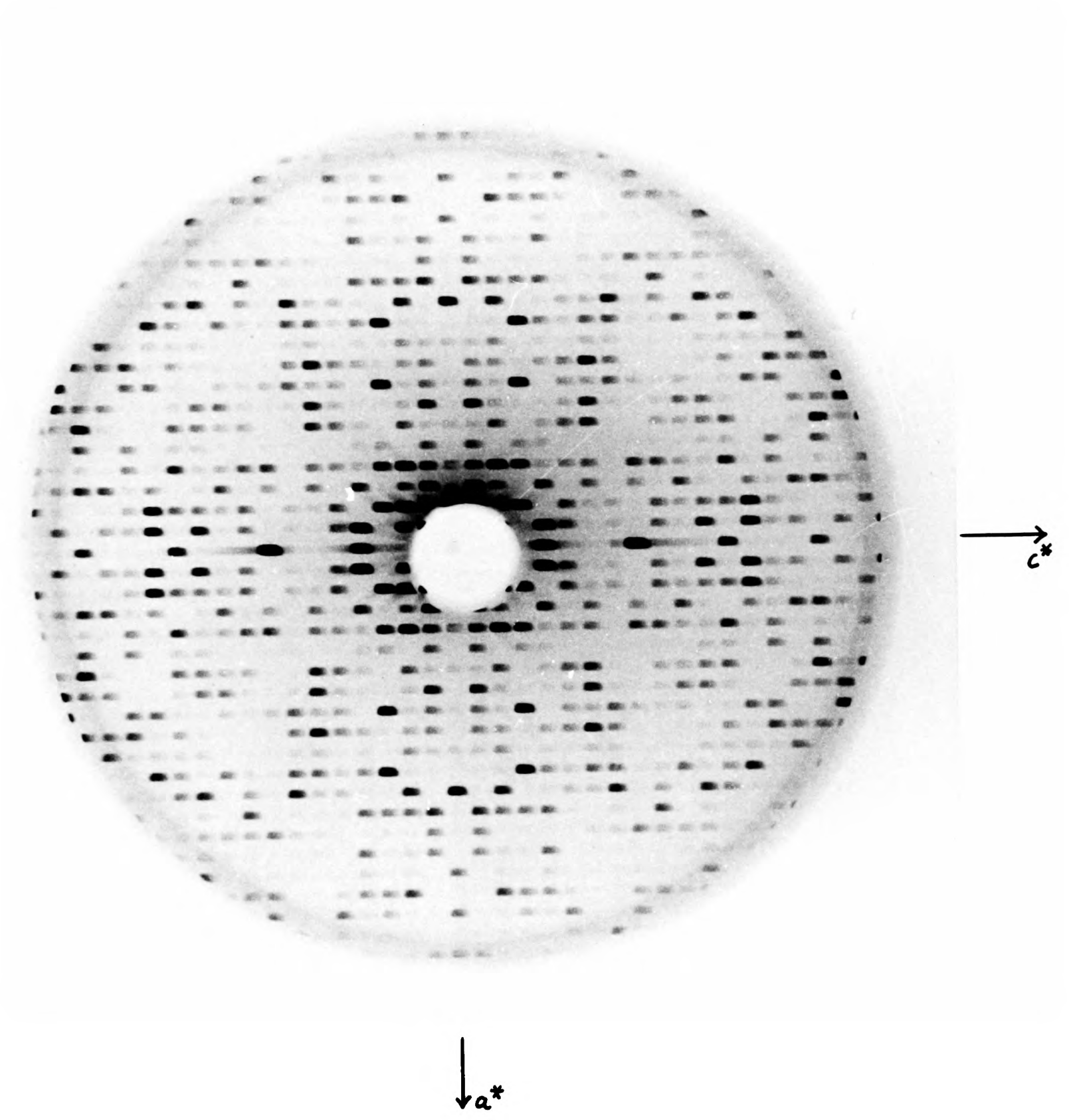
9° precession photograph of the (hko) zone of a native Ppb tetragonal crystal.

FIGURE 3.4b



The (hk1) zone of a native Ppb tetragonal crystal.

FIGURE 3.5



9° precession photograph of the (hol) zone of a native Ppb tetragonal crystal.

small differences between the subunits would not be shown by this method of averaging. However, the various interaction sites on the subunits would still be seen.

3.2 Tetragonal Crystals

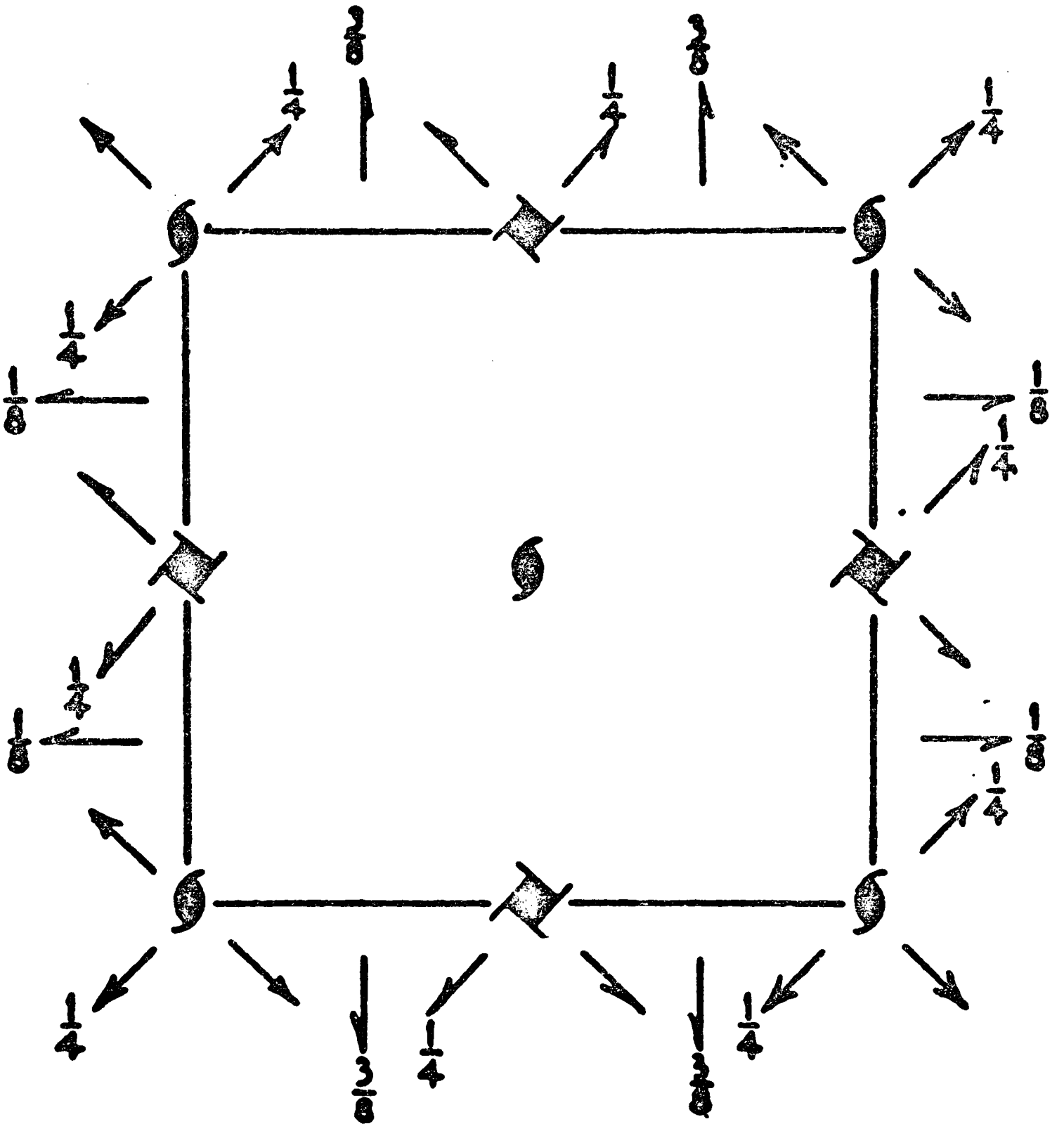
During a routine phosphorylase b extraction and purification Dr. P.A.M. Eagles and M.I. Iqbal observed large single crystals after the solution had stood undisturbed for several weeks at 4°C (Eagles et al (1972)). The protein was prepared from rabbit muscle by the method of Fischer and Krebs (1962) with small modifications, a notable one being that the muscle was first homogenised in a Waring Blender. The enzyme was recrystallised from a solution at pH 7.0 and 4°C containing:

1 mM	AMP
1 mM	dithiothreitol
10 mM	magnesium acetate
5 mM	Tris buffer.

The large single crystals were observed in this solution when the enzyme concentration was in the range 10 to 20 mg/ml. The crystals were in the form of square prisms, typical dimensions being 1.0 mm x 0.2 mm. x 0.2 mm.

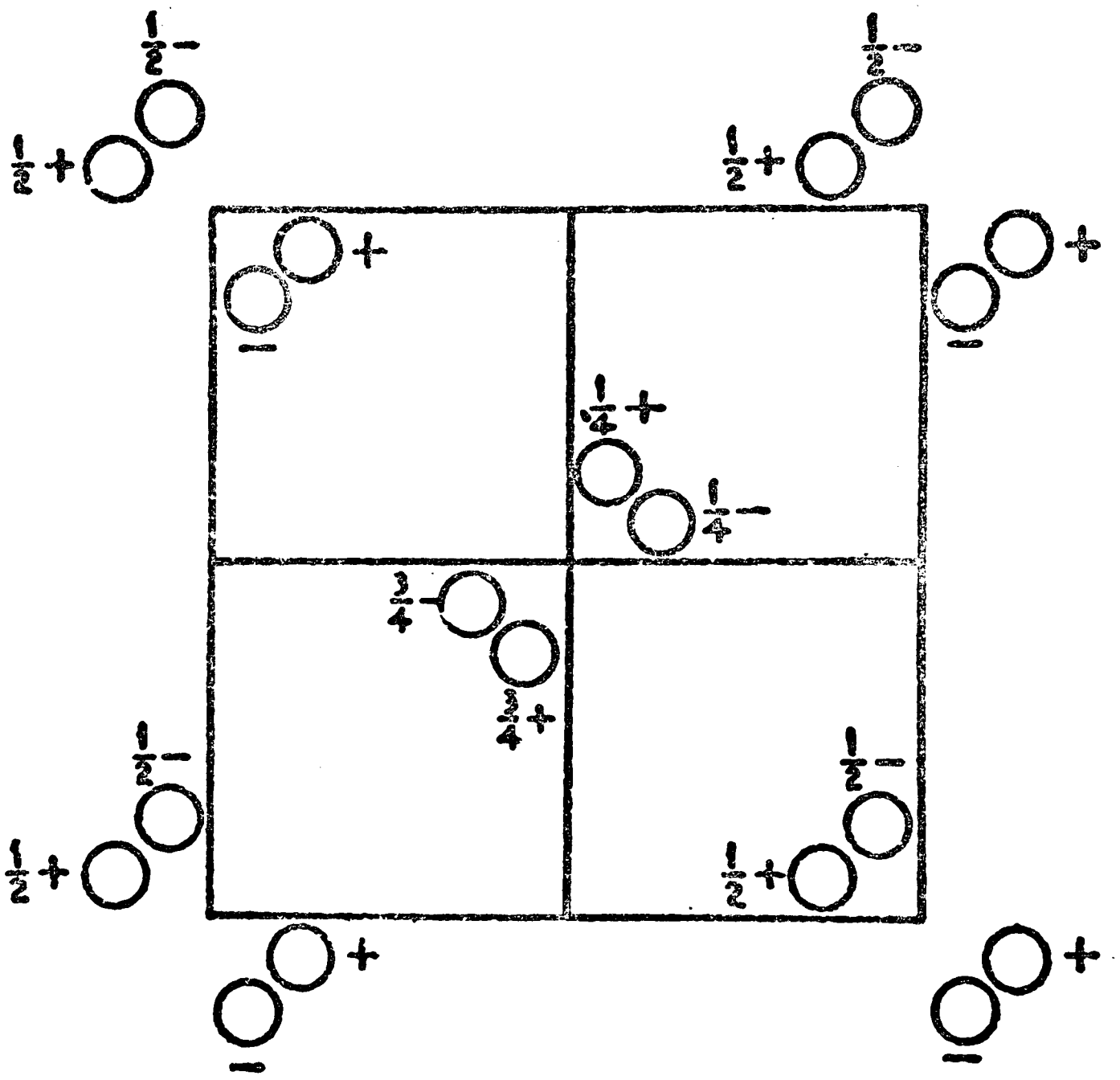
The spacegroup and cell dimensions of these crystals were investigated on a precession camera; they were found to diffract well, and in fact with subsequent crystals the diffraction pattern has been observed to extend to a lattice spacing of at least 3 Å. The hk0 and hk1 reciprocal lattice sections were found to have 4 mm symmetry (Figure 3.4). The crystals are, therefore, tetragonal, and, since protein crystals cannot contain mirror planes, belong to the point group 422. In the h0l zone (Figure 3.5), systematic absences were observed for the

FIGURE 3.6a



The symmetry elements of the space group $P4_12_12$

FIGURE 3.6b



The equivalent positions of the space group $P4_12_12$

The co-ordinates of the equivalent positions are:

$x,y,z;\ -x,-y,\frac{1}{2}+z;\ \frac{1}{2}-y,\frac{1}{2}+x,\frac{1}{4}+z;\ \frac{1}{2}+y;\frac{1}{2}-x,\frac{3}{4}+z;$

$y,x,-z;\ -y,-x,\frac{1}{2}-z;\ \frac{1}{2}-x,\frac{1}{2}+y,\frac{1}{4}-z;\ \frac{1}{2}+x,\frac{1}{2}-y,\frac{3}{4}-z.$

hOO reflections where $h \neq 2n$, and for the OOl reflections where $l \neq 4n$, thus there is a 2_1 screw axis parallel to the a* reciprocal lattice axis, and a 4_1, (or 4_3) screw axis parallel to the c* reciprocal lattice axis. The space group is, therefore, $P4_12_12$ or the enantiomorph $P4_32_12$. The unit cell dimensions were found to be:

$$a = b = 129.2\text{Å} \quad c = 116.2\text{Å} \quad V = 1.94 \times 10^6\text{Å}^3$$

The symmetry elements and eight equivalent positions of the space group $P4_12_12$ are shown in Figure 3.6. The unique set of reflections for this spacegroup is defined by the conditions:

$$h \geqslant 0 \quad k \geqslant 0 \quad l \geqslant 0 \quad k \leqslant h.$$

This is a 45° "wedge" up the c* axis; i.e. it is one sixteenth of the reflection sphere. By comparison the unique set of reflections in the space group $P2_1$ is defined by the conditions:

$$k \geqslant 0 \quad l \geqslant 0 \quad h \text{ running positive and negative.}$$

This is one quarter of the reflection sphere. Although the unit cell volume of the tetragonal crystals is slightly larger than that of the monoclinic form, the symmetry of the tetragonal cell reduces the number of unique reflections in the 6Å resolution sphere from approximately 9000 in the monoclinic form to 2660. The amount of labour involved in a structure determination using the tetragonal crystals is, therefore, reduced by a factor of four when compared with one using the monoclinic crystals- for this reason our efforts were concentrated on the tetragonal crystals.

The tetragonal unit cell has eight equivalent positions, and since the unit cell volume of these crystals is very similar to that of the monoclinic crystals which contain two tetramers

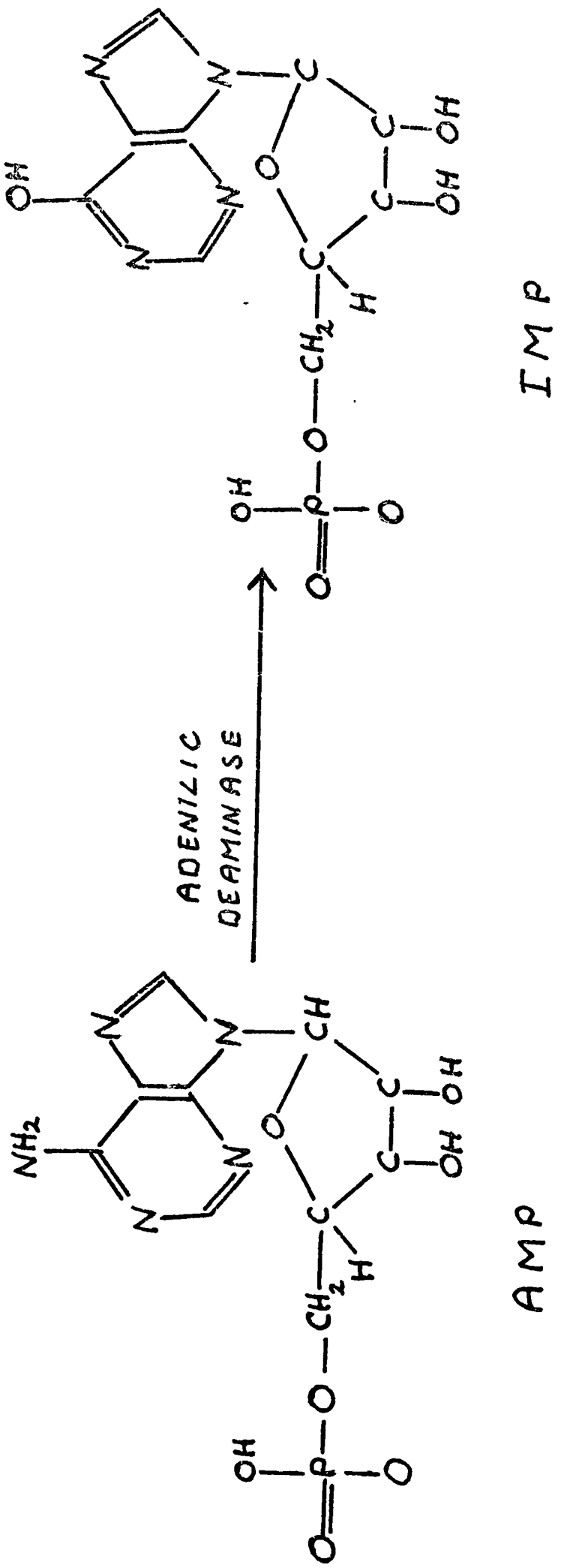
(i.e. 8 monomers), it seems most likely that the asymmetric unit in the tetragonal crystals is the phosphorylase monomer. Further confirmation of this view is found from the average value of Vm, the volume per unit molecular weight of protein crystals. Matthews (1968) gives the figure 2.4$\mathring{A}^3$ for the average value of Vm which, when applied to these phosphorylase crystals, gives the value 100,000 daltons for the weight of the asymmetric unit. In view of these arguments, no measurements of the density or solvent content of these crystals have been made.

Under the conditions used for crystallisation it seemed most likely that the Ppb was in the tetrameric state. However, there is no point in the space group $P4_12_12$ (or $P4_32_12$) where two 2-fold axes intersect, and there is no simple 4-fold rotation axis; therefore, if we follow the ideas of Monod et al (1965) and assume that multimeric proteins contain only rotational and no translational symmetry elements, it follows that the phosphorylase tetramer is not present in the tetragonal crystals. It is most unlikely that the monomeric species is present since phosphorylase is found to dissociate into monomers only under severe chemical conditions (see Chapter I). It appears, therefore, that the molecule is present as a dimer with the subunits related by the crystallographic 2-fold rotation axis.

3.2.1 The role of IMP

The absence of the tetramer under these conditions was puzzling, but a possible explanation was found at a later date when Dr. Madsen tried to grow more tetragonal crystals. He prepared the enzyme by the normal method of Fischer and Krebs (1962), and

FIGURE 3.7



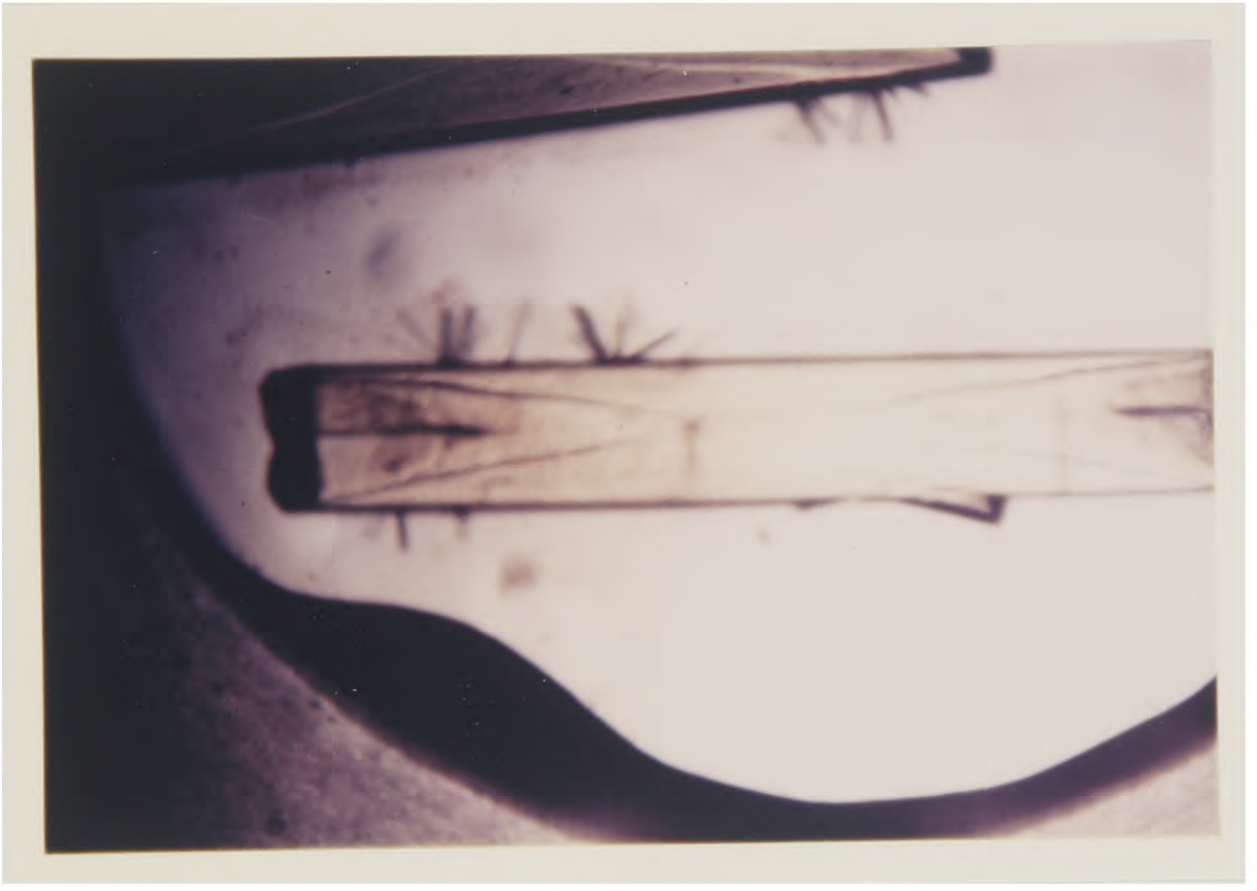
The conversion of AMP to IMP by adenilic deaminase.

did not homogenise the rabbit muscle. He was unable to grow crystals using enzyme prepared in this way. Substantial amounts of the nucleotide inosine mono-phosphate were found in the supernatant of the original crystals. IMP may be distinguished from AMP by spectral measurements; at pH 7 the maximum absorption of IMP occurs at a wavelength of 248 mμ, whereas for AMP the maximum absorption is at 259 mμ. In the first enzyme preparation, the homogenisation of the rabbit muscle had apparently released a certain amount of the enzyme adenilic deaminase, which subsequently contaminated the final enzyme solution. The function of adenilic deaminase is to convert AMP to IMP (Figure 3.7), and, therefore, the AMP which was added to the crystallisation solution was converted to IMP and this nucleotide induced crystallisation. IMP prevents tetramerization of phosphorylase (Black and Wang (1968)), and hence the existence of dimers rather than tetramers in the Ppb crystals could be rationalised. This chain of events was confirmed by adding IMP to pure, nucleotide free, Ppb which subsequently formed tetragonal crystals. The tetragonal crystals are now grown on a routine basis from a solution at pH 6.8 containing:

1	mM	IMP
1	mM	dithiothreitol
10	mM	magnesium acetate
5	mM	Tris buffer (or BES buffer).

The crystals are grown at 16°C in small glass tubes of approximately 1.5 mm internal diameter. It is found necessary to seed the crystallisation tubes otherwise a large number of very small crystals are produced. The crystals are typically 1.5 mm. long by 0.6 mm, in cross-section. The largest one grown as yet is

FIGURE 3.8



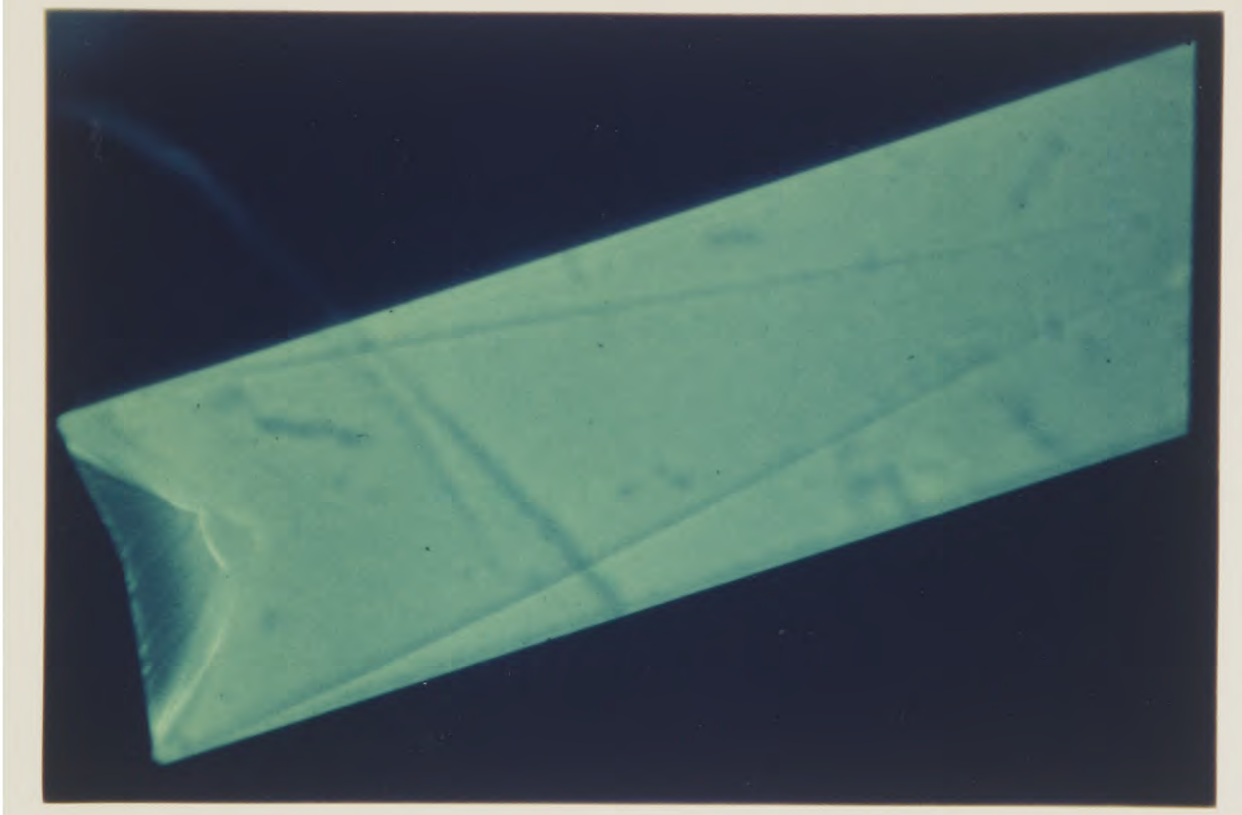
A native Ppb tetragonal crystal viewed in the (olo) direction under white light.

FIGURE 3.9



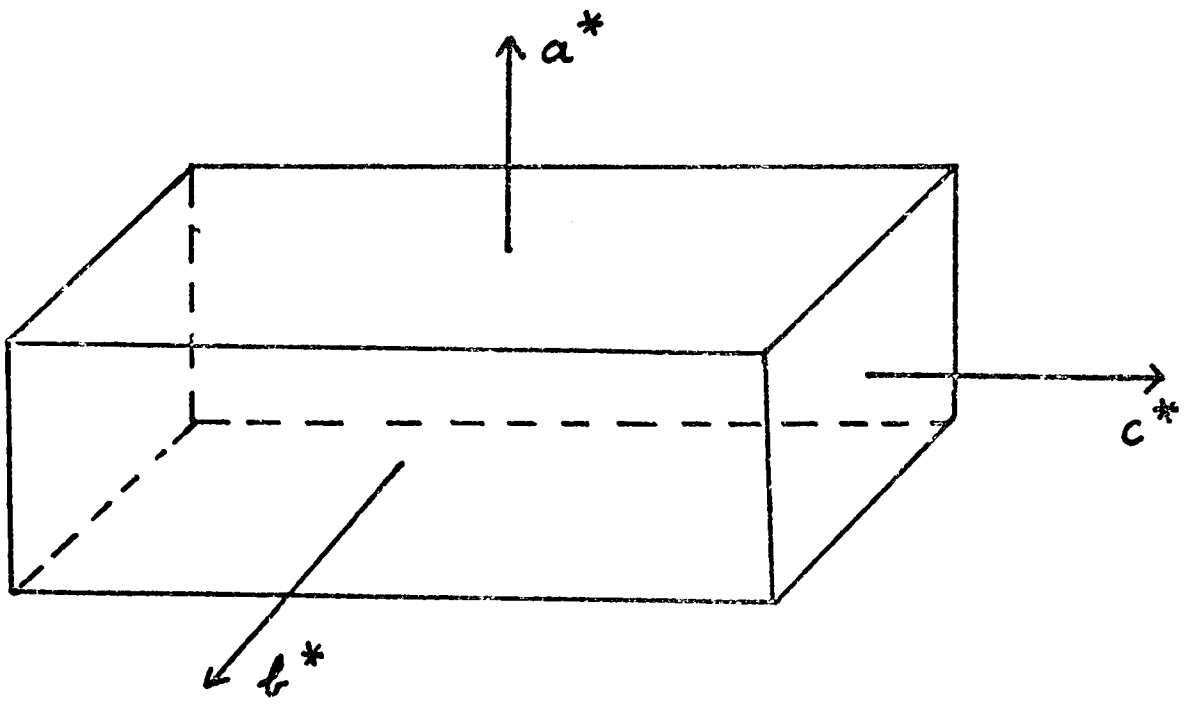
Native Ppb tetragonal crystals viewed under partially polarised light. This is the same view as the one shown in the Frontspiece where the crystal with its c^* axis perpendicular to the plane of the photograph is obscured because the plane of polarisation is not rotated by this axis.

FIGURE 3.10



The fluorescence of the pyridoxal-5-phosphate in a native Ppb crystal.The crystal was illuminated with the 334 and 365 nm. lines of a mercury vapour light, while a barrier filter allowed light of wavelength greater than 500 nm.,only, to reach the film.

FIGURE 3.11



The morphology of the phosphorylase b tetragonal crystals.

approximately 6 mm x 1.0 mm x 1.0 mm. Typical crystals are shown in the Frontispiece, and Figures 3.8, 3.9, 3.10; the crystal morphology is shown in Figure 3.11.

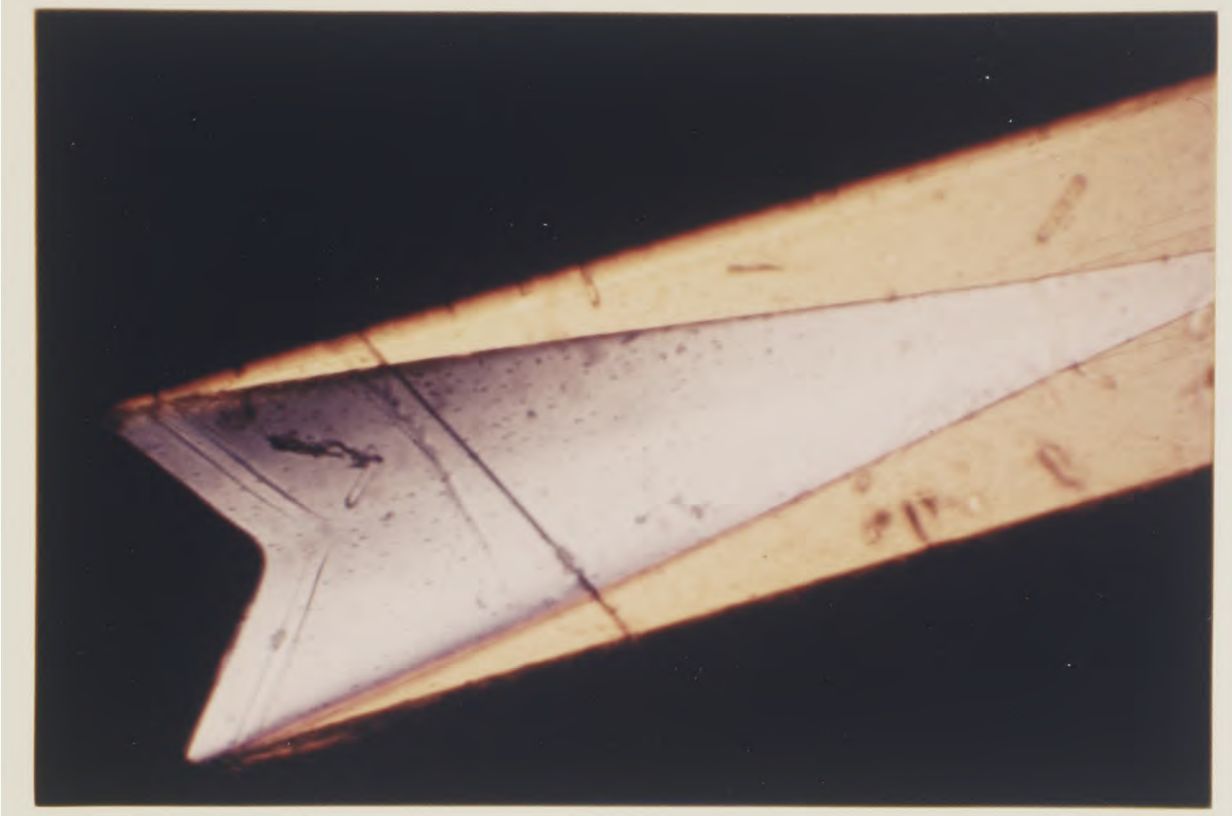
Crystals may be grown in the absence of IMP, though they grow much more slowly than in its presence; they are also more susceptible to radiation damage than crystals with the nucleotide. AMP prevents crystal growth completely. It appears that IMP stabilises a pre-existing conformation of the enzyme, and thereby facilitates crystal growth. The chemical evidence for the binding of IMP to Ppb is consistent with this reasoning.

3.2.2 The Mode of Growth

One of the most striking features of these crystals is the appearance of a cross on the crystal surface (Figure 3.9) when viewed down the a or b axis. The ends of the crystals, where the growth occurs, show an indentation when viewed in the same direction. Both these effects are shown clearly in Figure 3.12. where a crystal is seen between crossed polarisers. Figure 3.13 shows the indentation viewed along the (1$\bar{1}$0) direction. When viewed down the c axis, the end of the crystal appears as an indented pyramid; the growth points are clearly visible as "countours" inside the indentation. (Figure 3.14)

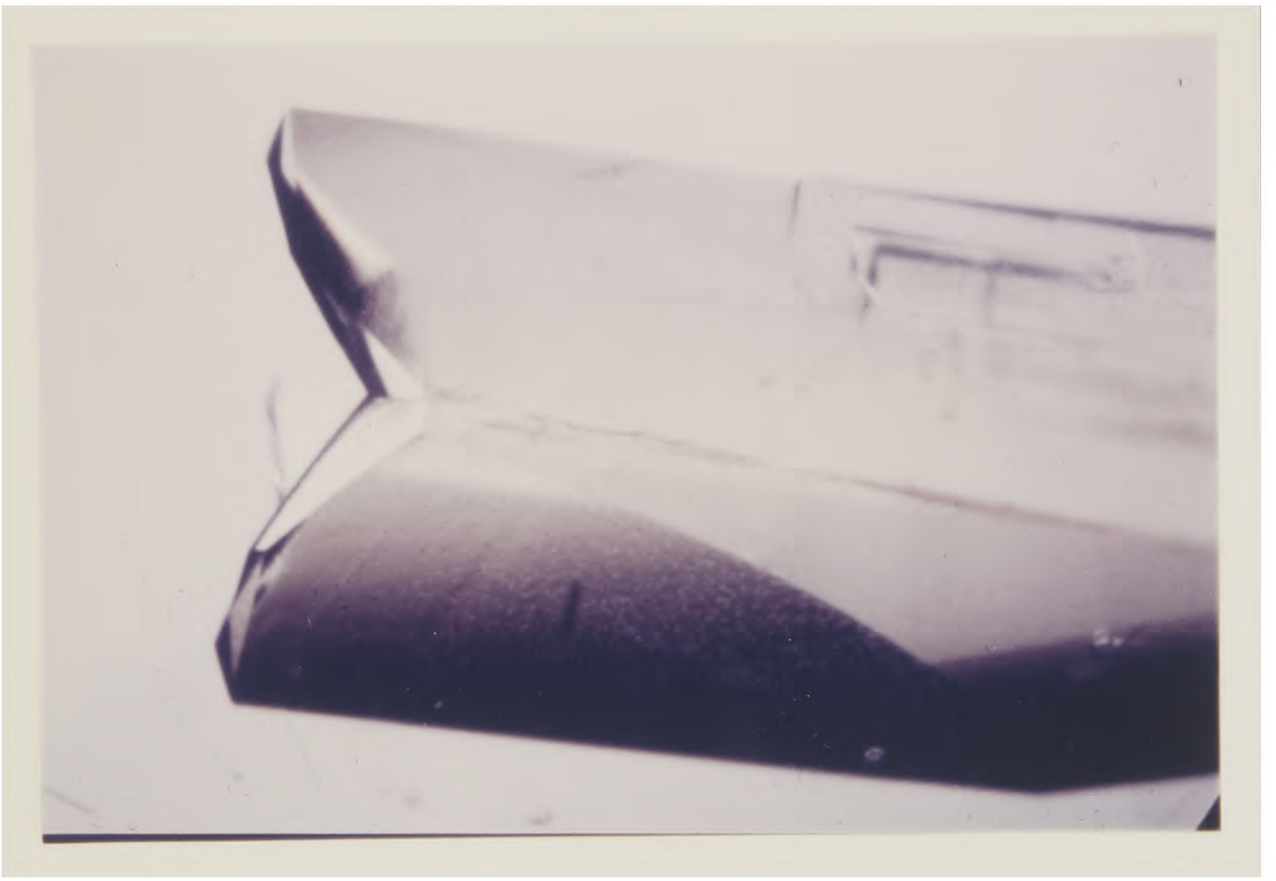
Similar "hourglass" effects have been observed in the crystals of some inorganic compounds grown in the presence of dyes. Examples are potassium sulphate crystals grown in presence of Acid Fuchsin, and potassium perchlorate crystals grown in the presence of Azofuchsin G (Buckley (1951), p.415). These hourglass inclusions are thought to be due to the trapping of the impurity on certain faces during crystal growth; this

FIGURE 3.12



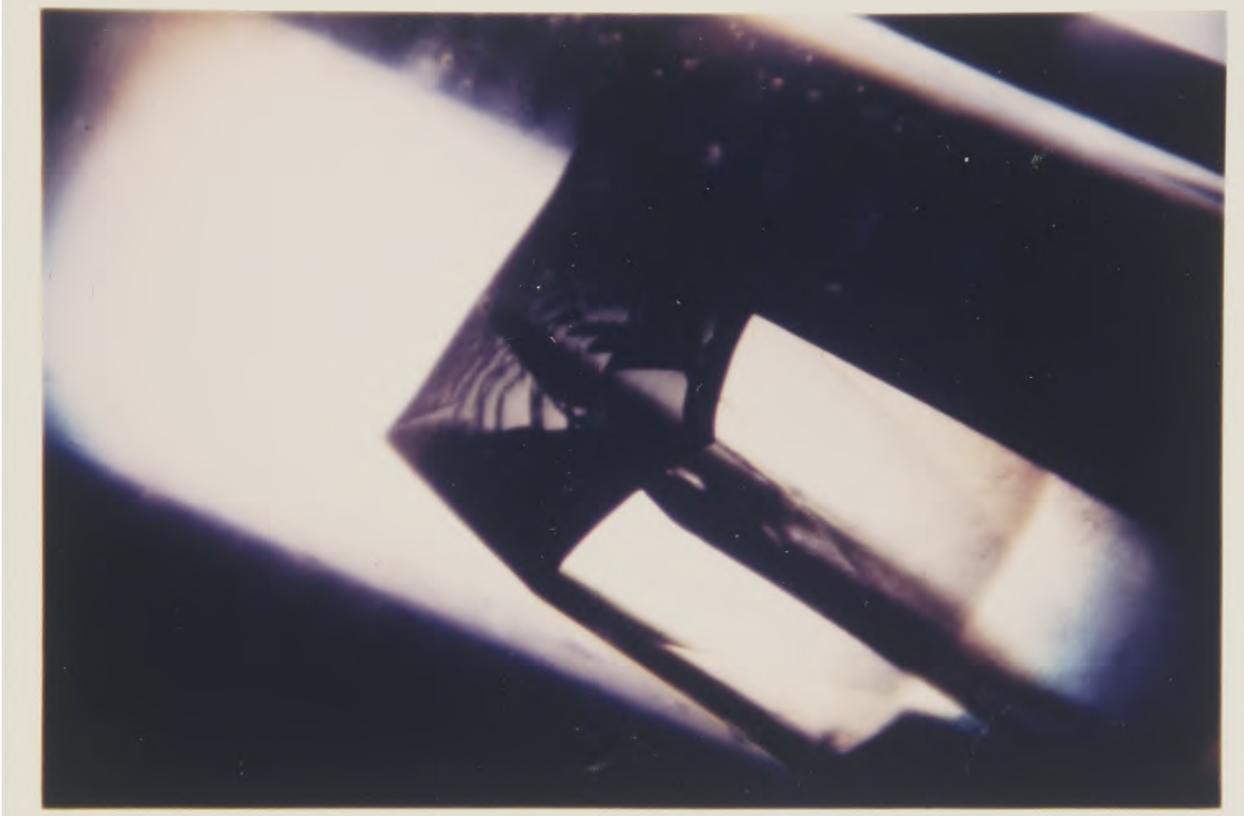
The "hourglass" and indentation effects in a native Ppb crystal viewed in the (olo) direction. The crystal is between crossed polarisers.

FIGURE 3.13



A methyl mercury chloride derivative crystal viewed in the (llo) direction, showing the indentation.

FIGURE 3.14



A native Ppb crystal showing the growth rings on the (ool) face.

requires that at least two distinct types of crystal face (those deposited upon, and those avoided) should be present in the initial stages of crystal growth. If the edges surrounding a crystal face are elevated above the level of the remainder of the face, impurity material may be trapped on the face during subsequent deposition.

Bunn (1933) has attributed indentation in crystal faces to impurities in the crystallisation solution. In this situation the more slowly growing crystal faces could reach equilibrium with the impurity whereas the more rapidly growing faces would have a composition more like the solution. These faces would then be unstable with respect to the solution and so re-dissolve leaving indentations.

Hourglass effects have been observed in rennin crystals and been shown to arise from impurity in the mother liquor (Bunn et al (1971)). They are also observed in crystals of aldolase (Johnson, L.N., private communication) and in the monoclinic crystals of Ppa and Ppb.

If an impurity is the cause of these effects in the tetragonal phosphorylase crystals, its origin is not immediately obvious. Since the effect is seen in crystals which contain IMP as well as those which do not contain it, this nucleotide does not appear to be the cause. Pyridoxal phosphate may be ruled out since it appears to be uniformly distributed throughout the crystals as observed by its fluorescence (Figure 3.10). Contamination by the buffer in the mother liquor does not appear to be the cause since the "hourglass" is seen in crystals grown in both Tris and BES buffers. Phosphorylase has several

different forms, as noted in Chapter 1, and so the presence of two or more of these forms could possibly account for the effect. However, any difference between the two regions of crystals is very small. This was shown by photographing the diffraction patterns from the centre and end of a crystal, similar to the one shown in Figure 3.9, using a very small collimator (0.2mm in diameter) on a precession camera. There were no observable intensity changes between these two diffraction patterns which suggests that the material in the two regions of the crystal was identical at least to the resolution of the photographs (5.5Å).

The re-entrant angles at the ends of the crystals are suggestive of twinning (Bunn (1961), Chapter II), but there is no evidence of this in their diffraction patterns.

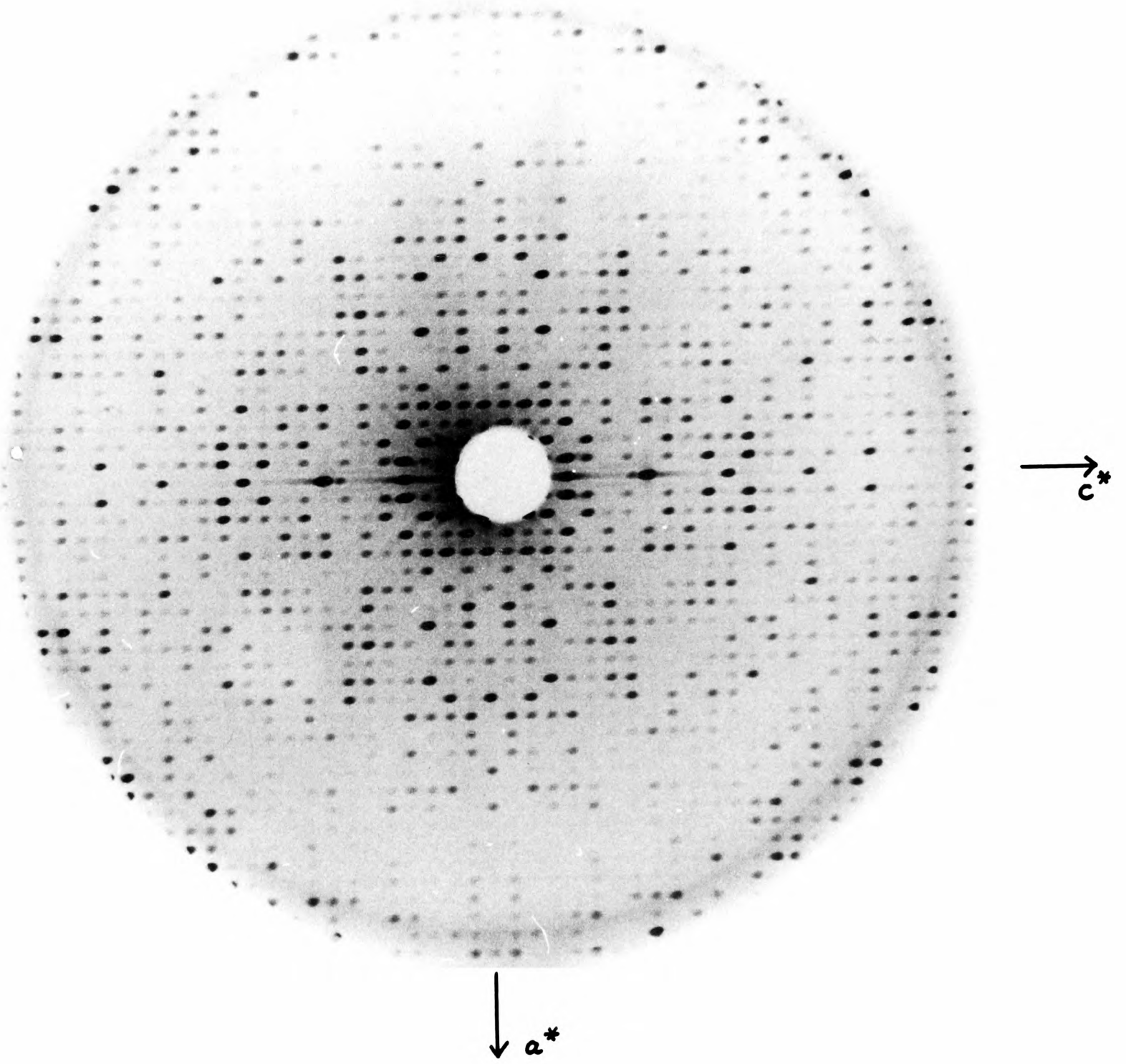
A further possible explanation of the hourglass and indentation effects is that material is laid down preferentially on the (100) or (010) faces, although crystals grow in the c direction. This causes the edges of the crystals to grow more quickly than the centre, hence forming the indentation. At a later stage material is laid down within the indentation, and the lines of the "hourglass" mark the boundary between this new material, and the older, outer material. The lines are clearly visible between crossed polarisers (Figures 3.9, 3.12 and the Frontispiece), which possibly indicates a lattice discontinuity at this boundary.

It has not been possible, yet, to discover which, if any, of these explanations is the correct one.

3.2.3 Heavy Atom Derivatives

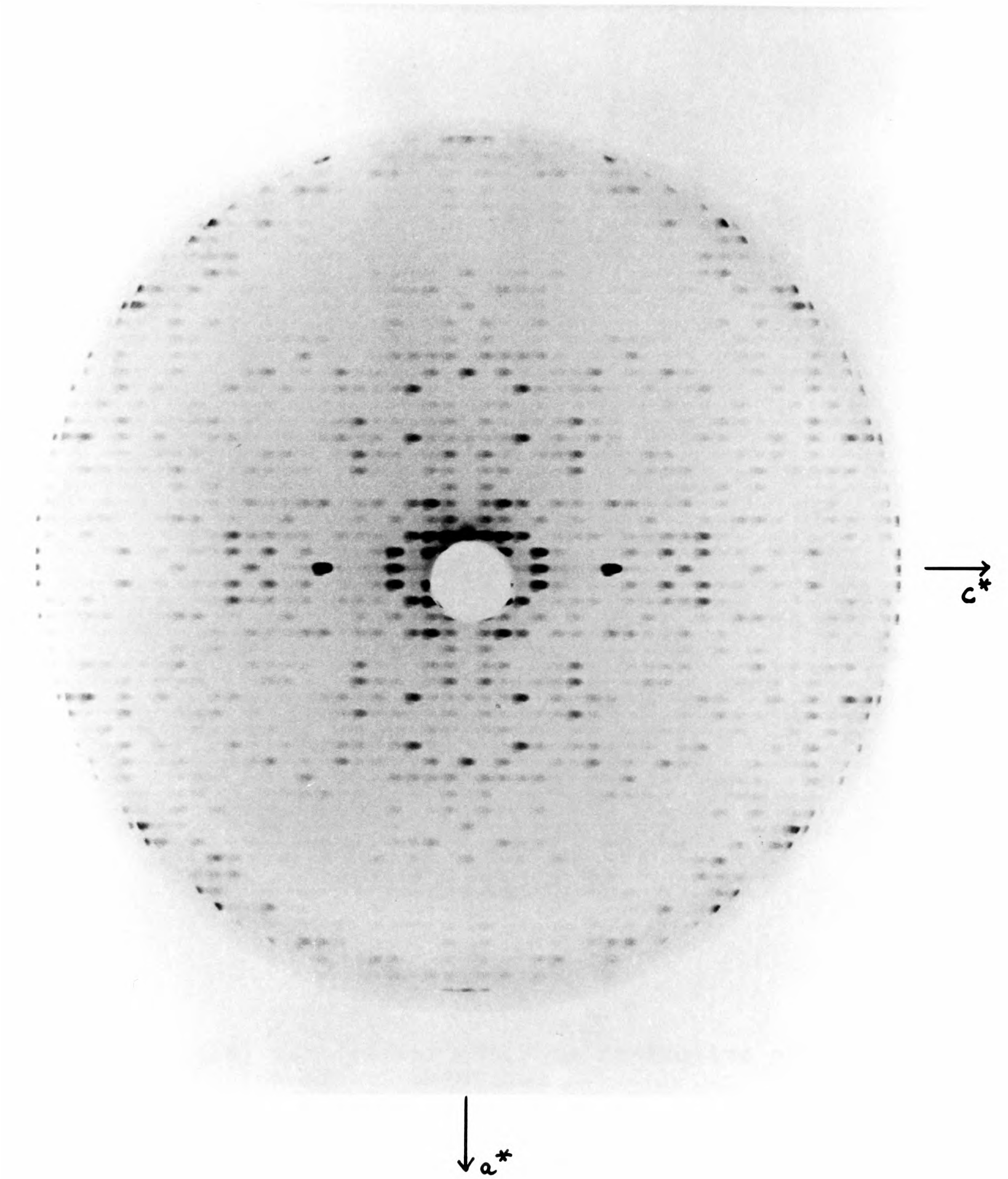
A search for heavy atom derivatives, produced by diffusing

FIGURE 3.15



The (hoℓ) zone of the platinum derivative of the Pp$\underline{b}$ tetragonal crystals.

FIGURE 3.16



The (h0ℓ) zone of the uranyl acetate derivative of the Pnb tetragonal crystals.

heavy metal compounds into the native crystals, was conducted on the original batch of crystals by Dr. Johnson. This search was hampered by the lack of an efficient means of measuring the intensities of the reflections from photographs of potential derivatives, and so the usefulness, or otherwise, of potential derivatives could be judged only qualitatively from the number of intensity changes observable by eye, and the degree of isomorphism judged from the unit cell dimensions. The approach to the heavy atom compounds tried was essentially one of trial and error while drawing on the experiences of other workers in the field.

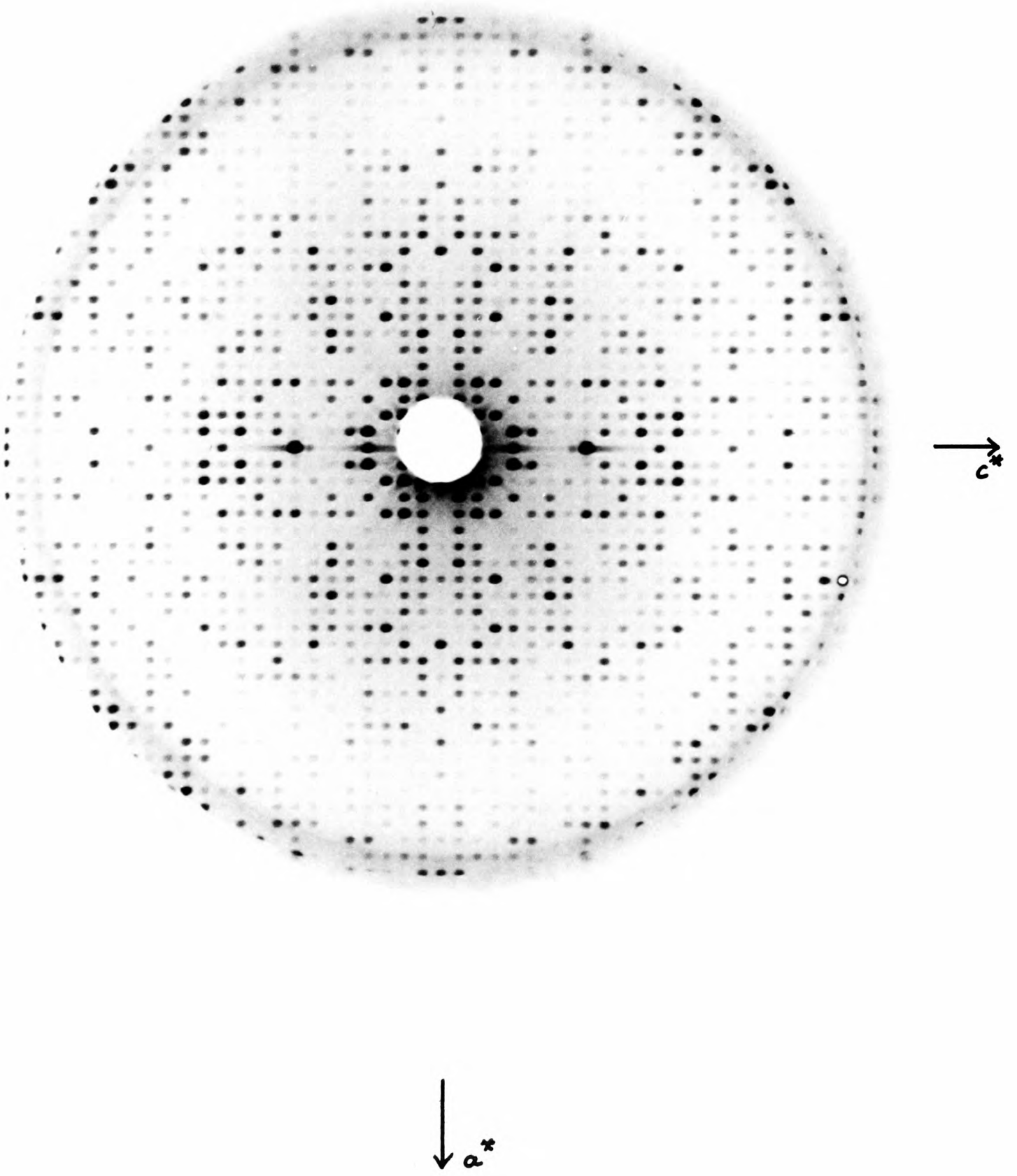
Of the various compounds tried, two gave what appeared to be reasonable intensity changes whilst remaining isomorphous with the native crystals; these compounds were the platinum diamino dichloride ion ($Pt(NH_3)_2Cl_2^{2-}$) and uranyl acetate ($UO_2(CH_3COO)_2$). (Figures 3.15, 3.16) The solutions into which the native crystals were placed in order to produce these derivatives were:

1. Platinum derivative:

1 mM	AMP	pH 7.0
10 mM	magnesium acetate	
5 mM	Tris buffer	
1 mM	$K_2Pt(NH_3)_2Cl_2$	

The crystals remained in this solution for approximately 2 days at 16°C. With later batches of crystals the 1 mM AMP was replaced by 1 mM IMP. The interaction of this platinum compound with proteins is probably via the displacement of the weakly bound chloride ions by the outer electrons of the sulphur of methionine. It was used in the structure determination of ribonuclease S (Wyckoff et al. (1967)). Despite the fact that

FIGURE 3.17



The (hoℓ) zone of the methyl mercury chloride derivative of the Ppb tetragonal crystals.

phosphorylase contains 22 methionine residues as well as many other potential binding sites, this platinum compound was found to give a good single site derivative of high occupancy.

2. Uranium derivative:

1 mM	AMP	pH 7.0
10 mM	magnesium acetate	
5 mM	Tris buffer	
0.5 mM	$UO_2(CH_3COO)_2$	

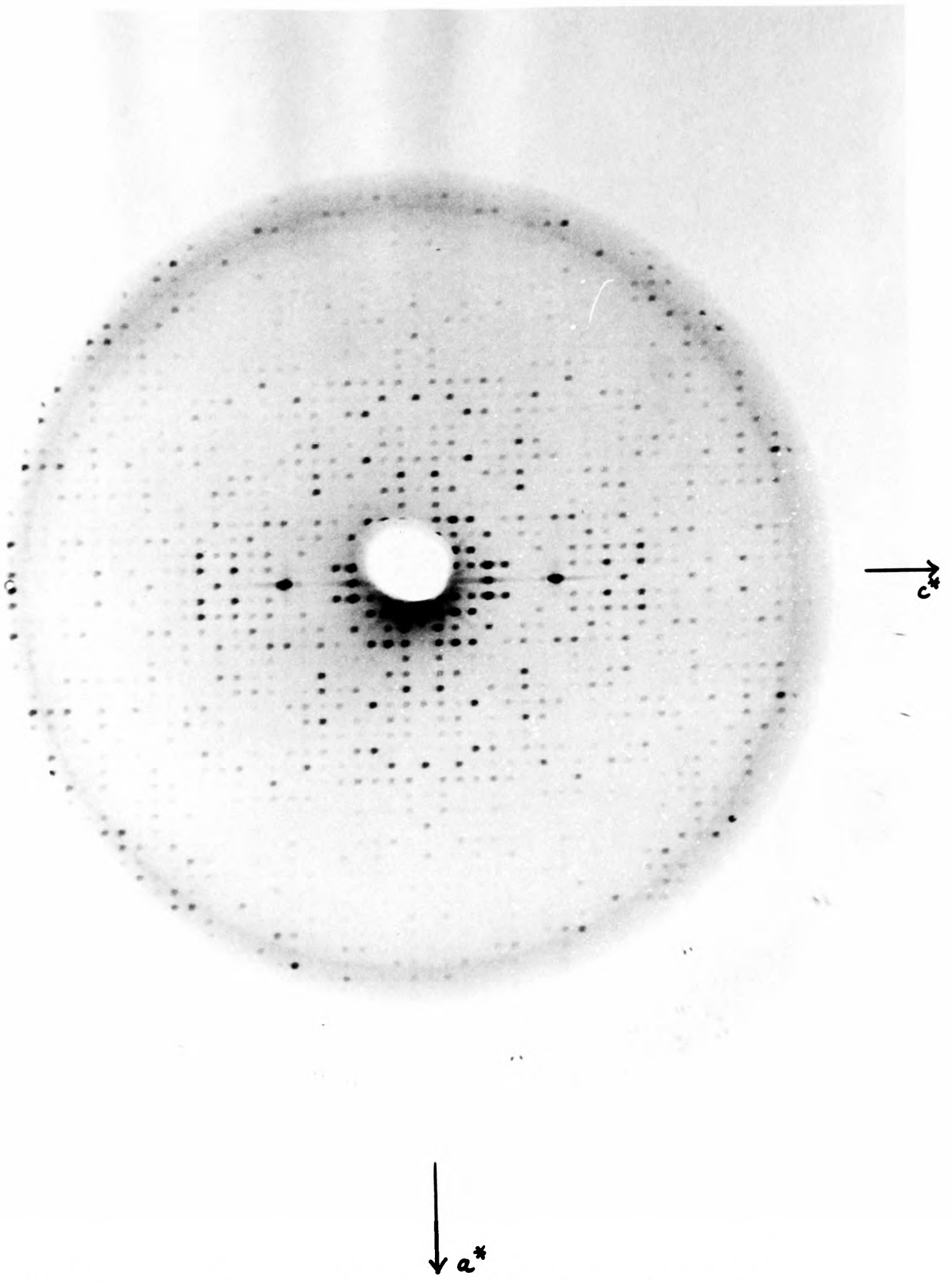
The soaking time for this derivative was 8 days at 16°C. Again for later batches of crystals the 1 mM AMP was replaced by 1mM IMP. Uranium has been found to bind to carboxyl groups in proteins; in particular it was used in the structure determination of hen egg-white lysozyme (Blake et al (1965)). It was hoped that a similar reaction would occur with phosphorylase.

More recently, Dr. Madsen has co-crystallised Ppb with methyl mercury chloride (CH_3HgCl) under conditions where there were two equivalents of mercury per monomer of enzyme. With these conditions it was hoped that mercury atoms would be covalently bound to the two reactive sulphydryl groups on the surface of the enzyme. Diffraction photographs of these crystals showed them to be isomorphous with the native enzyme; however only very small intensity changes were observable in the (h0l) and (hk0) zones (Figure 3.17).

Further diffusion experiments have been carried out recently, and a potentially useful derivative produced by soaking native crystals in a solution containing para-iodotoluene sulphonyl fluoride ("pipsyl"). This solution contained:

1 mM	IMP	pH 7.0
10 mM	magnesium acetate	
5 mM	BES	
5 mM	pipsyl	

FIGURE 3.18



The (hoℓ) zone of the pipsyl derivative of the Pp$\underline{b}$ tetragonal crystals.

The soaking time was 17 days at 16°C (Figure 3.18). The rationale behind using this compound was based on a very tentative suggestion from another laboratory that the serine which is phosphorylated in Pp<u>a</u> may exhibit slightly stronger nucleophilic properties than normally encountered in proteins. However, it now appears that this serine is not especially reactive. Nevertheless it was hoped that by using a relatively high concentration of pipsyl, the reaction with the protein would take place either at this unique site or at other nucleophilic sites..

It was necessary to collect diffractometer data on each of these potential derivatives before their usefulness, or otherwise could be judged.

3.2.4 <u>Strategy of Data collection</u>

If Bijvoet pairs of reflections are collected there are approximately 5300 measurements to give data to a resolution of 6Å. Photographic methods of data collection were impracticable since there was no available method of processing the films. Three diffractometers were considered for the data collection:

1. A five counter, five circle computer controlled diffractometer which had recently been developed in the laboratory. This machine was not available because of the demands on it from other projects at that time.

2. A five counter linear diffractometer. This machine is not really suitable for low resolution data collection when used in the five counter mode because of the frequent re-adjustments which are necessary when working at relatively small Bragg angles.

3. A four circle Hilger and Watts Y130 diffractometer controlled by a Digital Equipment Corporation PDP8 computer. This

is a very versatile, reliable machine which is relatively simple and quick to set up. The three dimensional data collection was undertaken using this machine.

With the four circle diffractometer approximately 40 reflections per hour may be measured using a counting time of 80 seconds per reflection. The 6Å data set may thus be collected in approximately 130 hours if each reflection and its anomalously related equivalent is measured. It was decided to use the ordinate analysis method (Watson et al (1970)) of data collection since this is somewhat faster than the conventional background, peak, background method, while retaining the same measurement statistics. Any small crystal slippage, which seemed quite likely with such a long data collection time, may be accommodated by this method, without having to reset the diffractometer.

When the tetragonal crystals are mounted in capillary tubes for data collection, in the manner described for the monoclinic crystals, they naturally lie with their c*/axes along the tube. On the diffractometer they can thus be most conveniently mounted with this axis parallel to the ϕ axis (Figure 2.4). This c* mount is a great advantage when it is remembered that in this space group the reflections (hkl) and (hk$\bar{l}$) are Bijvoet equivalent reflections. These Bijvoet pairs will have the same absorption correction in this setting (North et al (1968)), and, by stepping the diffractometer along the c* axis most quickly, they may be measured close together in time thus minimising the effect of radiation damage on the measurement of the anomalous scattering component. Such procedures are essential if the anomalous scattering from heavy atom derivatives of a protein of the size of phosphorylase is to be measured with

sufficient accuracy.

The standard computer programme supplied with the diffractometer by Hilger and Watts Ltd., was ammended so that only reflections for which $k \leqslant h$ were measured. The ordinate analysis routine is an overwrite to the standard programme, and was very kindly supplied to us by Dr. P.L. Wendell of the Laboratory of Molecular Enzymology, University of Bristol.

The reflections measured on the diffractometer were thus:

$$(h\ k\ l) \text{ and } (h\ k\ \bar{l}) \quad \text{where} \quad k \leqslant h.$$

The reflections were measured on an ω scan (i.e. each reflection was moved through its reflecting position by stepping the ω axis while the other axes remained stationary), using an equal number of steps for estimation of the peak and background intensities. The counting time, step size and number of steps were determined for each particular crystal, in such a way that the total scan width was at least twice the angular width of the widest reflection.

3.2.5 Setting up the Diffractometer

The diffractometer was set up for data collection in the conventional manner by positioning on reflections along the three principal axes. The goniometer arcs were first adjusted using a (001) reflection since in a c* mount the reflecting positions of these reciprocal lattice points are independent of the ϕ angle The (008) reflection was used for this purpose since it is very strong; it is in fact the strongest reflection in the data set. This reflection was also used to check the zero positions of the diffractometer axes. The positions of the a* and b* axes were determined by using the (1200) and (0 12 0) reflections respectively. Once the positions of these three axial reflections

had been accurately determined (i.e. to an accuracy of 0.02^{o}), the computer programme calculated the unit cell dimensions, and a setting matrix from which the positions of the other reflections in the data set could be generated. This setting matrix was checked on several reflections.

At this stage, the optimum sizes for the source and detector collimators were estimated empirically. Various sizes of collimator were investigated until the combination which gave the maximum peak intensity with the minimum background for the (008) reflection was found. Banner (1972) states that the diameter of the diffracted beam at the detector arises from four factors:

1. Crystal size: $A_C = \frac{C(S+D)}{S}$

2. Focal spot size $A_F = \frac{FD}{S}$

3. Wavelength spread in the beam: $A_D = 2\,\delta\theta D$ where $\delta\theta = \frac{\delta\lambda}{2d\cos\theta}$

4. Mosaic spread of the crystal: $A_M = 2MD\sin\theta$

where:

C is the crystal size in mm.
S is the source to crystal distance in mm.
D is the counter to crystal distance in mm.
F is the focal spot size in mm.
M is the mosaic spread in radians.

The overall diameter of the diffracted beam, A, is then given by:

$$A = A_C + A_F + A_D + A_M$$

For the four circle diffractometer:

S $\simeq$ 25 cm.

D $\simeq$ 25 cm

F = 0.4 mm.

If we assume a crystal of maximum dimension 1 mm. the various components have the values:

(1) A_C = 2.0 mm.

(2) A_F = 0.4 mm.

(3) Taking $\delta\lambda$ to be the wavelength difference between the copper $K\alpha_1$ and $K\alpha_2$ lines, 0.00382Å, and assuming 6Å resolution data:

$$A_D = \frac{2.\ 0.00382}{2.\ 6.\ 0.992}\ 250.$$

$$\therefore A_D = 0.16 \text{ mm.}$$

(4) Assuming a mosaic spread of 0.005 rad

$$A_M = 2.\ 0.005.\ 250.\ 0.128$$
$$= 0.32$$

The overall diffracted beam diameter is then approximately 2.9 mm., and so a detector collimator of at least this diameter should be used.

The optimum counting time, number of steps and step size were then estimated; the criterion being the best compromise between good counting statistics and low overall data collection time.

3.2.6 Absorption correction

The data were corrected for absorption using the semi-empirical method of North et al (1968). The absorption curve was measured on the (008) and (00$\bar{8}$) reflections both before and after the data collection run. If the absorption curve had not changed significantly during the data collection, the mean of the four curves was taken. In general the absorption was low with these crystals (normally less than 1.5) since they had square cross-sections.

3.2.7 Radiation Damage

The progress of radiation damage during the data collection was monitored by measuring three standard reflections after every 100 ordinary reflection measurements. By this procedure any discontinuities in the progress of the radiation damage were monitored. As a check on these standard reflections the first 100 (approximately) reflections measured during the data collection were re-measured after all the data had been collected. A linear radiation damage correction was applied to the data on the basis of the estimation of the damage from the standard reflections. This correction was then checked using these re-measured reflections and any further correction made if necessary.

The diffractometer controlling programme was written so that the first two standard reflections could be the (008) measured at $\phi = 0^{o}$ and the (008) measured at $\phi = 90^{o}$. Comparison of these two measurements of the (008) gave a monitor of any change in absorption during the data collection.

3.2.8 Diffractometer Practical Details

The diffractometer was fitted with a Phillips Fine-focus X-ray tube, with a copper anode and a Phillips Generator which was operated at 40 kV and 30 mA. A nickel filter was used to remove the majority of the white radiation and the copper K_{β} line. The counter was of the scintillation type with a sodium iodide crystal. The diffractometer was used in the equi-inclination setting.

The output from the diffractometer was in the form of paper tape; with the ordinate analysis programme the form of this output was six integers in the order:

H K L BACKGROUND PEAK WINDOW POSITION

The window position gave the step number at which the section of the total scan, which was to be used for the peak intensity, began. Thus a window position of zero or NS/2, where NS is the total number of steps in the scan, indicated crystal mis-setting or a very weak intensity, for the particular reflection in question.

3.2.9 Data Processing

The data processing was carried out on two computers: one was the laboratory's own Ferranti Argus 500 computer which has 12K words of core store available for data processing and magnetic tape backing storage; the other was the much larger I.C.L. 1906A, available through the Oxford University Computing Service, which has 256K words of core store plus disc, drum and magnetic tape backing store, and a sophisticated operating system.

The primary data (i.e. the data tapes as produced by the diffractometer) were processed on the Argus computer using a programme (PBMN 2/11) written by Dr. A.C.T. North. This programme checked the diffractometer tape for punching errors, and allowed any errors to be corrected. The standard deviation, σ_{No} on the background corrected intensity, No, was calculated for each reflection using the equations:

$$No = N - r\,n.$$

$$\sigma_{No} = \sqrt{\sigma_N^2 + r^2\sigma_n}$$

$$= \sqrt{N + r^2 n}$$

where N is the peak intensity

n is the background intensity

r is the ratio of the number of steps in the peak to the number in the background.

For all the data measured on the tetragonal Ppb crystals r had the value 1. The fractional standard deviation of No, $\sigma_{No/No}$, was

calculated, and if the value exceeded 100% the reflection was monitored. Any reflections for which the window position was zero or NS/2, where NS is the total number of steps in the scan, were rejected. The data were then corrected for absorption, and the Lorentz and Polarization factors applied. The LP factor for the equi-inclination setting is:

$$(LP)^{-1} = \frac{\sin 2\theta}{(1+\cos^2 2\theta)}$$ (Arndt and Willis (1966))

Finally, the reflections were output on to magnetic tape in the form:

$$h \quad k \quad l \quad F^2 \quad \sigma_{F^2}$$

The data were then transferred to the 1906A using the programme MGRD4 and stored in a file in this machine with a serial number allotted to each reflection. The linear radiation damage correction as estimated from a plot of the standard reflections was applied during this transfer. At this point the sums of the F^2 of the reflections measured at the beginning of the data collection, then repeated at the end of the data collection, were calculated and the ratio:

$$\frac{\Sigma F^2(\text{measured at beginning of data collection})}{\Sigma F^2(\text{measured at end of data collection})}$$

calculated. If this ratio differed significantly from unity, indicating that the radiation damage correction applied in the programme MGRD4 had been inadequate, a further linear correction was applied at a later stage of data processing. The remeasured reflections were then removed from the data set.

Checks were made on the agreement between equivalent reflections

(hkl and hk$\bar{l}$) within the data set using the programme TETEQUIV written by Dr. L.N. Johnson, but later modified. The ratios

$$S = \frac{\sum F^2(hkl)}{\sum F^2(hk\bar{l})} \qquad \text{and} \qquad R = \frac{\sum |F^2(hkl) - F^2(hk\bar{l})|}{\sum \overline{F^2}}$$

where calculated in ranges of h,k,l and $\sin^2\theta$. Only reflections for which both equivalents were measured were used in calculating the ratios. Reflections for which the F^2 of either equivalent differed by more than 6 x σ from the mean of the pair of reflections were monitored. The values of the ratio, S, were plotted for each of the four parameters so that any systematic trends could be seen. If necessary a scale factor was applied to the F^2 of the (hk$\bar{l}$) reflections to overcome such a trend. These scale factors were linear functions of the form:

$$A \times I + B$$

where I was h,k,l or (800 x $\sin^2\theta$). A second run of TETEQUIV was necessary in order to apply such a scale factor and check the resulting agreement between equivalent reflections.

As will be described later, the 6Å data sets were mostly collected from three crystals. At this point in the data processing the data from the separate crystals were merged together to form the complete 6Å data set using the programme Scale, Sort, Merge (SSM) written by Mrs. E. Dodson; any further radiation damage correction was applied here. Scale factors between the sets of data were calculated from overlapping reflections using the method of Hamilton, Rollett and Sparks (1965). Poor agreements between repeated measurements of the same reflection were monitored and a "Merging" R factor calculated using reflections repeated in

different data sets. This R factor was defined by:

$$R = \frac{\sum|F_1^2 - F_2^2|}{\sum(F_1^2 + F_2^2)}$$

where F_1 was the structure amplitude of a particular reflection measured in one data set, and F_2 was the structure amplitude of the same reflection measured in a second data set.

Some values of Merging R factors for different proteins are:

2.5Å data set of tetragonal Hen Egg-white lysozyme in 3M urea 3.6%
(K.W. Snape (private communication))

3.0Å data set of Phosphoglycerate Kinase; native crystals 5.0%
(P.R. Evans (private communication))

3.0Å data set of Phosphoglycerate Kinase; Ethyl Mercury Phosphate crystals 10%
(P.R. Evans (private communication))

The output from SSM was a merged set of structure amplitudes in the form:

$$h \quad k \quad l \qquad F^2 \quad \sigma_{F^2}$$

The sets of native and derivative data were then collected together using the programme Collect Assorted Data (CAD) written by Mrs. E. Dodson. The native-derivative scale factor was calculated and applied using the programme ANSC written by P.R. Evans. The scale factor, K, was applied to the derivative data in such a way as to satisfy the relationship:

$$K\frac{\sum F_{pH}^2}{\sum F_p^2} = 1$$

The scale factor was plotted in ranges of h,k,l, $\sin^2\theta/\lambda^2$ and F_p^2, and a linear function calculated for each of these ranges. The choice of scale was then applied in a second run of ANSC. Large

differences between anomalously related reflections were monitored; the values of Matthews Empirical k (Chapter 2) were calculated in ranges of $\sin^2\theta/\lambda^2$, and the mean isomorphous change in the structure amplitudes:

$$\langle |F_{pH} - F_p| \rangle$$

and mean fractional isomorphous change:

$$\left\langle \frac{|F_{pH} - F_p|}{F_p} \right\rangle$$

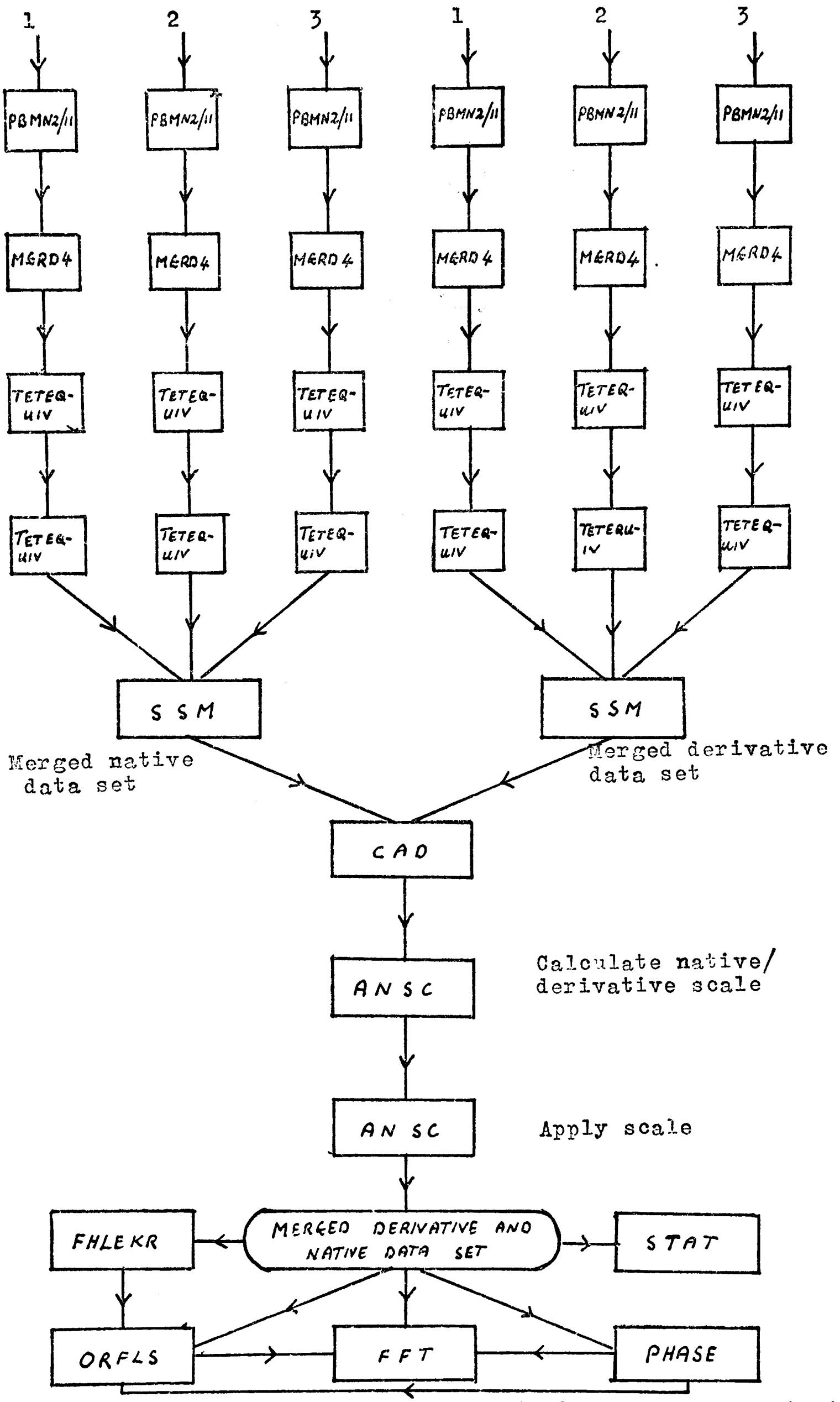
calculated. After scaling the data were in the form:

h k l $4\sin^2\theta/\lambda^2$ F_p σ_p F_{pH} σ_{pH} Δ_{anom} σ_{anom}

where Δ_{anom} is the anomalous difference $(F_{pH}^{+} - F_{pH}^{-})$ with a standard deviation σ_{anom}. The last four integers were stored for each derivative.

A variety of operations could then be carried out on the merged set of native and derivative data. Difference Patterson, and later difference Fourier, syntheses were calculated using the Fast Fourier Transform programme (FFT) written originally by Dr. L. Ten Eyck (M.R.C. Unit of Molecular Biology, Cambridge), and modified by Mrs. E. Dodson and P.R. Evans. Heavy atom positions were refined using the programme ORFLS written originally by Dr. P. Main (University of York) and modified by K.S. Wilson and Mrs. E. Dodson. This programme uses a full matrix least squares refinement; it may be used for refinements using centric data only, F_{HLE} coefficients or phased refinement. F_{HLE} coefficients and a Kraut scale factor (Chapter 2) could be calculated using empirical Matthews k values in a programme FHLEKR written by Dr. G. Bentley and P.R. Evans.

FIGURE 3.19



The data processing scheme for typical native and derivative sets of data each measured on 3 crystals.

Phase angles were calculated by the method of Blow and Crick (1959) and North (1965) using the programme PHASE written by Dr. G. Bentley and M.J. Geisow. Wilson and Crick-Magdoff plots were computed on the native and derivative data using the programme STAT. Figure 3.19 gives an outline of the scheme of data processing.

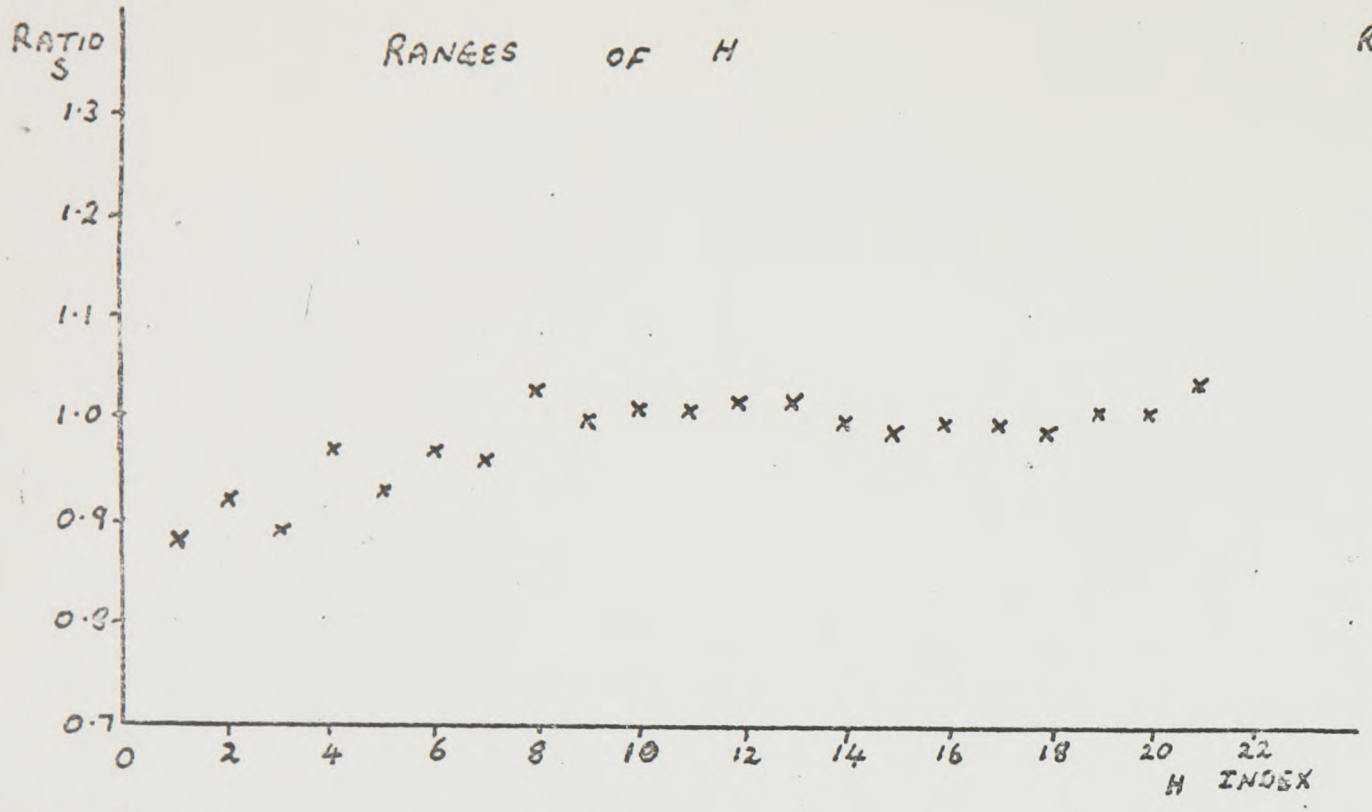
3.2.10 Initial Attempts at Data collection

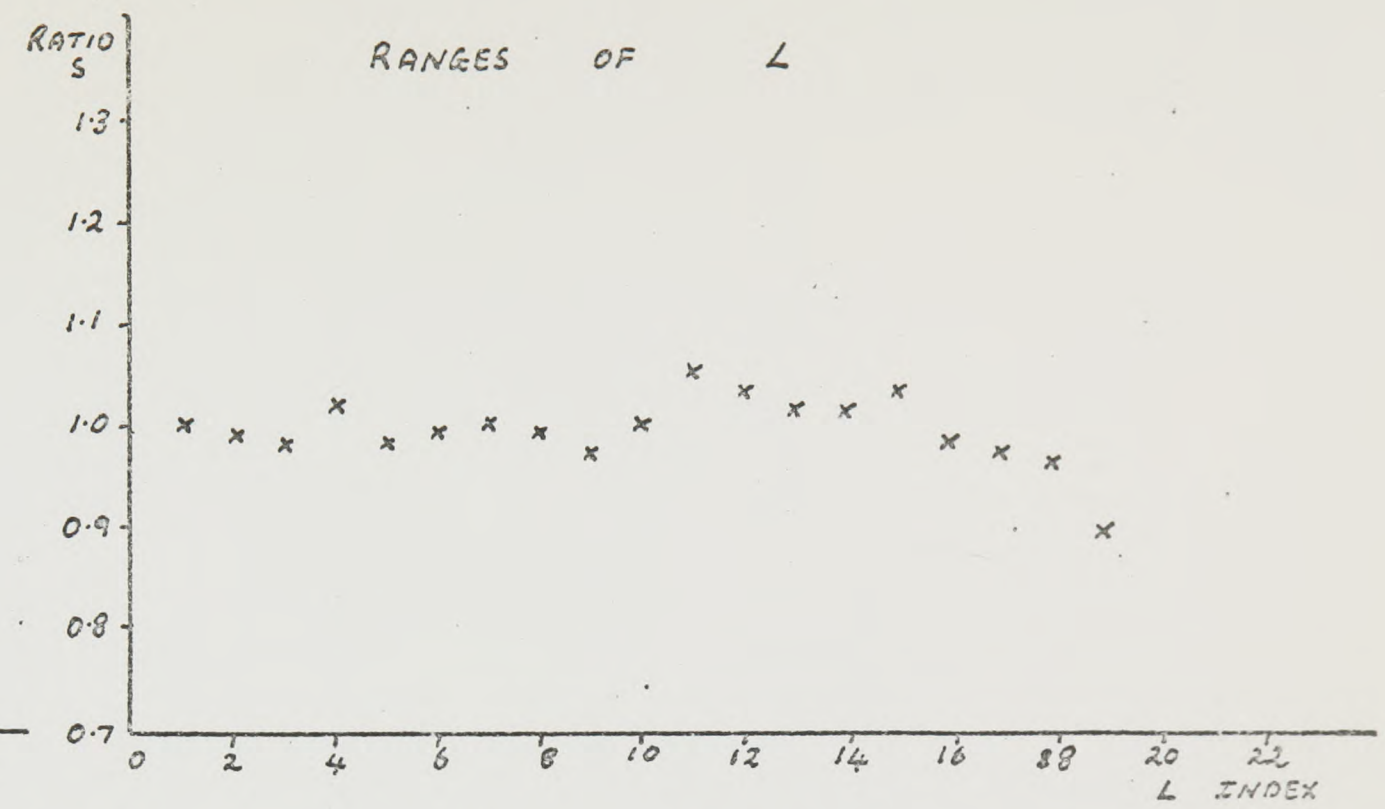
Several attempts were made to collect three dimensional data on the original crystals grown by Dr. Eagles and M. Iqbal. However, the crystals were small with the result that the diffraction data were weak, and therefore poorly measured. The whole 6Å data set was collected on one crystal in each case with the result that the radiation damage was very high: 25% for the native; 18% for the uranium derivative; 26% for the platinum derivative. No useful information was derived from the sets of data.

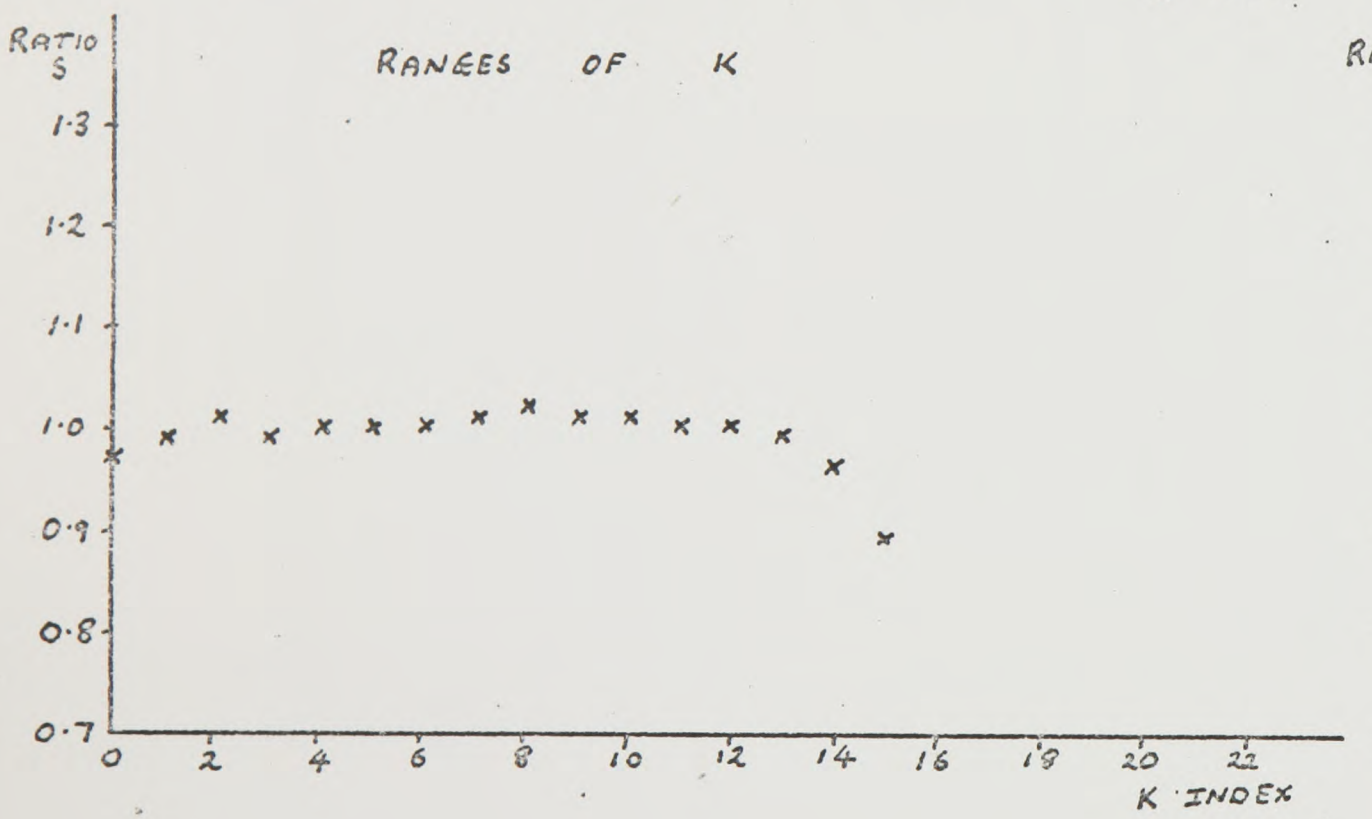
3.2.11 The 6Å Resolution Data

When Dr. Madsen had obtained the new, large crystals it was decided to collect the 6Å resolution data from three crystals. The radiation damage would thus be reduced to approximately 10% on each crystal, which was considered to be satisfactory. Each crystal was used for a different resolution range, the ranges being chosen so that the 6Å data set was divided into three shells with approximately the same number of reflections in each one. The limits on the Bragg angles of the shells were chosen so that there were common reflections between the data sets in order that the sets could be scaled together. The three shells with their limiting Bragg angles were:

6.0Å	- 6.9Å	Maximum θ	7.4°	Minimum θ	6.4°
6.9Å	- 8.7Å	Maximum θ	6.5°	Minimum θ	5.0°
8.7Å	- ∞	Maximum θ	5.2°	Minimum θ	1.2°







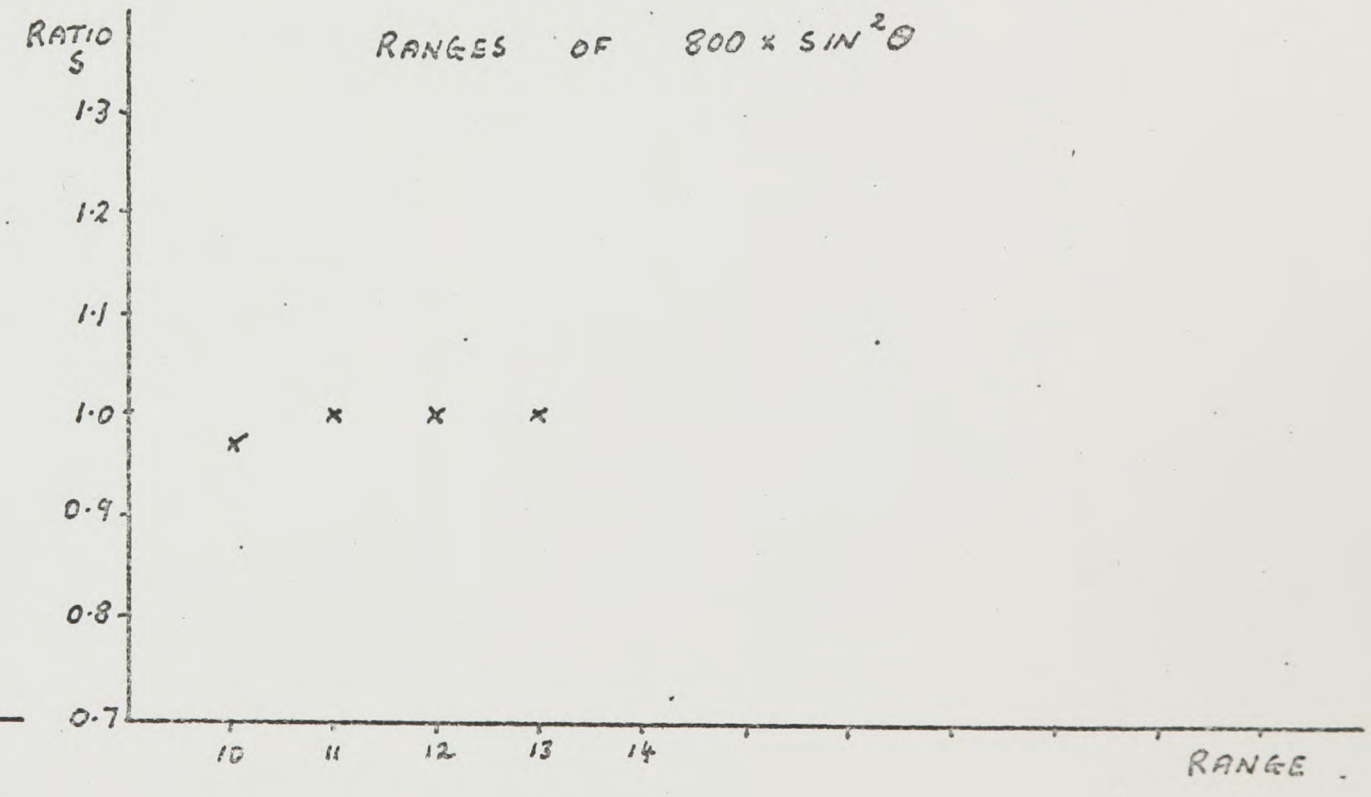


FIGURE 3.20
The agreement between equivalent reflections for crystal 206

TABLE 3.1

NATIVE CRYSTALS - PHYSICAL PARAMETERS

Crystal Number	Crystal size (mm) axbxc	Shell	Cell dimensions from 4 circle
206	1.0 x 1.0 x 2.2	6.0Å - 6.9Å	a = b = 129.70Å c = 115.91Å
207	1.1 x 1.1 x 1.8	8.7Å → ∞	a = b = 129.39Å c = 115.53Å
208	1.0 x 1.0 x 2.4	6.9Å - 8.7Å	a = b = 129.07Å c = 116.29Å

TABLE 3.2

NATIVE CRYSTALS - PRIMARY DATA PROCESSING

Crystal Number	Total no. of Reflections Processed	No. of SD failures (1)	No of back-ground failures (2)	Maximum Absorption correction
206	1923	2	8	1.110
207	2003	2	8	1.111
208	2043	0	2	1.437

Notes:

1. A reflection was counted as a standard deviation (SD) failure if: $\frac{\sigma_{No}}{No} \geq 1.0$

2. A reflection was counted as a background (BG) failure if the peak window was at either extremity of the reflection scan. These reflections were rejected.

Approximately 2000 reflections were collected on each crystal. The total data collection time for the full 6Å data set was approximately six days on the four-circle diffractometer.

(a) Native Data; Crystals 206, 207, 208

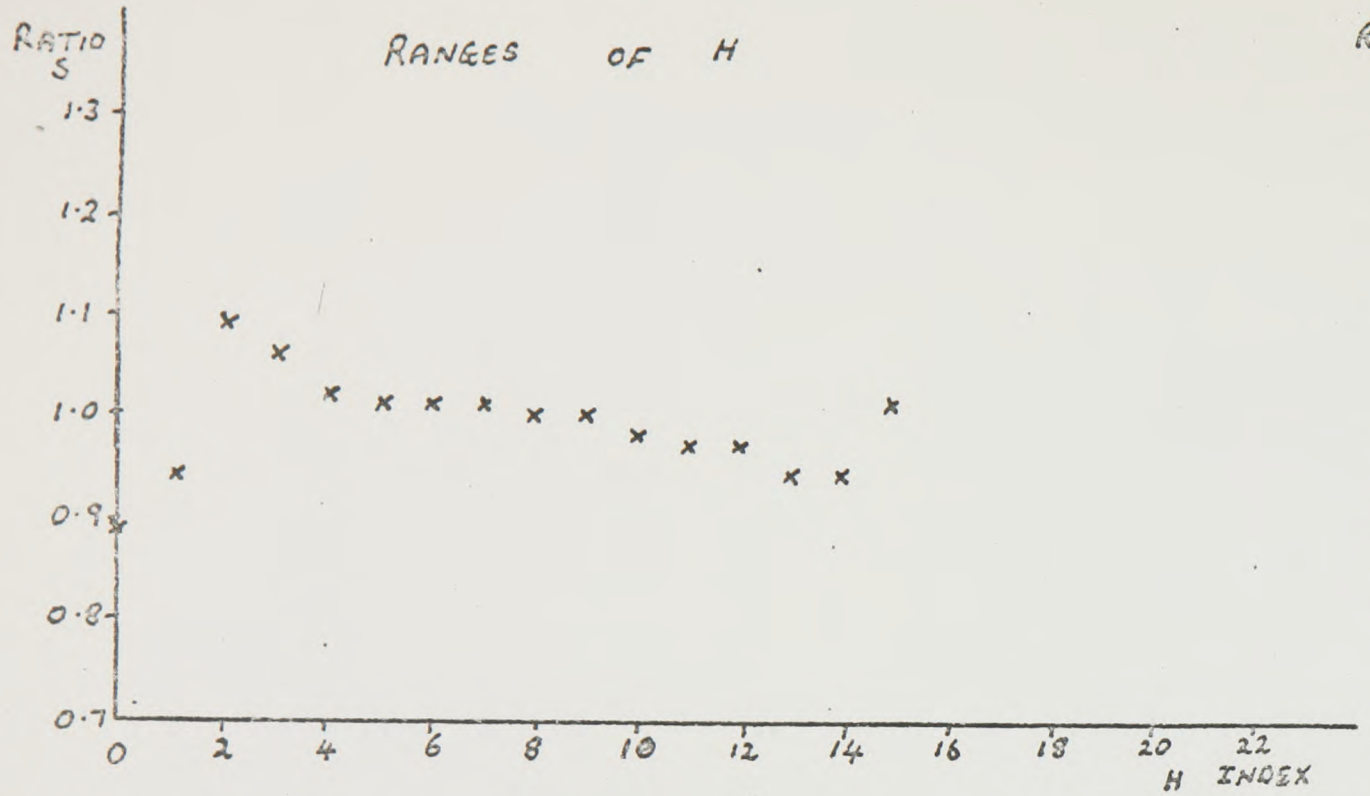
The sizes of the crystals, and the unit cell dimensions measured from them on the diffractometer are shown in Table 3.1. All these crystals were large and diffracted x-rays strongly. A source collimator of 1.4 mm diameter and a detector collimator of 5.0 mm. were used for each crystal. The reflection peaks were scanned using 50 steps of 0.02^{o} counting for 2 seconds per step. The primary data processing statistics are shown in Table 3.2.

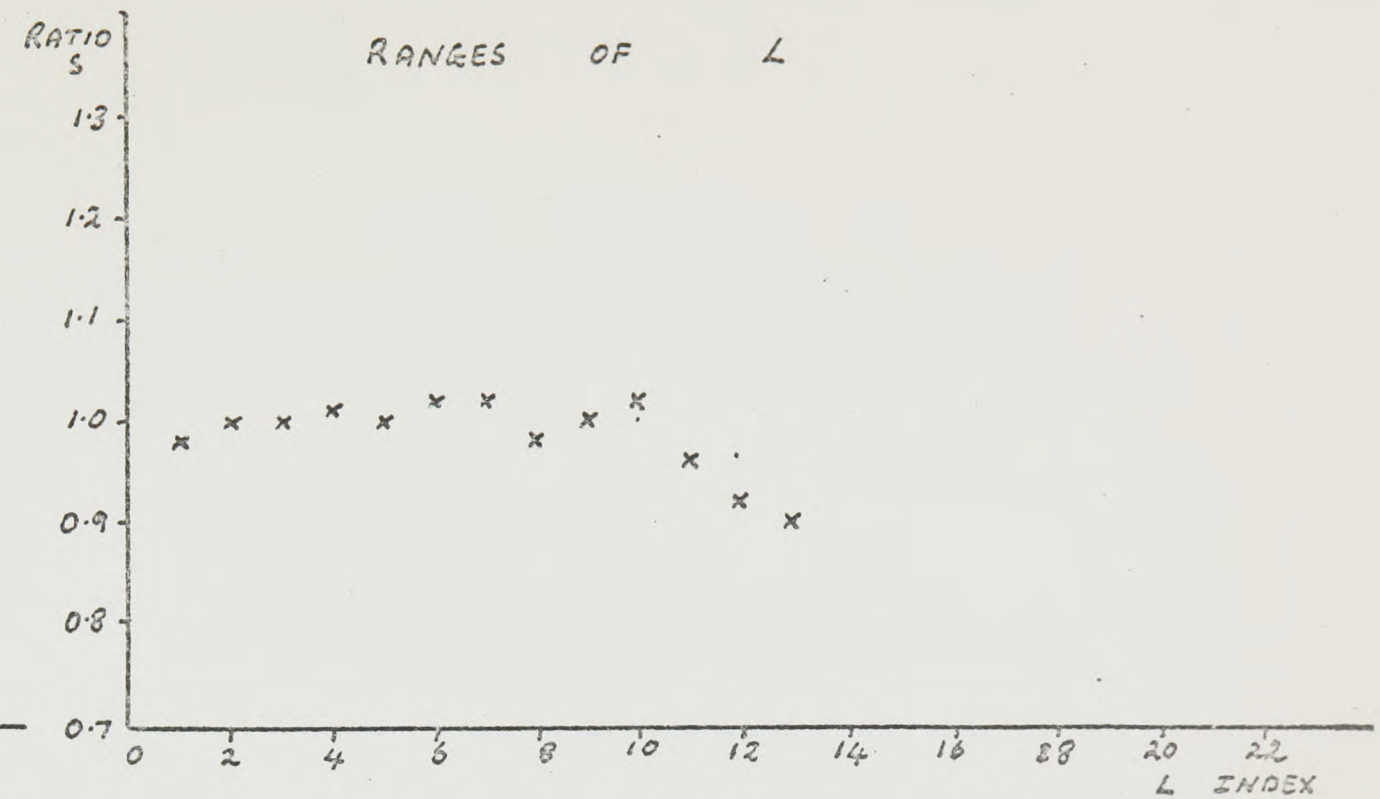
Crystal 206. The radiation damage as estimated from the standard reflections was 12% and so a linear radiation damage correction with a slope of 6.667×10^{-5} was applied to the data. However, it was found by comparison of the sums of the intensities of 115 reflections measured at the beginning and end of the data collection, that this correction was too high. A further linear correction was applied to scale down the intensities of the reflections measured at the end of the data collection by 0.967.

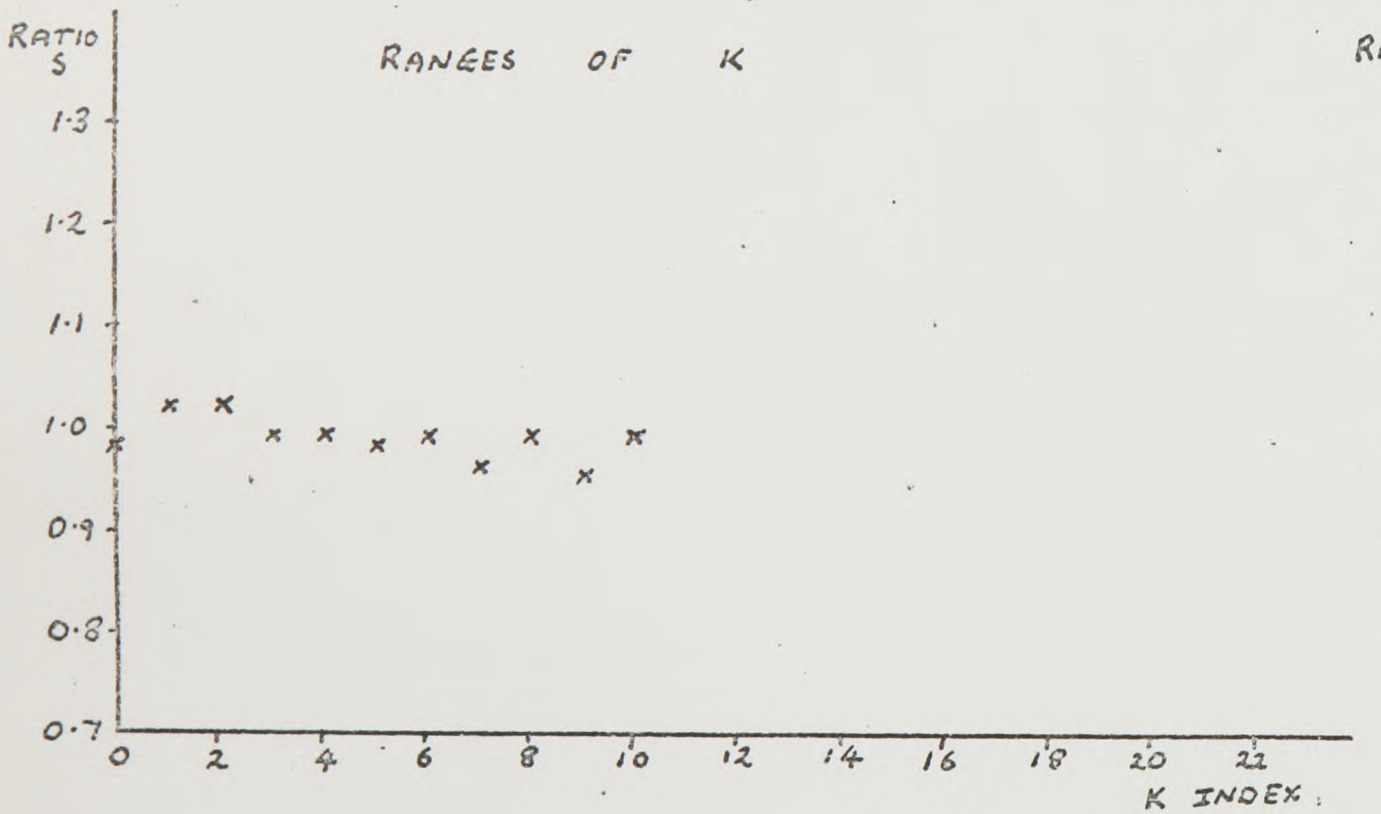
The agreement between equivalent reflections was analysed using the programme TETEQUIV, and a scale applied to the F^2 of the $(hk\bar{l})$ reflections given by the equation:

$$\text{Scale} = 0.9936 + |l| \times 0.0044.$$

The plots of the ratio S (see below). versus hkl and $\sin^2\theta$ after this scale factor had been applied are shown in Figure 3.20. The overall agreement between equivalent reflections was:







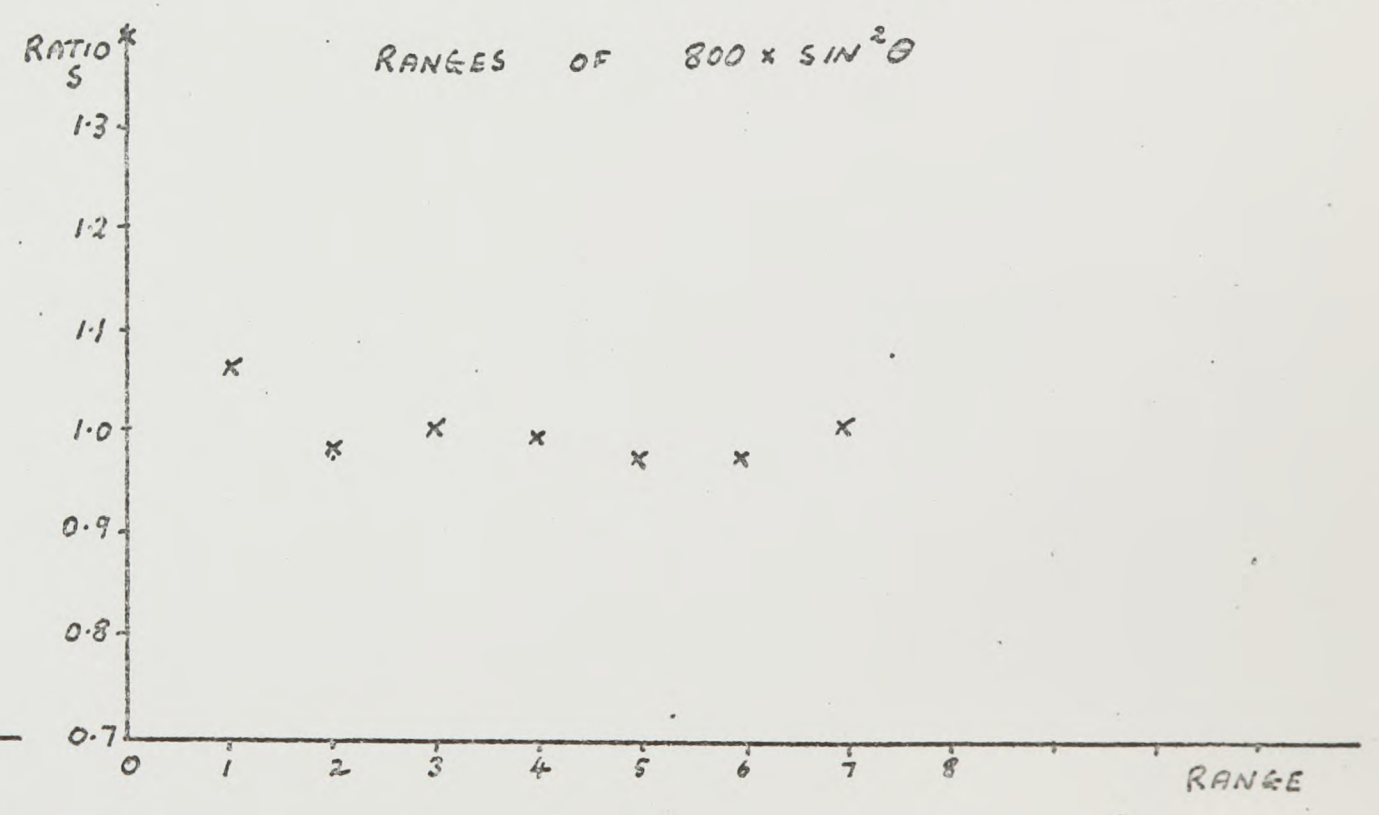


FIGURE 3.21
The agreement between equivalent reflections for crystal 207

	No. of Refl. pairs	S	R
Centric Data	137	0.9690	11.53%
Acentric Data	734	1.0017	8.13%
Overall	871	0.9967	8.65%

where $S = \sum F^2(hkl) / F^2(hk\bar{l})$

$$R = \frac{\sum |F^2(hkl) - F^2(hk\bar{l})|}{\sum \overline{F^2}}$$

Crystal 207

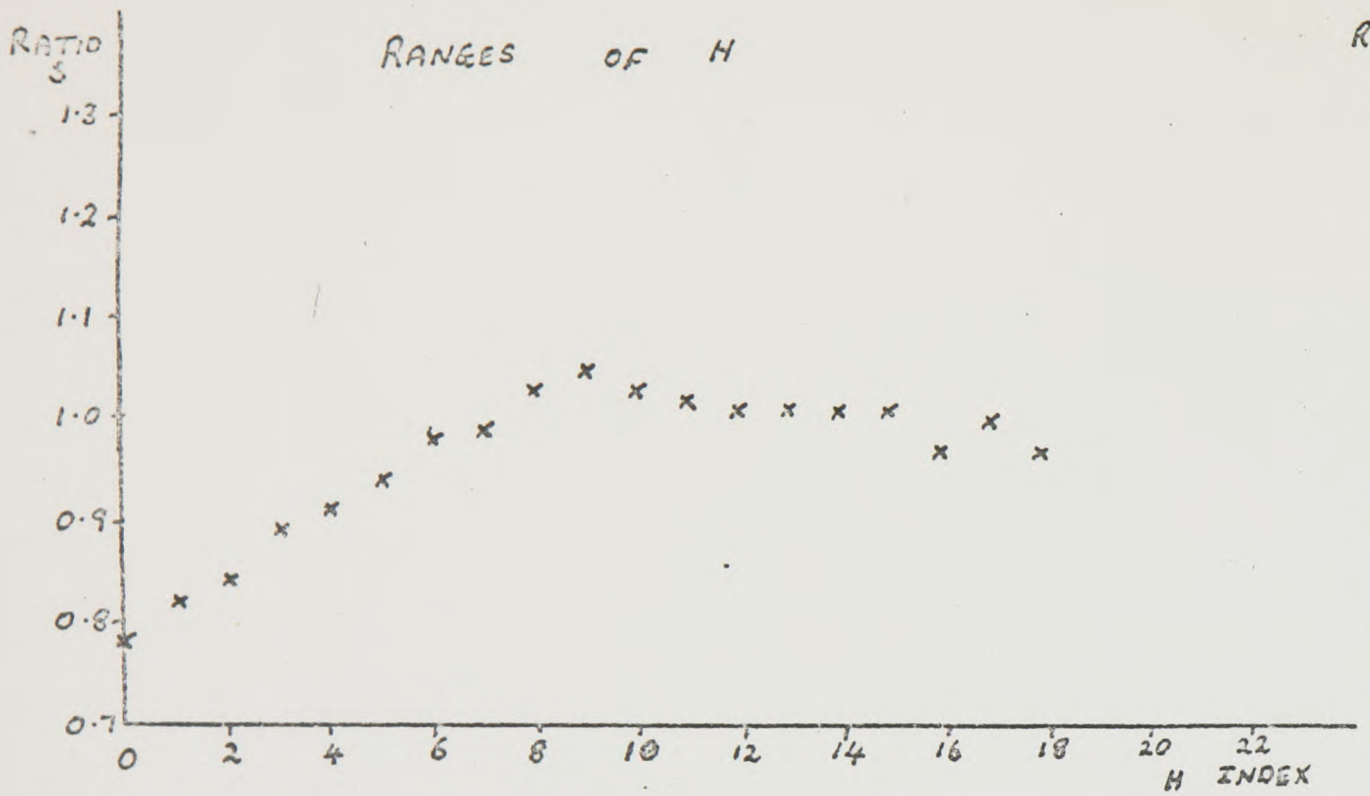
No radiation damage corrections were applied to this data. A scale factor was applied to the F^2 of the $(hk\bar{l})$ reflections of the form:

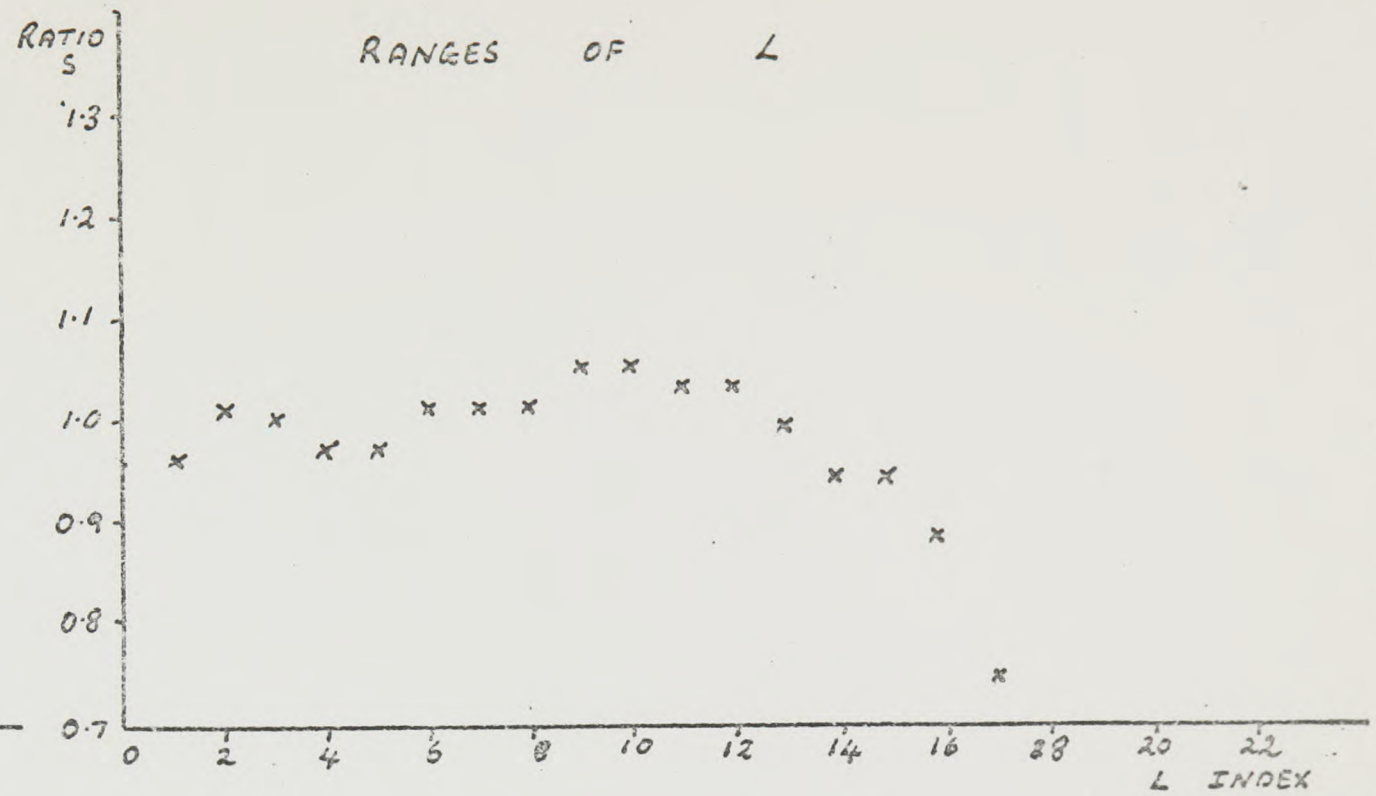
$$\text{Scale} = 1.0582 + |l| \times 0.0139$$

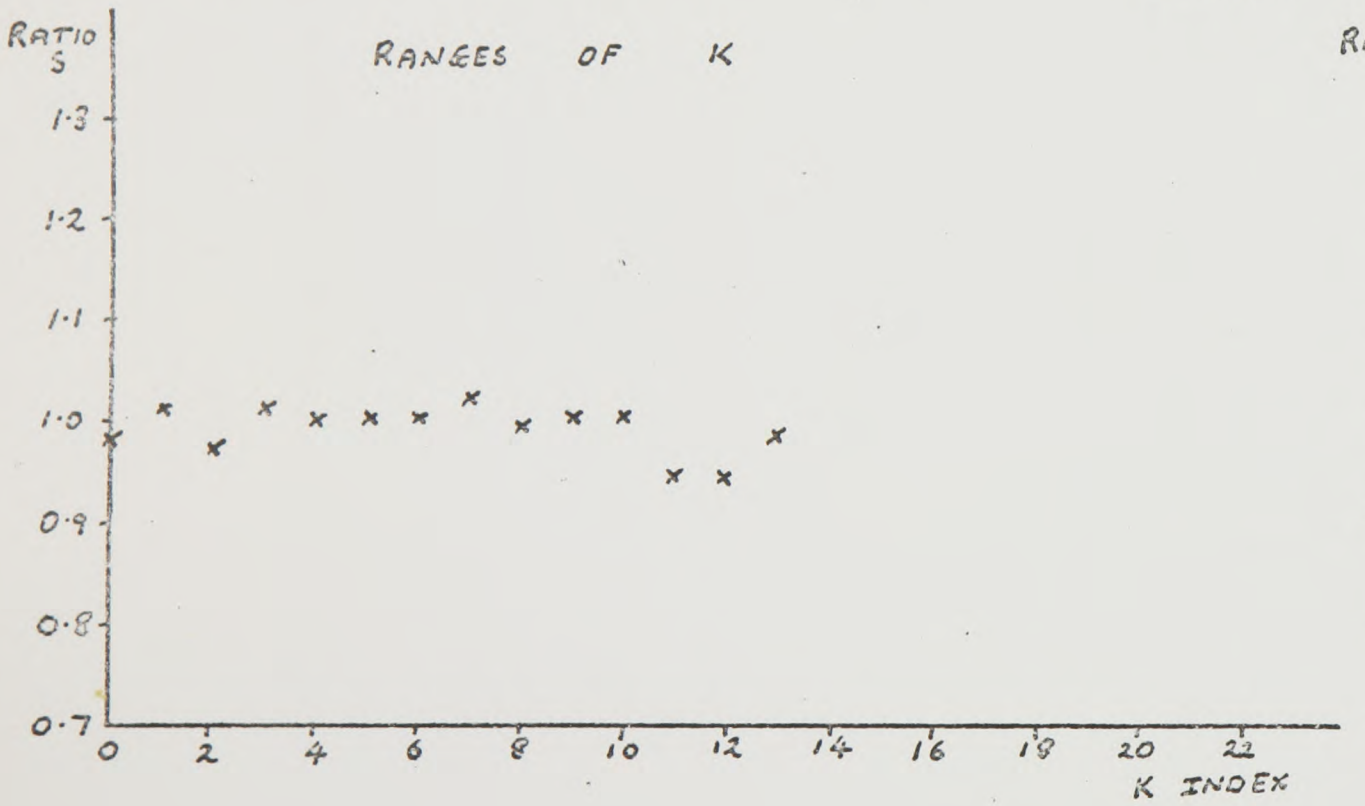
The plots of the ratio, S, are shown in Figure 3.21.

The overall agreement between equivalent reflections was:

	No. of Refl. Pairs	S	R
Centric Data	250	0.9955	13.27%
Acentric Data	641	0.9952	8.95%
Overall	891	0.9953	10.18%







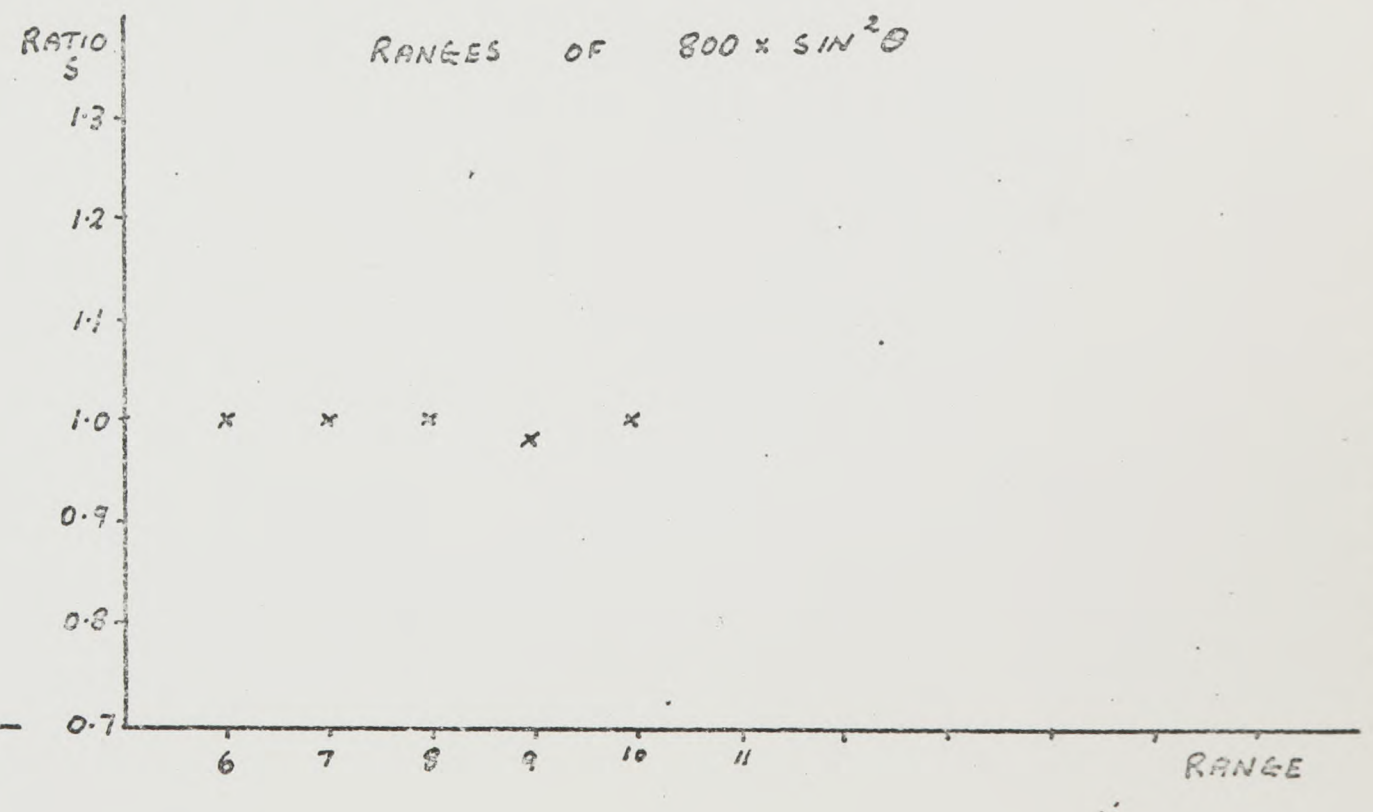


FIGURE 3.22
The agreement between equivalent reflections for crystal 208

Crystal 208

No radiation damage correction was applied to this data. A scale factor was applied to the F^2 of the (hk$\bar{l}$) reflections of the form:

$$\text{Scale} = 1.0272 + |l| \times 0.0130$$

After application of this scale, the overall agreement between equivalent reflections was:

	No. of Refl. Pairs	S	R
Centric Data	170	0.9628	13.48%
Acentric Data	762	1.0035	10.21%
Overall	932	0.9956	10.83%

The plots of the ratio, S, versus h,k,l, and $\sin^2\theta$ are shown in Figure 3.22.

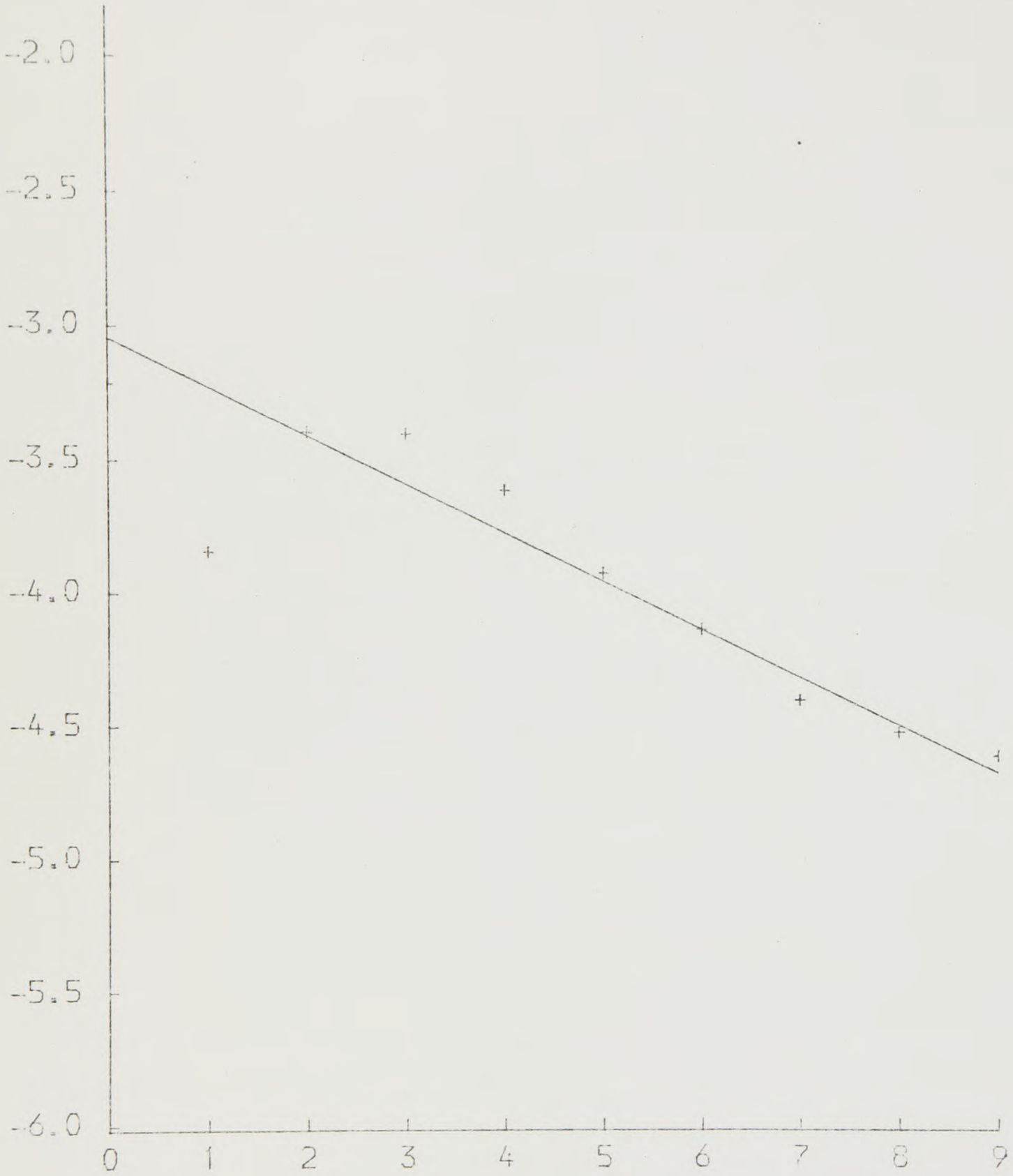
Crystal to Crystal Scaling

The crystals were scaled together on the basis of F^2 using the programme Scale Sort Merge. The numbers of overlapping reflections between the files were:

Crystal number	Scale
208/207	398
208/206	349

The crystals were scaled on to crystal no.208 since this crystal

FIGURE 3.23



PT(NH3)2 OV NAT WILSON PLOT

The Wilson plot for the native data.

In this, and subsequent Wilson and Crick-Magdoff plots, the ordinate is $\sin^2\theta/\lambda^2$ scaled to give the 10 points on the graph. The difference between the ordinates is 0.00077 $Å^{-2}$.

gave the strongest diffracted intensities. The scale factors converged after eight cycles of refinement to:

Crystal number	Scale
208	1.0
207	2.306
206	1.349

These scale factors were applied and the data sets merged to give the 6Å data set with 2708 independent reflections. The merging R factor was 5.22%.

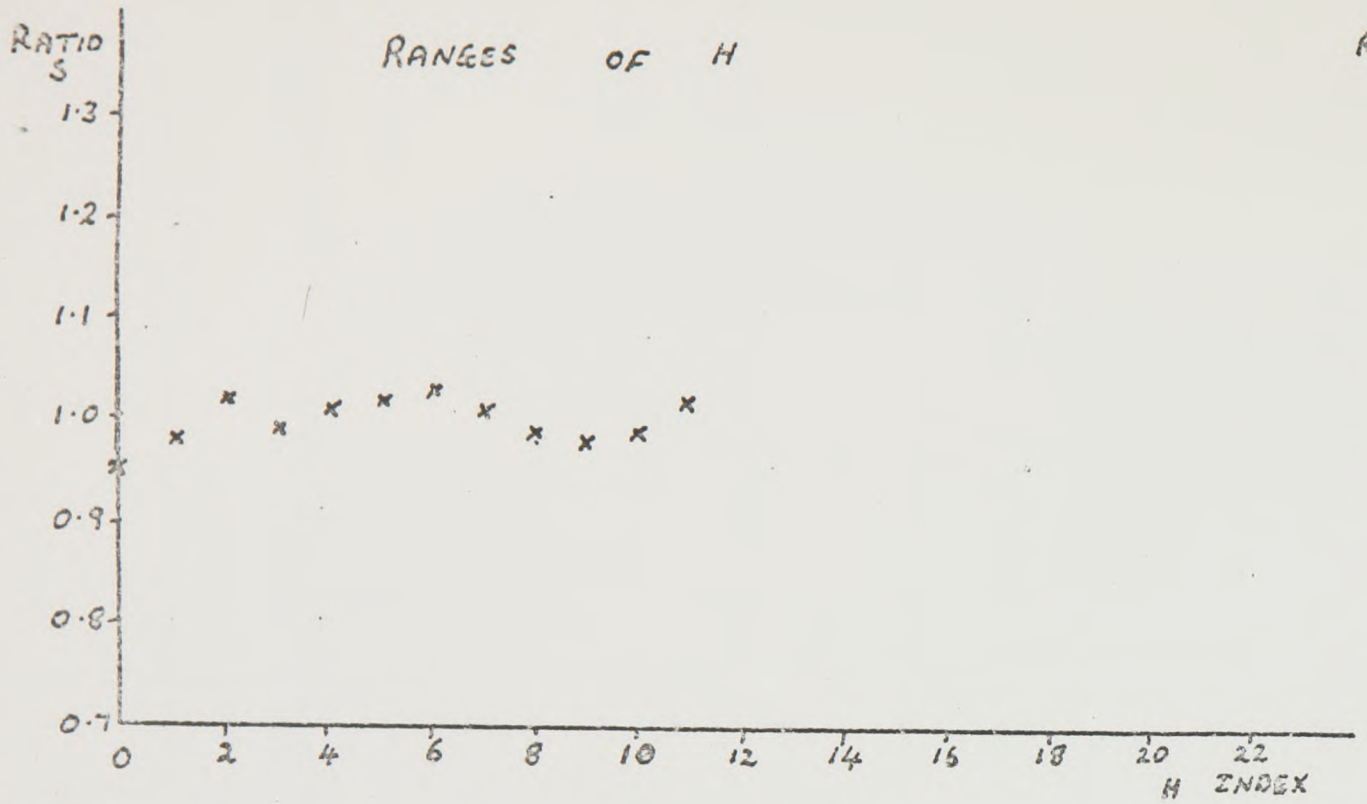
The Wilson Plot for the native data is shown in Figure 3.23. The intercept of this plot gives an absolute scale factor of 21.0

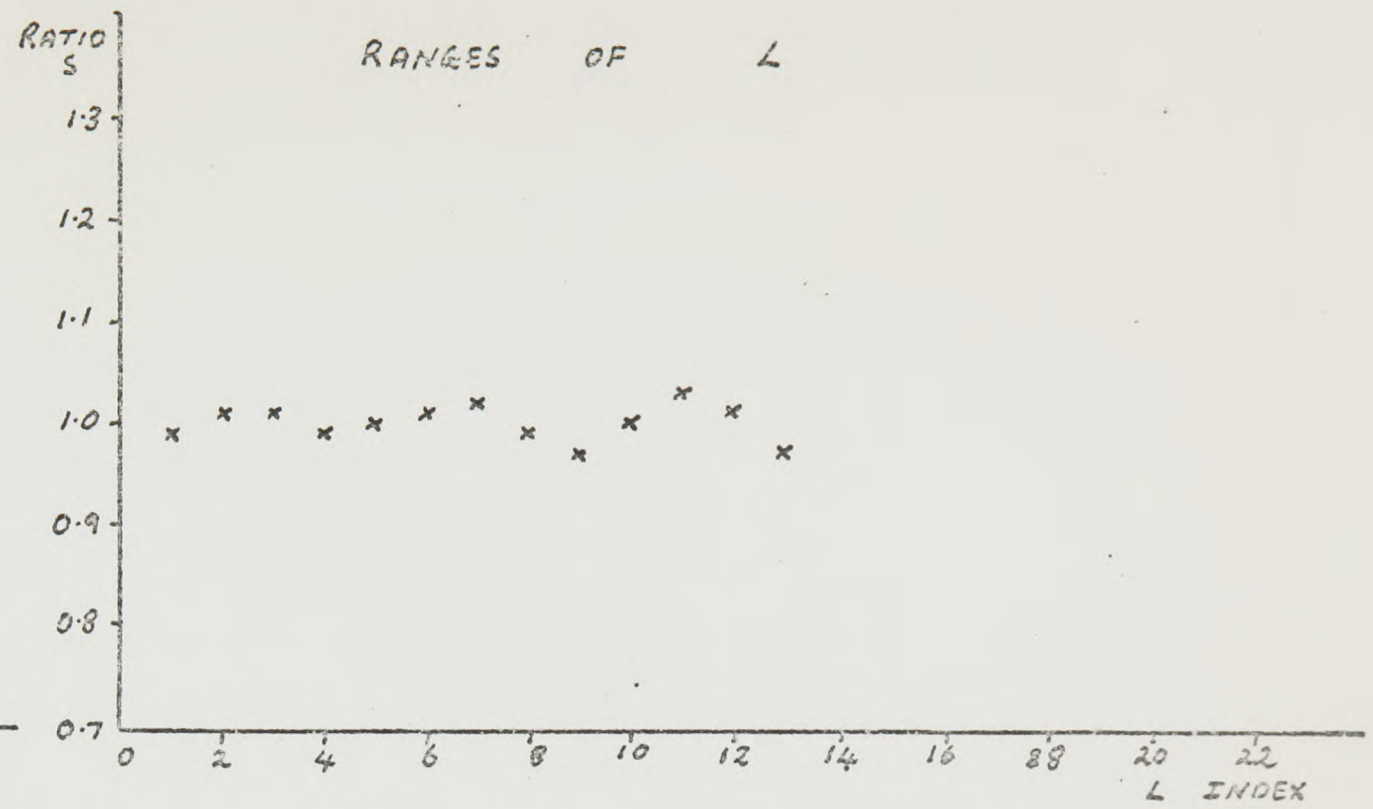
(b) Platinum Derivative Data; Crystals 240- 241; 242

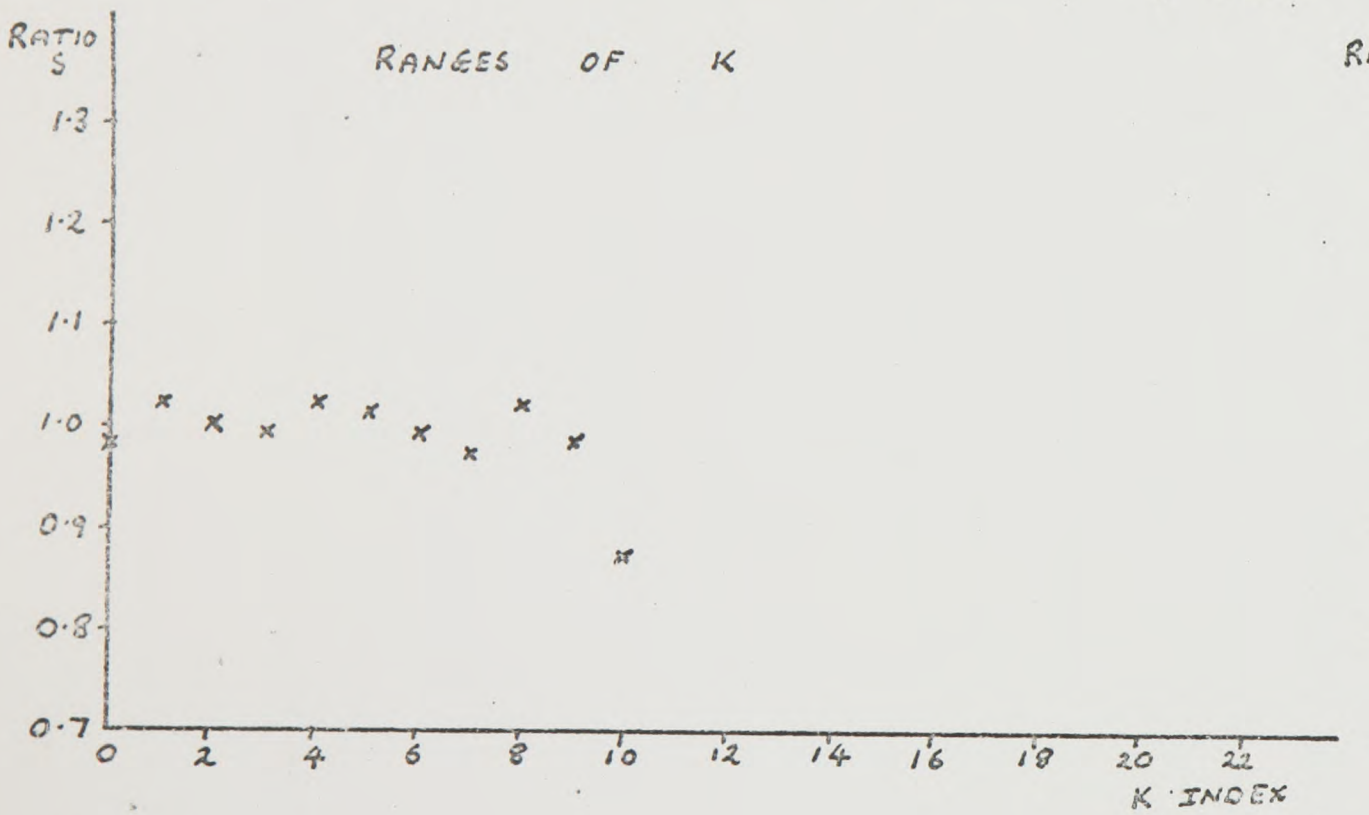
These three derivative crystals were produced by soaking three native crystals in the same solution containing platinum diaminodichloride. The soaking time was the same for each crystal to try to ensure that the occupancies of any platinum sites would be the same in each crystal. The dimensions of the crystals and unit cell dimensions measured from them are shown in Table 3.3.

A 1.4 mm source collimator and 3.5 mm. detector collimator were used for each crystal. The scan for each crystal comprised 0.02° steps on the ω axis counting for 2 secs per step; 40 steps were used for crystal numbers 240 and 241, and 44 steps for number 242. The primary data processing statistics are given in Table 3.4.

Crystal 240 There was a very large change in the absorption curve of this crystal during the data collection, due possibly to mother liquor condensing around the crystal. The







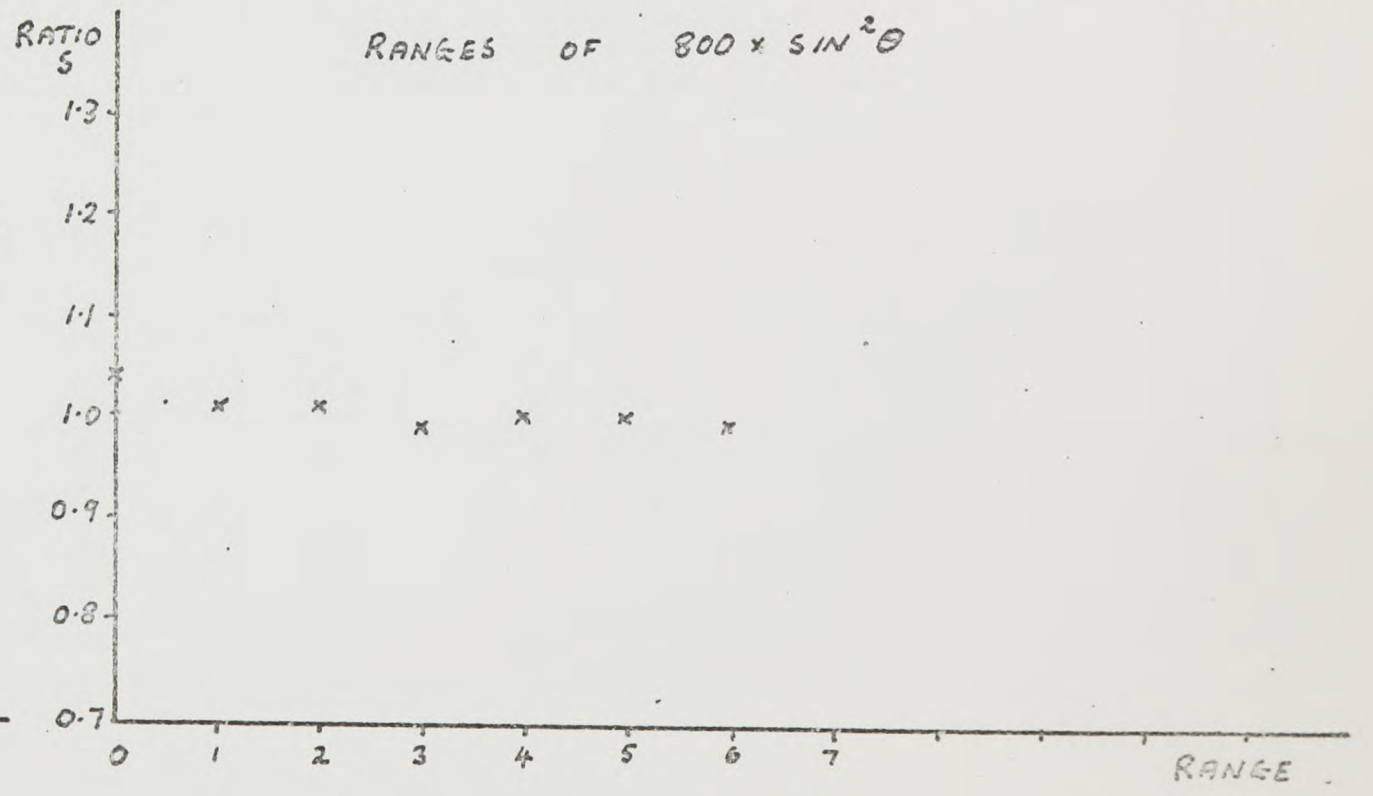


FIGURE 3.24
The agreement between equivalent reflections for crystal 240A

TABLE 3.3

PLATINUM DERIVATIVE CRYSTALS - PHYSICAL PARAMETERS

Crystal Number	Crystal size (mm) a x b x c	Shell	Unit cell dimensions from 4 circle
240	0.5 x 0.5 x 1.0	8.7Å - ∞	a = b = 129.39Å c = 116.29Å
241	0.5 x 0.5 x 1.3	6.9Å - 8.7Å	a = b = 129.39Å c = 116.29Å
242	0.7 x 0.7 x 1.1	6.0Å - 6.9Å	a = b = 129.39Å c = 116.67Å

TABLE 3.4

PLATINUM DERIVATIVE CRYSTALS - PRIMARY DATA PROCESSING

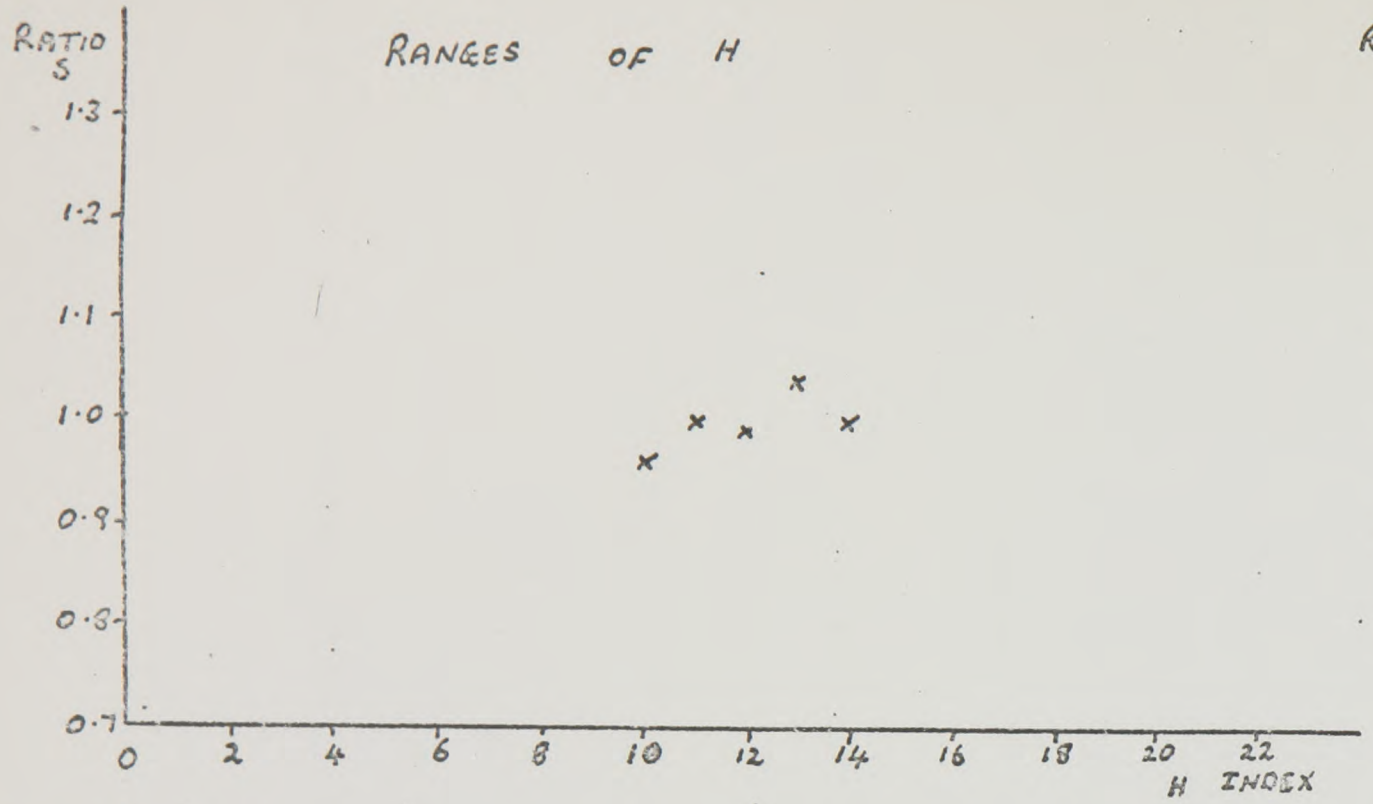
Crystal Number	Total no. of Reflections Processed	No. of SD failures	No. of back-ground failures	Maximum Absorption Correction
240	2511	53	41	1.823
241	2336	60	51	1.391
242	2195	100	88	1.079

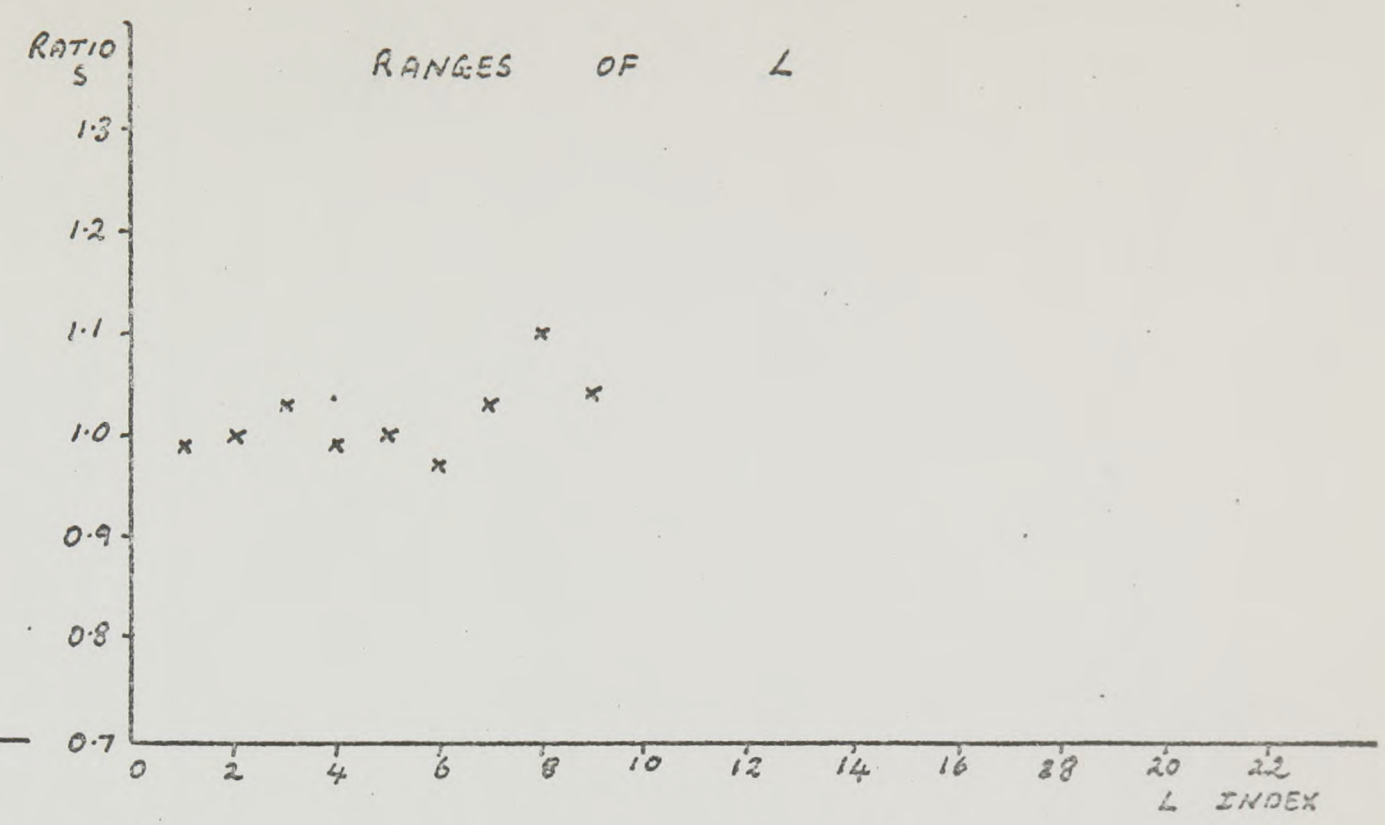
shape of the curve remained the same, though the maximum absorption increased from 1.371 to 1.823. By plotting the ratio of the intensities of the (008) measured at $\phi = 0^{o}$ and $\phi = 90^{o}$, which were used as standard reflections, versus reflection number, it was found that this change in absorption occurred during the period between the measurement of the standard reflections at reflection number 1400 and the measurement at reflection number 1500. The data was, therefore, split into two sets: set 240A comprised reflections 0 - 1500, while set 240B comprised reflections 1400 to the end. The overlapping reflections (1400-1500) were to be used for scaling the two sets together. Set 240A was processed with the absorption curve measured at the start of the data collection, while 240B was processed with the absorption curve measured at the end of the data collection. The radiation damage as estimated from the plot of the standard reflections was 10.8%; a linear correction factor with a gradient of 6.0×10^{-5} was, therefore, applied to the data. Comparison of the intensities of reflections measured at the start and end of the data collection showed that the intensities of the reflections measured at the end of the data collection should be scaled up by a factor 1.040. A further linear function was used to do this.

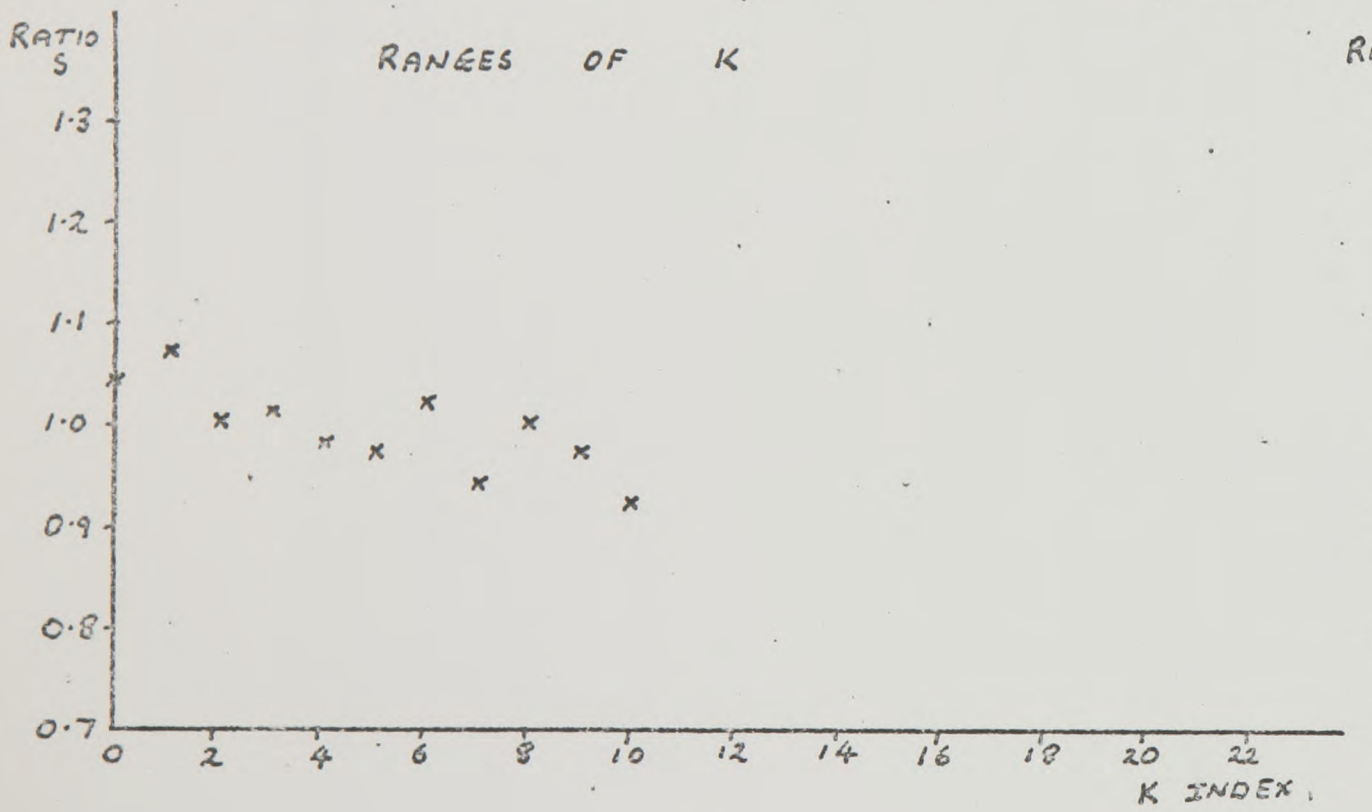
The agreement between equivalent reflections was analysed separately for the two sets of data. The intensities of the $(hk\bar{l})$ reflections of set 240A were scaled by a factor given by:

$$\text{Scale} = 1.022 + |l| \times 0.0045$$

The resulting plots of the ratio S are shown in Figure 3.24. The overall agreement was:







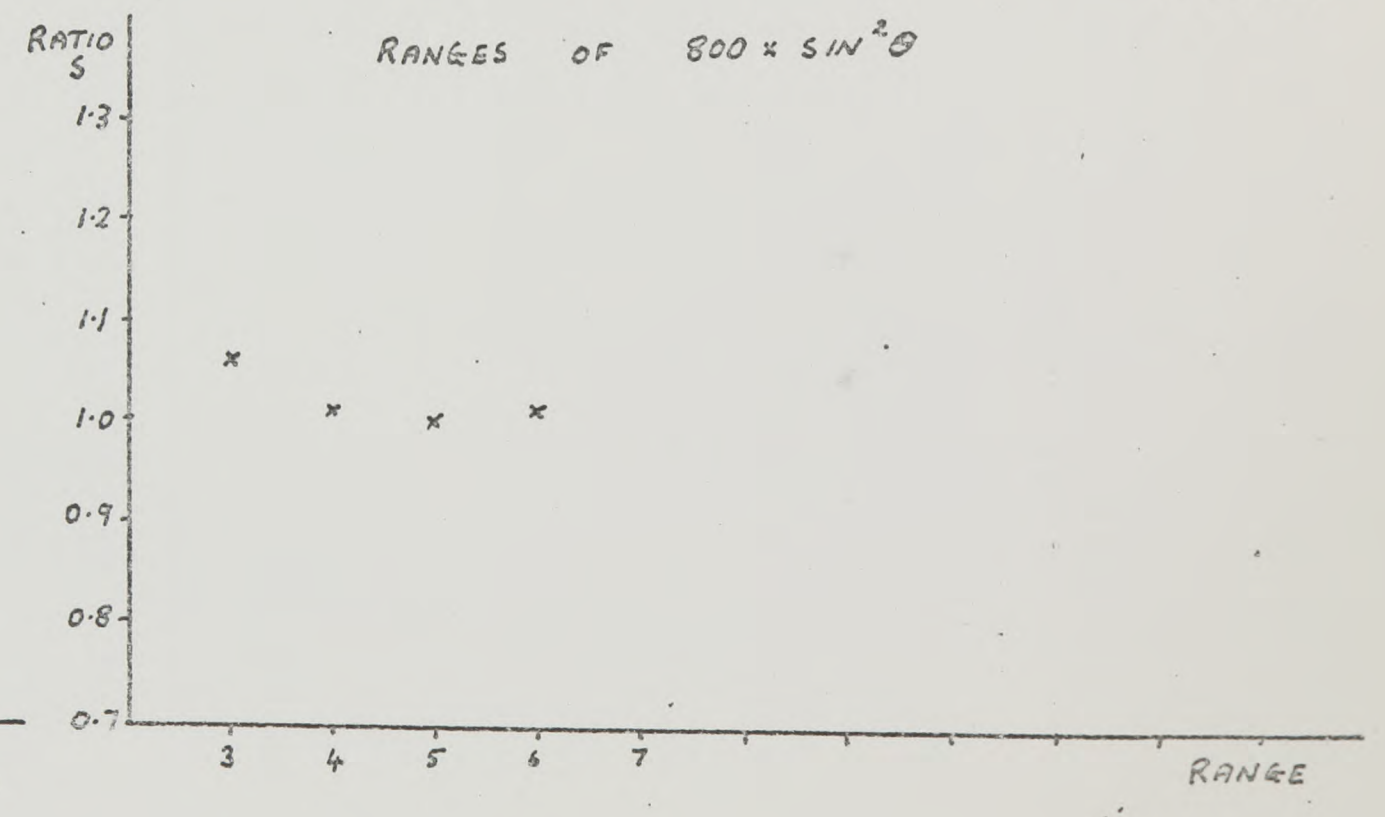
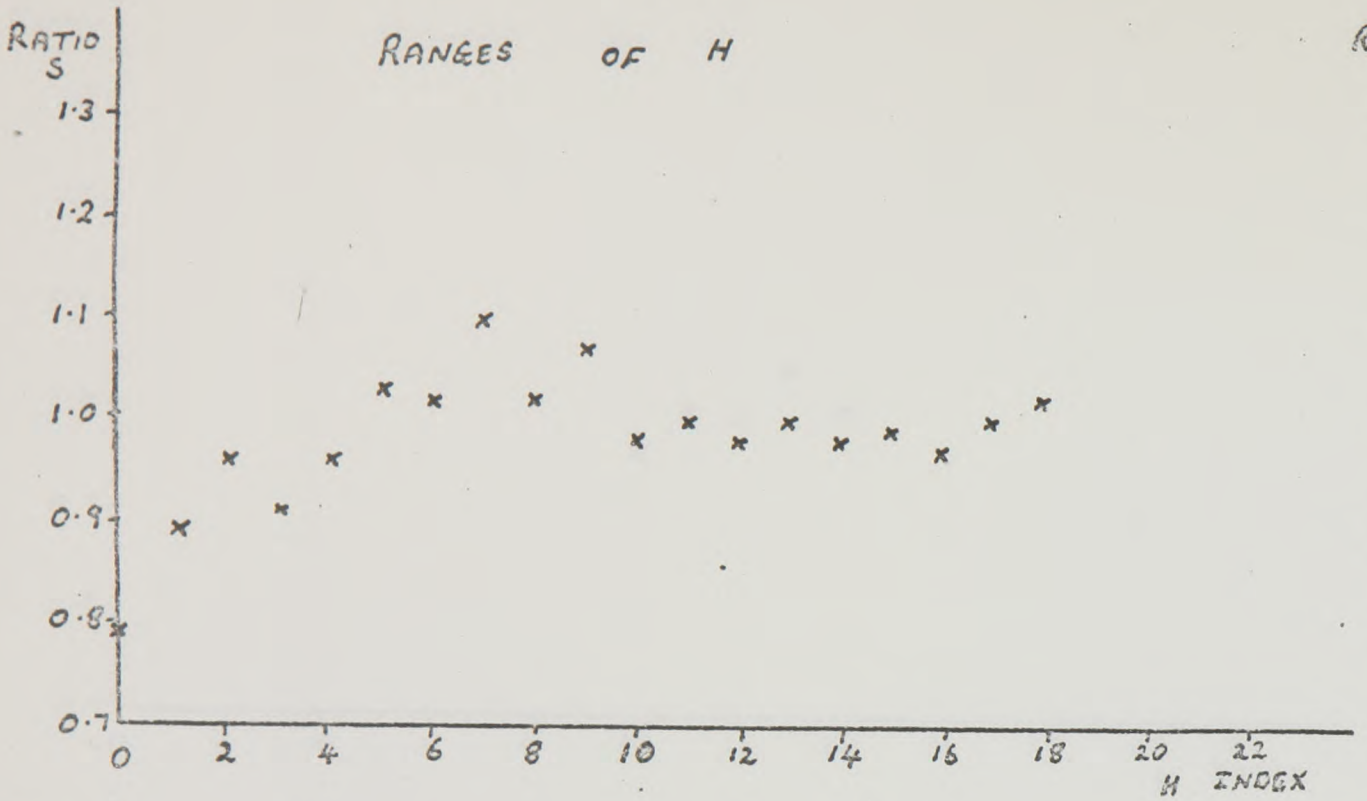
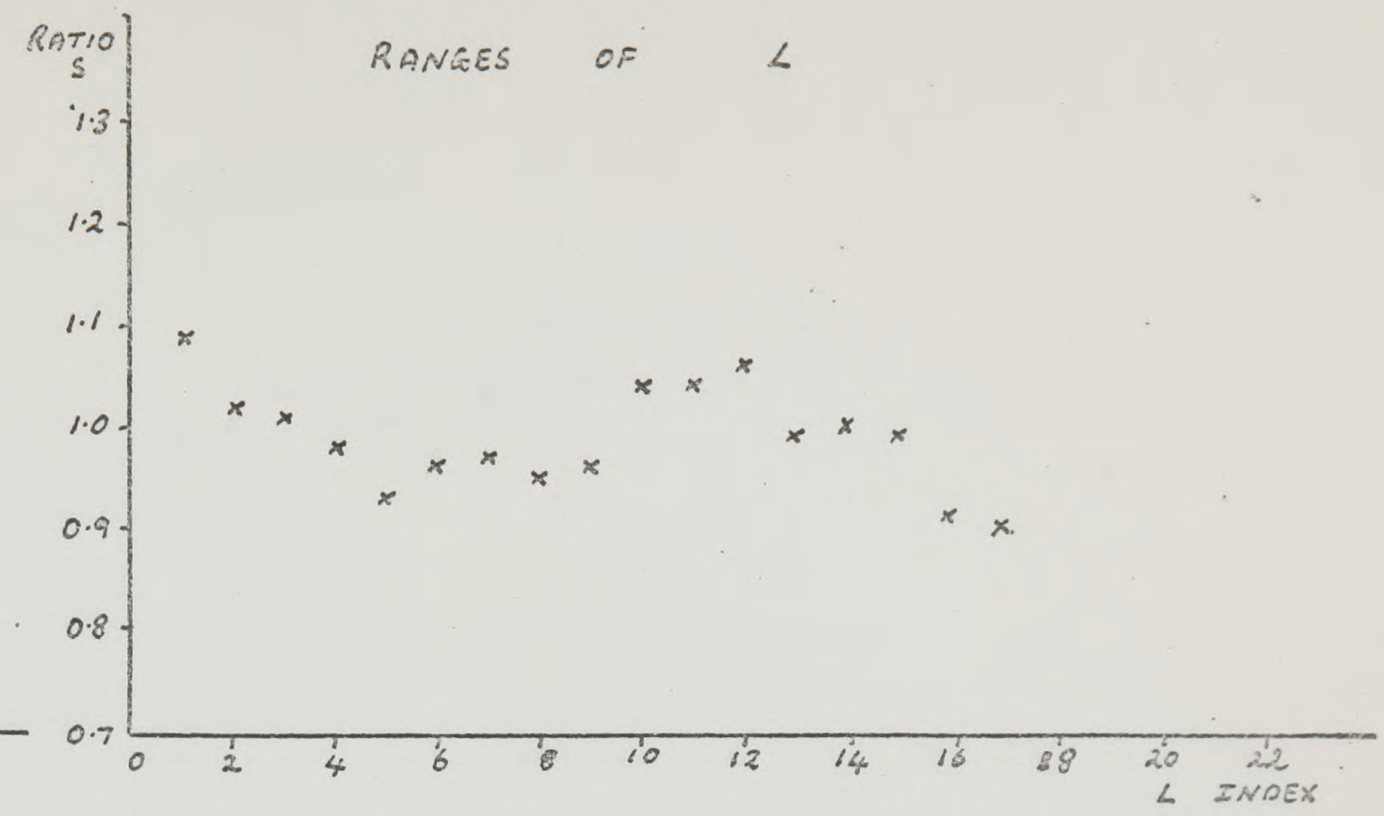
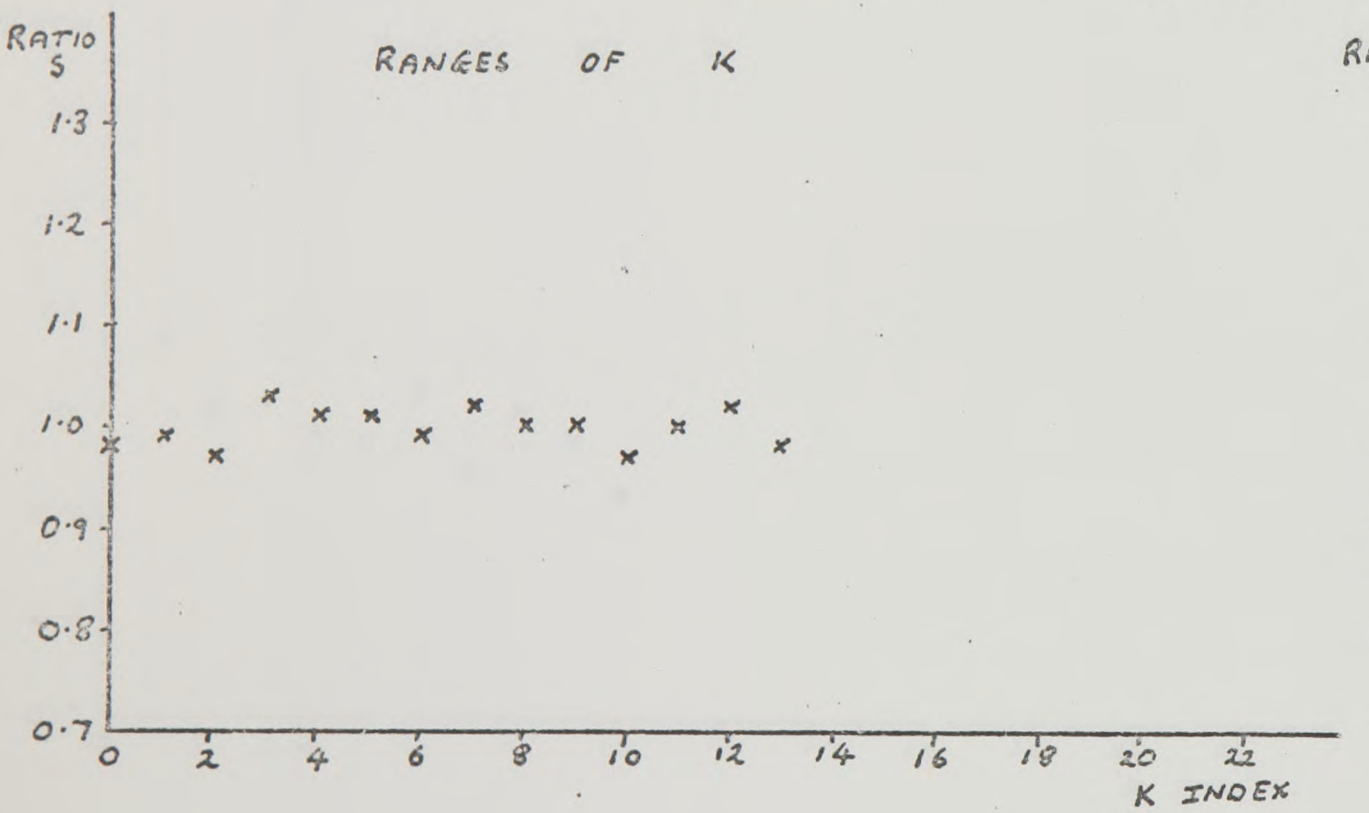


FIGURE 3.25
The agreement between equivalent reflections for crystal 2403







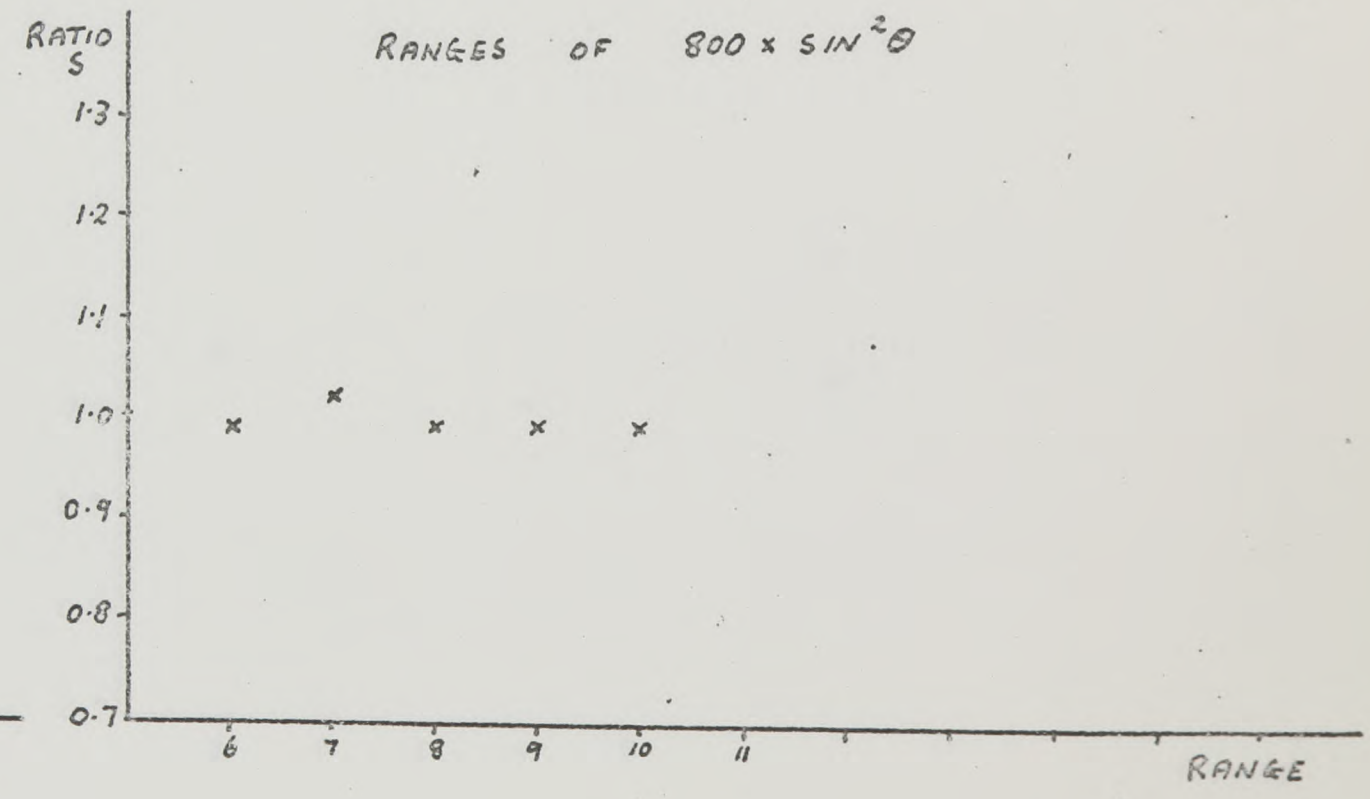


FIGURE 3.26
The agreement between equivalent reflections for crystal 241

	No. of refl. pairs	S	R
Centric data	205	0.9877	7.17%
Acentric data	474	1.0045	9.18%
Overall	679	0.9992	8.55%

For the set 240B the intensities of the (hk$\bar{l}$) reflections were scaled by a factor:

$$\text{Scale} = 0.9480 + |l| \times 0.0179$$

Figure 3.25 shows the resulting plots of the ratio S, while the overall agreement was:

	No. of refl. pairs	S	R
Centric data	27	1.0243	6.84%
Acentric data	142	0.9999	10.89%
Overall	169	1.0045	10.12%

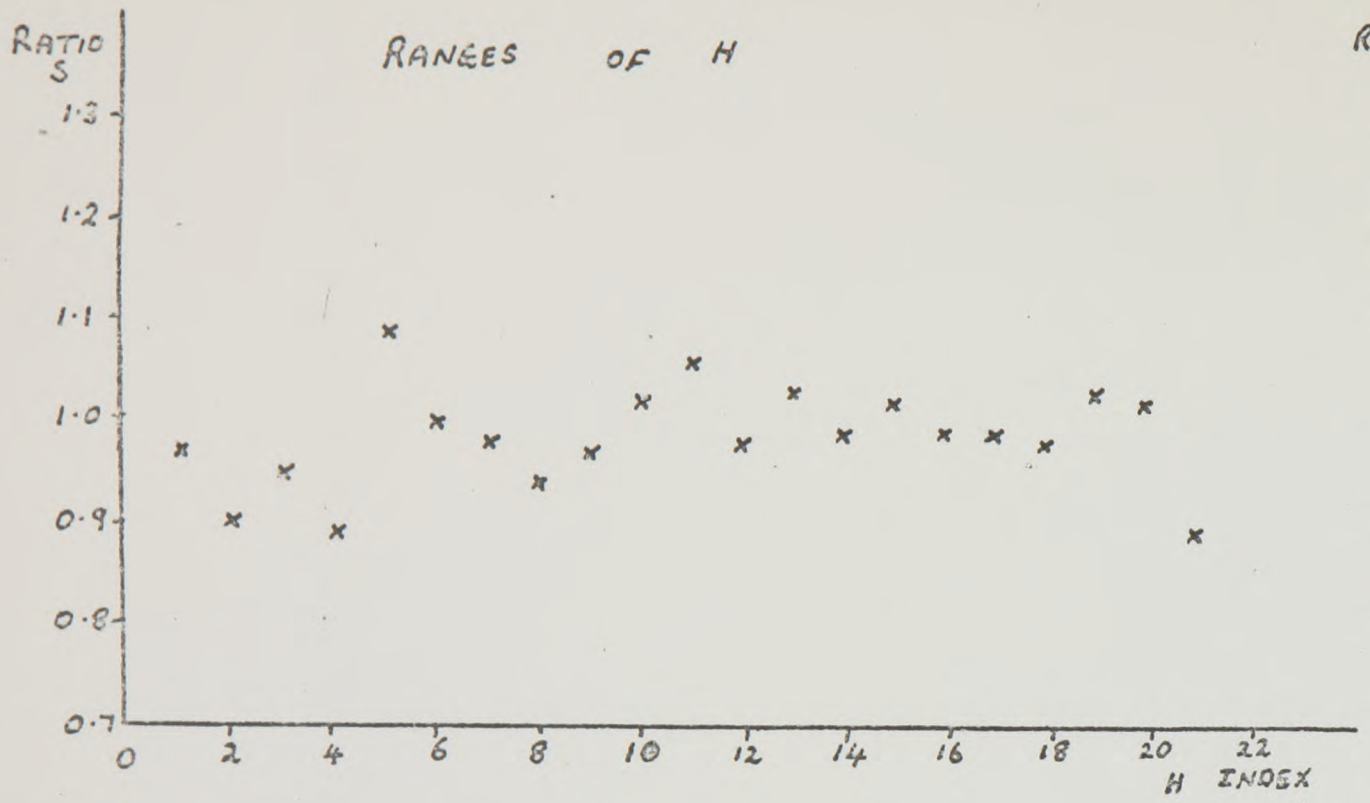
Crystal 241 The radiation damage as estimated from the plots of the standard reflections was 5.6% and, therefore, a linear correction factor with a gradient of 2.80 10^{-5} was applied to the data. The remeasured reflections showed that a further linear radiation damage correction rising to 1.035 was necessary.

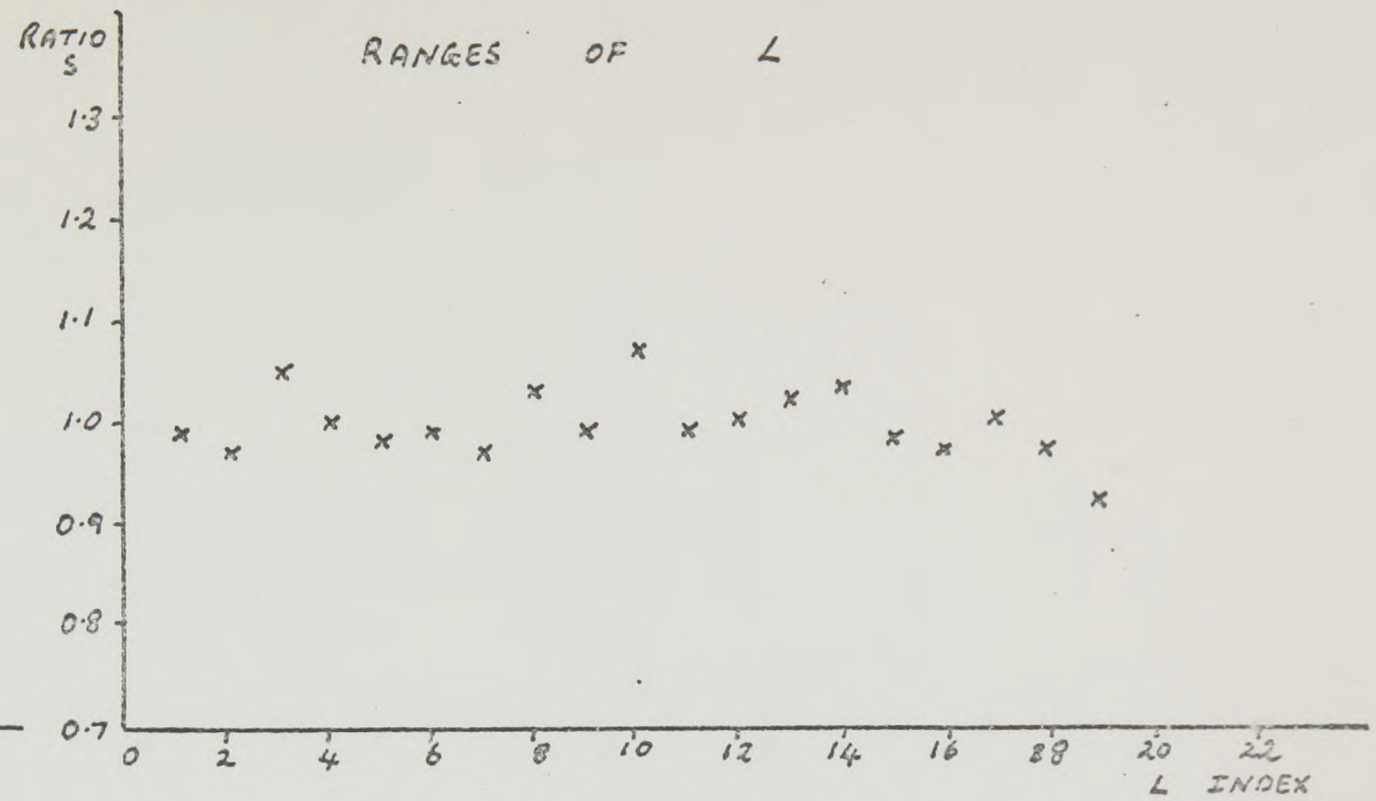
After the initial analysis of the agreement between equivalent reflections, a scale factor was applied to the intensities of the (hk$\bar{l}$) reflections of the form:

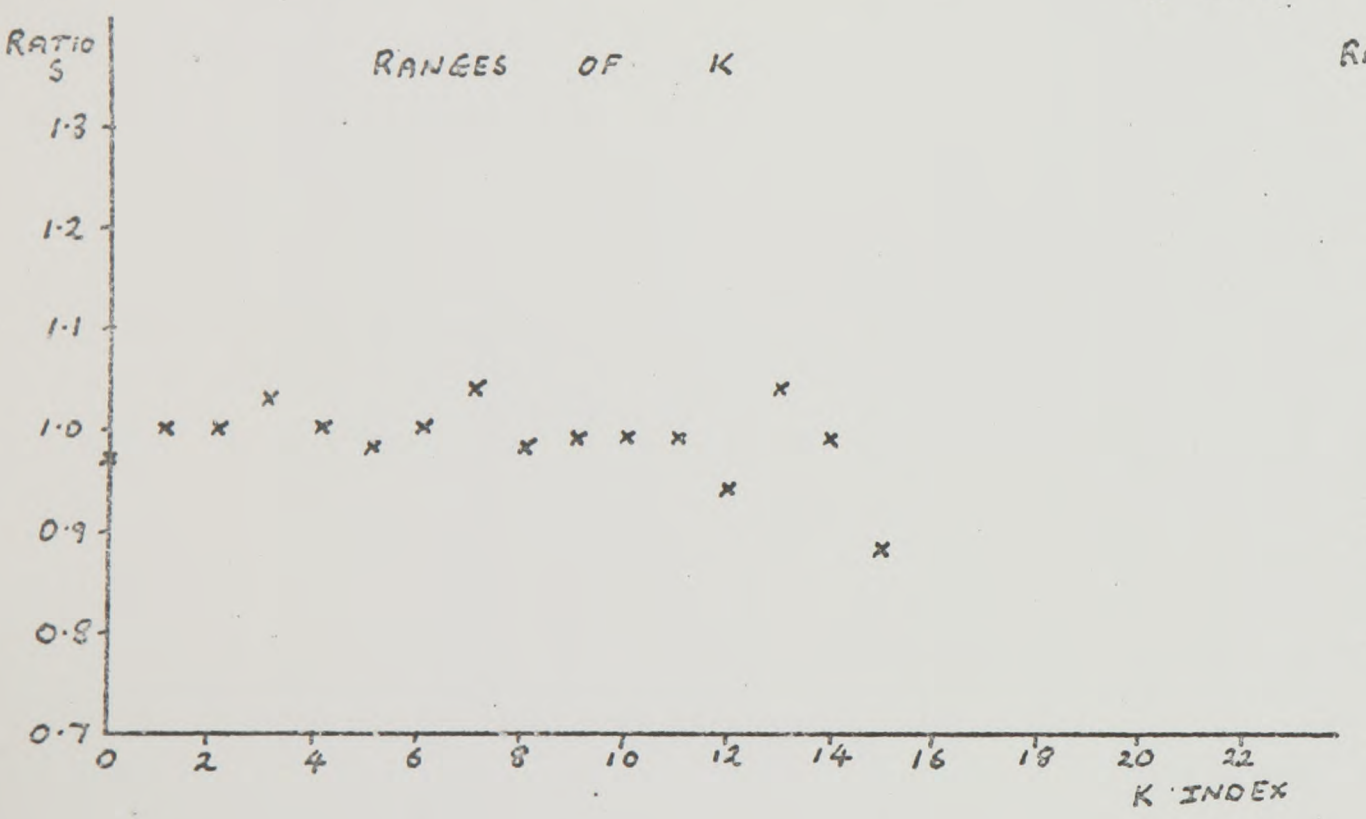
$$\text{Scale} = 0.9073 + |l| \times 0.0180$$

The resulting plots of S are shown in Figure 3.26, while the overall agreement was:

	No. of refl. pairs	S	R
Centric data	160	0.9861	11.9%
Acentric data	753	1,0004	13.6%
Overall	913	0.9975	13.26%







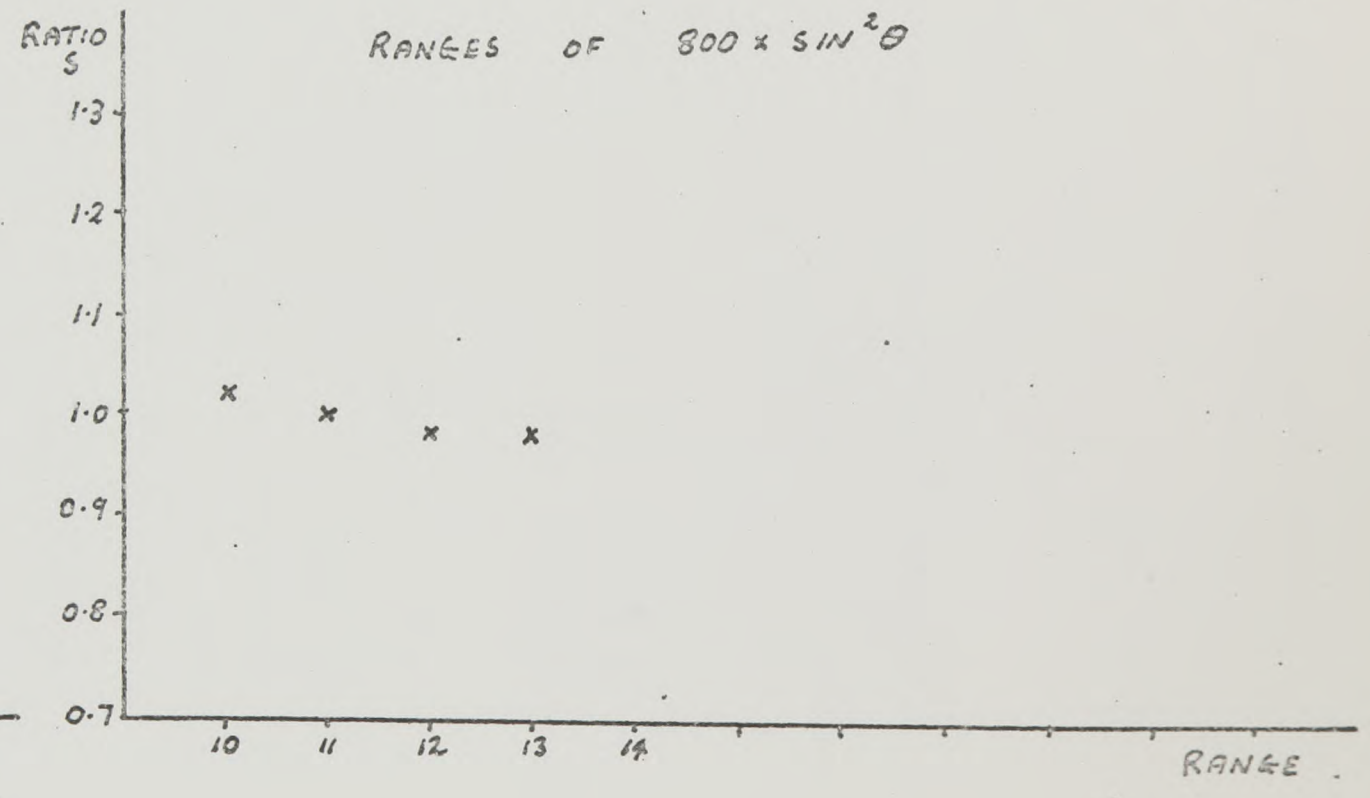


FIGURE 3.27
The agreement between equivalent reflections for crystal 242

Crystal 242. The radiation damage according to the plot of the standard reflections was 10.0%, and so a linear correction factor with a gradient of 5.56×10^{-5} was applied to the data. A further linear correction rising to 1.045 was shown to be necessary from the intensities of the remeasured reflections.

The analysis of the agreement between equivalent reflections showed that the scale factor to be applied to the intensities of the $(hk\bar{l})$ reflections was:

$$\text{Scale} = 0.9622 + |l| \times 0.0067$$

The resulting plots of S are given in Figure 3.27, while the overall agreement was:

	No of refl. pairs	S	R
Centric data	117	0.9709	16.53%
Acentric data	678	1.0004	16.02%
Overall	795	0.9959	16.10%

Crystal to Crystal Scaling

The four sets of data were scaled on to the set number 241. The numbers of overlapping reflections between the data sets were:

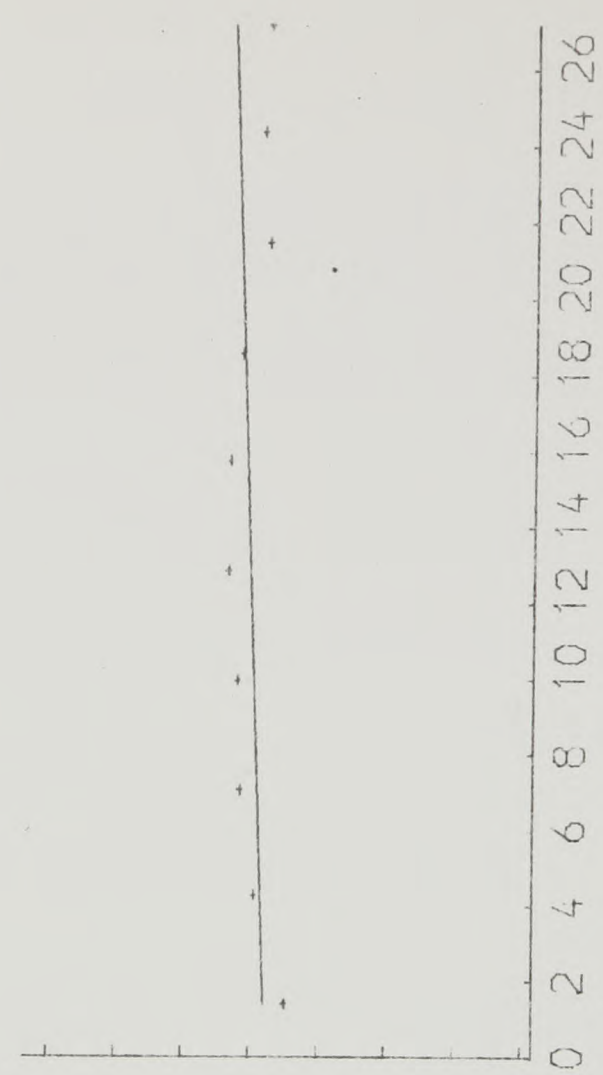
240A/240B	124
240A/241	123
240B/241	106
241/242	158

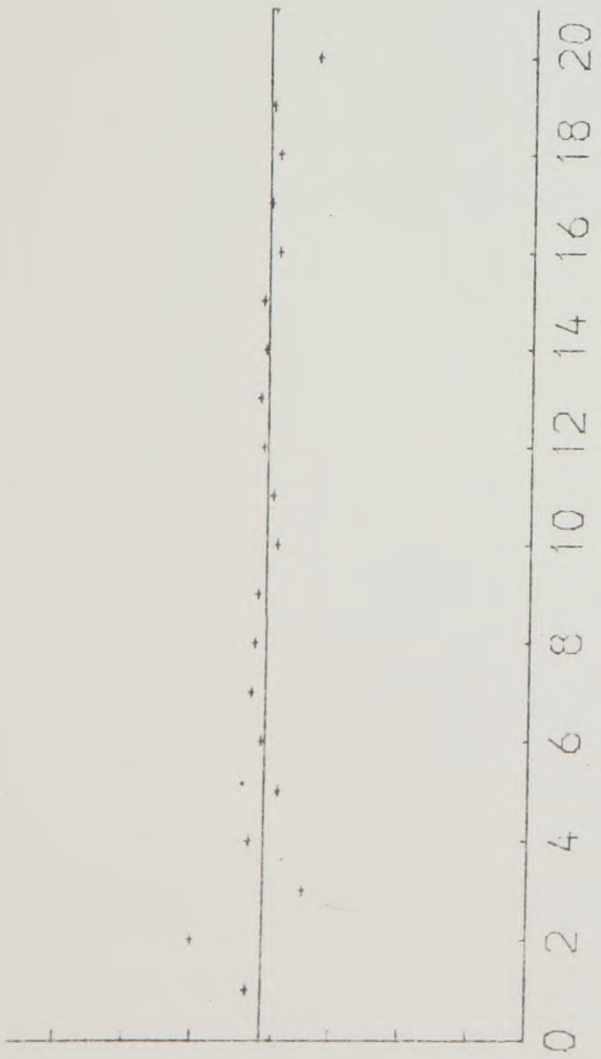
After 5 cycles of refinement, the crystal to crystal scale factors converged to:

FIGURE 3.28

The plots of $\sum F_P^2 / \sum F_{PH}^2$ for the platinum derivative.







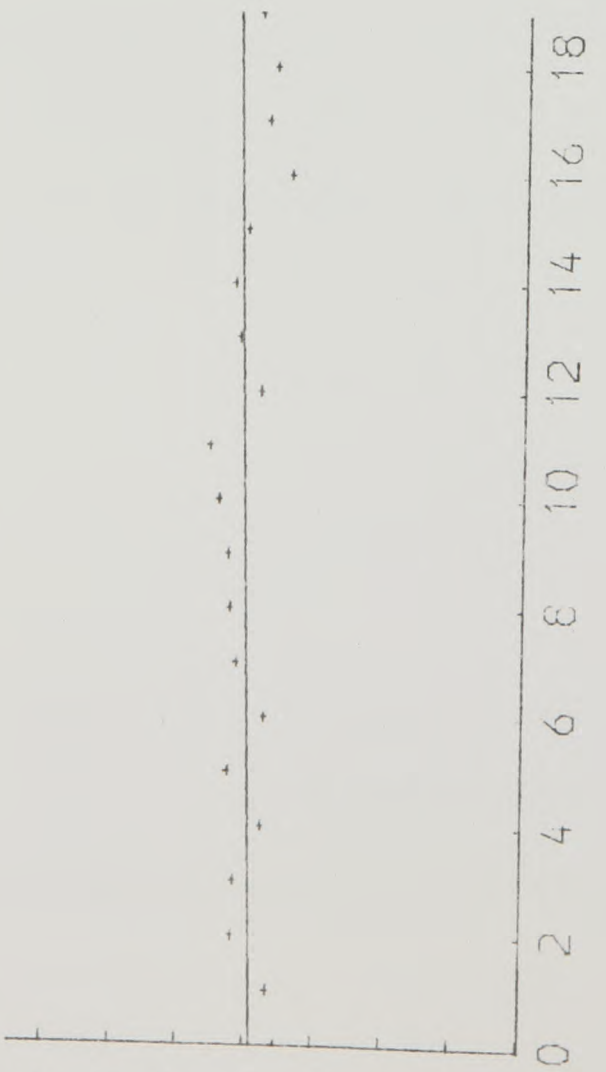
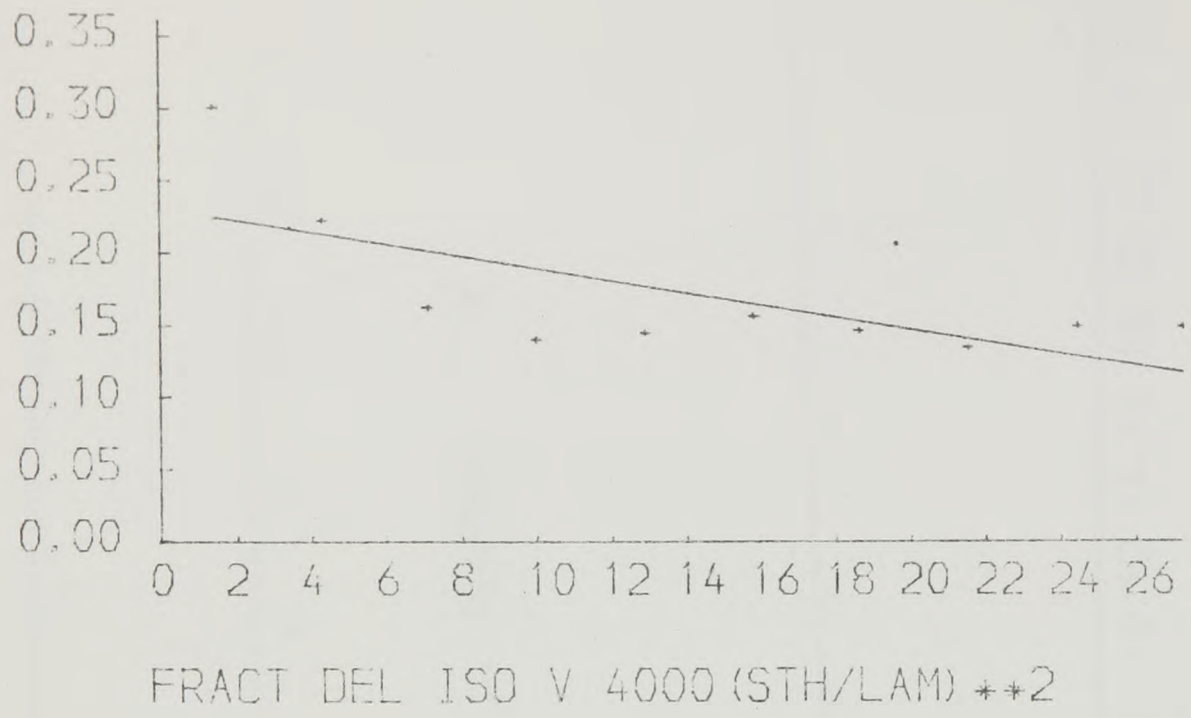
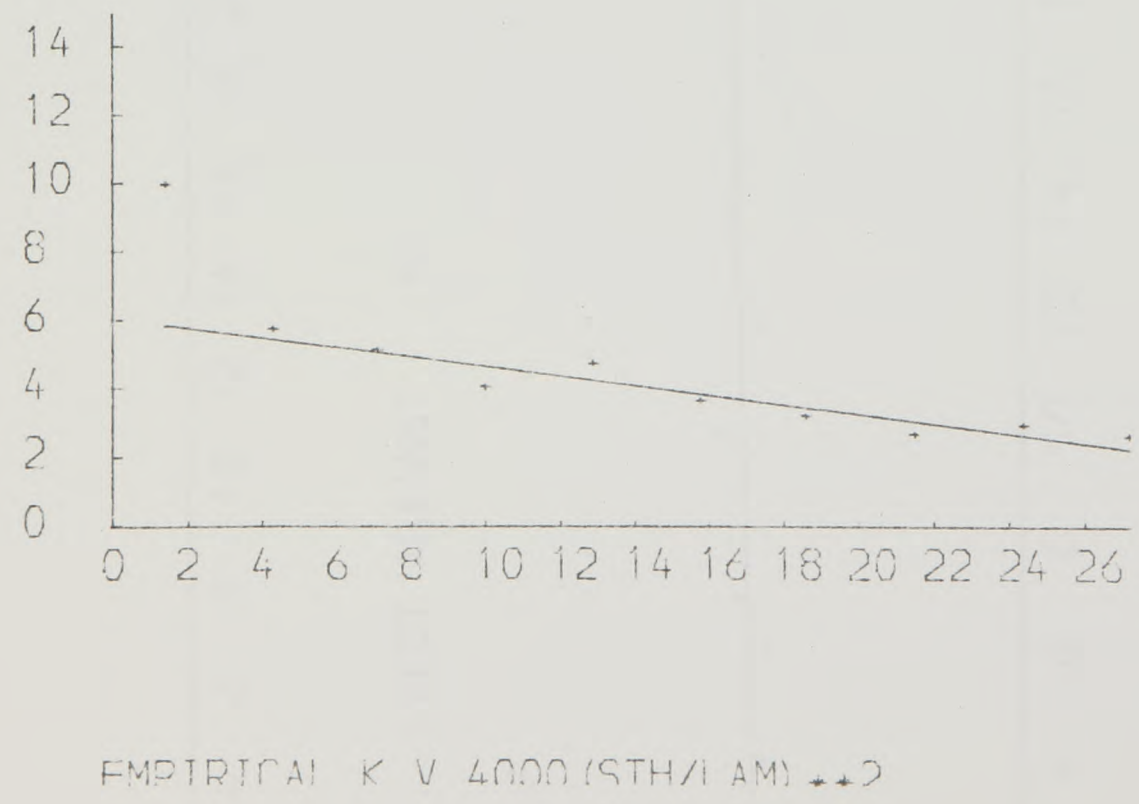


FIGURE 3.29



The plot of the mean fractional isomorphous difference for the platinum derivative.

FIGURE 3.30



The plot of the empirical k value for the platinum derivative.

Crystal number	Scale factor
241	1.0
242	1.051
240A	1.674
240B	1.664

After application of these scales the data set comprised 4679 independent reflections [the Bijvoet pairs had not been averaged at this stage] with a merging R factor of 5.26%

Derivative to Native Scaling

The platinum derivative data were scaled on to the native data by the application of a scale factor to the F^2 of the derivative data of the form:

$$\text{Scale} = 5.5818 + h \times 0.00796$$

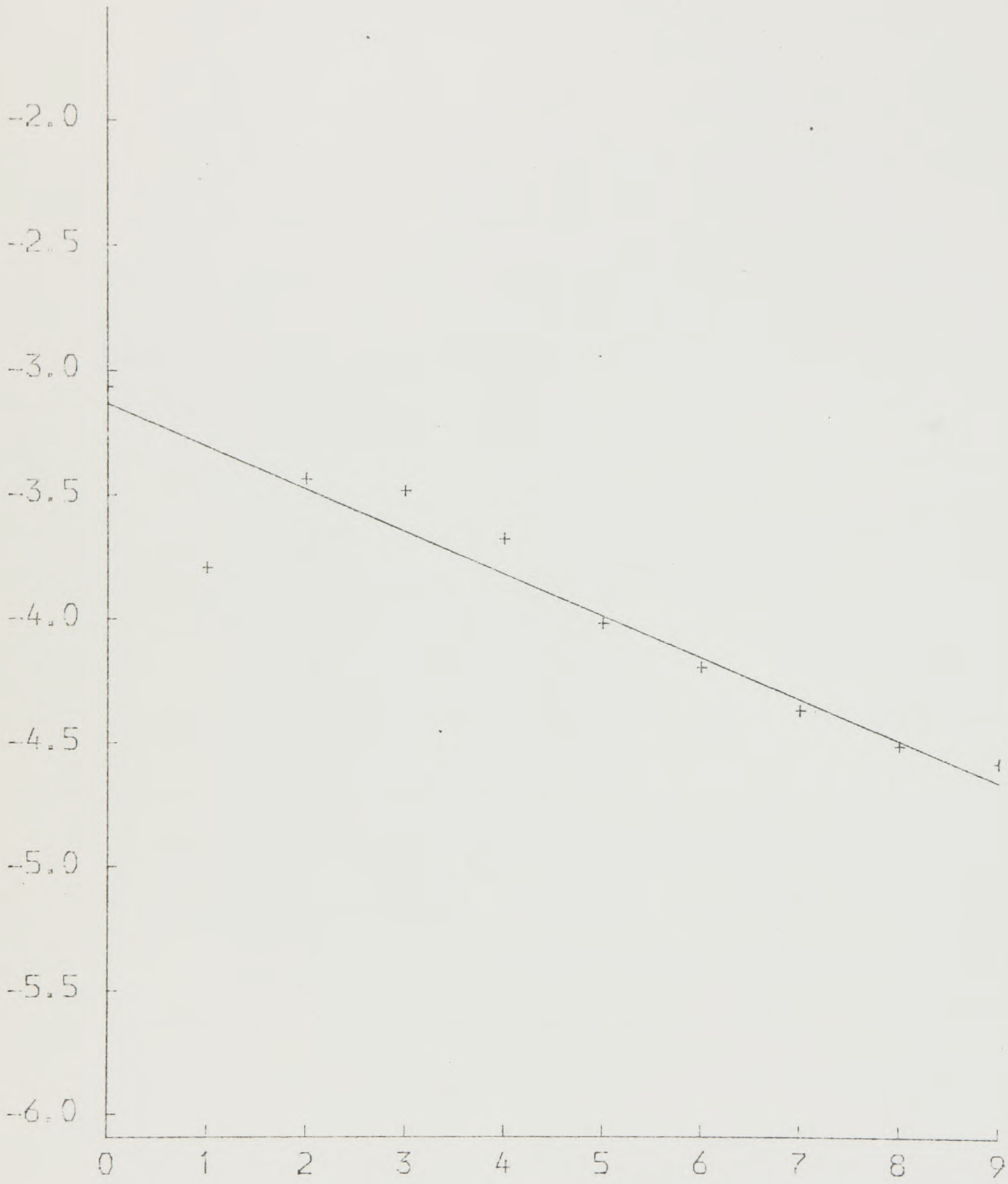
The resulting plots of the ratio $\sum F_p^2 / \sum F_{pH}^2$ in ranges of h,k,l and $4 \sin^2\theta/\lambda^2$ are shown in Figure 3.28; the overall ratio $\sum F_p^2 / \sum F_{pH}^2$ was 1.0083. There were 2626 pairs of reflections where both native and derivative structure amplitudes had been measured. The mean fractional isomorphous change was 16.22% with a mean isomorphous change of 32.5. Figure 3.29 shows the variation of the mean fractional isomorphous change with $\sin^2\theta/\lambda^2$.

The empirical k value (equation 2.11) fell off quickly with $\sin^2\theta/\lambda^2$ as shown in Figure 3.30 indicating that the isomorphous changes are weak at the higher Bragg angles. The overall empirical k value, estimated on 1872 acentric reflections, was 3.68.

Structure amplitudes for the native, and all derivatives are given in the Appendix.

Standard, heavy atom, and comparative Wilson plots (equations 2.13, 2.14, 2.15) were constructed assuming one

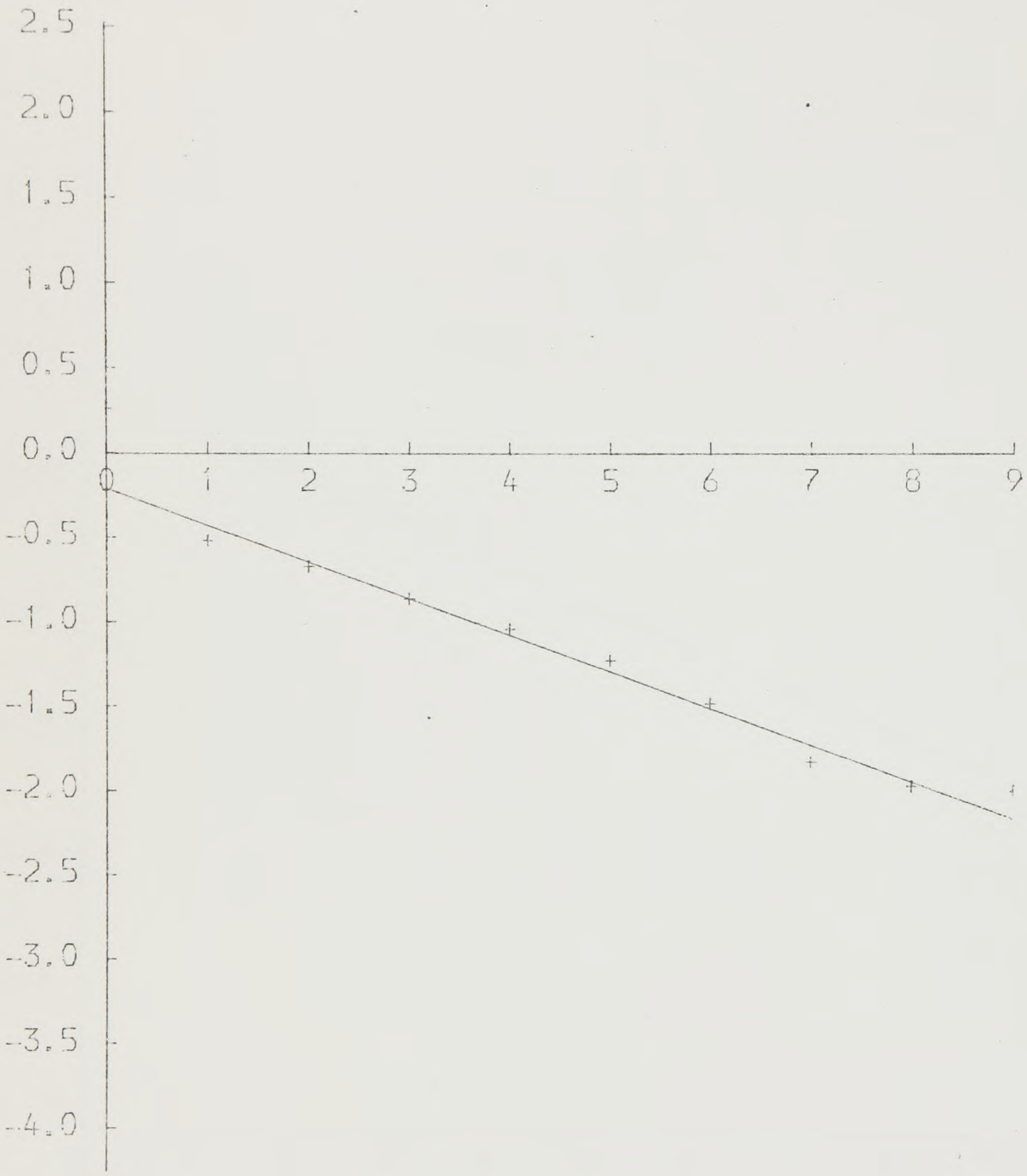
FIGURE 3.31



PT(NH3)2 CV DER WILSON PLOT

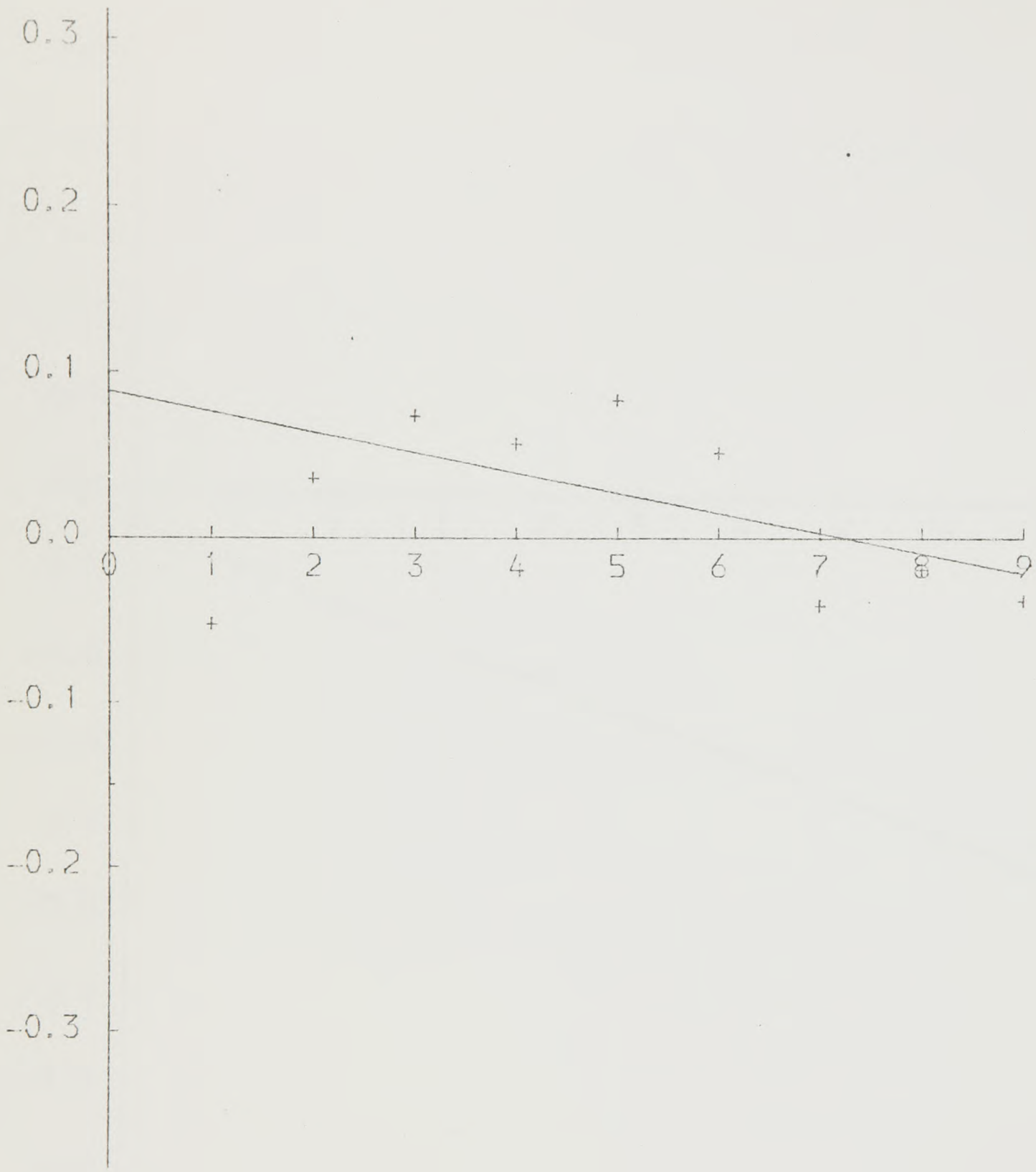
The Wilson plot for the platinum derivative.

FIGURE 3.32



The Heavy Atom Wilson plot for the platinum derivative.

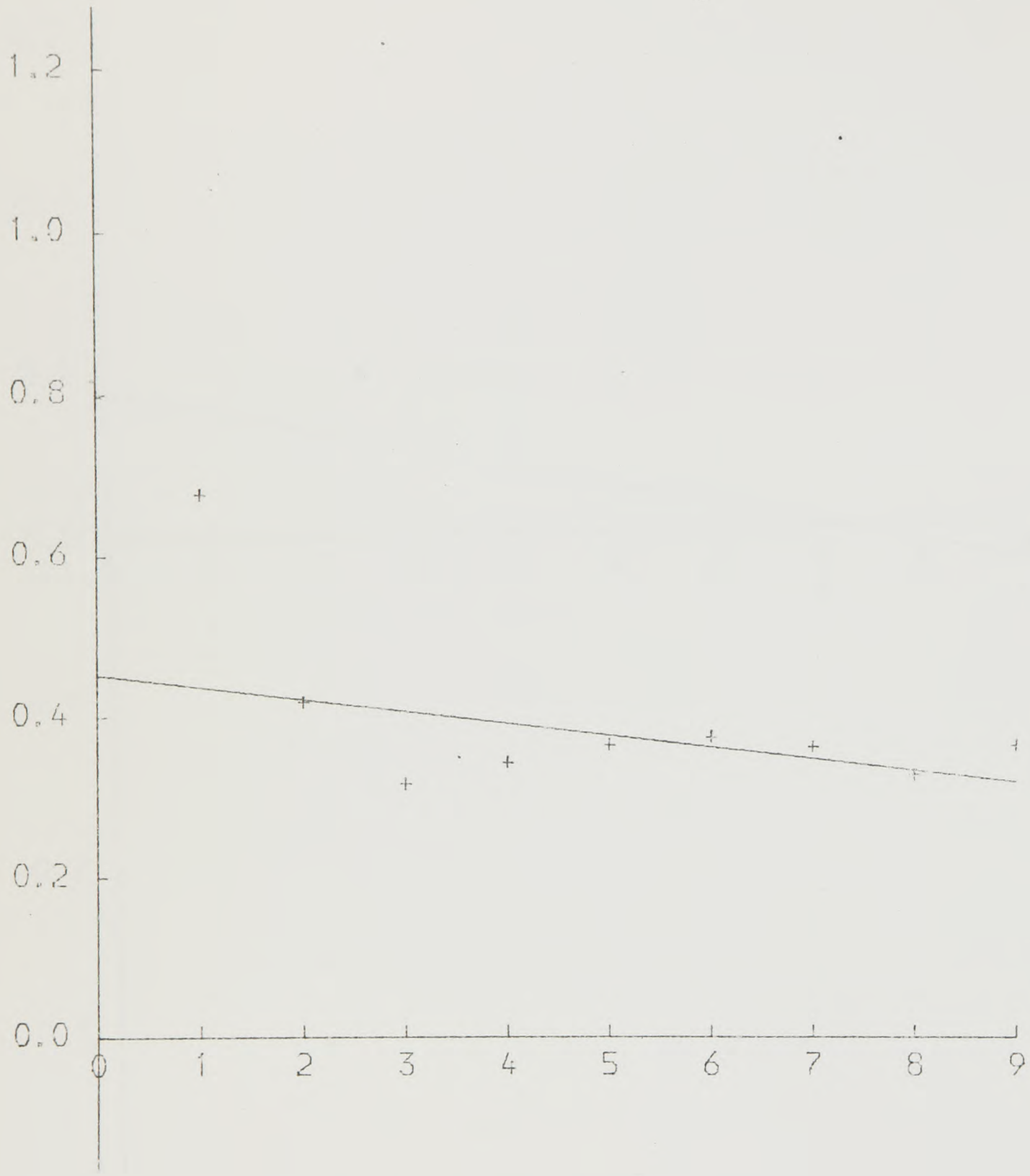
FIGURE 3.33



PT(NH3)2 OV COM WILSON PLOT

The Comparative Wilson plot for the platinum dreivative.

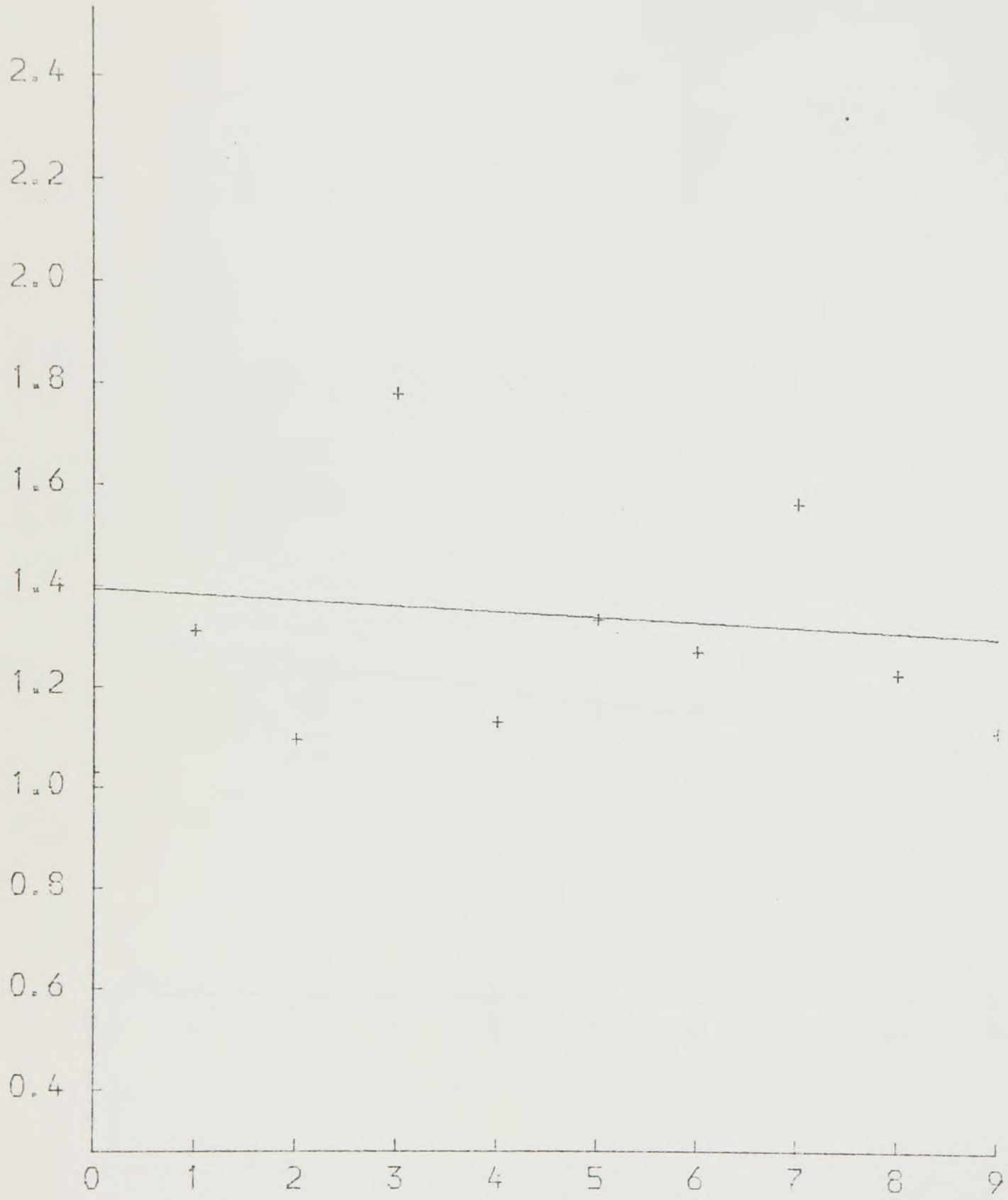
FIGURE 3.34



PT(NH3)2 OVERALL CRICK PLOT

The Crick-Magdoff plot for the platinum derivative.

FIGURE 3.35



The Crick-Magdoff ratio plot for the platinum derivative.

TABLE 3.5

Platinum derivative - Theoretical and observed fractional change in intensity

Mean $\sin^2\theta/\lambda^2$	Centric terms		Acentric terms	
	Theoretical	Observed	Theoretical	Observed
0	0.26369	0.79099	0.18646	0.76742
0.00077	0.26492	0.78281	0.18733	0.59668
0.00154	0.26615	0.43445	0.18820	0.39649
0.00231	0.26739	0.46086	0.18907	0.25856
0.00309	0.26863	0.37703	0.18995	0.33327
0.00386	0.26987	0.44957	0.19083	0.33649
0.00463	0.27112	0.43663	0.19171	0.34340
0.00540	0.27237	0.50458	0.19260	0.32215
0.00617	0.27363	0.38035	0.19348	0.31035
0.00694	0.27488	0.38728	0.19437	0.34859

platinum site per monomer; these are shown in Figures 3.31, 3.32, 3.33. The heavy atom plot gave a temperature factor of 141 and an absolute scale factor of 1.2. This high value for the temperature factor is due to the relatively low resolution of the data used.

The Crick-Magdoff Plot is shown in Figure 3.34 and the plot of the ratio of the fractional change in intensity of the centric terms to that of the acentric terms in Figure 3.35. Theoretical values for the fractional change in intensity were computed for the centric and acentric terms assuming one platinum binding site per monomer; these values are compared with the observed values in Table 3.5. It was apparent from these figures that the low angle intensity changes were excessively large, possibly due to changes in solvent between the native and derivative crystals.

Difference Patterson

A difference Patterson synthesis (equation 2.8) was computed using all the data to 6Å resolution. The Patterson was clearly soluble in terms of one site with fractional unit cell coordinates:

x	=	23/64	y	=	10/64	z	=	22/64
	=	0.3594		=	0.1563		=	0.3438

No other sites could be found from the Patterson.

Difference Pattersons in this space group are complicated by the large number of vectors arising from the eight equivalent positions. The coordinates of the self-vectors are given in Table 3.6. All the peaks carry the same weight, and for a single site should be 1/8 of the origin peak. Inspection of

FIGURE 3.36a

The platinum derivative difference Patterson map.

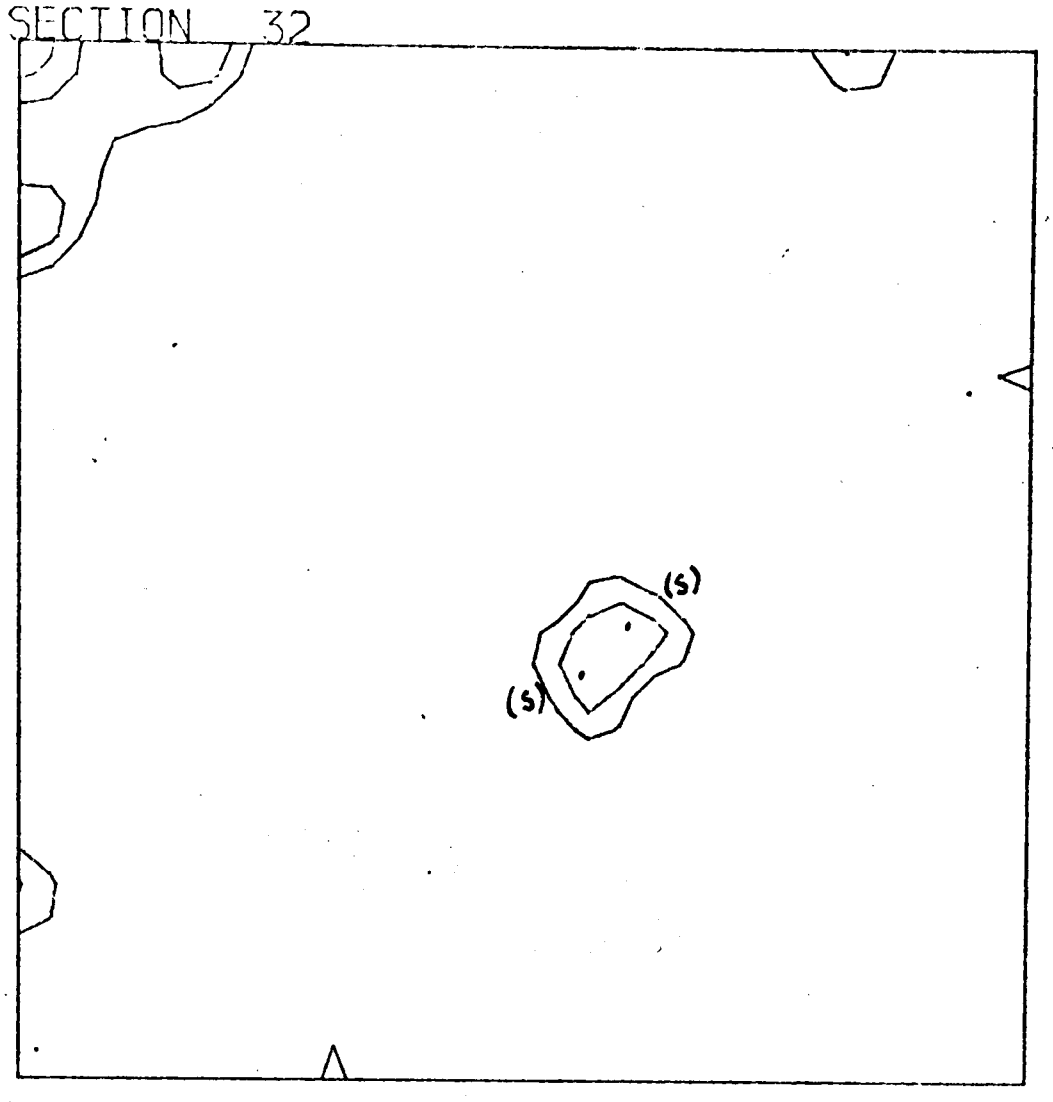
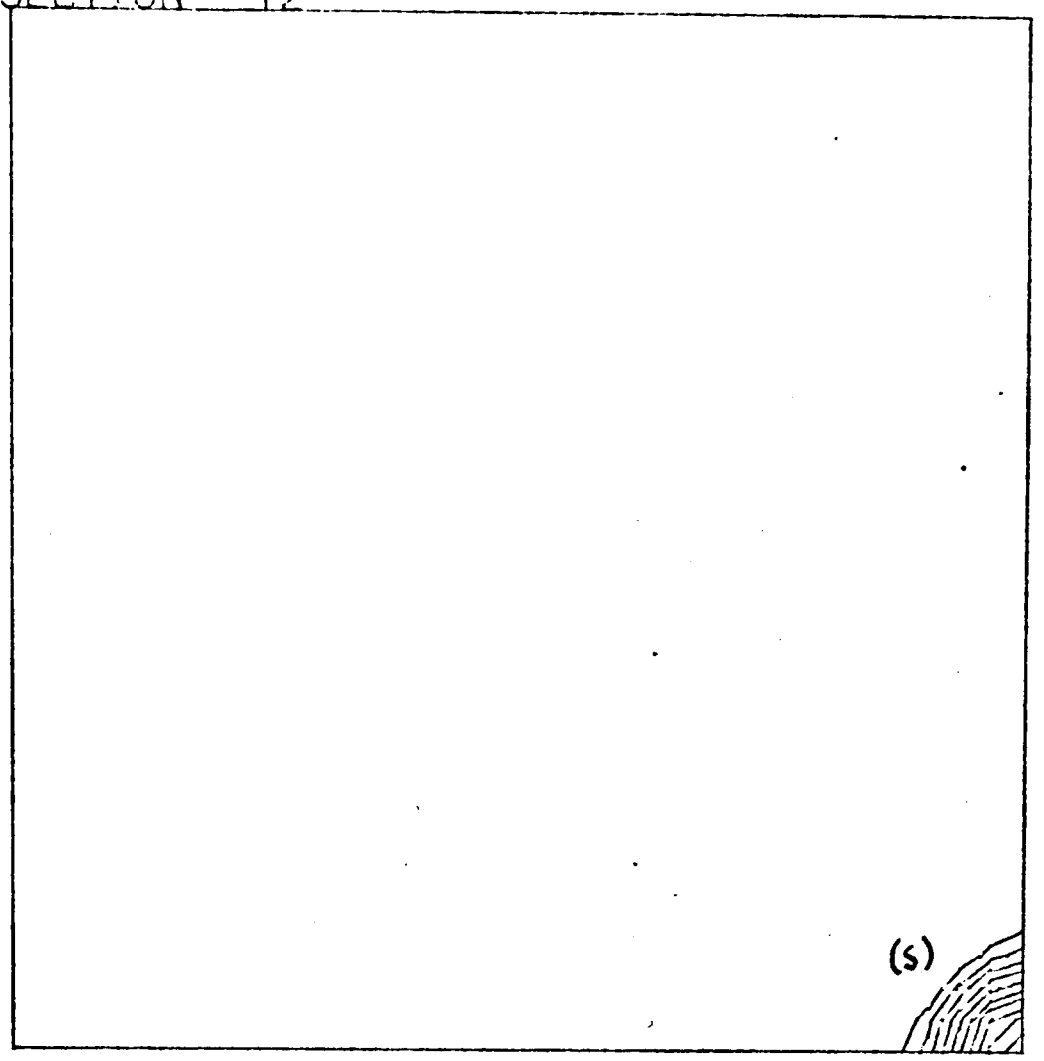


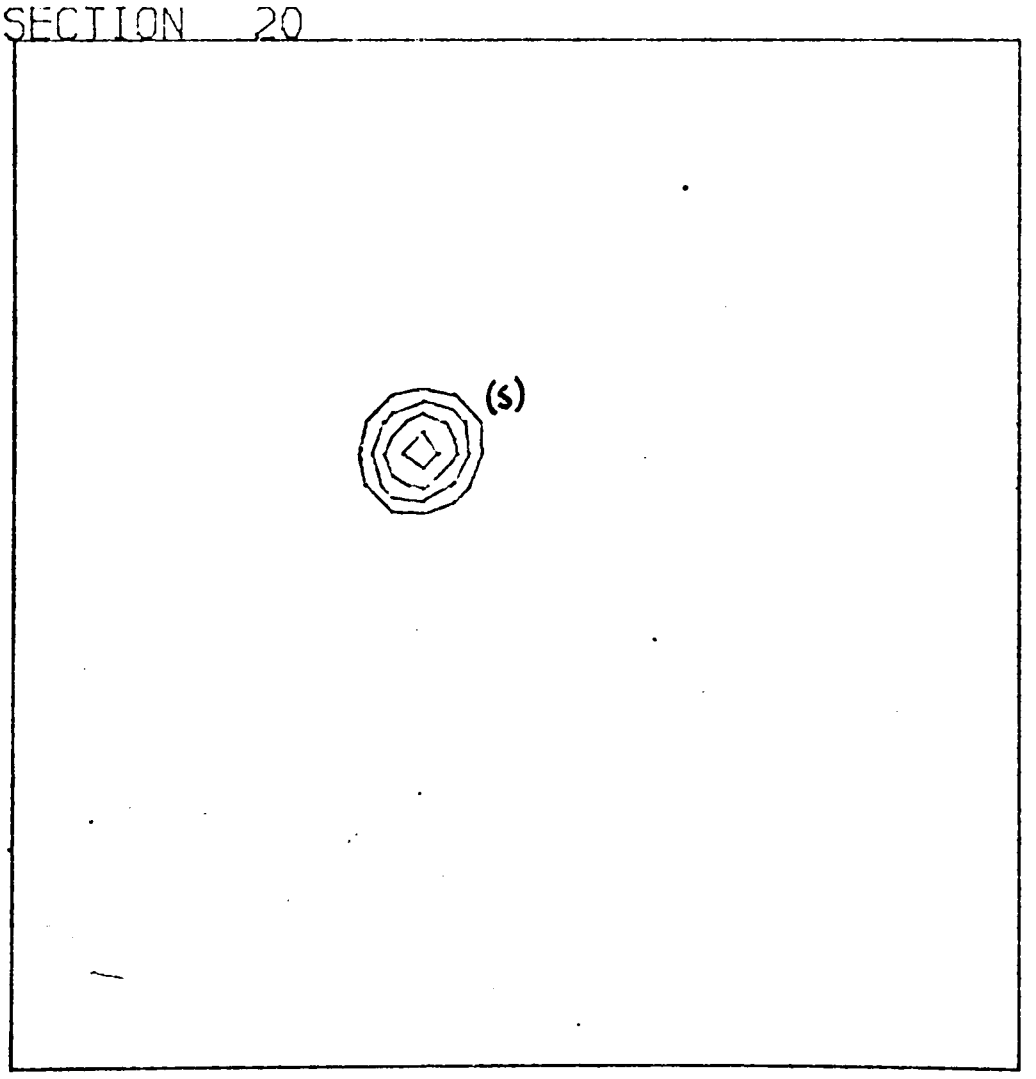
FIGURE 3.36b

SECTION 12



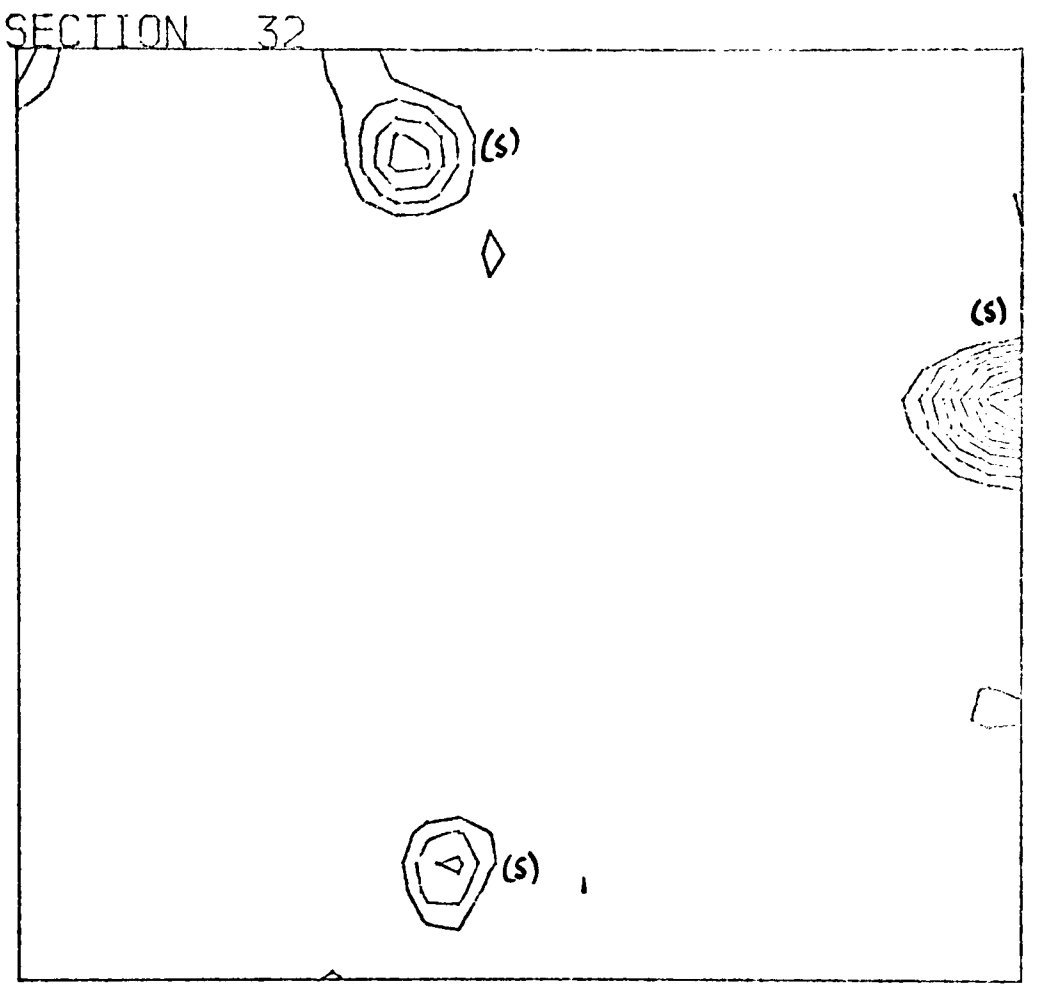
PT DIFF PATTERSON Z SECT
w = 12/64 section

SECTION 20



PT DIFF PATTERSON Z SECT
w = 20/64 section

FIGURE 3.36c



PT DIFF PATERSON Y = 1/2 SECTION

v = ½ section

TABLE 3.6

$P4_12_12$ Difference Pattersons

$P4_12_12$ equivalent positions:

(1) x,y,z (2) $\bar{x},\bar{y},z+\frac{1}{2}$ (3) $\frac{1}{2}-y, \frac{1}{2}+x, \frac{1}{4}+z$

(4) $\frac{1}{2}+y, \frac{1}{2}-x, \frac{3}{4}+z$ (5) $y,x,\bar{z}$ (6) $\bar{y}, \bar{x}, \frac{1}{2}-z$

(7) $\frac{1}{2}-x, \frac{1}{2}+y, \frac{1}{4}-z$ (8) $\frac{1}{2}+x, \frac{1}{2}-y, \frac{3}{4}-z.$

Self vectors in Patterson.

Vectors between sites (1) and (2) etc. reduce to

$u = 2x \quad v = 2y \quad w = \frac{1}{2}$
$u = 2y \quad v = 2x \quad w = \frac{1}{2}$

Vectors between sites (2) and (3) etc. reduce to

$u = x-y+\frac{1}{2} \quad v = x+y+\frac{1}{2} \quad w = \frac{1}{4}$
$u = x+y+\frac{1}{2} \quad v = x-y+\frac{1}{2} \quad w = \frac{1}{4}$

Vectors between sites (1) and (7) etc. reduce to

$u = \frac{1}{2} \quad v = 2y+\frac{1}{2} \quad w = 2z+\frac{1}{4}$
$u = \frac{1}{2} \quad v = 2x+\frac{1}{2} \quad w = 2z+\frac{3}{4}$

Vectors between sites (3) and (5) etc. reduce to

$u = 2x+\frac{1}{2} \quad v = \frac{1}{2} \quad w = 2z+\frac{3}{4}$
$u = 2y+\frac{1}{2} \quad v = \frac{1}{2} \quad w = 2z+\frac{1}{4}$

Vectors between sites (1) and (5) etc. reduce to

$u = (x-y) \quad v = (x-y) \quad w = 2z.$

Vectors between sites (1) and (6) etc. reduce to

$u = (x+y) \quad v = (x+y) \quad w = 2z+\frac{1}{2}$

the table of self vectors shows that all the coordinates of a site may be found from the peaks on the sections:

$$w = \tfrac{1}{2}$$
$$w = \tfrac{1}{4}$$
$$v = \tfrac{1}{2}$$

The peaks corresponding to the vectors

$$u=v= (x-y) \qquad w = 2z$$
$$u=v= (x+y) \qquad w = 2z+\tfrac{1}{2}$$

serve as conformation of the coordinates.

Figure 3.36 shows these sections of the difference Patterson for the platinum derivative with the sites corresponding to the solution marked (s). The origin vector of the Patterson was of height 6300 and the map was contoured from the 200 level in steps of 100.

An anomalous difference Patterson (equation 2.9) was computed, but many of the expected peaks were absent due to the weakness, and hence poor quality of the anomalous data.

Refinement

Despite the poor quality of the anomalous Patterson, F_{HLE} coefficients (equation 2.10) were calculated using the empirical k values derived earlier. Reflections were omitted if their F_{HLE} coefficients were greater than 150, or F_{HUE} coefficients were less than 200. The low values for the empirical k's resulted in the F_{HLE} coefficients being very similar to the isomorphous differences. However, by choosing the reflections as indicated above, only the better measured reflections were used. F_{HLE} coefficients were obtained for 2238 reflections of which 1672 were acentric. A type of Kraut scale factor (equation 2.17) with a value of 1.036 was found

/for the

derivative using the F_{HLE}.coefficients.

The 2238 F_{HLE} coefficients were used in the refinement cycles. In the first instance 4 cycles of refinement were attempted refining the three positional coordinates and the occupancy of the site. The R factor (equation 2.18) after this was53.6%. The shifts in the site parameters were:

	start	finish
x	0.3594	0.3592
y	0.1563	0.1569
z	0.3438	0.3441
Occupancy	0.2	0.2164

The temperature factor was held constant at 15.0. A difference fourier was computed using the coefficients:

$$(F_{HLE} - f_c)e^{i\alpha_H}$$

No further sites were evident from this map, however, the density at the site was low, but surrounded by high density, indicating that an increase in temperature factor was necessary. A further set of 7 refinement cycles was computed in which the positional parameters were refined in each cycle, but the occupancy and temperature factors were refined separately in alternate cycles. This was necessary due to the high correlation between occupancy and temperature factor. The shifts in these parameters were:

	start	finish
x	0.3594	0.3592
y	0.1563	0.1569
z	0.3438	0.3443
Occupancy	0.2164	0.2947
Temperature Factor	39.0	93.1

TABLE 3.7

Platinum derivative R factors, lack of closure errors (E) and RMS calculated heavy atom contribution (RMS f_c) after refinement.

$\sin^2\theta/\lambda^2$ interval	No. of Refls	R%	E	RMS f_c
0 -0.0007	74	56.1	49.06	53.84
0.0007-0.0014	144	47.9	43.89	55.16
0.0014-0.0021	192	48.9	36.03	55.11
0.0021-0.0028	227	46.9	32.10	50.05
0.0028-0.0035	247	51.0	30.48	48.94
0.0035-0.0042	267	47.0	29.44	44.05
0.0042-0.0049	277	51.5	27.41	42.14
0.0049-0.0056	279	54.6	24.41	39.10
0.0056-0.0062	262	54.0	22.16	36.97
0.0062-0.0069	268	58.9	23.45	33.02

The R factor was 51.0%. The variation with $\sin^2\theta/\lambda^2$ of R factor, F_{calc} and lack of closure error, estimated on the centric data, are shown in Table 3.7. Again there was no indication of further sites in the difference fourier map, which also indicated that the single site had been fully refined. The high temperature factor seemed to be due to the large low resolution F_{HLE} coefficients; when only the data in the 15Å to 6Å region was refined, subsequently, the temperature factor fell to 70.9.

A further set of 4 refinement cycles using the 687 centric reflections was computed, refining the positional parameters and the occupancy with the temperature factor held constant at 15.0. The R factor after these 4 cycles was 64.7%, and the site parameters were:

x	0.3601
y	0.1574
z	0.3427
Occupancy	0.2089

The fact that only one site could be found was surprising in view of the Crick-Magdoff statistics. However, native protein phase angles were calculated for the centric zones, the mean figure of merit being 58.2%; the atomic parameters used were those from the best refinement (R factor of 51.0%). Three dimensional native phase angles (most probable phase angles) were also calculated using the anomalous scattering data. Phase angles were calculated with both positive and negative signs on the anomalous differences, since the correct signs were not known at this time; i.e. the "positive" sign gave anomalous differences

TABLE 3.8

Co-crystallised Methyl Mercury Crystals - Physical Parameters

Crystal number	Crystal size (mm) a x b x c	Shell	Unit cell dimensions from 4 circle
231	0.6 x 0.6 x 1.8	6.0Å - 7.5Å	a = b = 129.39Å c = 116.68Å
232	0.6 x 0.6 x 1.8	6.9Å - 8.7Å	a = b = 129.39Å c = 116.68Å
233	0.5 x 0.5 x 1.1	8.7Å - ∞	a = b = 128.76Å c = 117.06Å
234	0.7 x 0.7 x 1.7	6.0Å - 7.5Å	a = b = 128.14Å c = 117.45Å

TABLE 3.9

Co-crystallised Methyl Mercury Crystals - Primary Data Processing

Crystal Number	Total no. of Reflections Processed	No. of SD failures	No. of back-ground failures	Maximum Absorption Correction
231	2642	54	81	1.388
232	2379	9	11	1.149
233	1968	2	2	1.369
234	1828	34	29	1.142

defined by:

$$\Delta F_{anom} = F_{pH}(hkl) - F_{pH}(hk\bar{l})$$

and the "negative" sign gave anomalous differences defined by:

$$\Delta F_{anom} = F_{pH}(hk\bar{l}) - F_{pH}(hkl)$$

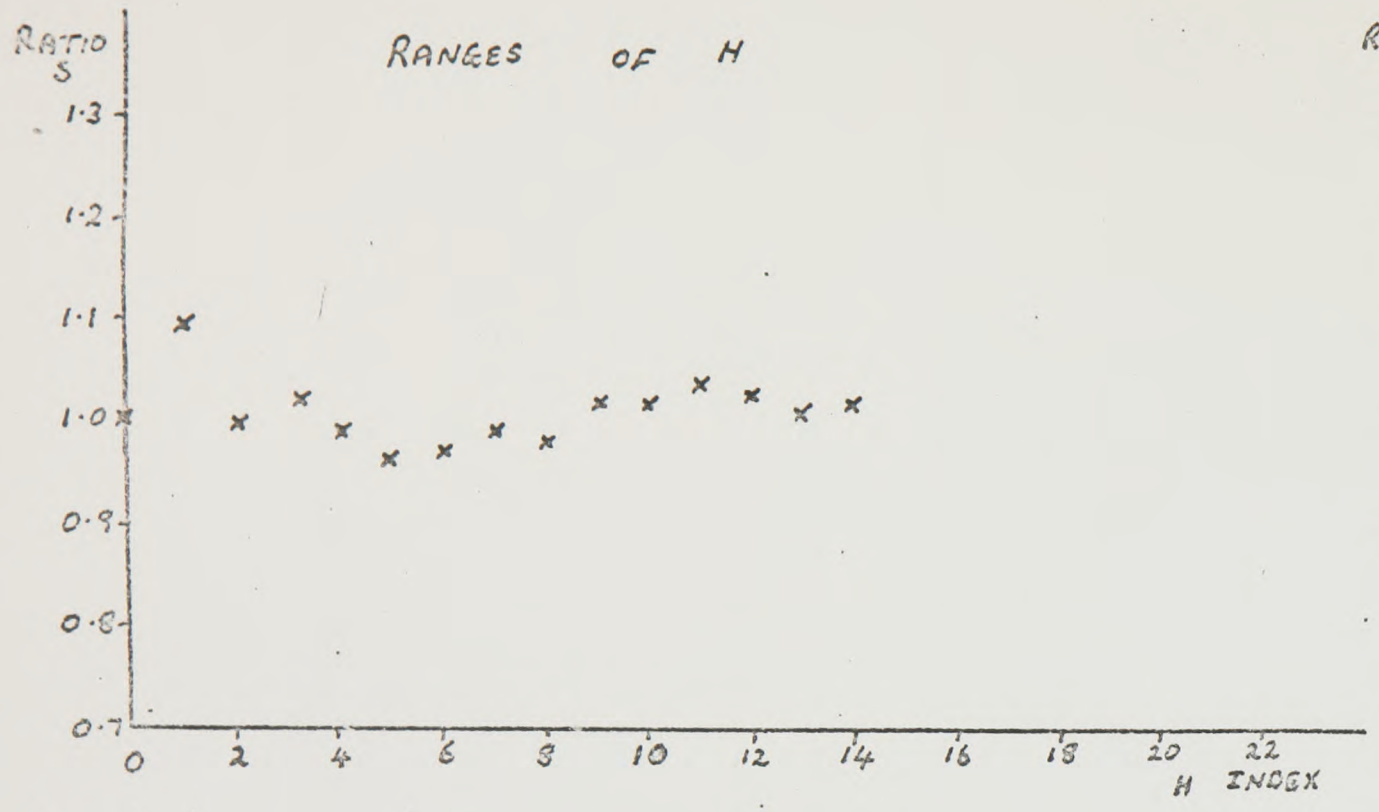
The mean figure of merit for each set of phase angles was 49.6% on 2617 reflections. The isomorphous lack of closure errors used in the phase calculations were those given by the refinement (Table 3.7) and the anomalous lack of closure errors were set at one third of the isomorphous values.

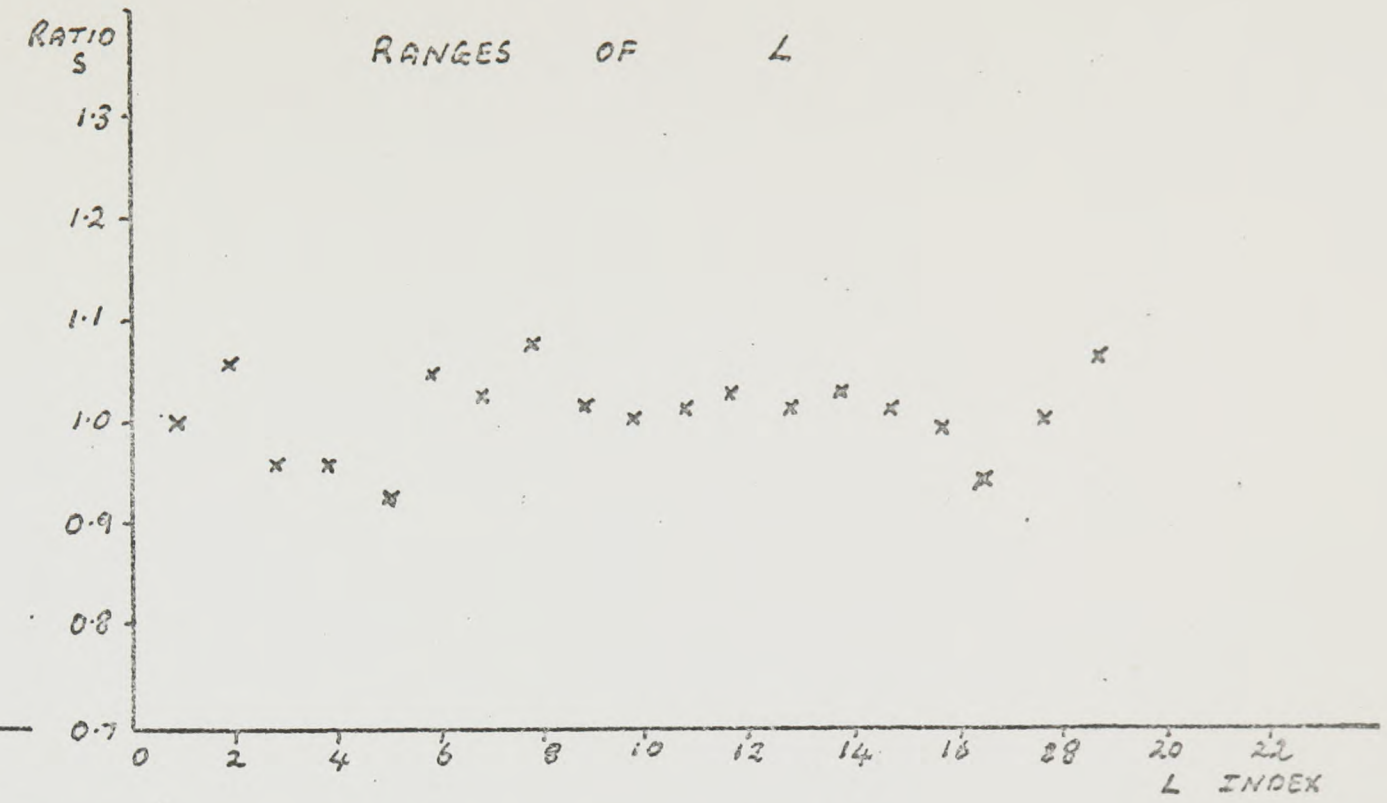
The ambiguity over the sign of the anomalous contribution arises because the "hand" of the heavy atom coordinate system, relative to the right-hand system used to index the reciprocal lattice, is unknown. The ambiguity is resolved by use of a second heavy atom derivative when only one sign for the anomalous contribution will be consistent with this second heavy atom site. Alternatively, it may be possible to choose between the two signs for the anomalous contribution by comparing the two native electron density maps computed using the two possible sets of phase angles and choosing the more realistic one.

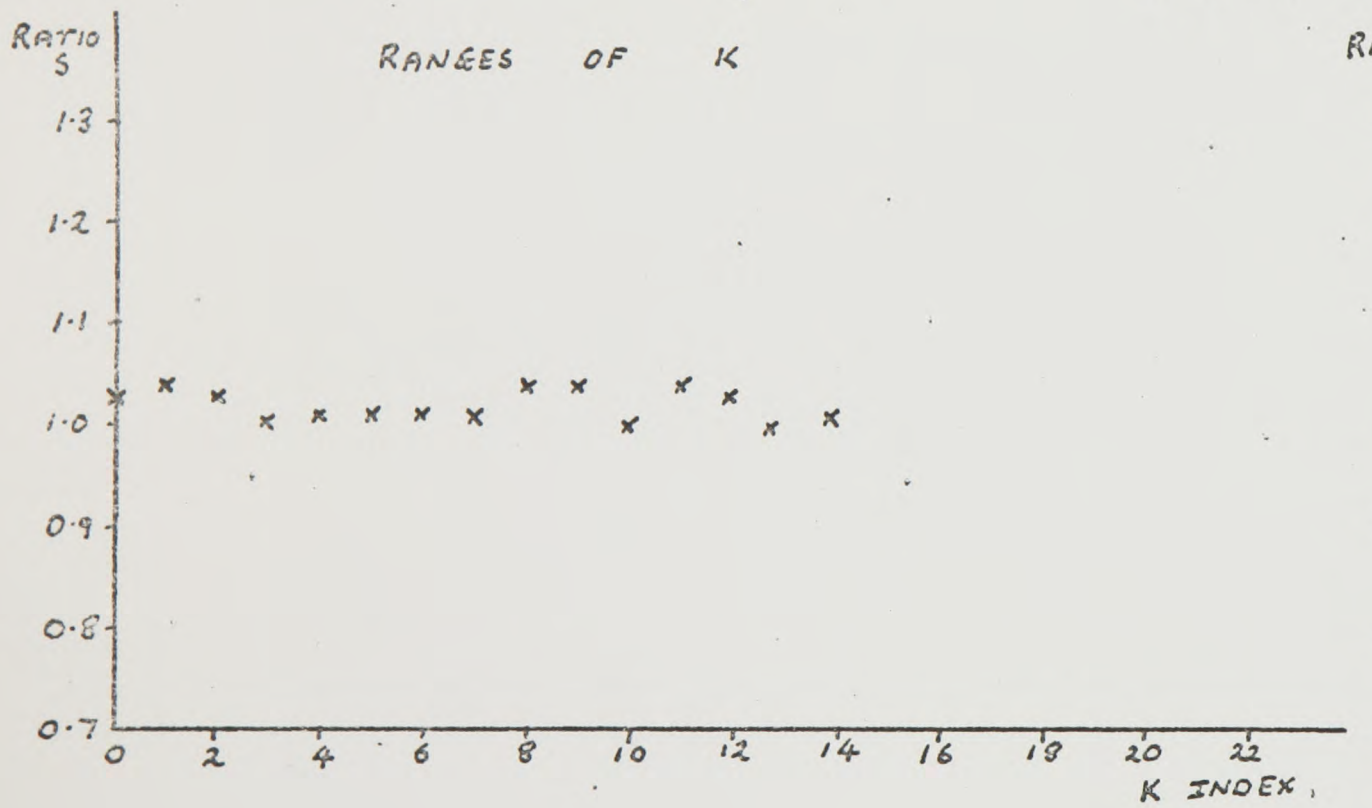
(c) Co-crystallised Methyl Mercury Crystals; numbers 231,232,233,234.

The crystal sizes and unit cell dimensions measured from them are shown in Table 3.8, and the primary data processing statistics in Table 3.9.

An attempt was made to measure this data set in only two shells (6.0Å to 7.5Å and 7.5Å to ∞). However, due to the high radiation damage on the first crystal, this was not possible, and four crystals had to be used for the data set.







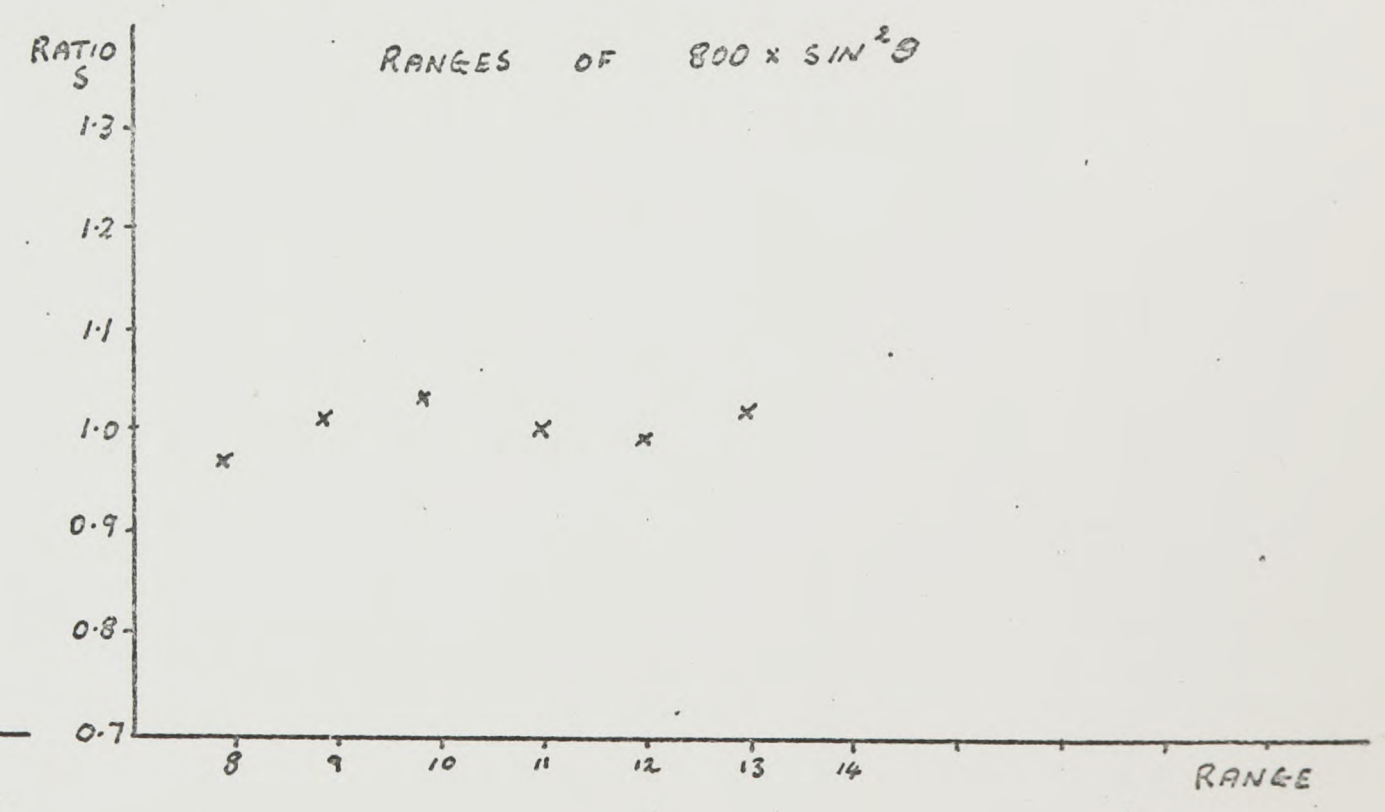


FIGURE 3.37
The agreement between equivalent reflections for crystal 231

Crystal 231 This data was collected using a 1.4 mm source collimator and 3.5 mm detector collimator. The reflections were scanned using 40 steps of 0.02^{o} on the ω axis counting for 2 seconds per step.

Because of the large number of reflections collected on this crystal, the radiation damage was very high (approximately 30% estimated on the standard reflections). A linear correction with a slope of 1.153×10^{-4} was applied to the intensities, and comparison of 105 reflections measured at the beginning and end of the data collections showed that a further linear correction rising to 1.025 should be applied. In view of the high radiation damage, it was decided to use only half this data; 1274 reflections were retained, i.e. reflections (00 $\bar{1}\bar{6}$) to (14 14 7).

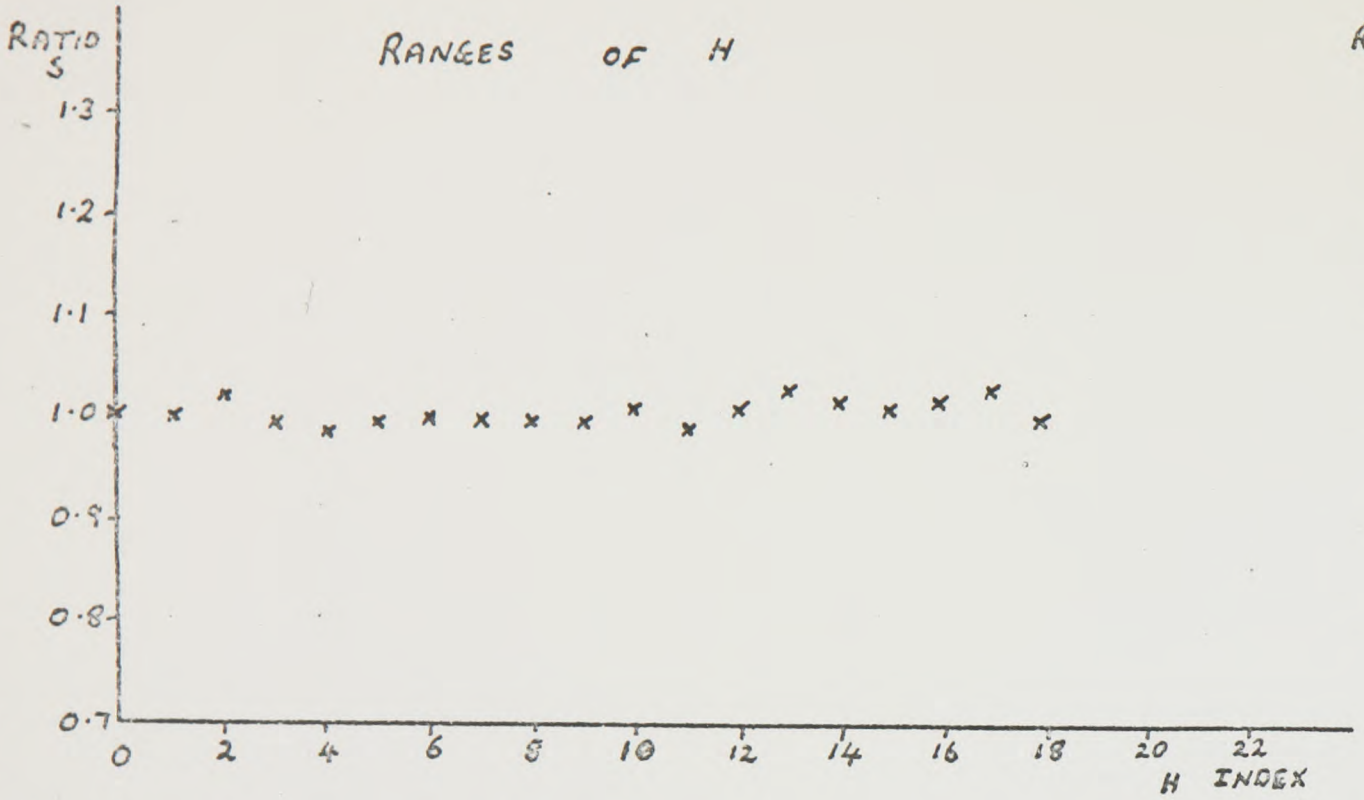
The analysis of the equivalent reflections showed that no scales needed to be applied. The overall agreement between the equivalent reflections was:

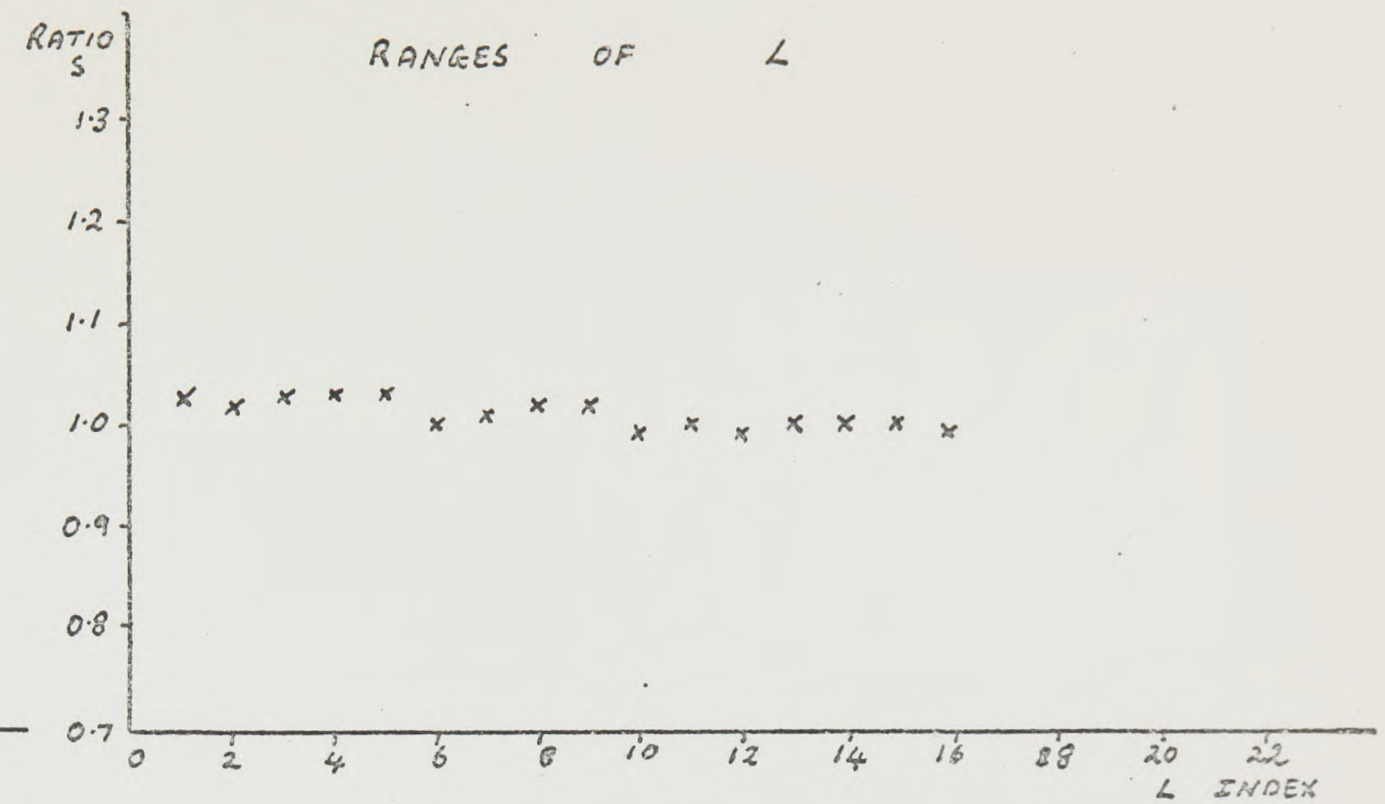
	No. of Refl. Pairs	S	R
Centric data	138	1.0175	8.36%
Acentric data	472	1.0088	10.75%
Overall	610	1.0111	10.11%

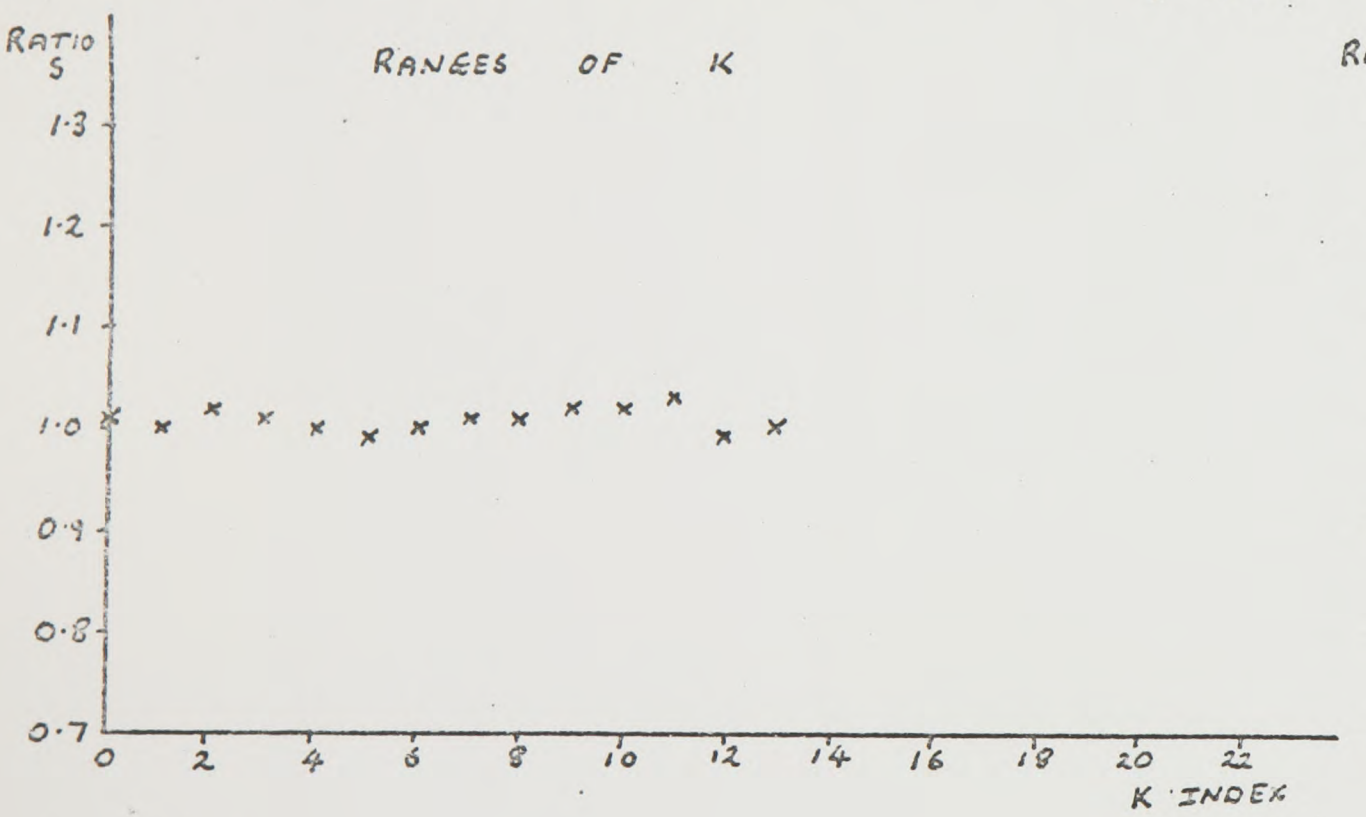
The plots of the ratio S are shown in Figure 3.37

Crystal 232. A 1.4 mm source collimator and 2.5 mm detector collimator were used for this data set. The reflections were scanned using 40 steps of 0.02^{o} on the ω axis counting for 2 seconds per step.

A radiation damage correction of 15% [slope 8.333×10^{-5}] was applied to the intensities. The analysis of the







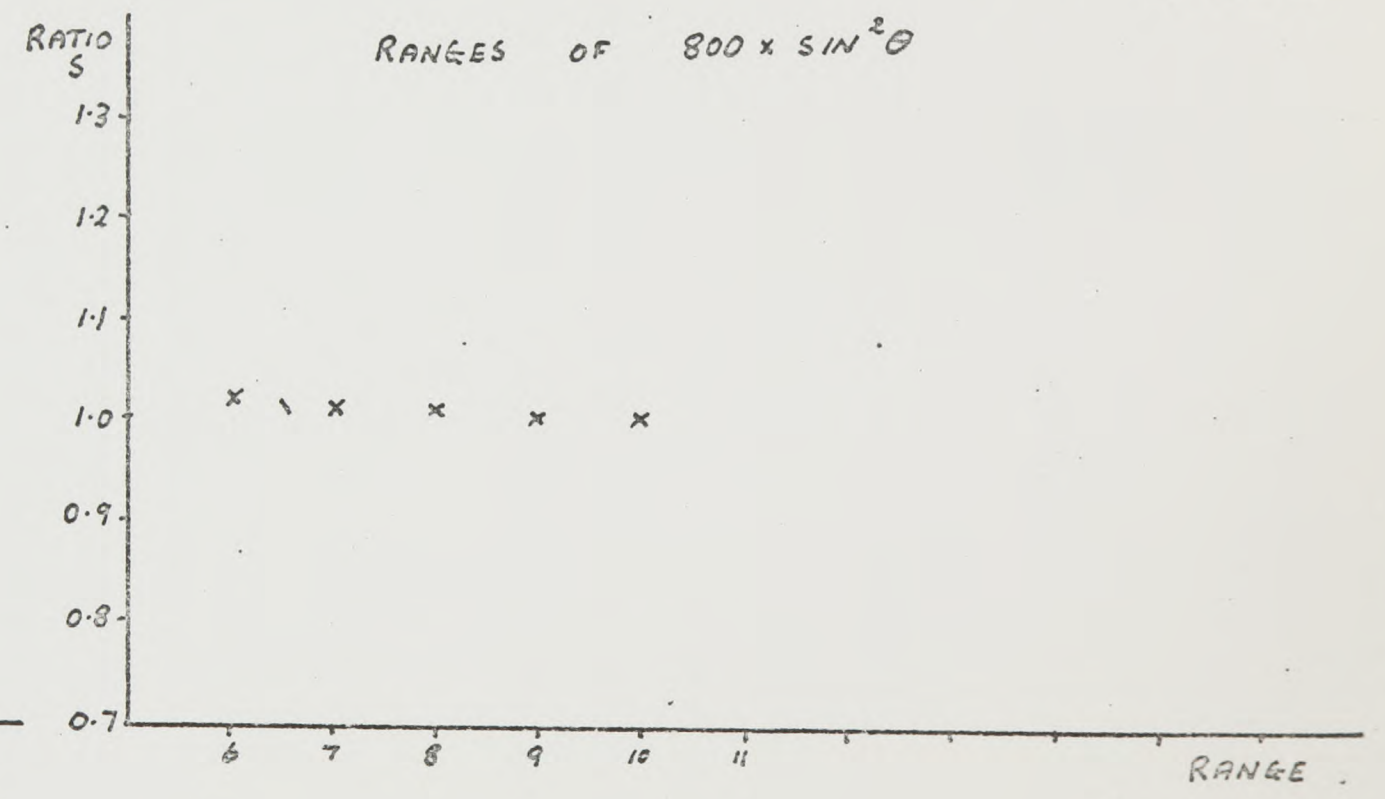


FIGURE 3.38
The agreement between equivalent reflections for crystal 232

agreement between equivalent reflections showed that a scale factor varying with h had to be applied to the intensities of the $(hk\bar{l})$ reflections. This scale factor was:,

$$\text{Scale} = 0.9591 + h \times 0.0011.$$

after scaling, the agreement between equivalent reflections was:

	No. of refl. pairs	S	R
Centric data	162	1.0056	5%
Acentric data	719	1.0087	6.28%
Overall	881	1.0081	6.02%

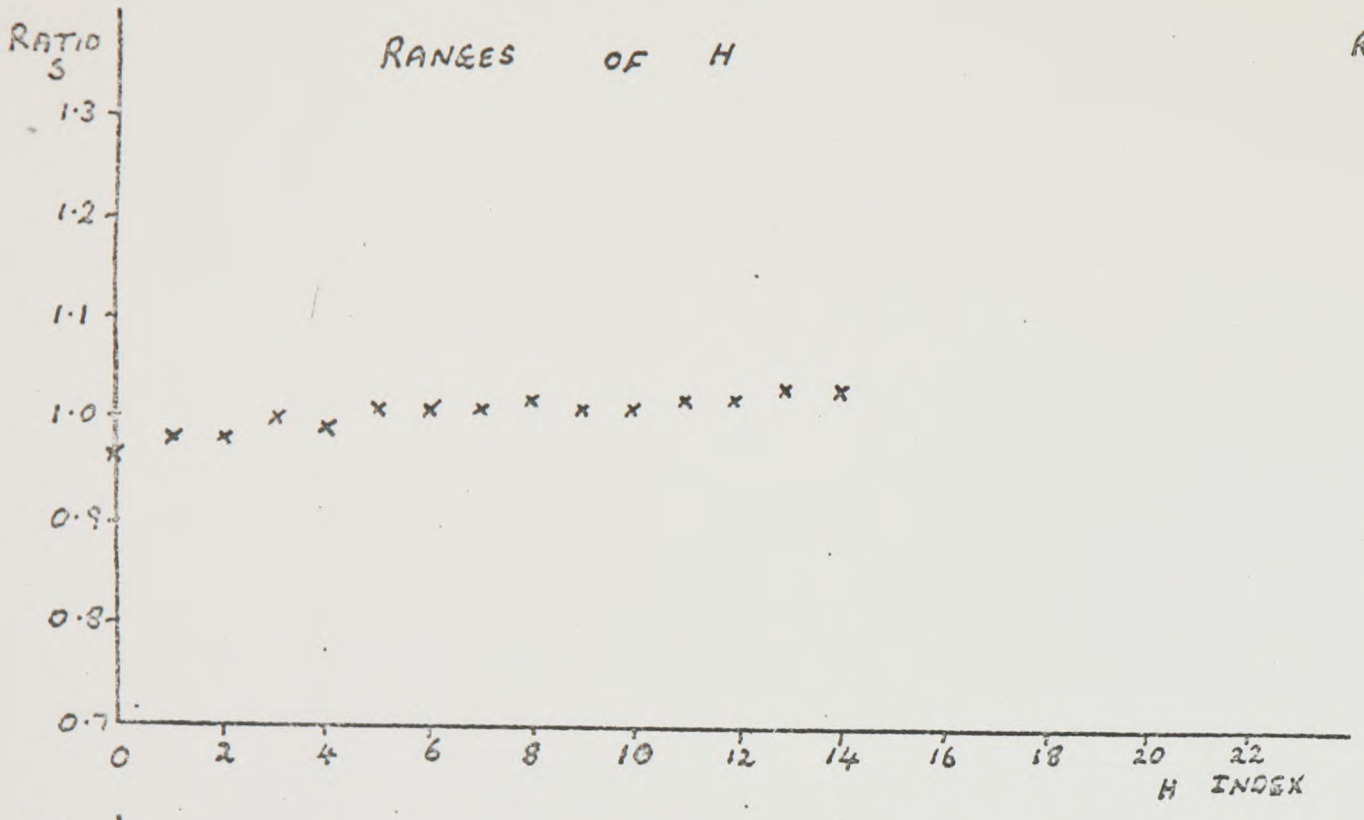
The plots of S are shown in Figure 3.38.

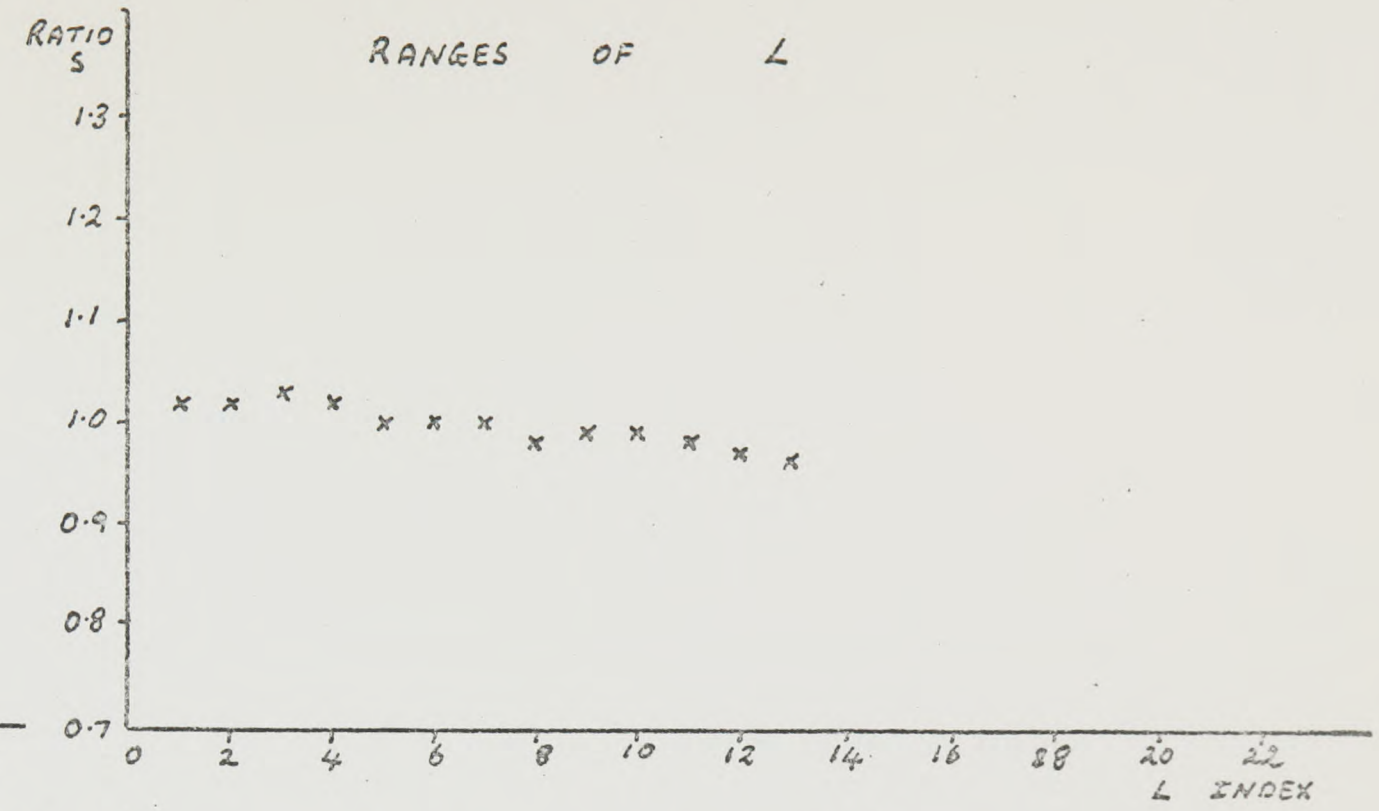
Crystal 233. This data set was collected using a 1.4 mm source collimator and 3.5 mm detector collimator, and the reflections scanned with 44 steps of 0.02° on the ω axis counting for 2 seconds per step.

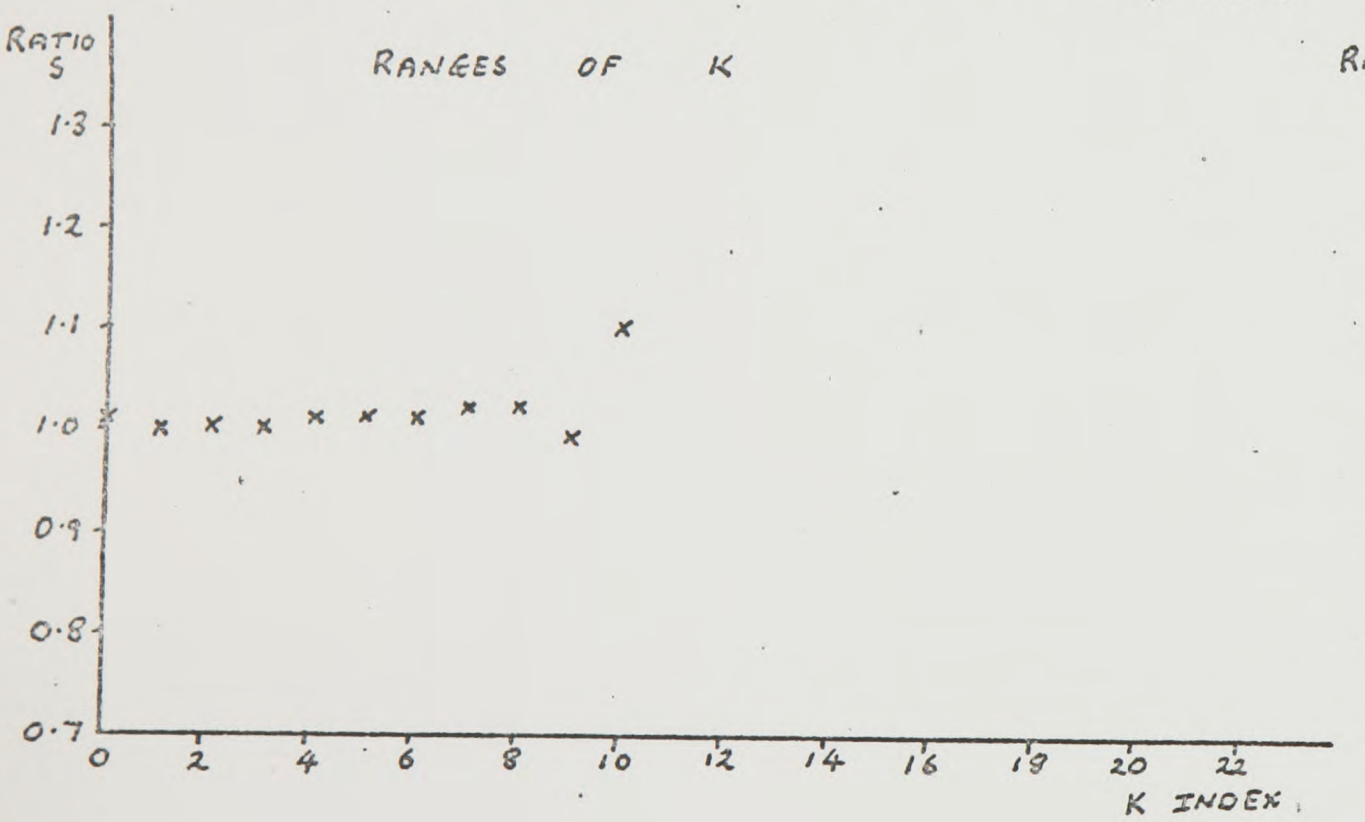
The radiation damage as estimated on the standard reflections was 6.5%, and so a linear correction factor with a slope of 3.62×10^{-5} was applied to the intensities. Comparison of the intensities of 148 reflections measured at the beginning and end of the data collection showed that this radiation damage correction had been too high. A linear correction running from 1.0 to 0.9879 was then applied to the data.

Analysis of the equivalent reflections showed that a scale factor varying with $\sin^2\theta$ had to be applied to the intensities of the $(hk\bar{l})$ reflections. This scale factor was given by

$$\text{Scale} = 0.9638 - (800 \times \sin^2\theta) \times 0.0034.$$







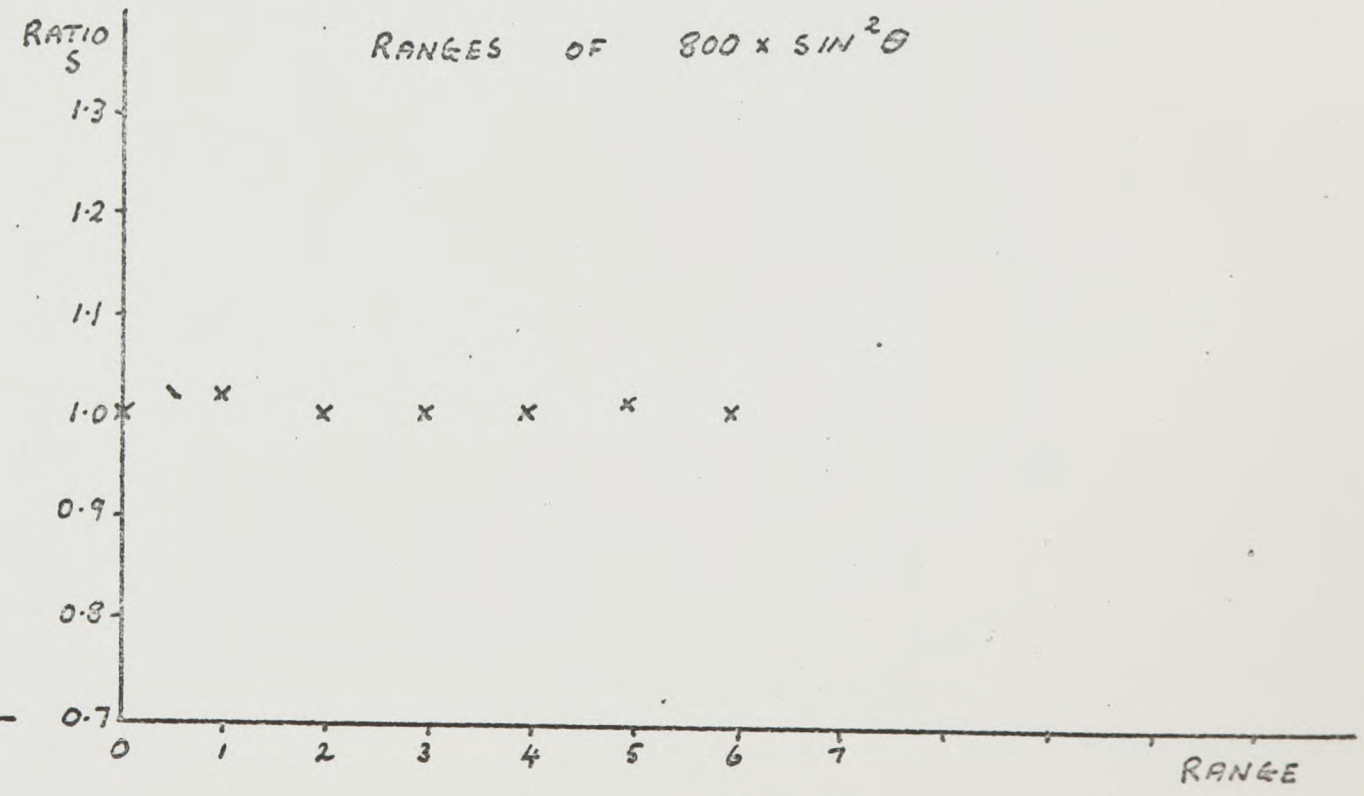


FIGURE 3.39

The agreement between equivalent reflections for crystal 233

After scaling the overall agreement between the equivalent reflections was:

	No. of refl. pairs	S	R
Centric data	240	1.0025	4.63%
Acentric data	605	1.0065	5.56%
OVERALL	845	1.0052	5.26%

The plots of S are shown in Figure 3.39.

Crystal 234. The data collected from this crystal were intended to complete the shell started with crystal 231, and so the data collection was started at reflection (14 8 $\bar{1}\bar{2}$), giving approximately 100 reflections overlapping with crystal 231.

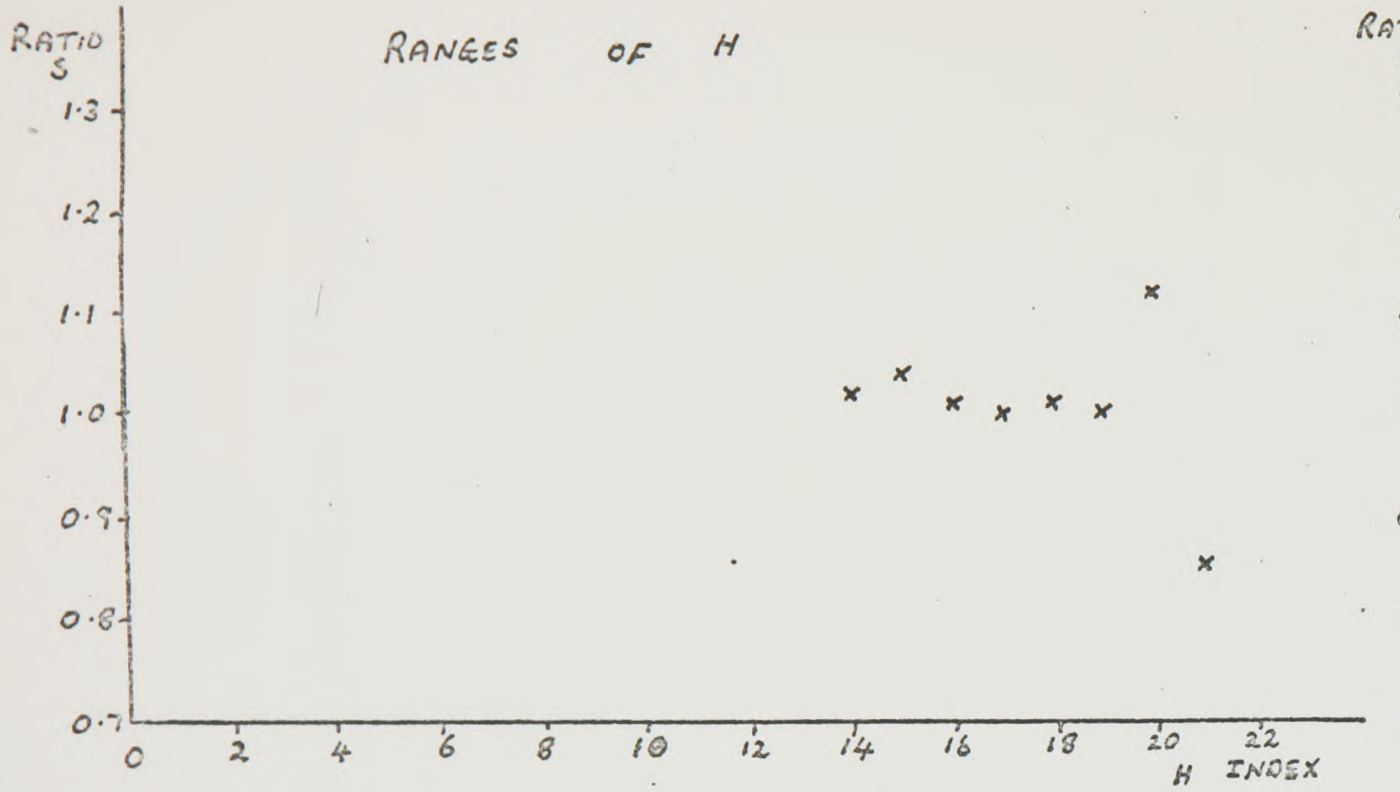
A 1.4 mm. source collimator and 3.5 mm. detector collimater were used, and the reflections scanned using 48 steps of 0.02^{o} on the ω axis counting for 2 seconds per step.

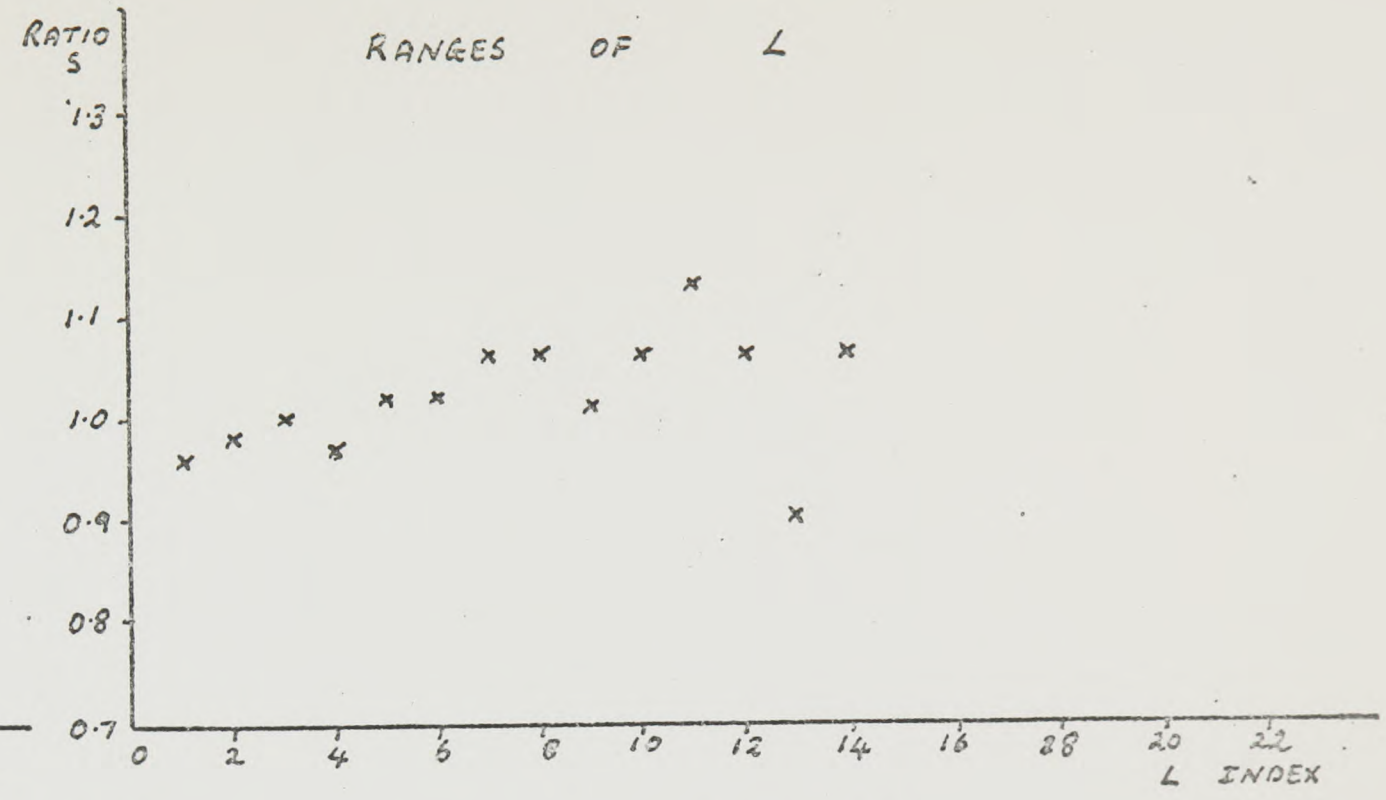
Estimation of the radiation damage on the standard reflections gave a figure of 5.8%; a linear correction with a slope of 4.46×10^{-5} was applied to the intensities. An extra linear correction varying from 1.0 to 1.0188 was applied to the data based on the ratio of the sums of the intensities of 100 reflections measured at the beginning and end of the data collection.

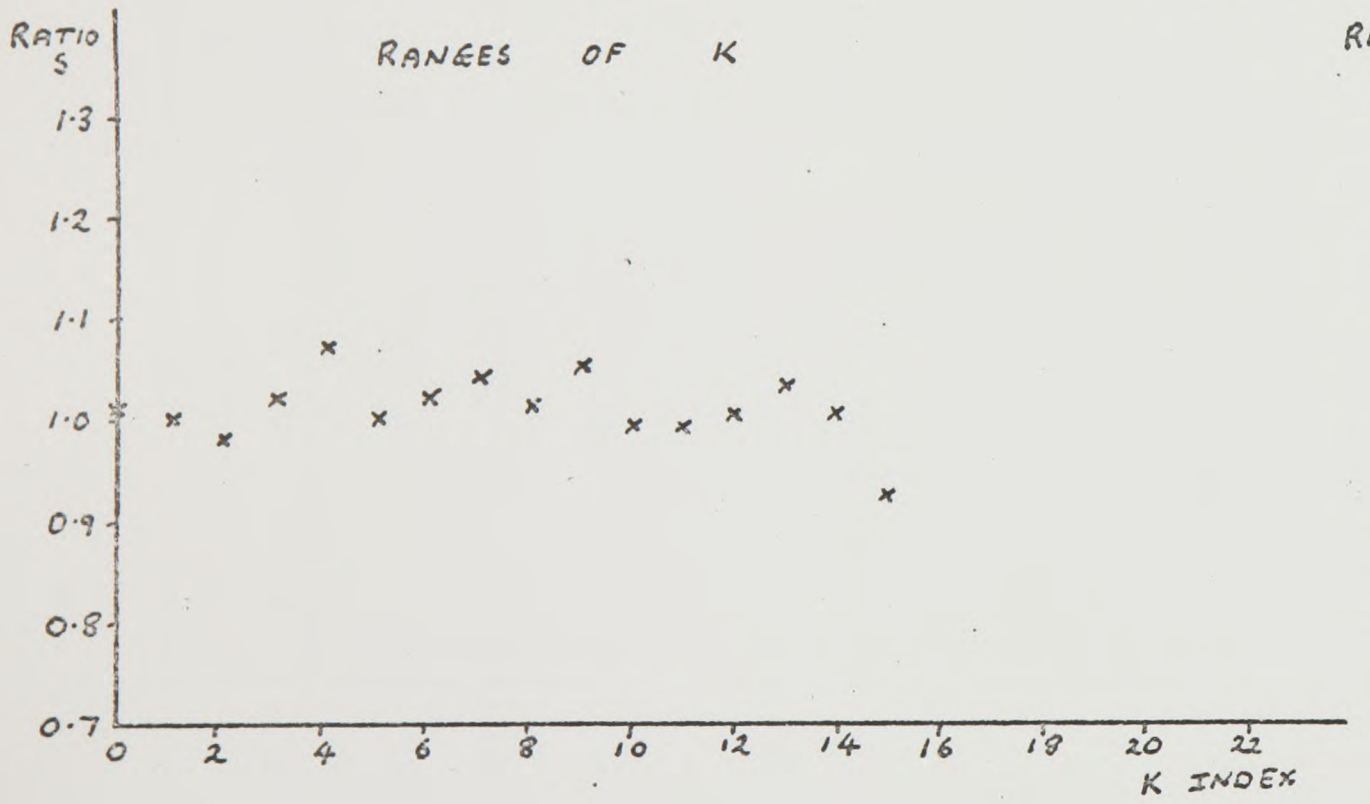
A scale factor given by:

$$\text{Scale} = 1.0809 - |l| \times 0.009$$

was applied to the intensities of the ($hk\bar{l}$) reflections. After scaling the overall agreement between the equivalent reflections was:







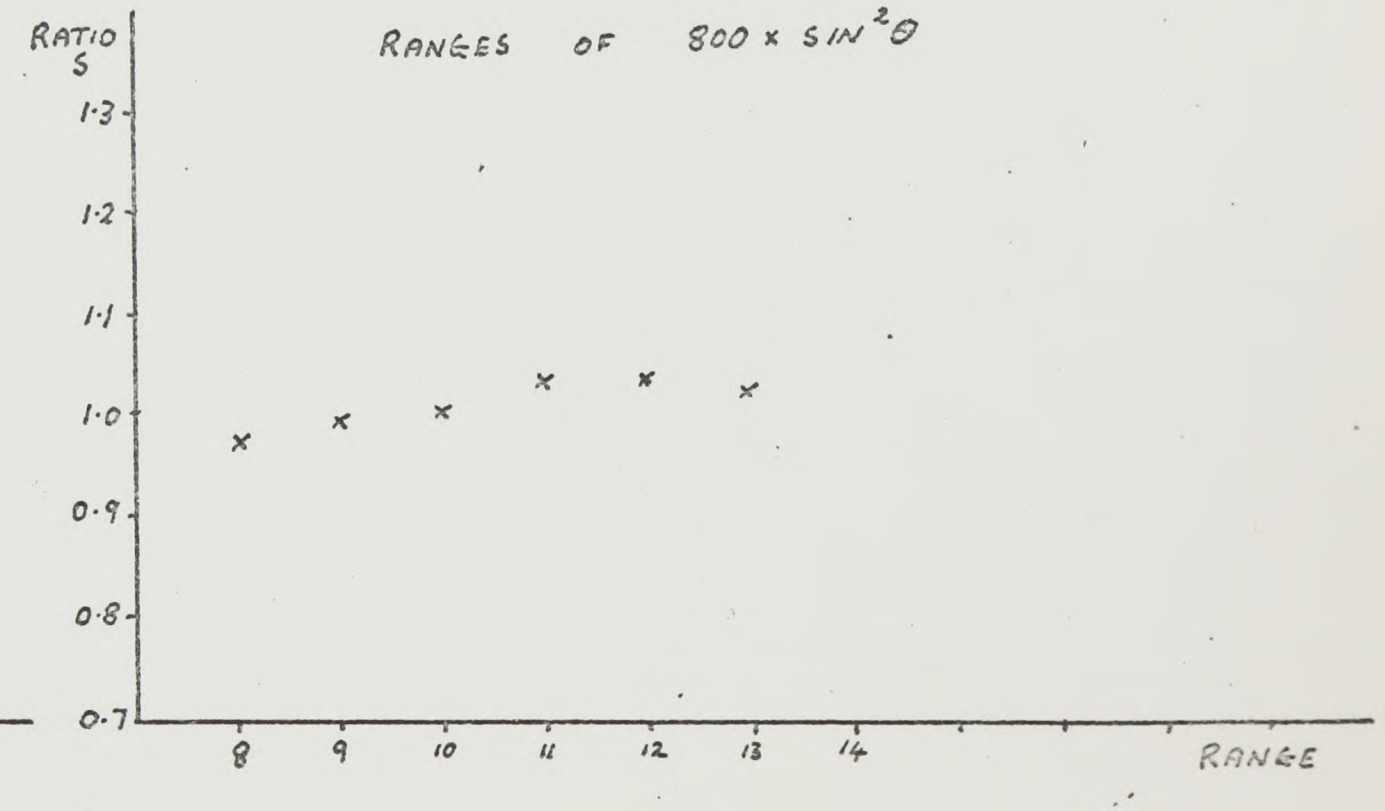


FIGURE 3.40
The agreement between equivalent reflections for crystal 234

	No. of refl. pairs	S	R
Centric data	61	1.0000	10.38%
Acentric data	542	1.0152	13.11%
Overall	603	1.0136	12.83%

Figure 3.40 gives the plots of S.

Crystal to Crystal Scaling

The four sets of data were scaled on to the set from crystal 231. The numbers of overlapping reflections between the sets of data were:

231/232	481
231/234	117
232/233	73
232/234	369

The scale factors converged after 5 cycles of refinement to:

Crystal number	Scale factor.
231	1.0
232	1.336
233	1.569
234	1.279

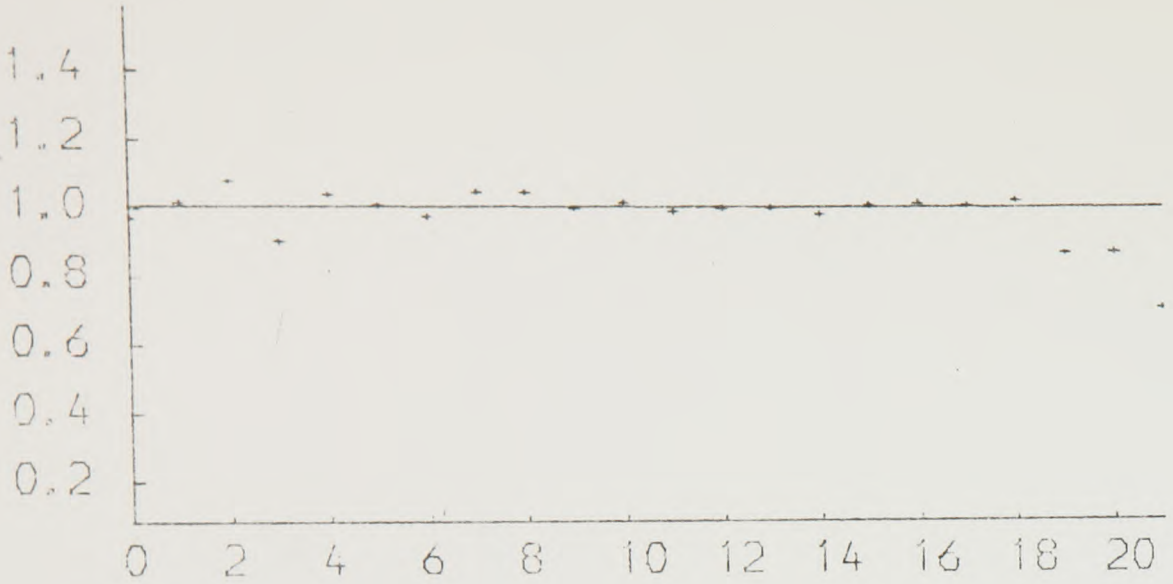
The merged data set comprised 4652 independent reflections with a merging R factor of 4.61%

Derivative to Native Scaling

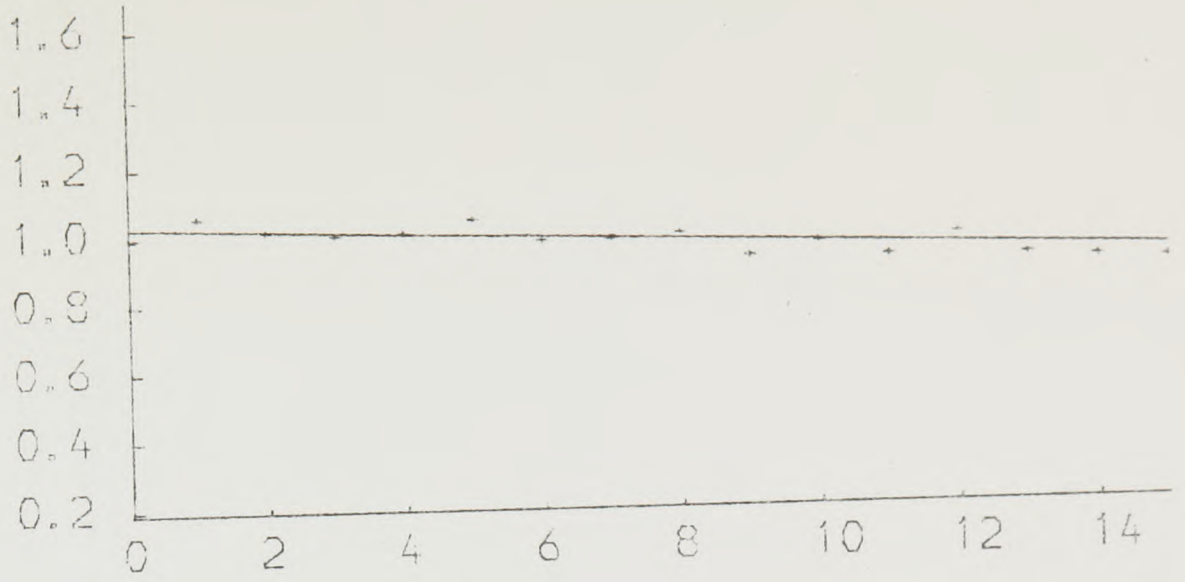
These derivative data were scaled on to the native data using a scale factor, applied to the F^2 of the derivative data, given by:

$$\text{Scale} = 1.114 + 27.602 \times 4 \sin^2\theta/\lambda^2$$

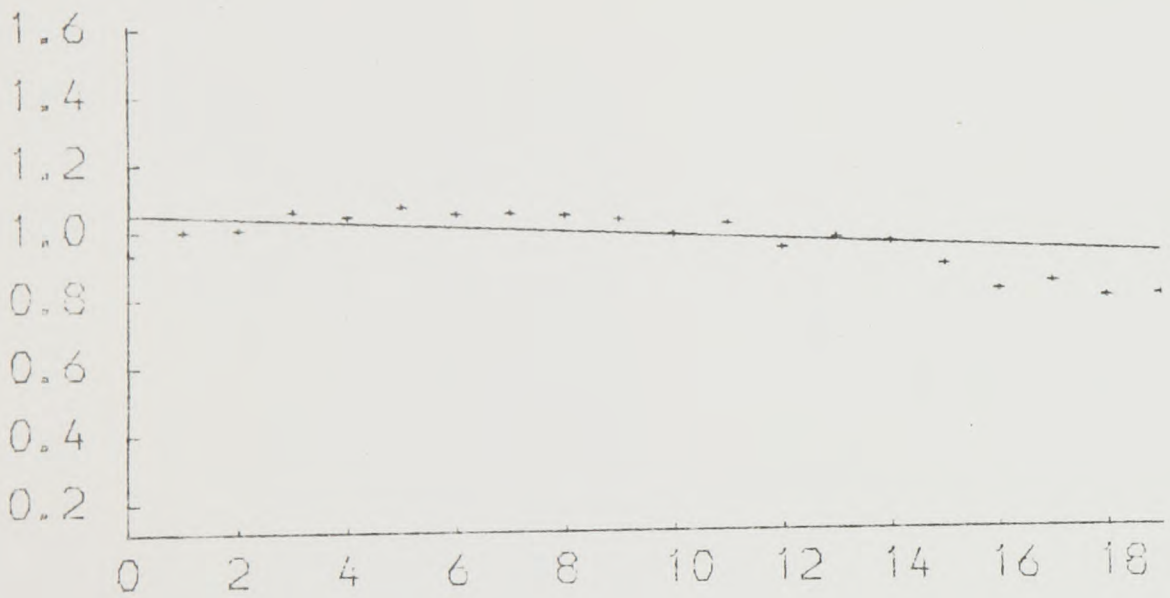
The plots of the ratio $\sum F_p^{\,2}/\sum F_{pH}^{\,2}$ after scaling are shown in



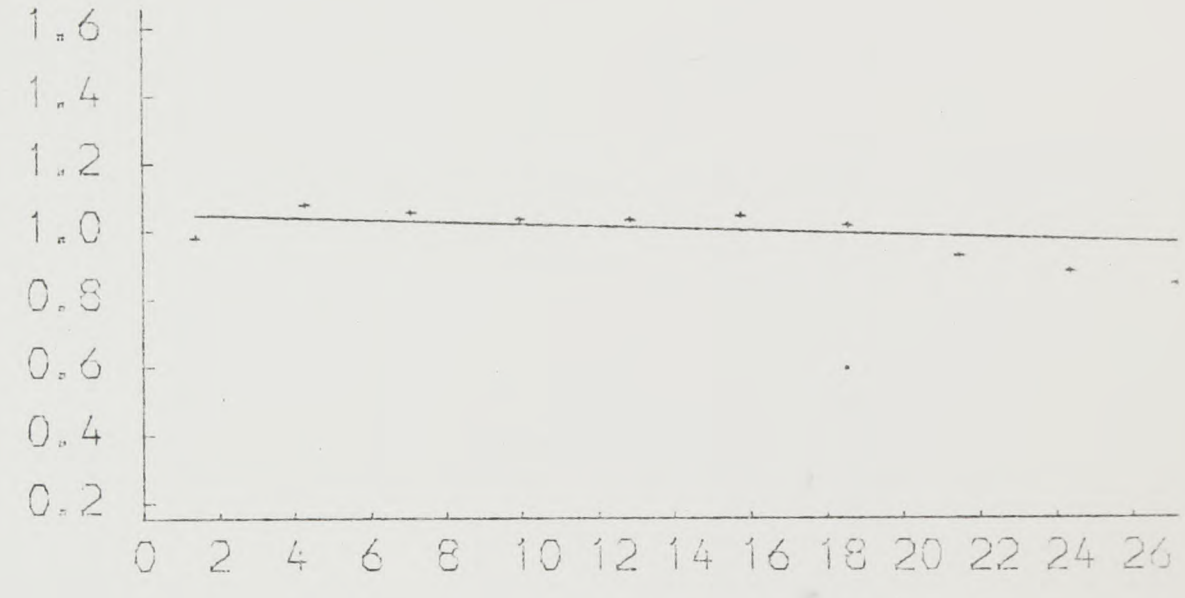
COMEHG .PLOT AGAINST H



COMEHG .PLOT AGAINST K



COMEHG .PLOT AGAINST L

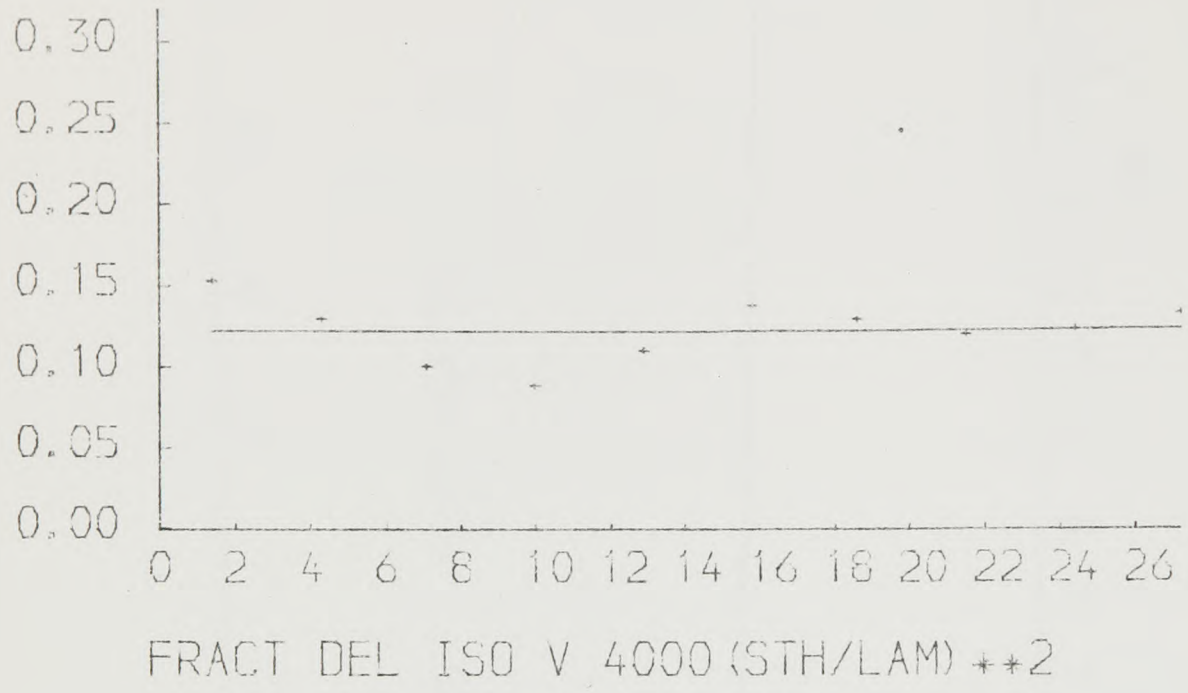


COMEHG .PLOT AGAINST (STH/L**2)*4000

FIGURE 3.41

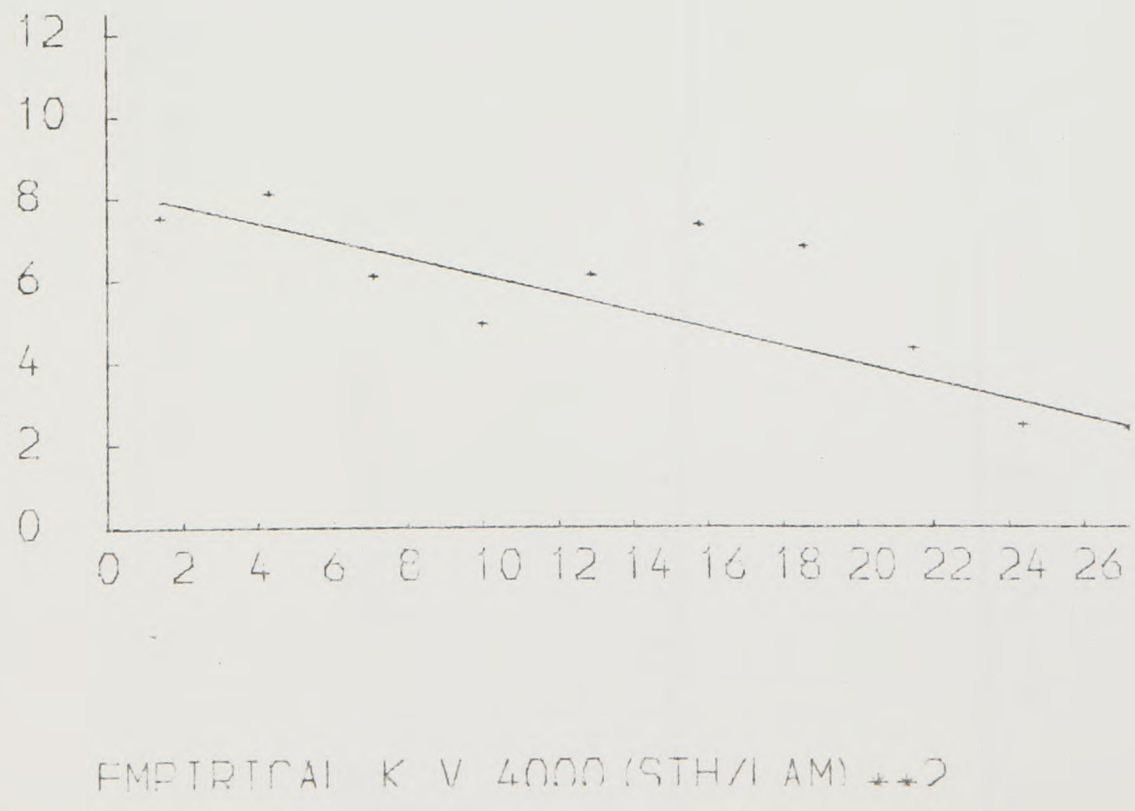
The plots of $\sum F_p^2 / \sum F_{pH}^2$ for the methyl mercury chloride derivative.

FIGURE 3.42



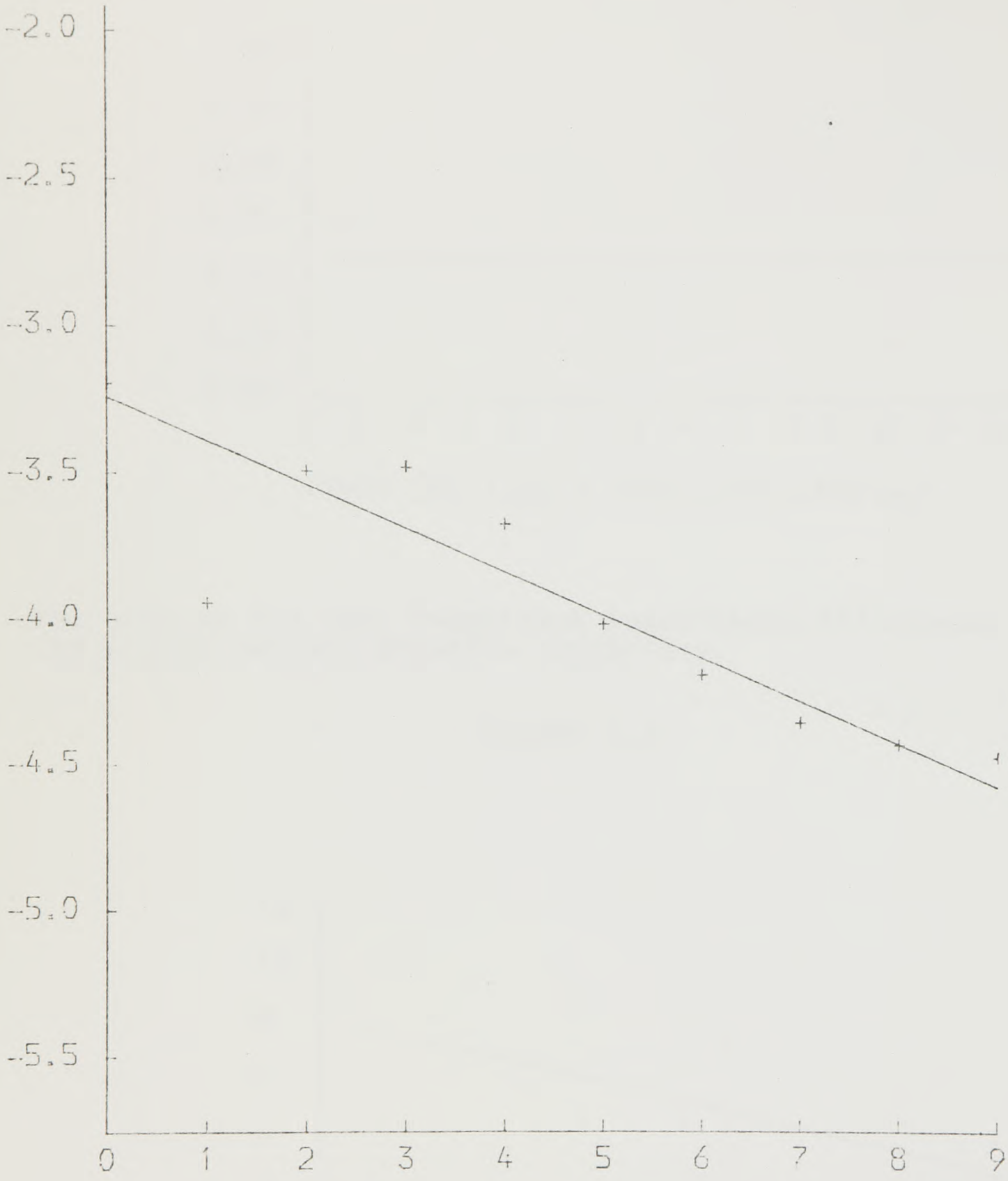
The plot of the mean fractional isomorphous difference for the methyl mercury chloride derivative.

FIGURE 3.43



The plot of the empirical k value for the methyl mercury chloride derivative.

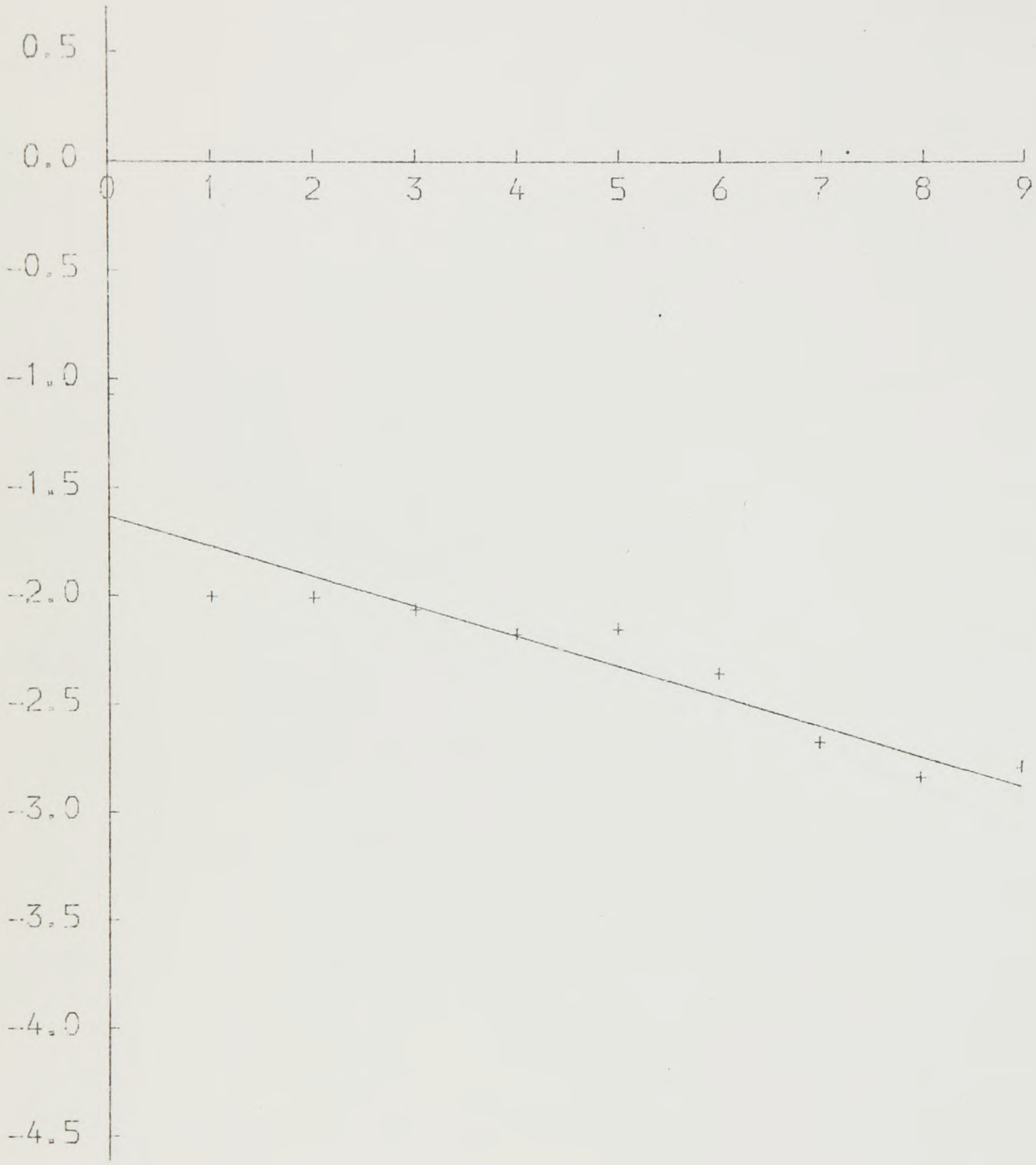
FIGURE 3.44



COMEHG OV DER WILSON PLOT

The Wilson plot for the methyl mercury chloride derivative.

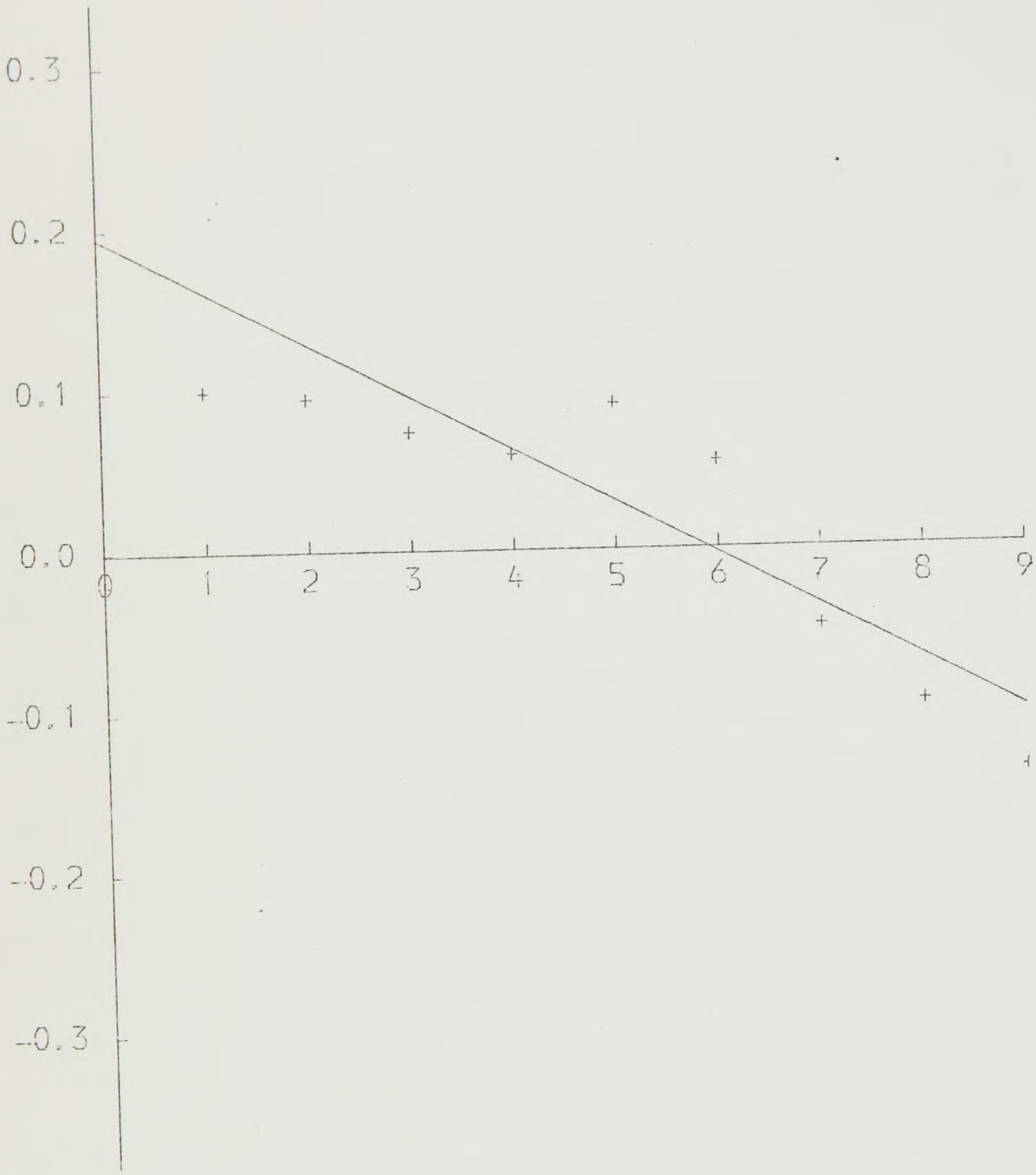
FIGURE 3.45



COMEHG OV H A WILSON PLOT

The Heavy Atom Wilson plot for the methyl mercury chloride derivative.

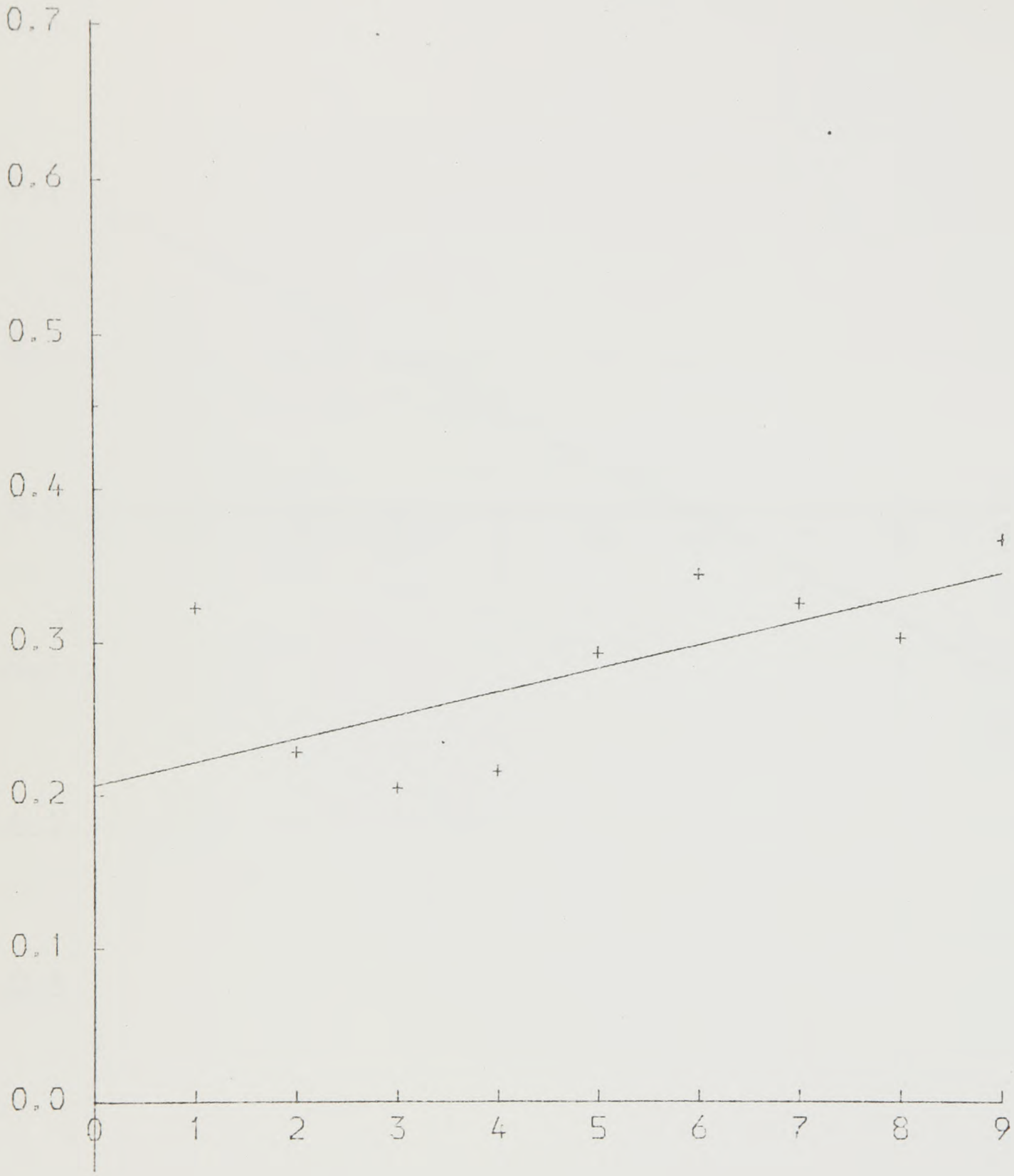
FIGURE 3.46



COMEHG OV COM WILSON PLOT

The Comparative Wilson plot for the methyl mercury chloride derivative.

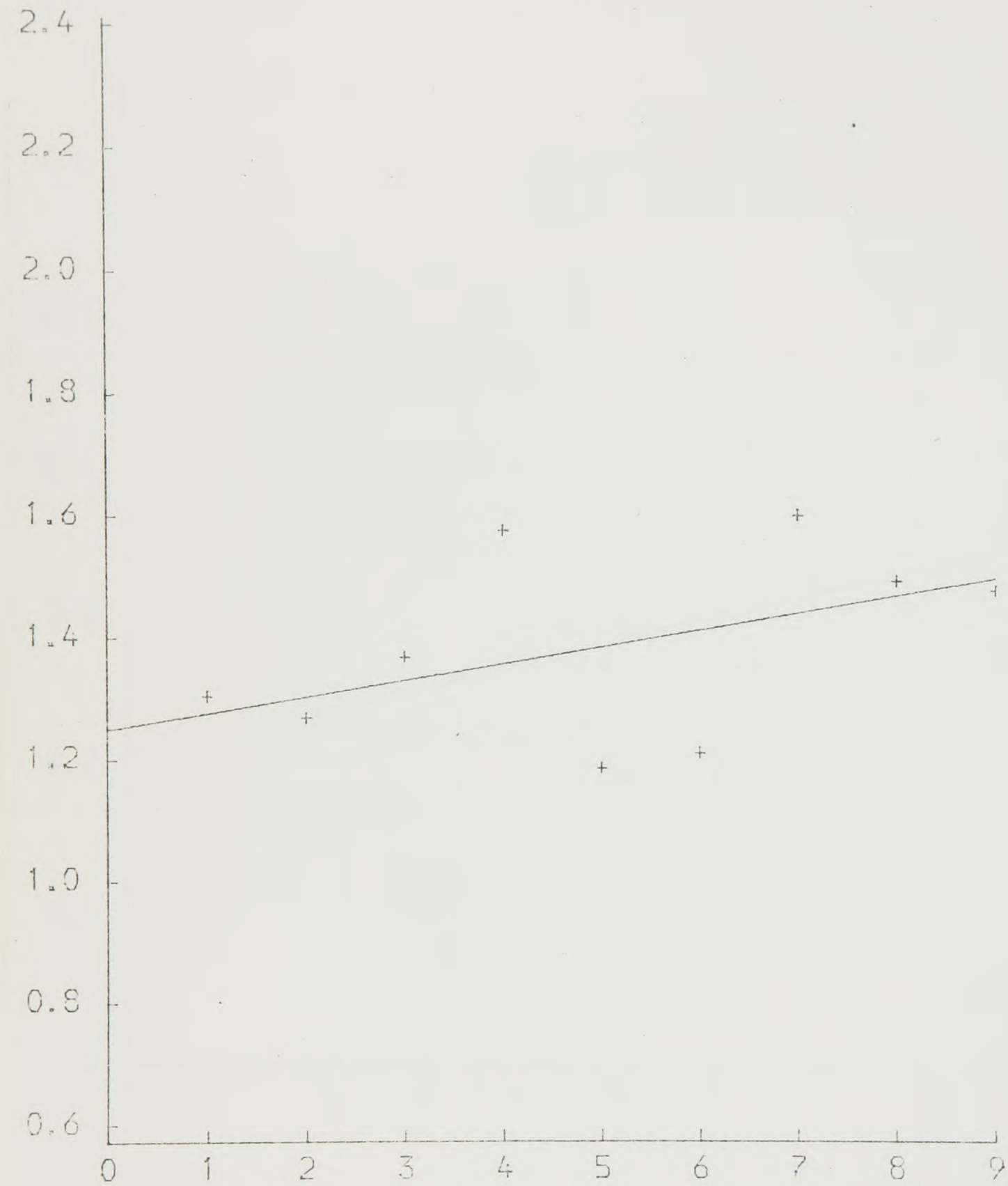
FIGURE 3.47



COMEHG OVERALL CRICK PLOT

The Crick-Magdoff plot for the methyl mercury chloride derivative.

FIGURE 3.48



The Crick-Magdoff ratio plot for the methyl mercury derivative.

TABLE 3.10

Co-crystallised methyl mercury - Theoretical and observed fractional change in intensity

Mean $\sin^2\theta/\lambda^2$	Centric terms		Acentric terms	
	Theoretical	Observed	Theoretical	Observed
0	0.38248	0.48221	0.27045	0.26800
0.00077	0.38428	0.37130	0.27173	0.28452
0.00154	0.38610	0.25169	0.27301	0.19818
0.00231	0.38792	0.25540	0.27430	0.18637
0.00309	0.38974	0.29357	0.27559	0.18600
0.00386	0.39157	0.33237	0.27688	0.28022
0.00463	0.39341	0.38891	0.27818	0.32102
0.00540	0.39525	0.45812	0.27948	0.28613
0.00617	0.39709	0.39882	0.28078	0.26744
0.00694	0.39894	0.45604	0.28209	0.30926

Figure 3.41; the overall ratio $\sum F_p^2 / \sum F_{pH}^2$ was 0.9997. There were 2640 reflections where both native and derivative structure amplitudes had been measured. The mean isomorphous difference was 24.3, and the mean fractional isomorphous difference was 12.1%. Figure 3.42 shows the variation of the mean fractional isomorphous change with $\sin^2\theta/\lambda^2$.

The empirical k varied with $\sin^2\theta/\lambda^2$ as shown in Figure 3.43. F_{HLE} coefficients were calculated and those reflections for which F_{HLE} was greater than 150 or F_{HUE} was less than 150 were rejected. This left 2504 reflections. The Kraut scale factor was found to be 1.018.

The standard, heavy atom and comparative Wilson plots are shown in Figures 3.44, 3.45, 3.46. The heavy atom plot gave a temperature factor of 90.1 and an absolute scale factor of 5.1.

Figure 3.47 shows the Crick-Magdoff plot, and 3.48 the ratio plot. The observed fractional change in intensity for the centric and acentric data is compared with the theoretical values computed assuming 2 fully occupied mercury sites per monomer in Table 3.10. The rather low fractional changes in intensities indicate less than the full occupation of any mercury binding sites.

Difference Patterson and Difference Fourier Syntheses

Difference Patterson syntheses with the full data set and with only data within the 15Å to 6Å region were computed, and also an F_{HLE} Patterson was computed. All these Pattersons had the same major features, but no solution could be found.

The native phase angles as estimated from the platinum

TABLE 3.11

URANIUM DERIVATIVE CRYSTALS - PHYSICAL PARAMETERS

Crystal Number	Crystal size (mm) a x b x c	Shell	Unit cell dimensions from diffractometer
211	0.6 x 0.6 x 2.2	6.9Å - 8.7Å	a= b= 129.07Å c= 115.91Å
212	0.6 x 0.5 x 1.0	6.0Å - 6.9Å	a= b= 129.07Å c= 116.29Å
213	0.4 x 0.4 x 0.8	8.7Å - ∞	a= b= 128.45Å c= 116.29Å

TABLE 3.12

URANIUM DERIVATIVE CRYSTALS - PRIMARY DATA PROCESSING

Crystal Number	Total no of Reflections Processed	No. of SD failures	No. of background failures	Maximum Absorption Correction
211	1886	22	38	1.234
212	1682	170	240	1.273
213	2095	207	208	1.351

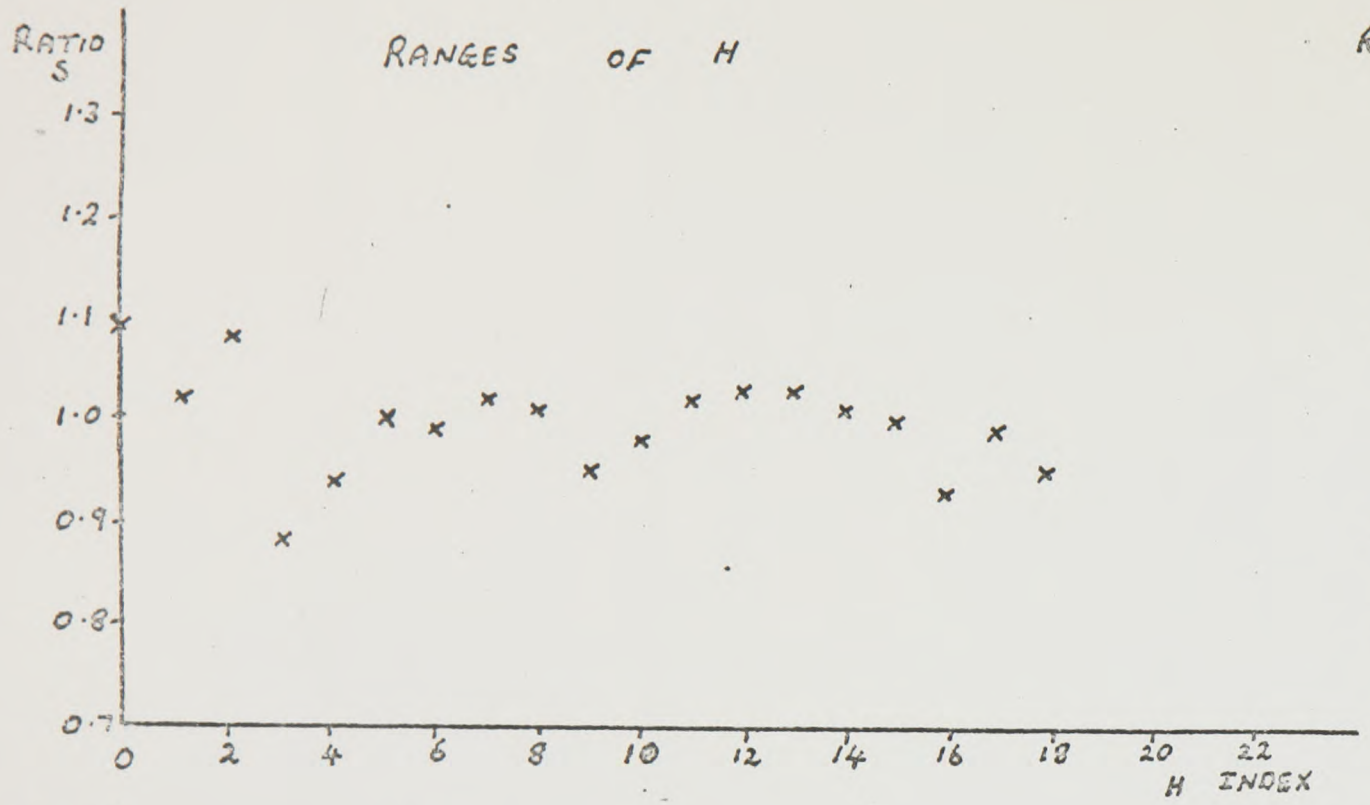
derivative were used to compute difference fourier maps for the (hk0) and (h0l) zones as well as the three dimensional data. The terms in these fouriers were weighted by the figures of merit of the phase angles. No mercury binding sites could be found in any of these difference fourier maps.

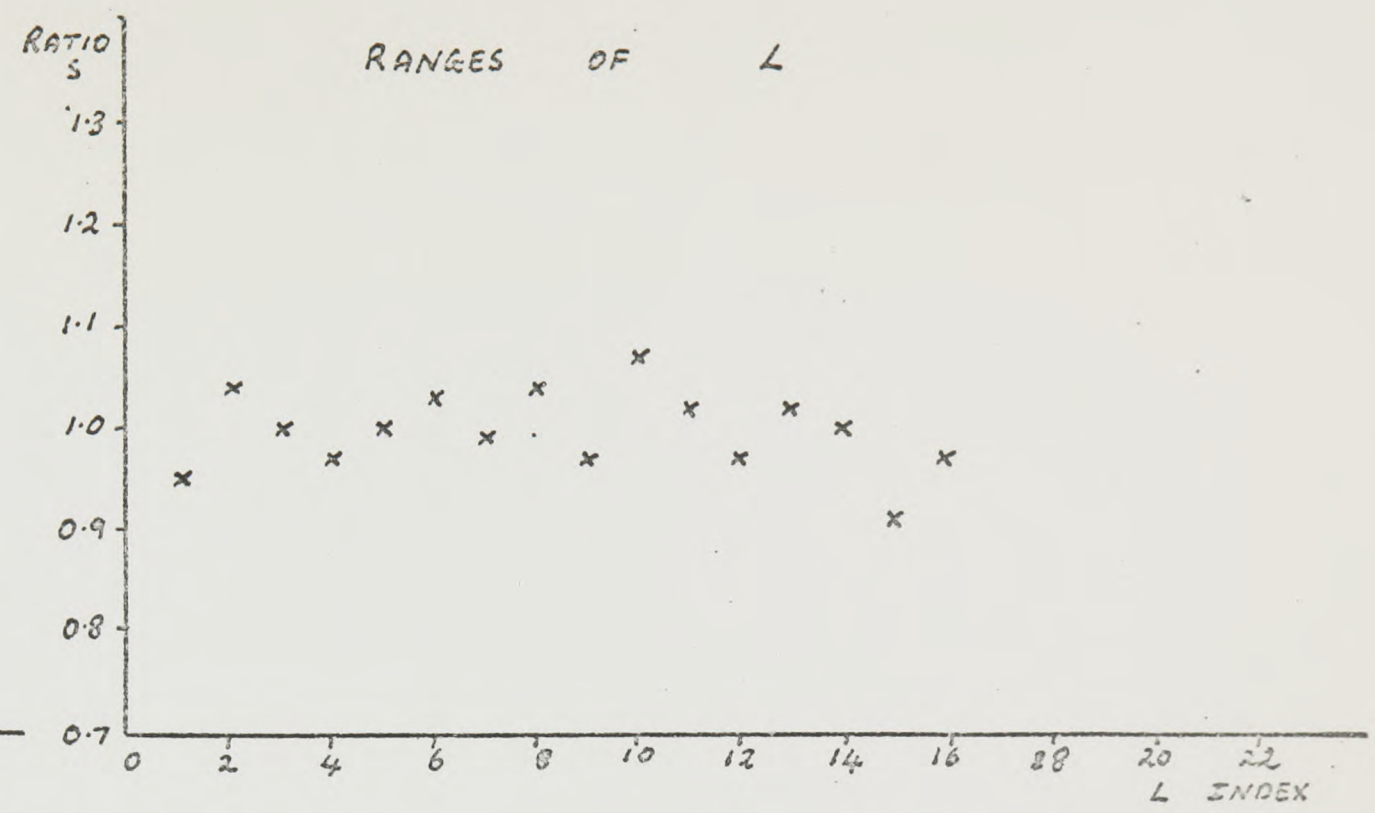
This lack of success suggested that the mercury could have been lost from the crystals during irradiation; particularly since there is evidence that x-radiation damages the -SH groups in phosphorylase (Damjanovich et al (1967)). The crystals were, therefore, subjected to neutron activation analysis in an effort to determine the mercury content. The analysis was carried out by the Activation Analysis Unit at A.E.R.E. Harwell. The results showed that the mercury was still present in the crystals in approximately the correct quantities. It is possible that the mercury had become delocalised during the data collection and hence could not be found from the x-ray data. Alternatively, since the sulphydryl groups are on the surface of the molecule, the mercury atoms may have too much thermal movement to be located by x-ray techniques.

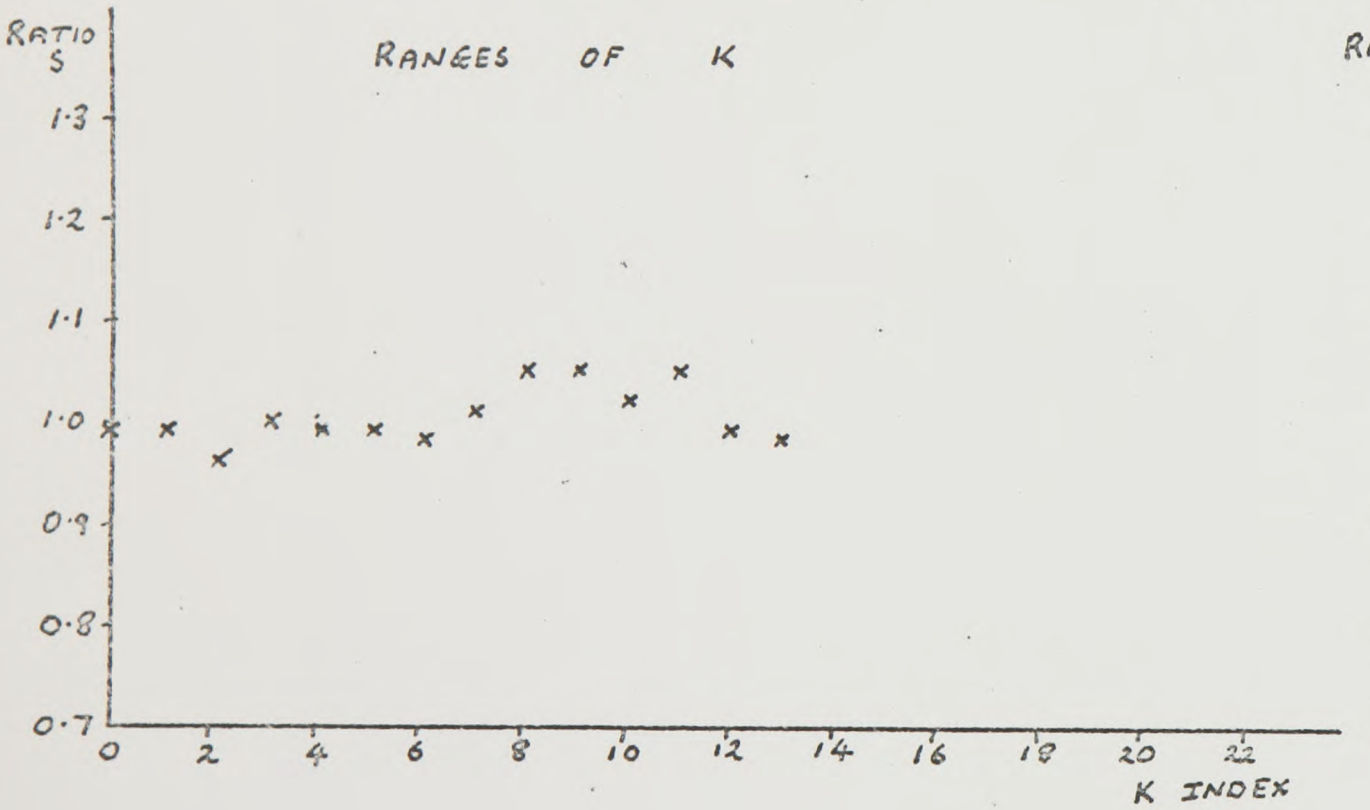
(d) Uranyl Acetate Derivative Crystals;numbers 211,212,213.

Several native crystals were soaked in the uranium acetate solution in an effort to produce identical heavy atom occupancies. The crystals were found to crack in the solution and so the derivative crystals were of poorer quality than the ones used for the previous data sets. The three best crystals were chosen for the data collection.

The physical parameters of the crystals and the primary data processing statistics are shown in Tables 3.11 and 3.12 respectively.







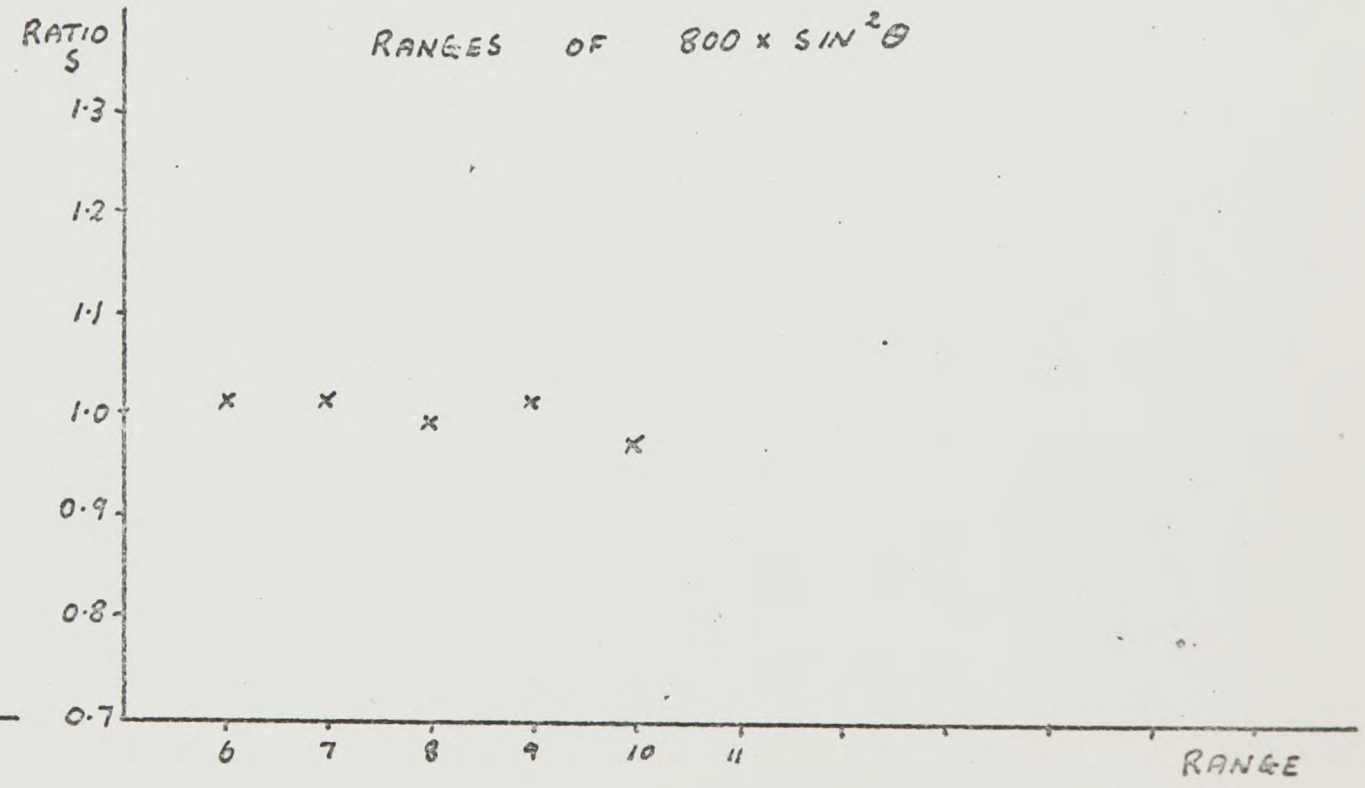


FIGURE 3.49
The agreement between equivalent reflections for crystal 211

Crystal 211

These data were collected using a 1.4 mm source collimator and 5.0 mm. detector collimator, and the reflections scanned using 60 steps of 0.02^{o} on the ω axis counting for 2 seconds per step.

The radiation damage was estimated at 20.4% from the plot of the standard reflections. A linear correction with a slope of 1.105×10^{-4} was therefore, applied to the data.

Analysis of the equivalent reflections indicated that a scale factor varying with l should be applied to intensities of the $(hk\bar{l})$ reflections. This scale factor was:

$$\text{Scale} = 0.9879 + |l| \times 0.0068.$$

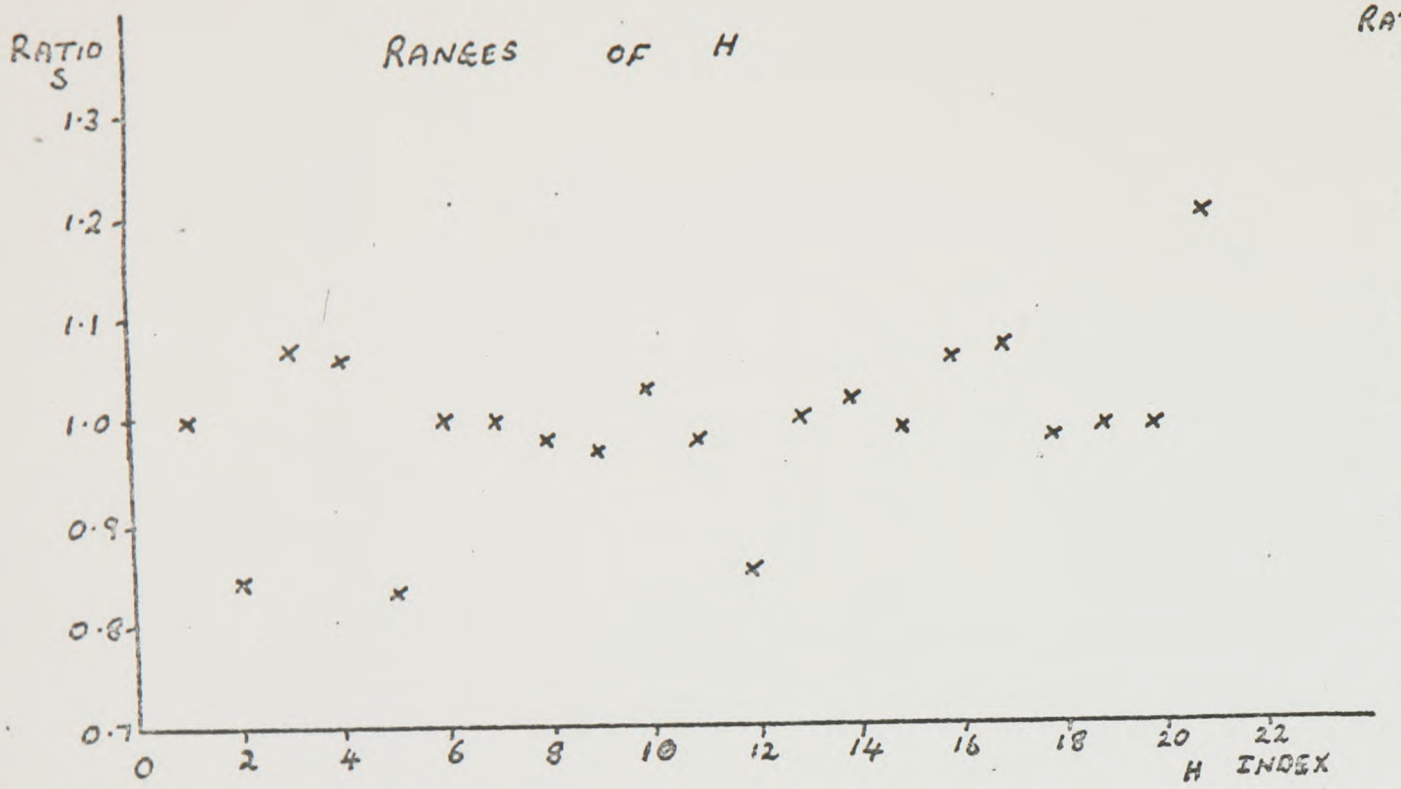
The plots of S after scaling are shown in Figure 3.49, while the overall agreement between equivalent reflections was:

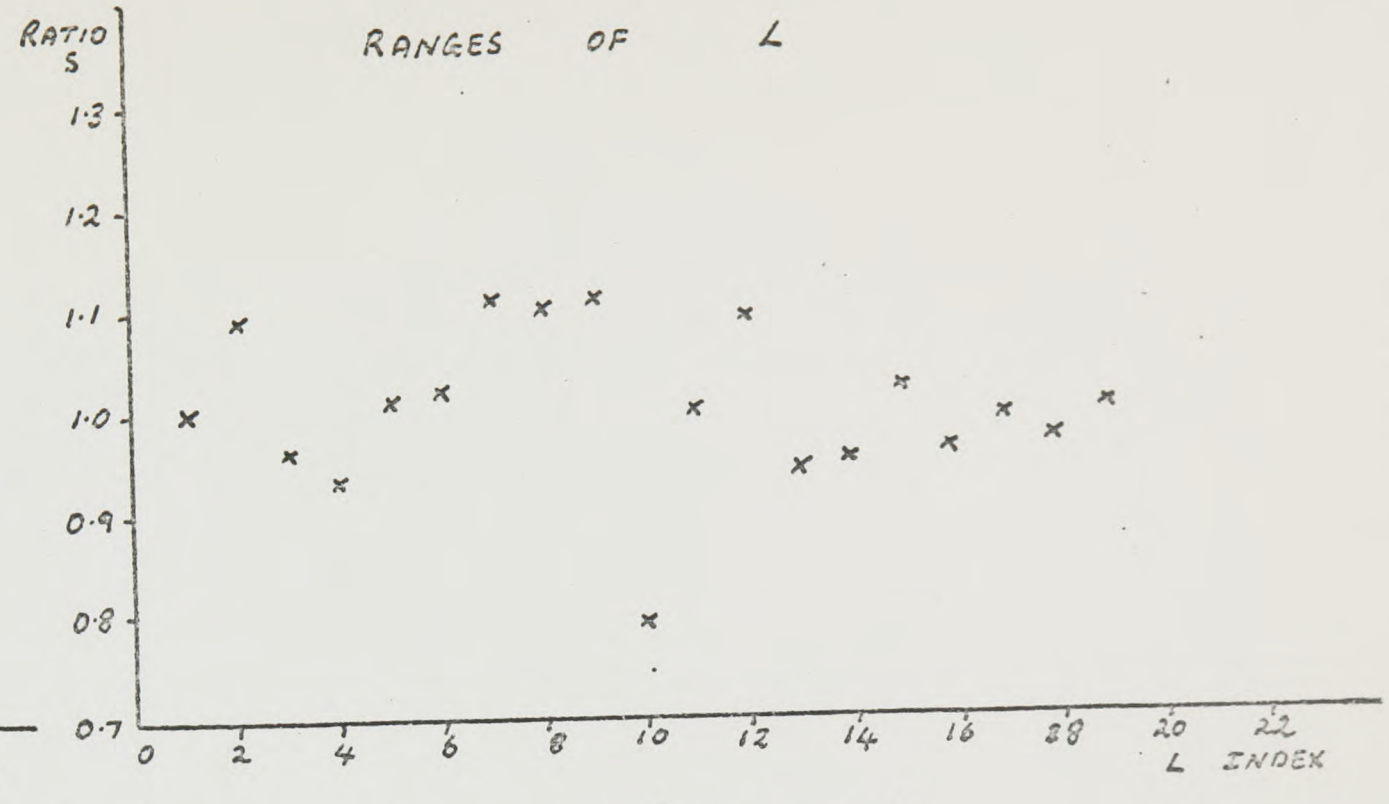
	No. of refl. pairs	S	R
Centric data	156	0.9846	17.96%
Acentric data	725	1.0014	16.75%
Overall	881	0.9983	16.97%

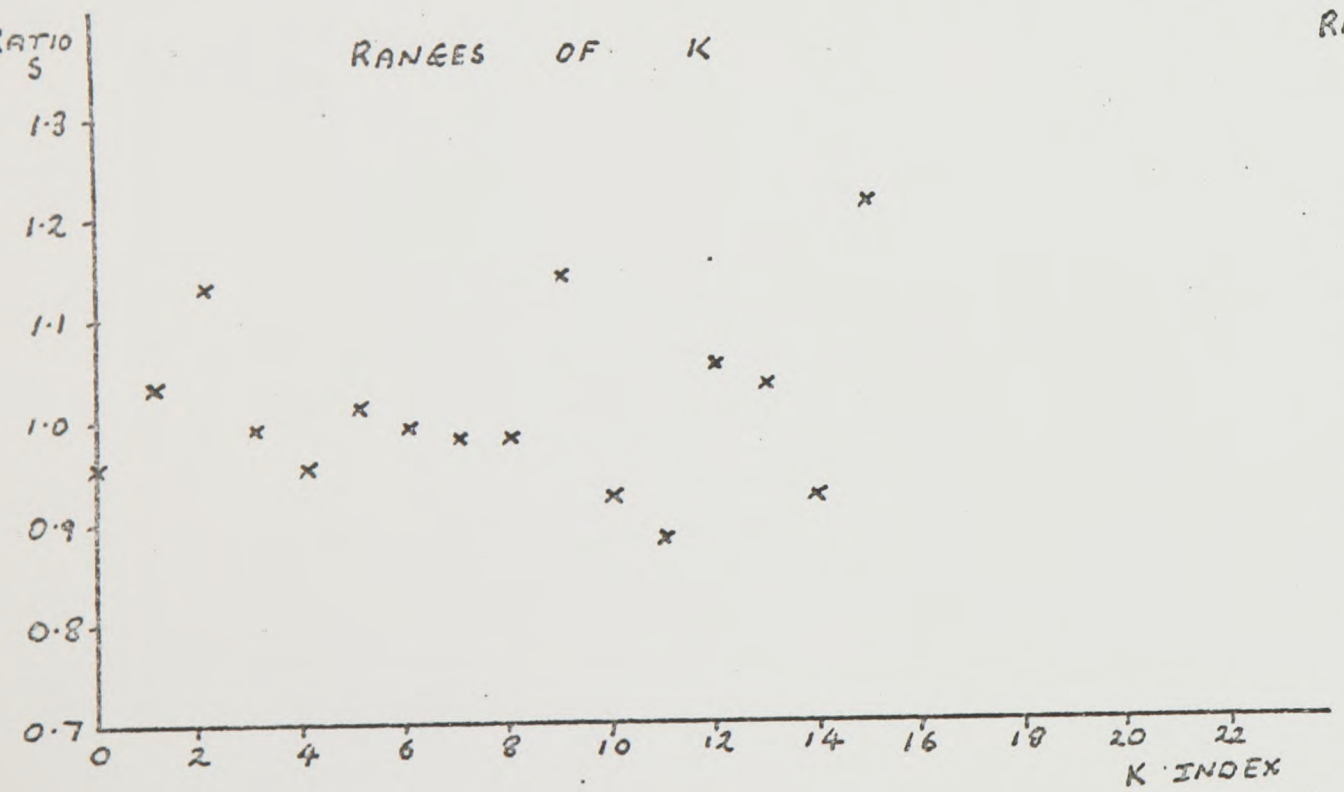
Crystal 212

For this crystal a source collimator of 1.4 mm. and detector collimator of 3.5 mm. were used, and the reflections scanned using 40 steps of 0.02^{o} in the ω axis counting for 2 seconds per step.

The radiation damage as estimated on the standard reflections was 5.4%, the gradient of the linear correction being 3.12×10^{-5}. This correction was shown to be adequate by comparison of the intensities of 88 reflections measured at the beginning and







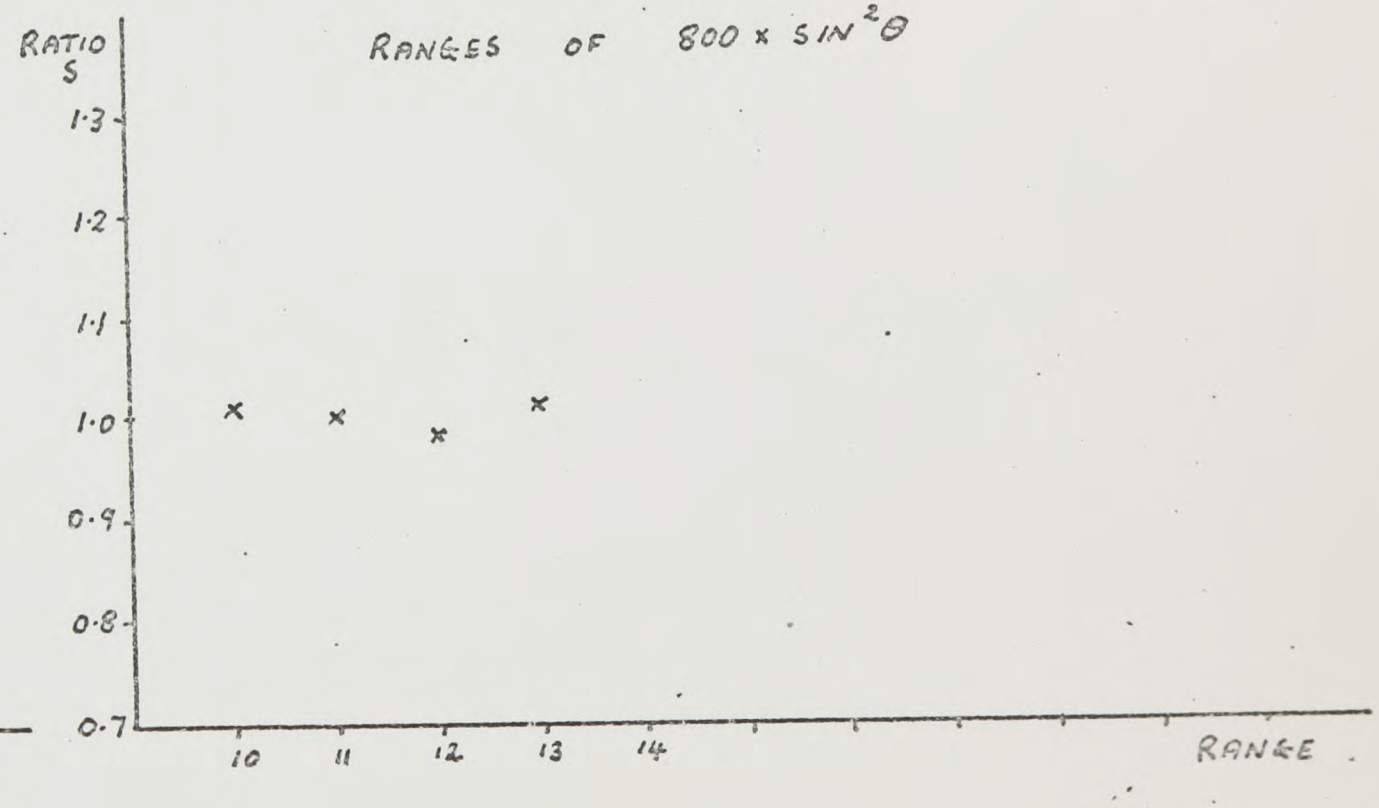


FIGURE 3.50
The agreement between equivalent reflections for crystal 212

end of the data collection.

The intensities of the (hkl̄) reflections were multiplied by a scale factor which varied with $\sin^2\theta$ according to the equation:

$$\text{Scale} = 1.1465 - 0.0140 \times (800 \times \sin^2\theta).$$

After scaling the overall agreement between equivalent reflections was:

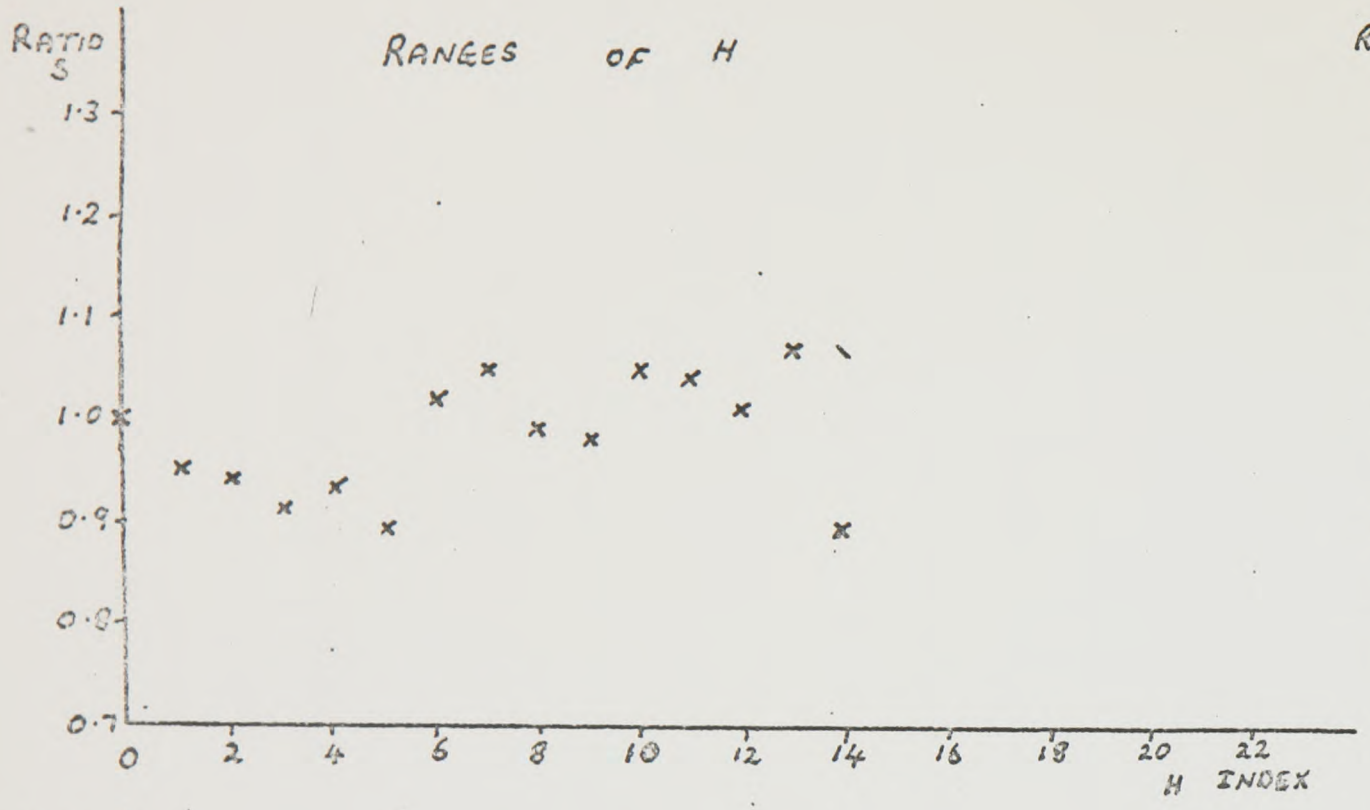
	No. of refl. pairs	S	R
Centric data	98	0.9765	21.18%
Acentric data	495	1.0026	26.19%
Overall	593	0.9982	25.36%

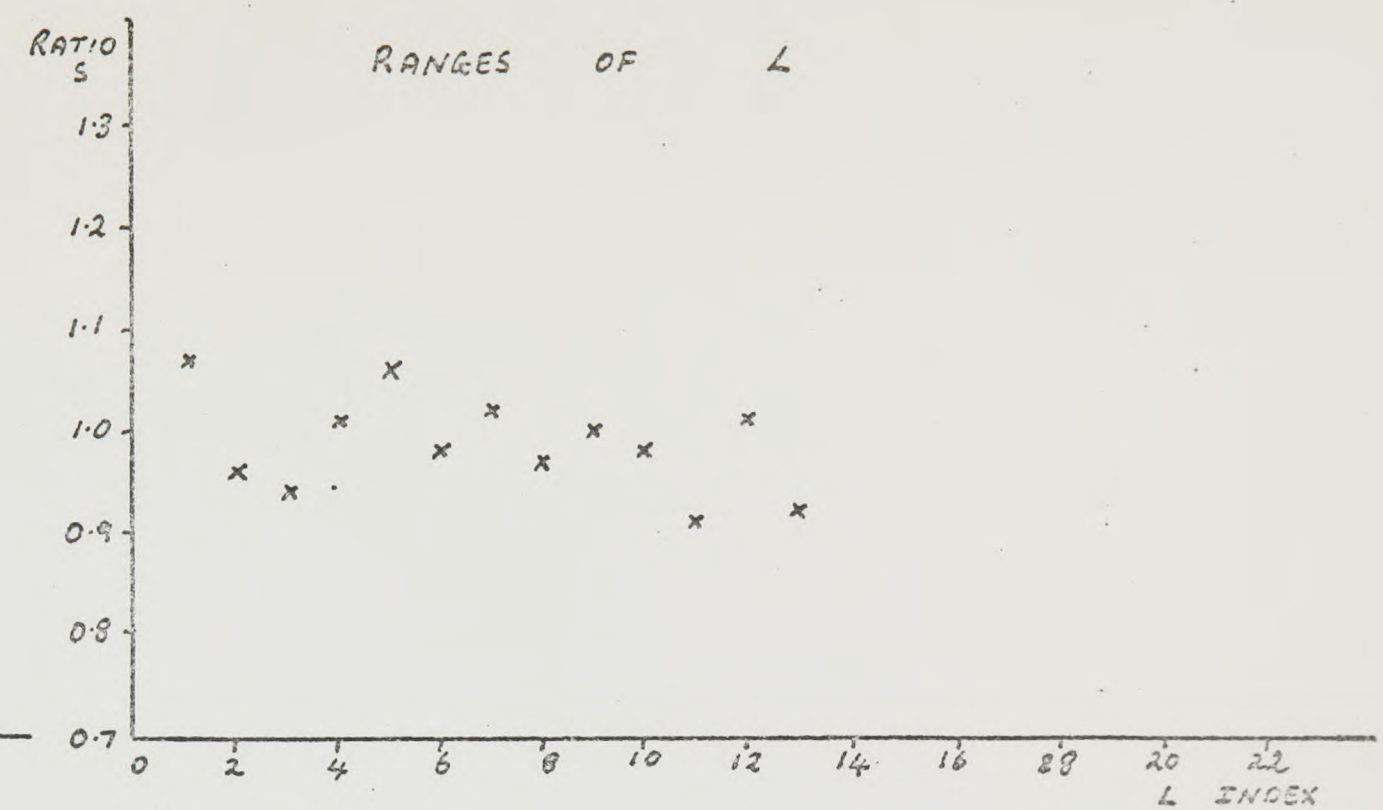
The plots of S are shown in Figure 3.50.

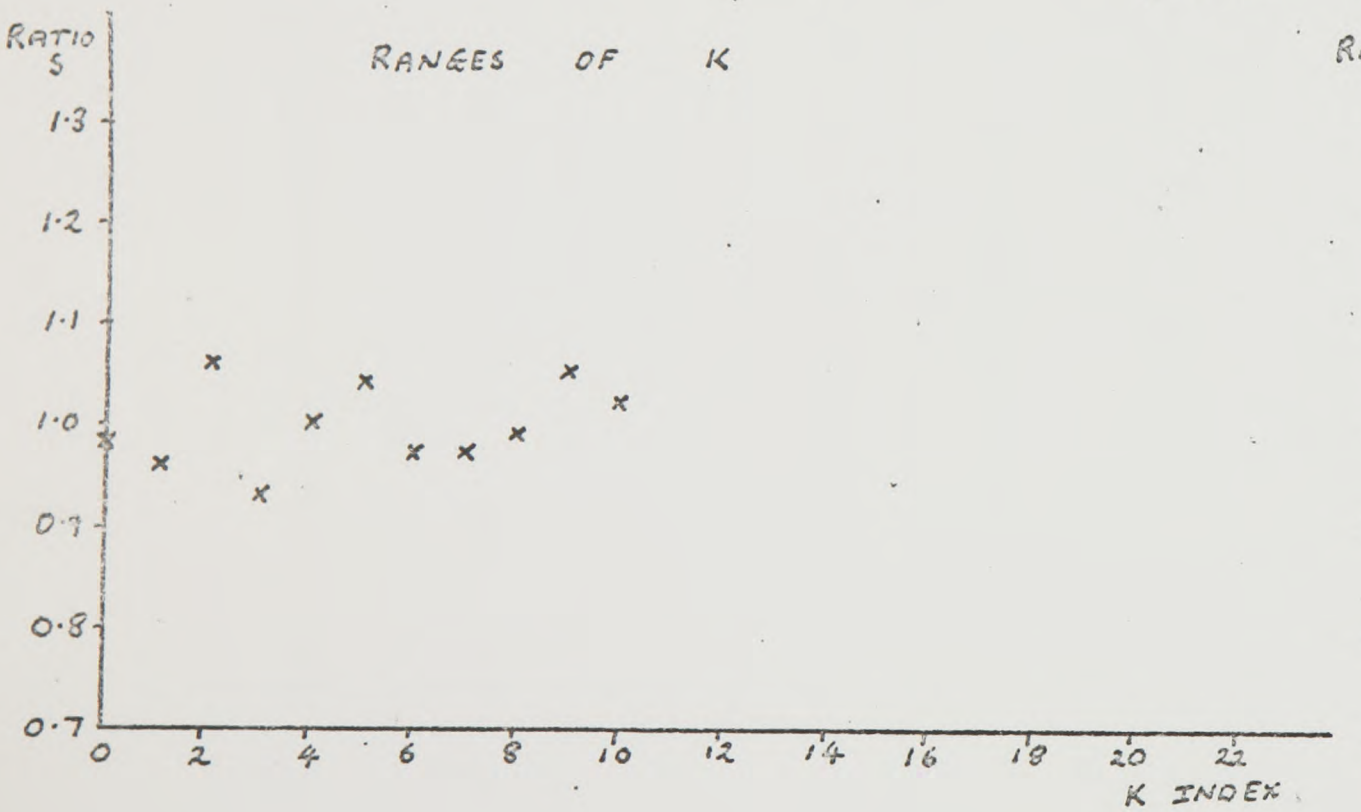
Crystal 213

A 1.4 mm. source collimator and 3.5 mm. detector collimator were used for this crystal. The reflections were measured in 38 steps of 0.03° on the ω/axis counting for 3 seconds per step.

The peak profile of one standard reflection, the (008) measured at $\phi = 0^\circ$, was found to broaden during the data collection. However, there was no noticeable effect on other reflections and so the data collection was continued. The radiation damage estimated on the remaining two standard reflections was 16%; a linear correction with a gradient of 8.6×10^{-5} was applied. This correction was found to be too high when a comparison of 95 reflections measured at the beginning and end of the data collection was made. A further linear correction varying between 1.0 and 0.9211 was, therefore, applied to the data.







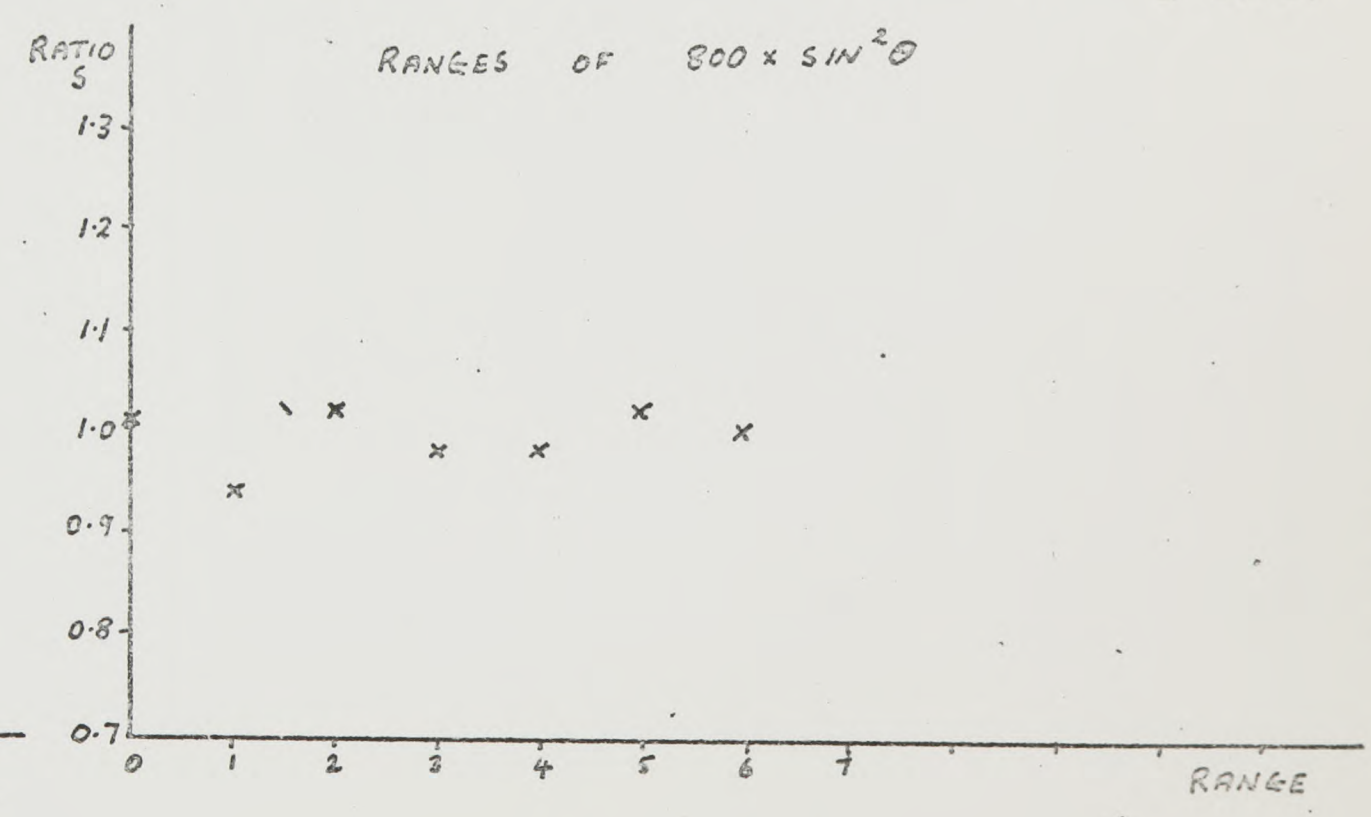


FIGURE 3.51
The agreement between equivalent reflections for crystal 213

A scale factor varying with $\sin^2\theta$ was applied to the intensities of the (hk$\bar{l}$) reflections. This scale factor was:

$$\text{Scale} = 0.9431 + 0.0161 \times (800 \times \sin^2\theta)$$

The plots of S after scaling are shown in Figure 3.51, while the overall agreement between equivalent reflections was:

	No. of refl. pairs	S	R
Centric data	174	0.9701	17.51%
Acentric data	507	1.0009	25.25%
Overall	681	0.9925	23.16%

Scaling crystals together

The three sets of data were scaled on to the set from crystal 211. The numbers of overlapping reflections between the sets of data were:

211/212	120
211/213	208

After 8 cycles of refinement, the scale factors converged to:

Crystal number	Scale factor
211	1.0
212	2.553
213	5.891

The merged set of data comprised 4375 independent reflections with a merging R factor of 12.89%

Derivative to Native Scaling.

The derivative data were scaled on to the native set by application of a scale factor, which varied with $4\sin^2\theta/\lambda^2$, to the intensities of the derivative reflections. This scale

FIGURE 3.52

The plots of $\Sigma F_p^2 / \Sigma F_{PH}^2$ for the uranyl acetate derivative.

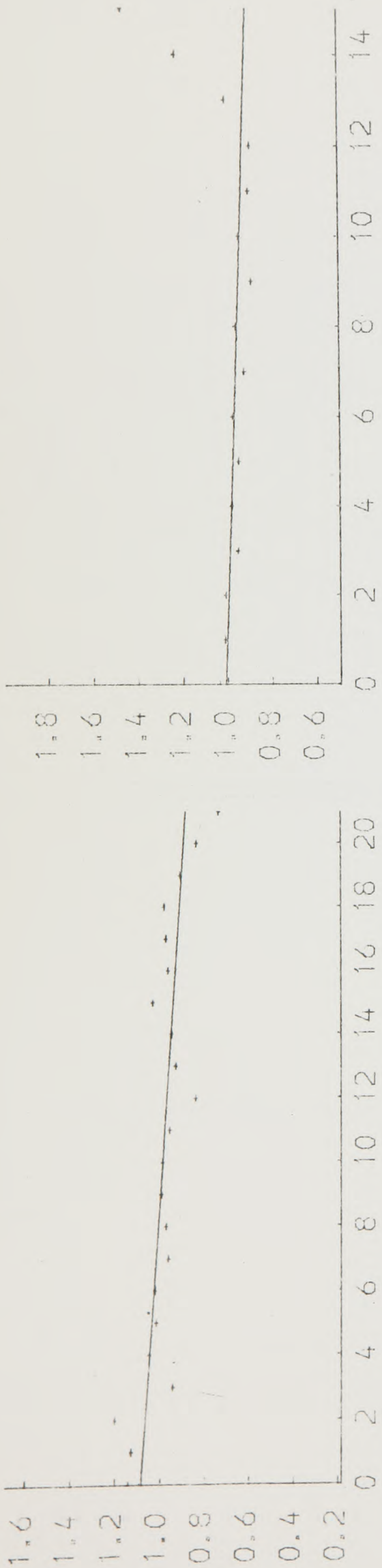
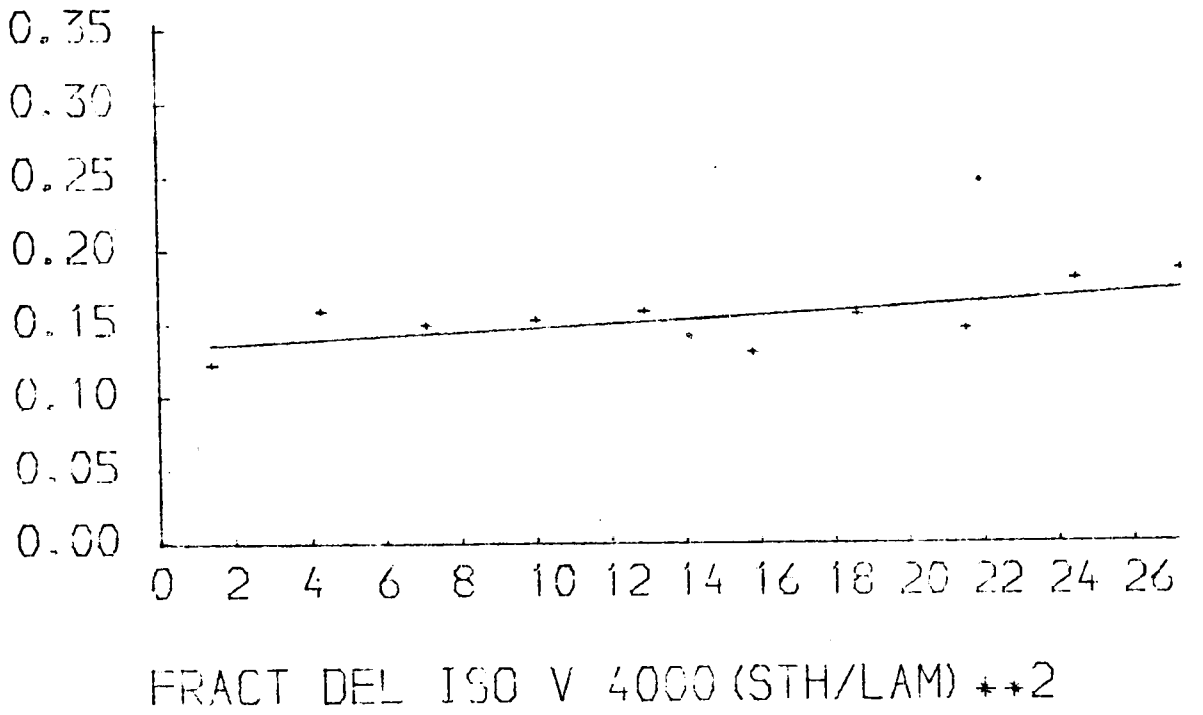
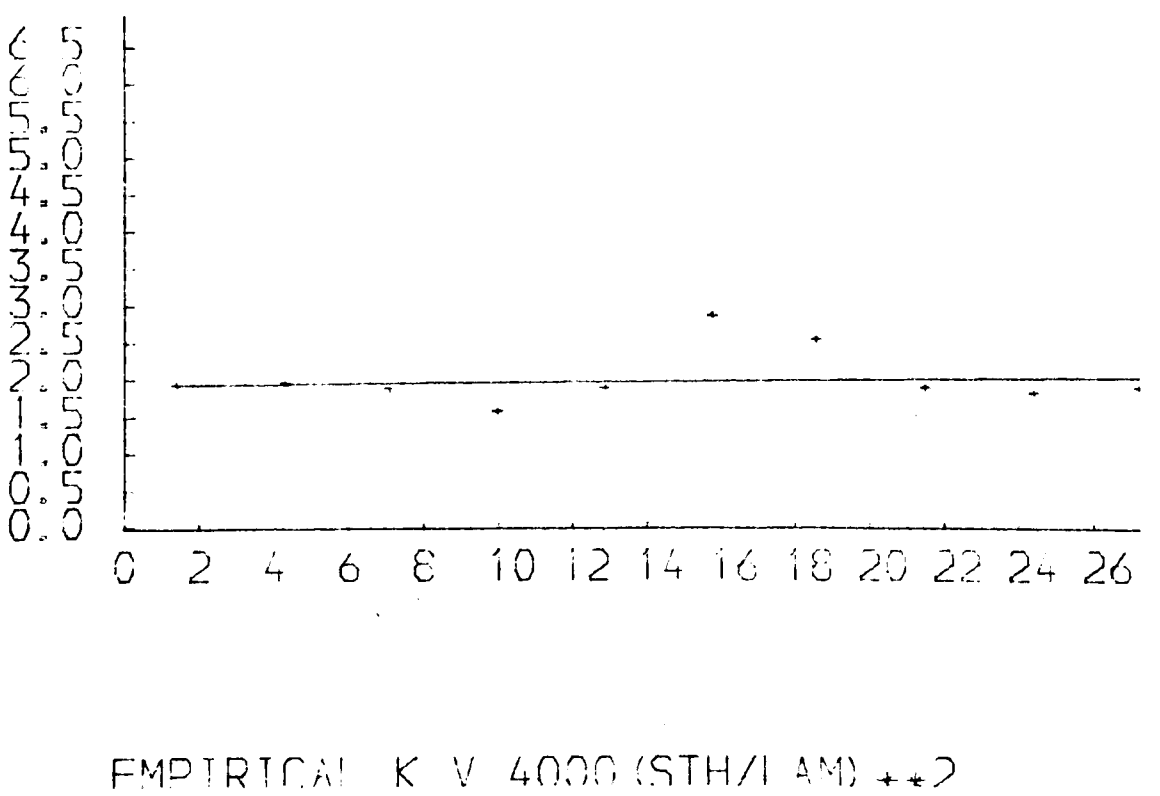


FIGURE 3.53



The plot of the mean fractional isomorphous difference for the uranyl acetate derivative.

FIGURE 3.54



The plot of the empirical k value for the uranyl acetate derivative.

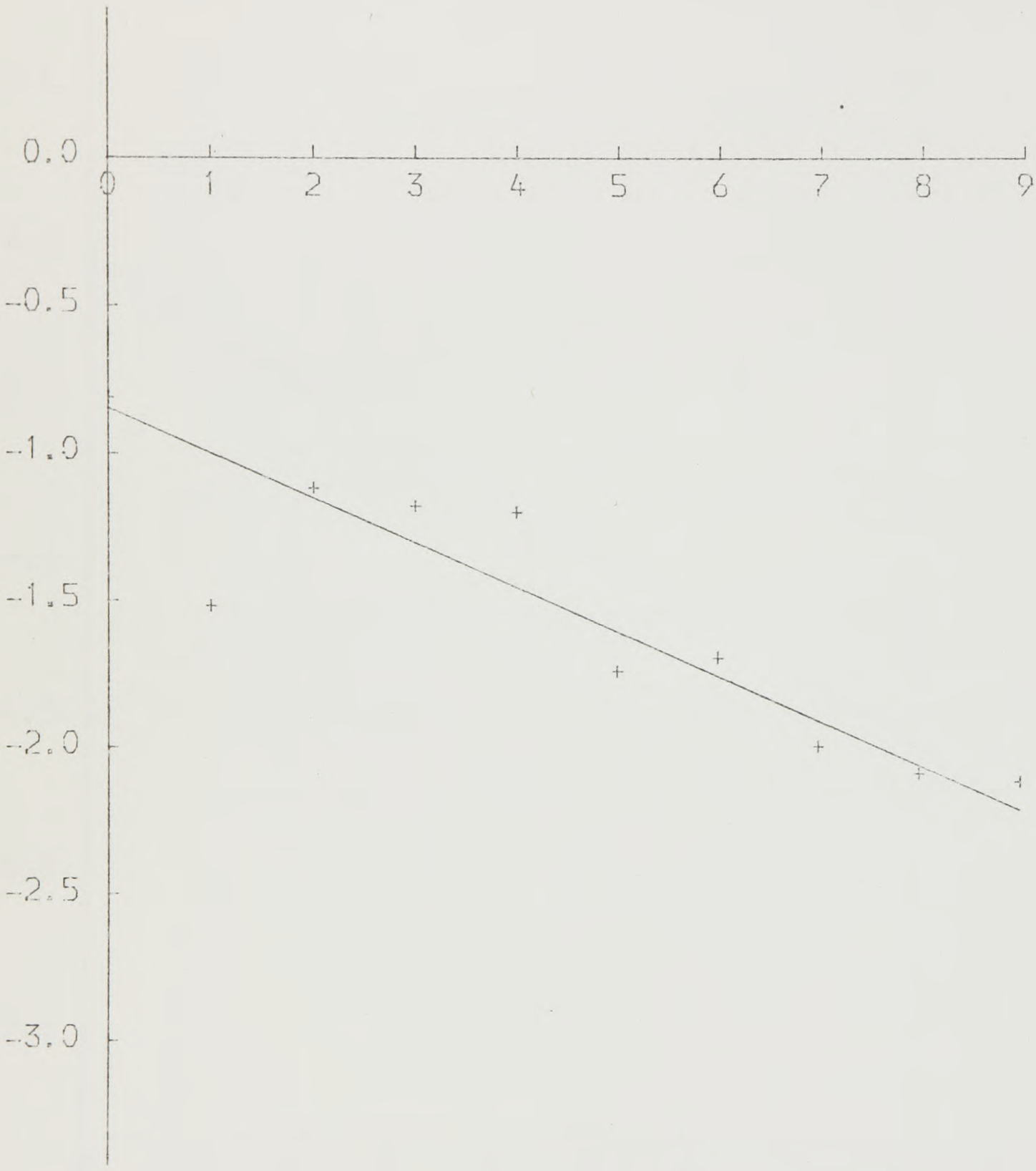
FIGURE 3.55



UO2AC OV DER WILSON PLOT

The Wilson plot for the uranyl acetate derivative.

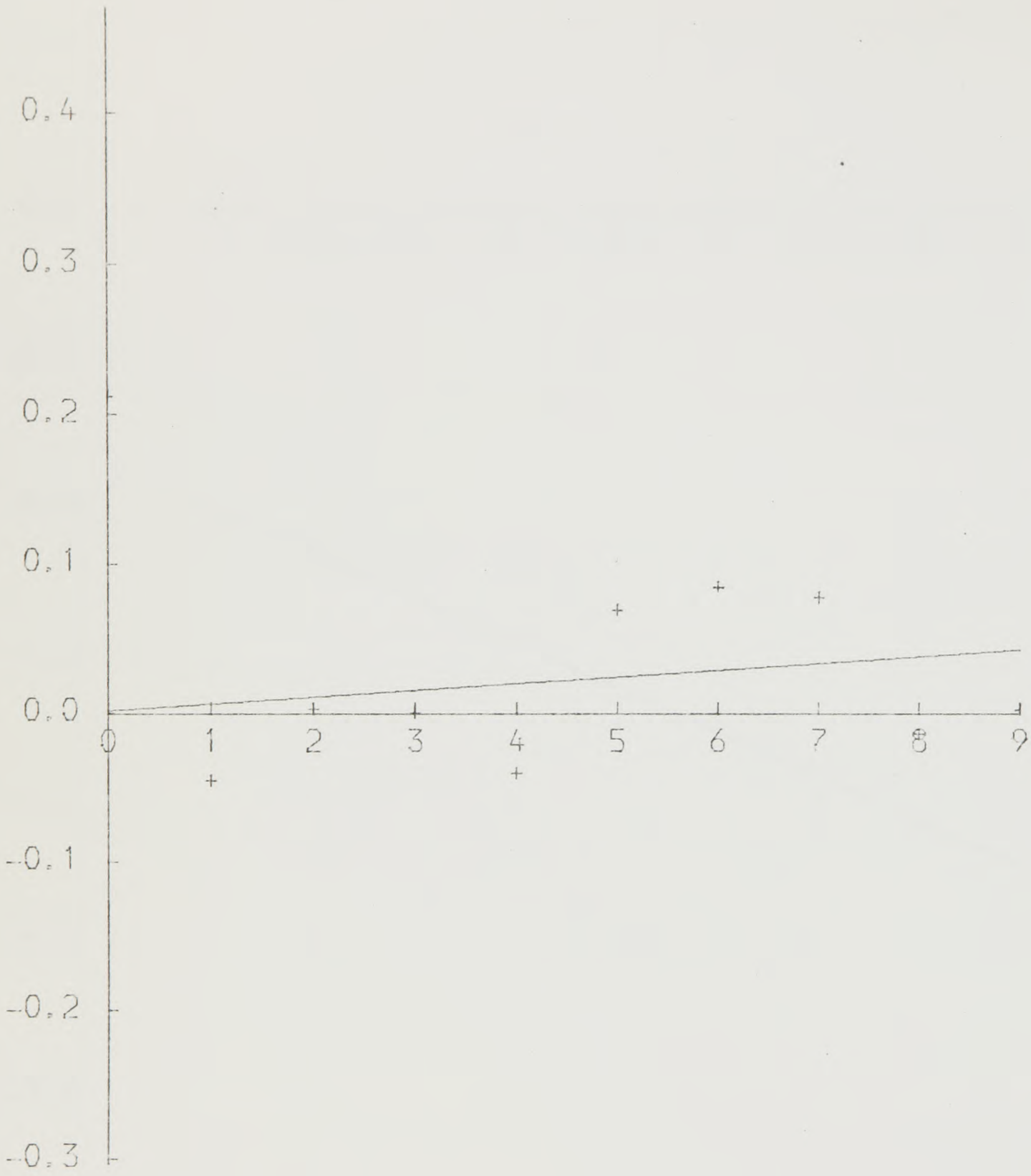
FIGURE 3.56



UO2AC OV H A WILSON PLOT

The Heavy Atom Wilson plot for the uranyl acetate derivative.

FIGURE 3.57



UO2AC OV COM WILSON PLOT

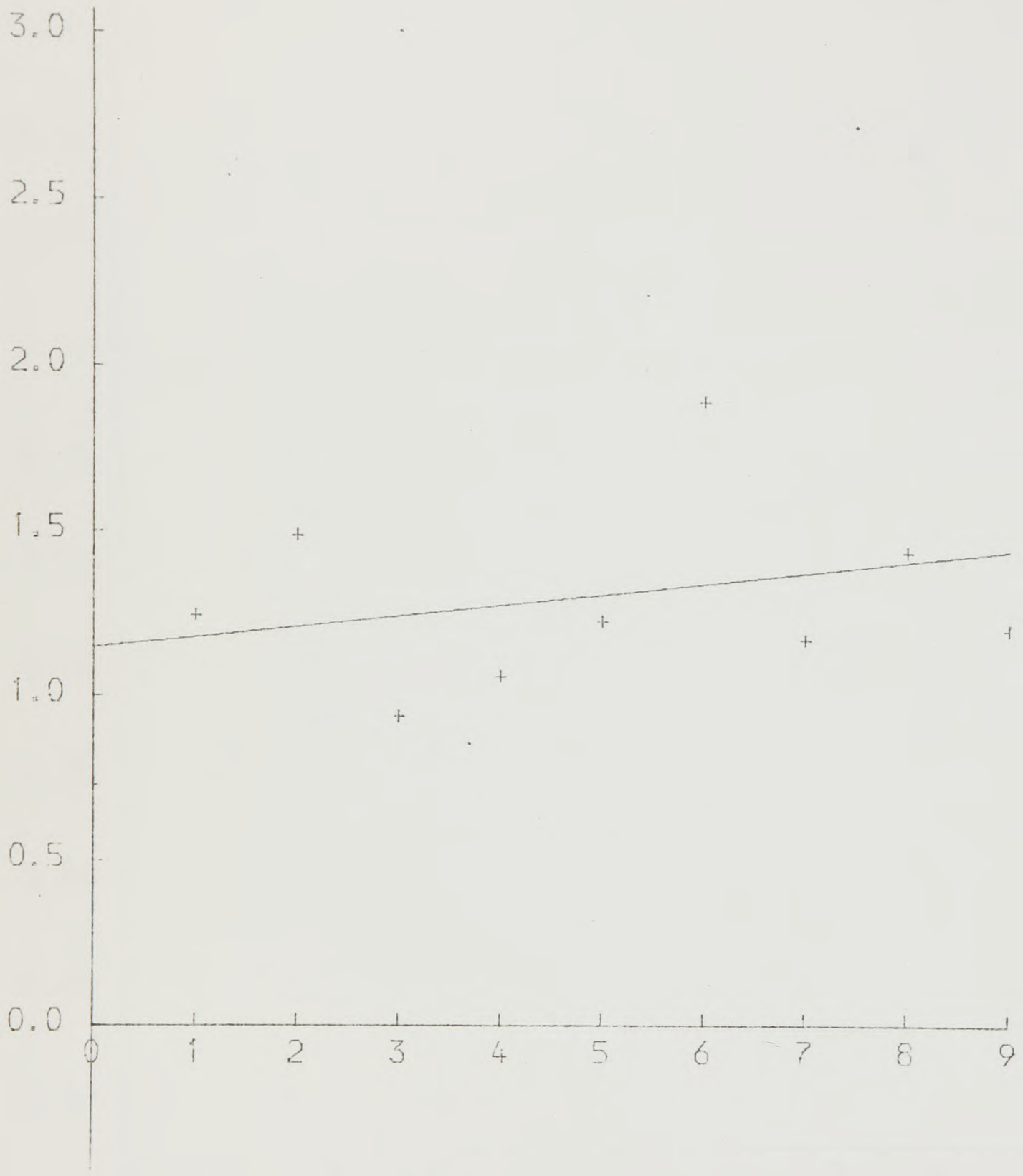
The Comparative Wilson plot for the uranyl acetate derivative.

FIGURE 3.58



The Crick-Magdoff plot for the uranyl acetate derivative.

FIGURE 3.59



UO2AC RATIO CRICK PLOT

The Crick-Magdoff ratio plot for the uranyl acetate derivative.

TABLE 3.13

Uranium acetate derivative crystals - Theoretical and observed fractional change in intensity.

Mean $\sin^2\theta/\lambda^2$	Centric terms		Acentric terms	
	Theoretical	Observed	Theoretical	Observed
0	0.31102	0.35813	0.21992	0.49115
0.00077	0.31260	0.34992	0.22104	0.28060
0.00154	0.31418	0.44518	0.22216	0.29862
0.00231	0.31577	0.29523	0.22328	0.31405
0.00309	0.31736	0.41143	0.22441	0.38680
0.00386	0.31895	0.35125	0.22553	0.28525
0.00463	0.32055	0.66148	0.22666	0.34866
0.00540	0.32216	0.48657	0.22780	0.41445
0.00617	0.32376	0.62357	0.22893	0.43293
0.00694	0.32537	0.47756	0.23007	0.39704

factor was of the form:

$$\text{Scale} = 1.122 - 12.678 \times (4 \sin^2\theta/\lambda^2)$$

Plots of the ratio $\sum F_p^2/\sum F_{pH}^2$ after scaling are shown in Figure 3.52; the overall ratio was 0.9794. There were 2566 pairs of native and derivative reflections with a mean fractional isomorphous difference of 15.5%, the mean isomorphous difference being 31.2. Figure 3.53 shows the variation of the mean fractional isomorphous difference with $\sin^2\theta/\lambda^2$.

The empirical k values were very low for this derivative, the mean k being 1.98, and varied with $\sin^2\theta/\lambda^2$ as shown in Figure 3.54. In view of the very low empirical k values no F_{HLE} coefficients were computed.

The standard, heavy atom, and comparative Wilson plots are shown in Figures 3.55, 3.56, 3.57. The temperature factor from the heavy atom plot was 98.3 and the absolute scale factor was 2.3.

Figure 3.58 shows the Crick-Magdoff plot, and Figure 3.59 the centric to acentric plot. The observed fractional change in intensity is compared with the observed value for the centric and acentric data in Table 3.13. The theoretical values were computed assuming one uranium binding site per monomer. These figures seem to be compatible with at least one uranium binding site.

Difference Patterson and Difference Fourier Syntheses

A three-dimensional difference Patterson synthesis was computed, but no solution in terms of uranium binding sites could be found.

Difference fourier maps using the native phases

TABLE 3.14

PIPSYL DERIVATIVE CRYSTALS - PHYSICAL PARAMETERS

Crystal number	Crystal size (mm) a x b x c	Shell	Unit cell dimensions from diffractometer.
272	0.4 x 0.3 x 0.9	6.9Å - 8.7Å	a= b= 128.76Å c=116.29Å
273	1.0 x 0.4 x 0.9	6.0Å - 6.9Å	a= b= 127.99Å c= 116.29Å
274	1.0 x 0.4 x 0.9	8.7Å - ∞	a= b= 127.99Å c=116.29Å

TABLE 3.15

PIPSYL DERIVATIVE CRYSTALS - PRIMARY PROCESSINGS STATISTICS

Crystal Number	Total no. of Reflections Processed	No. of SD failures	No. of back-ground Failures	Maximum Absorption Correction
272	1847	192	188	1.531
273	1979	196	243	1.614
274	1908	73	148	1.665

estimated from the platinum derivative were computed for the hk0 and h0l zones as well as the three dimensional data. As before the terms in these fouriers were weighted by the figures of merit of the phase angles. No uranium binding sites could be found in these fouriers.

These uranium derivative data were of poorer quality than the earlier sets, due mainly to the quality of the crystals after soaking in the heavy atom solution. Possibly the data were too poorly measured to show the small isomorphous changes accurately.

(e) Pipsyl Derivative Crystals- numbers 272,273,274

These three crystals were all soaked in the same pipsyl solution. The physical parameters and primary data processing statistics are shown in Tables 3.14 and 3.15 respectively.

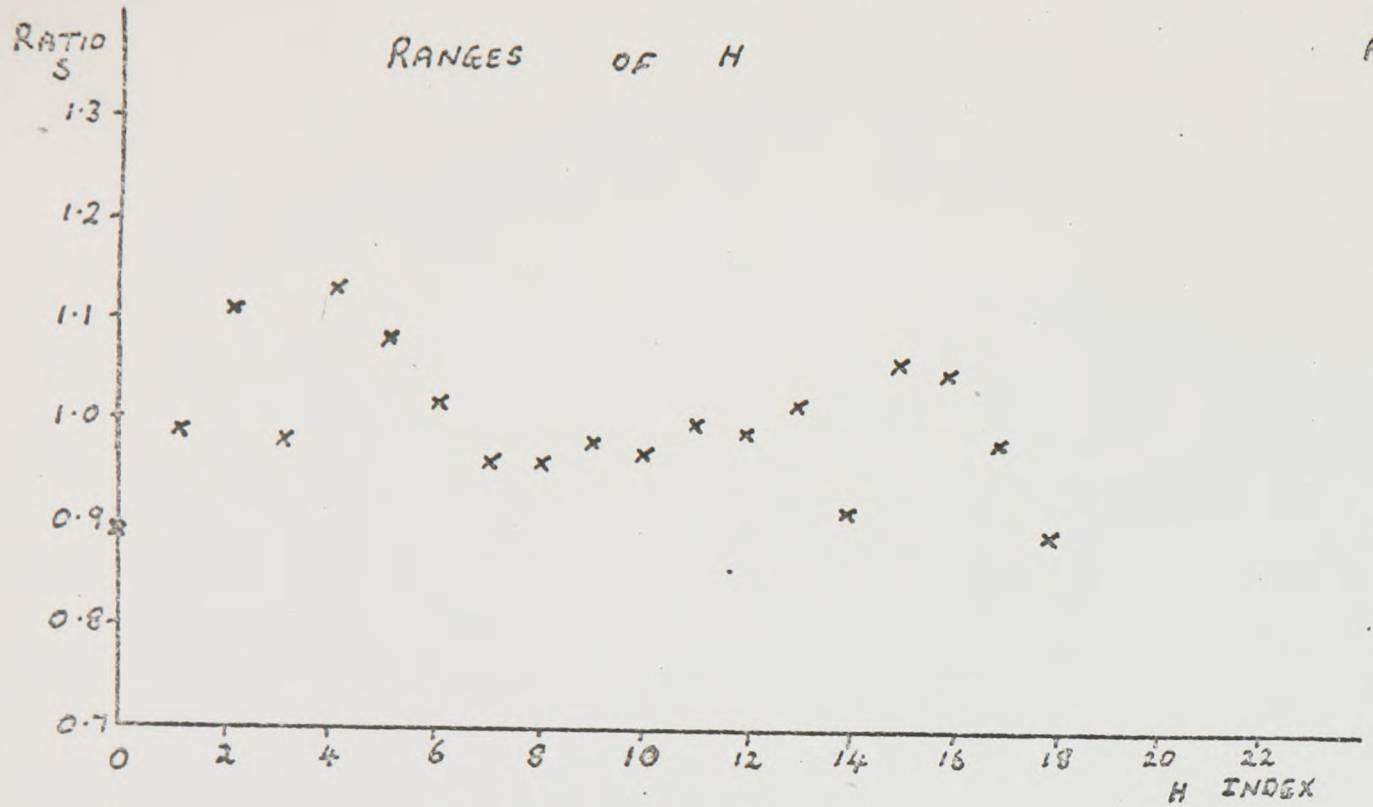
A 1.4 mm source collimator and 3.5 mm. detector collimator were used for each of the crystals, and, in each case, the reflections were scanned using 40 steps of 0.02^{o} on the ω axis, counting for 2 seconds per step.

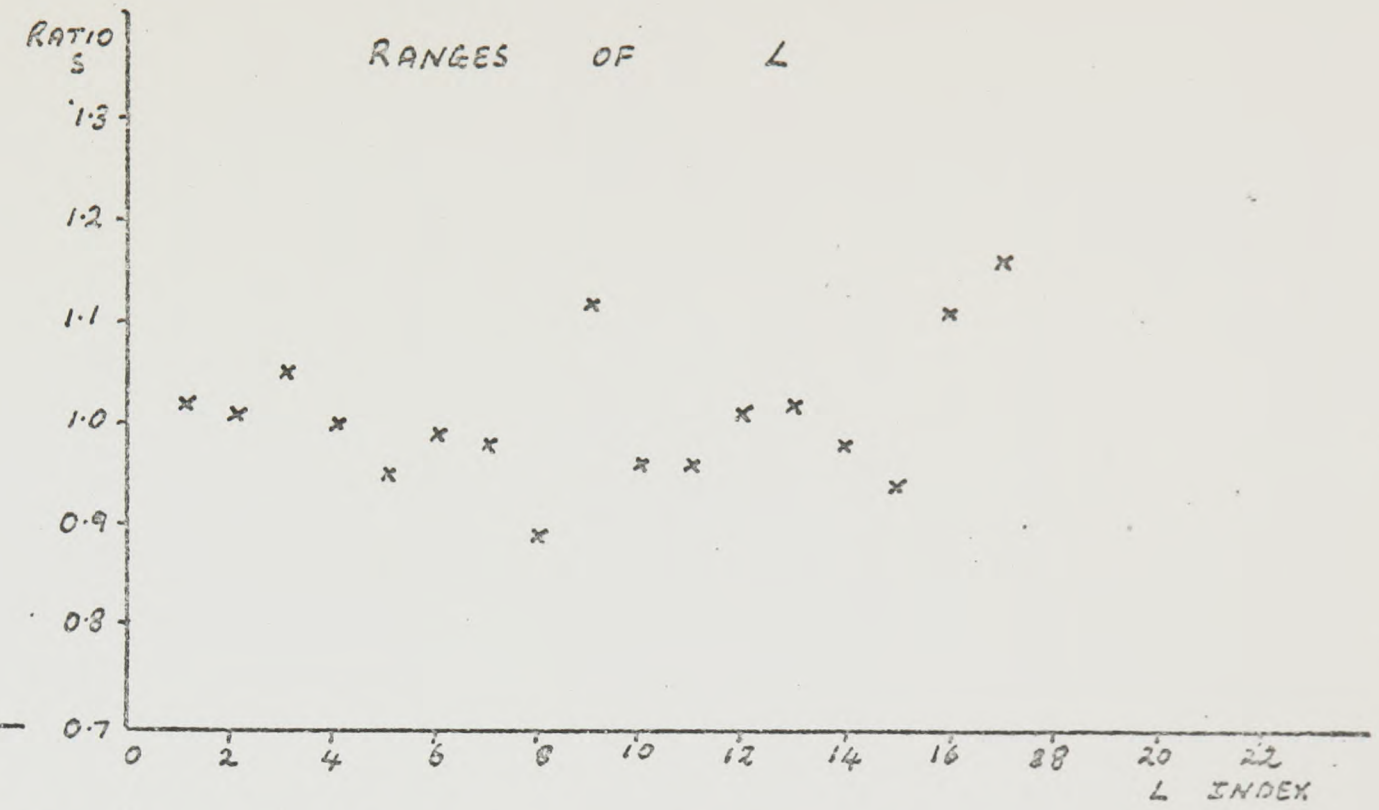
Crystal 272 The radiation damage as estimated from the standard reflections was 12%; a linear correction with a gradient of 6.30×10^{-5} was applied to the data. After comparing 88 reflections measured at the beginning and end of the data collection a further correction varying between 1.00 and 1.0260 was found to be necessary.

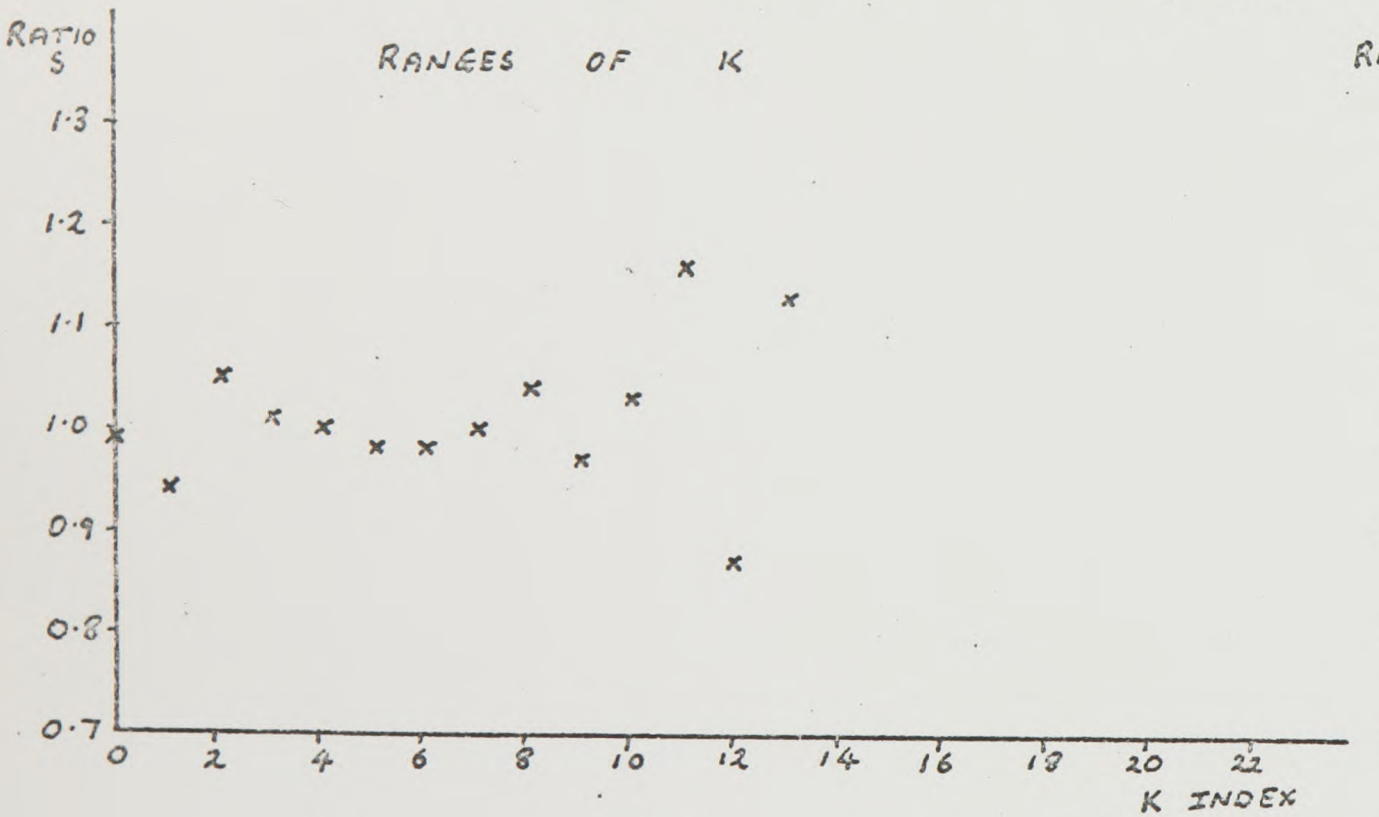
A scale factor varying with $\sin^2\theta$ was applied to the intensities of the $(hk\bar{l})$ reflections- this scale factor was:

$$\text{Scale} = 1.0677 - 0.0130 \times (800 \times \sin^2\theta)$$

After scaling, the overall agreement between the equivalent







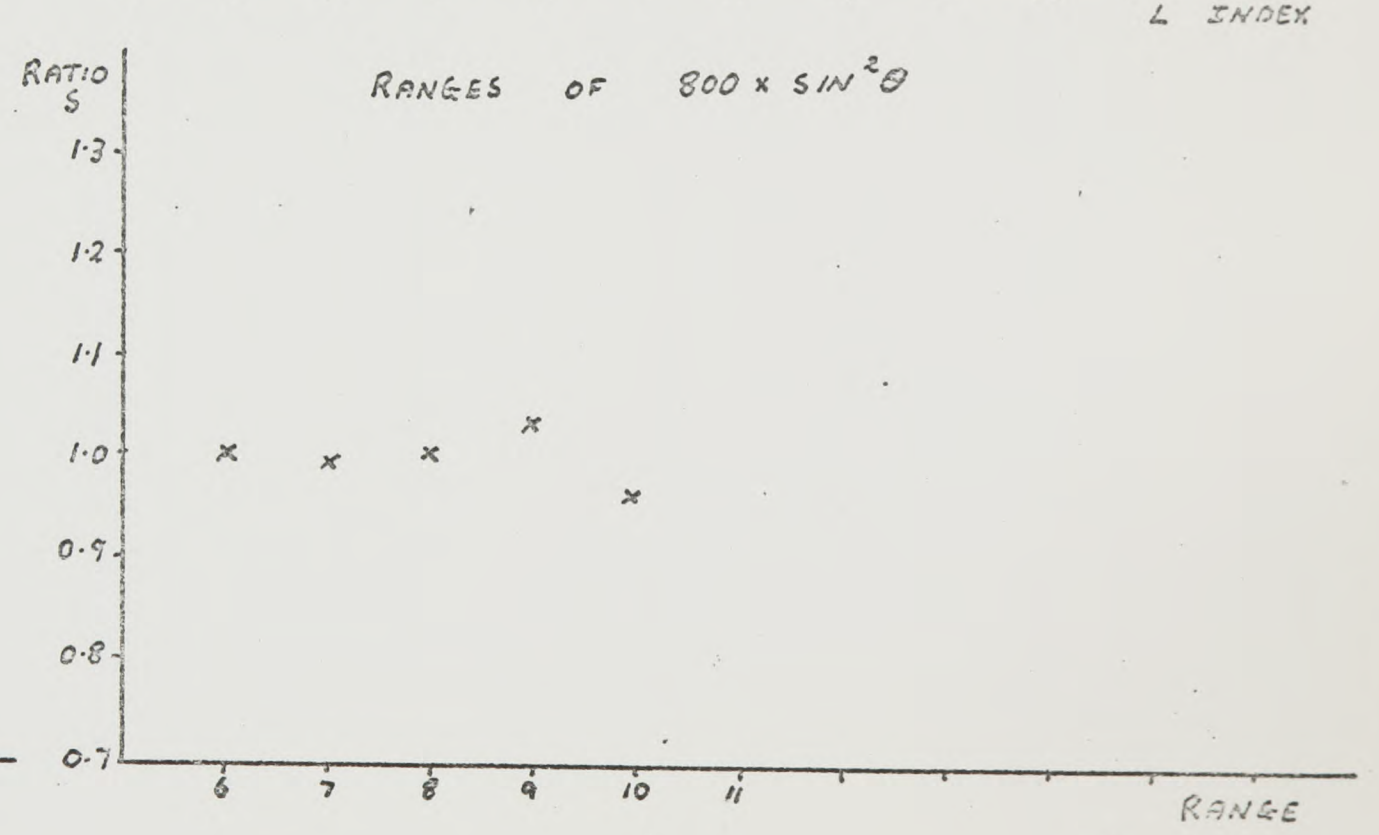
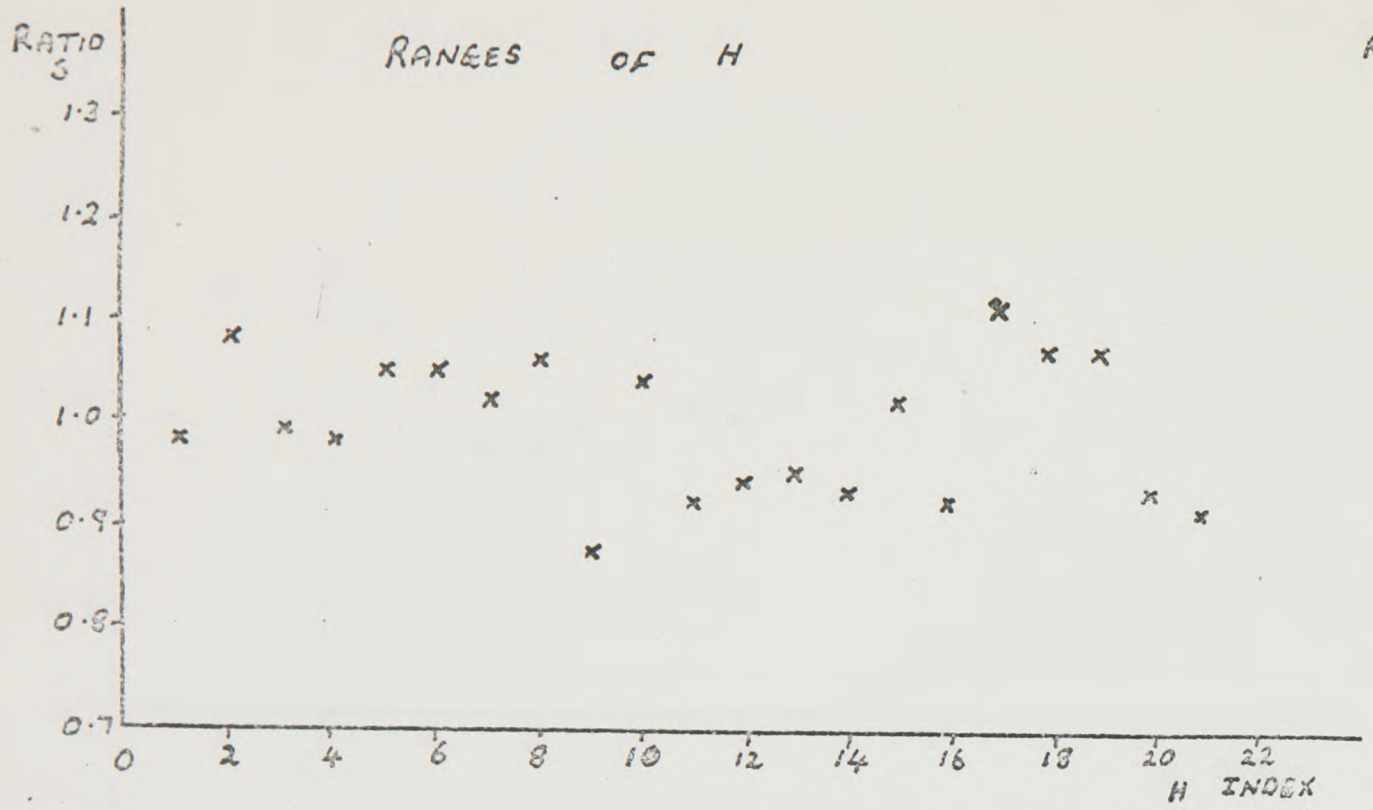
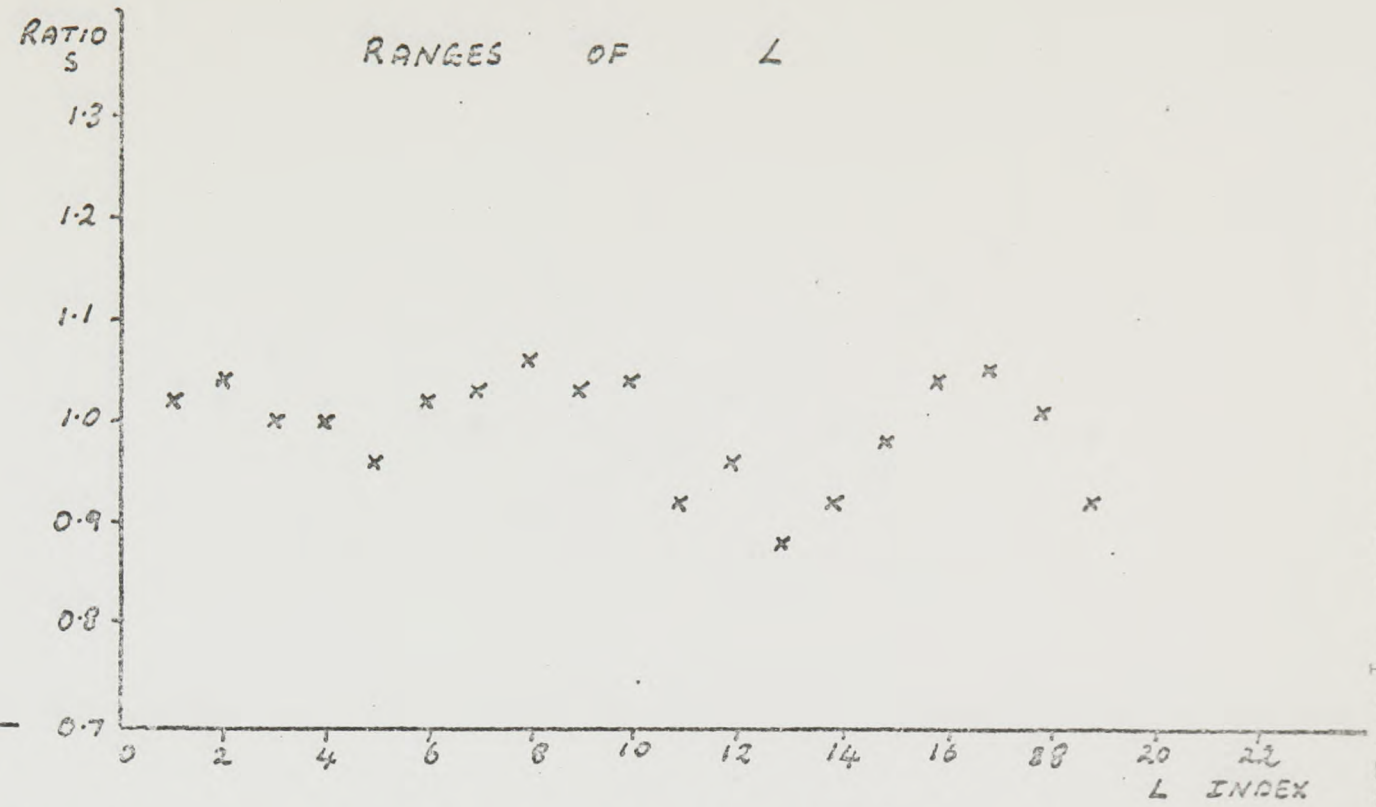
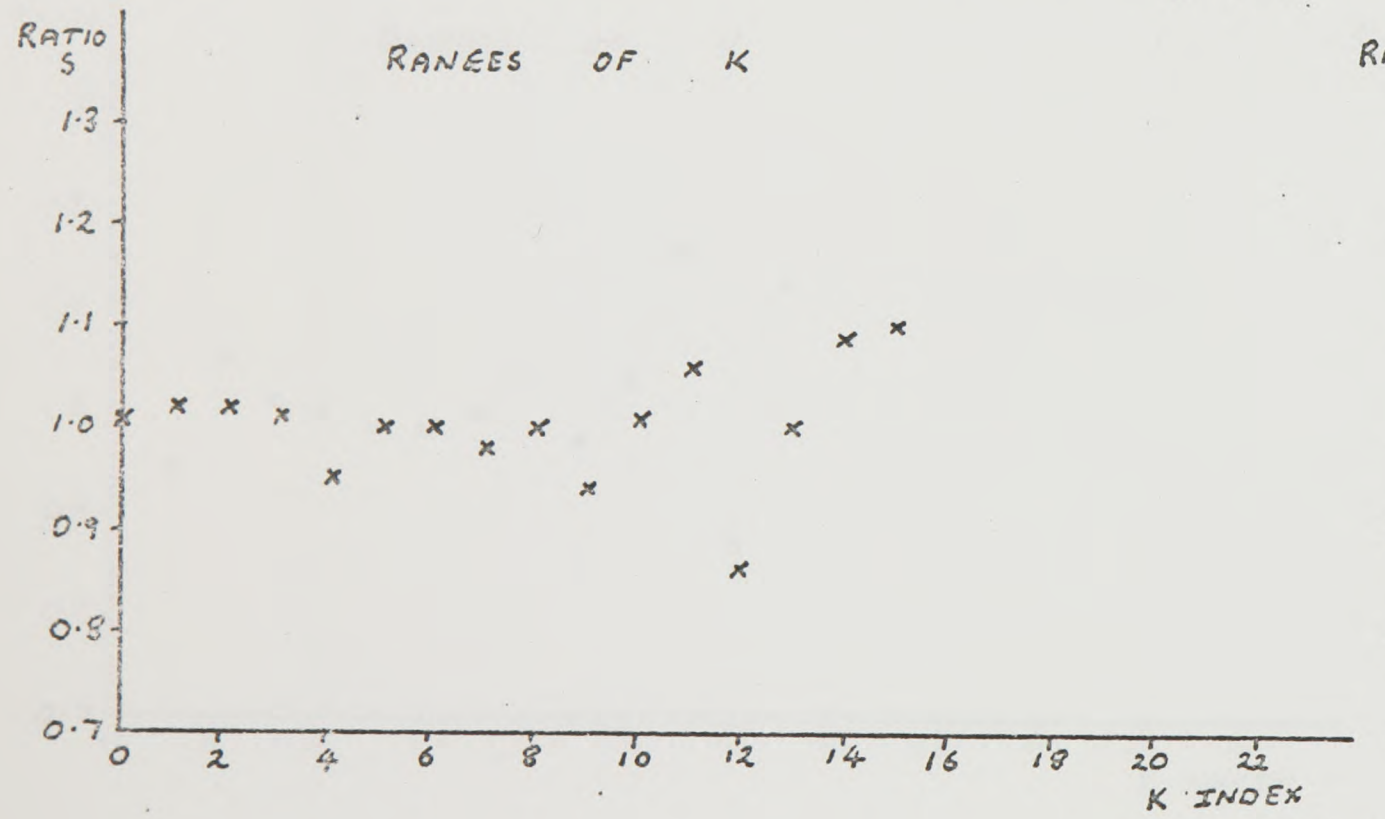


FIGURE 3.60

The agreement between equivalent reflections for crystal 272







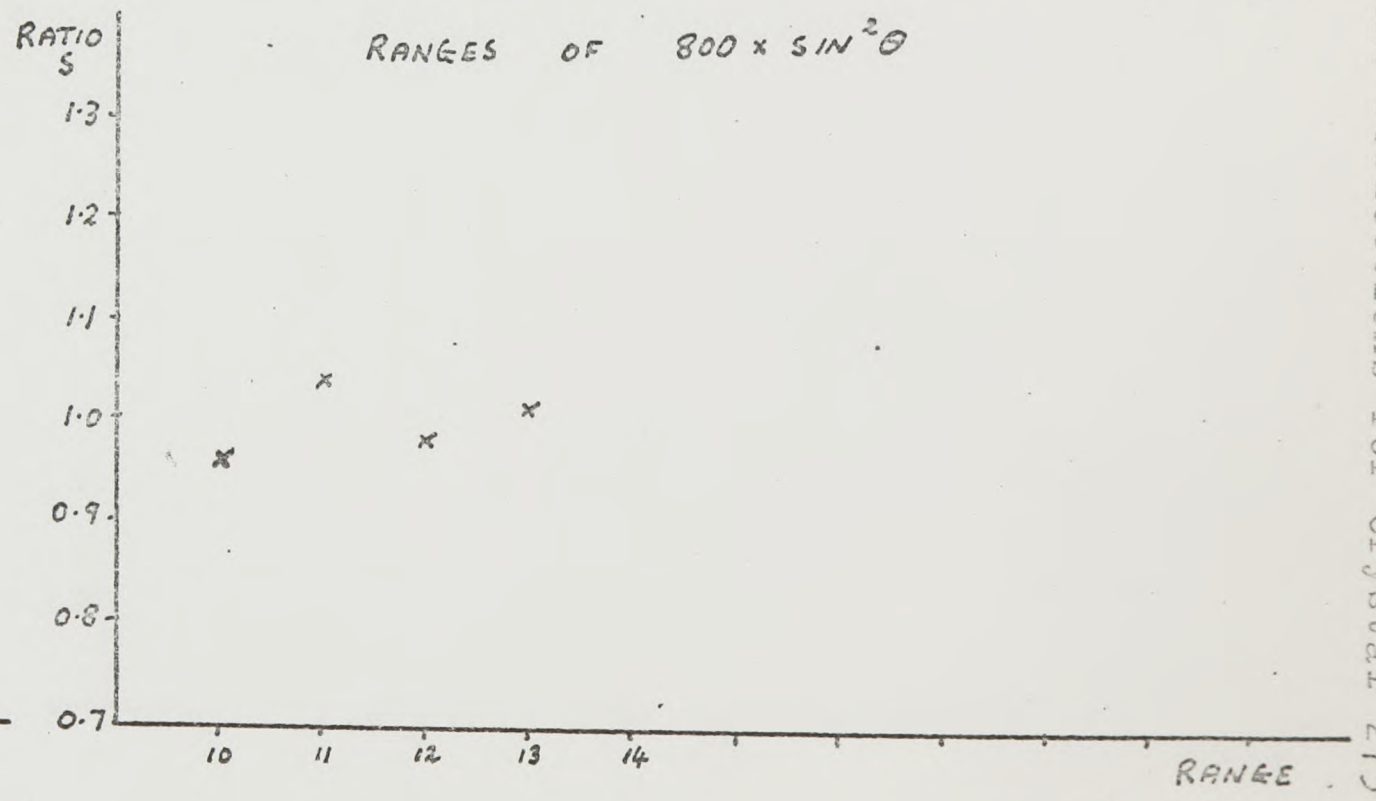


FIGURE 3.61

The agreement between equivalent reflections for crystal 273

reflections was:

	No. of refl. pairs	S	R
Centric data	123	1.0073	23.06%
Acentric data	554	0.9949	25.44%
Overall	677	0.9971	25.00%

The plots of S are shown in Figure 3.60.

Crystal 273

The radiation damage as estimated on the standard reflections was 9%; a linear correction with a slope of 5.40 x 10^{-5} was applied to the data. Comparison of 86 reflections measured at the beginning and end of the data collection indicated that a further linear correction varying between 1.0 and 1.0848 should be applied.

The intensities of the (hk$\bar{l}$) were multiplied by a scale factor which varied with $\sin^2\theta$ according to the relationship:

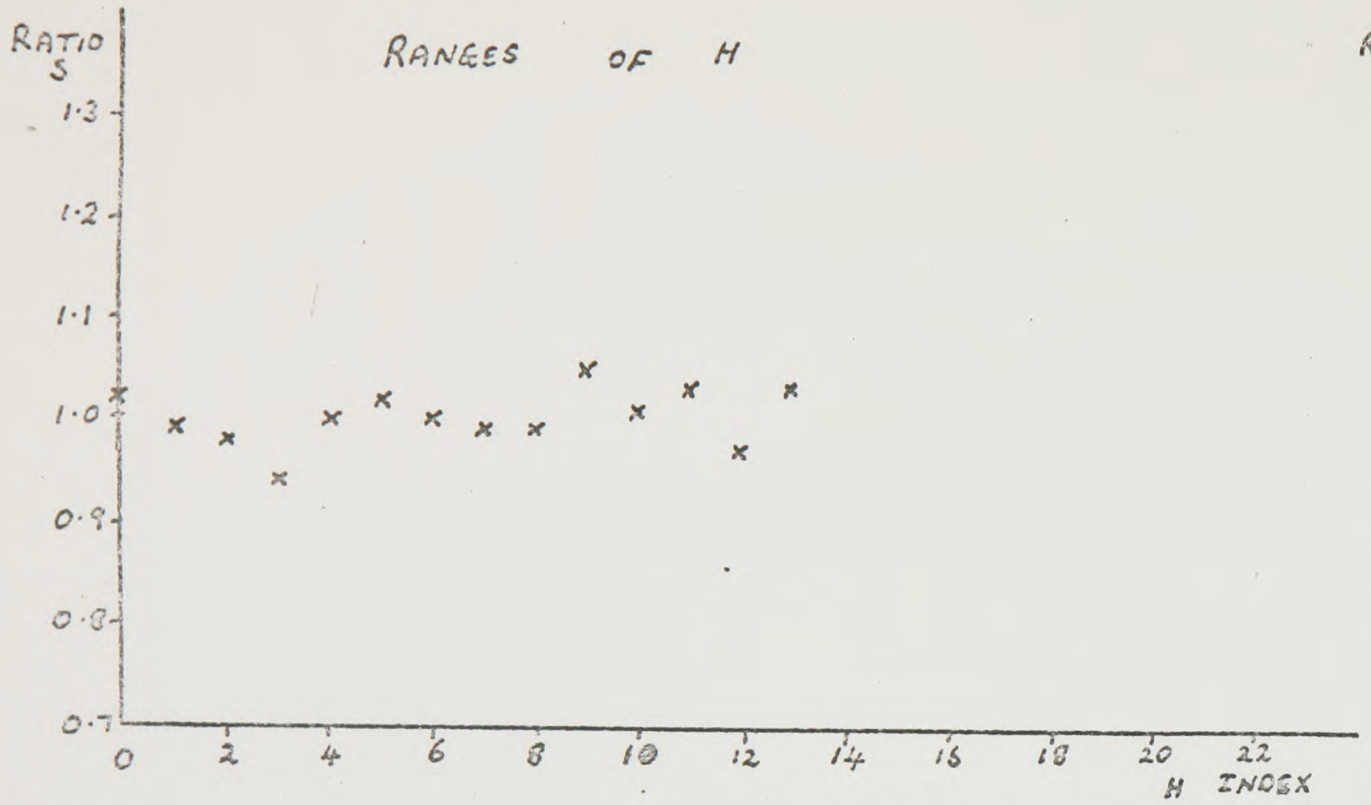
$$\text{Scale} = 0.8123 + 0.0165 \times (800 \times \sin^2\theta)$$

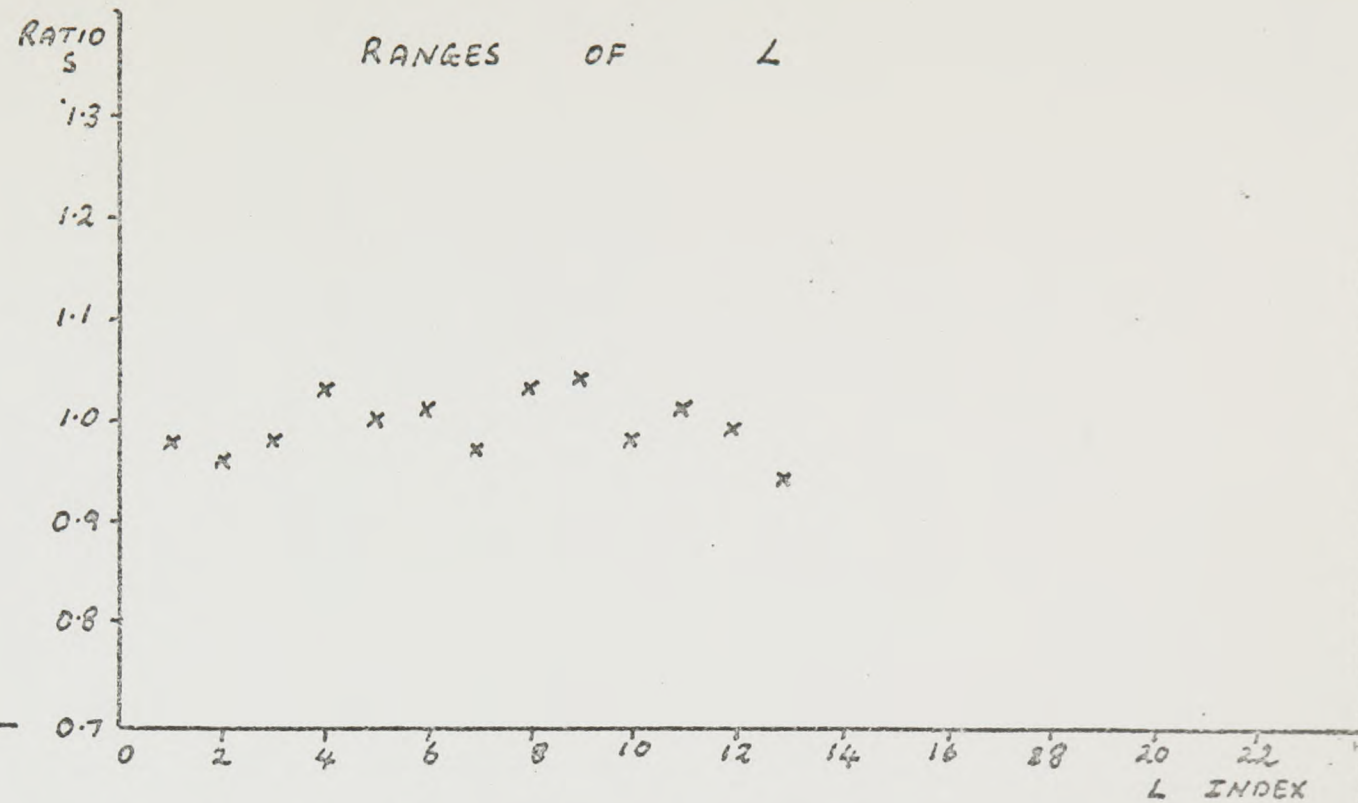
The plots of S after scaling are shown in Figure 3.61, while the overall agreement between equivalent reflections was:

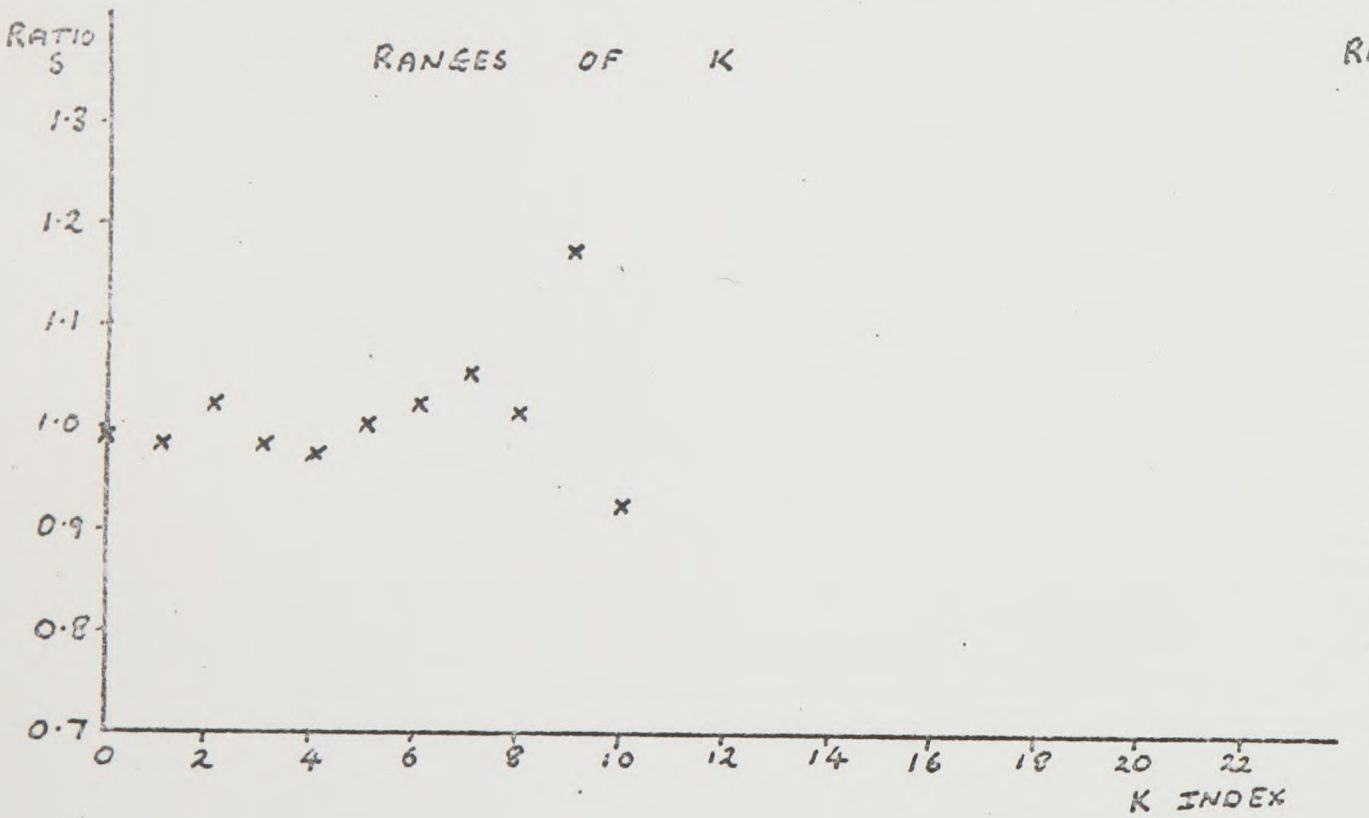
	No. of refl. pairs	S	R
Centric data	98	1.0157	20.58%
Acentric data	566	0.9929	21.26%
Overall	664	0.9964	21.15%

Crystal 274 No other good pipsyl derivative crystals were available, and so crystal 273 was used again for this shell of data. The radiation damage, particularly at low values of $\sin^2\theta/\lambda^2$, had been small in the previous data collection.

During this data collection the radiation damage was ~~estimated from the standard reflections to be 7%; a linear correc~~







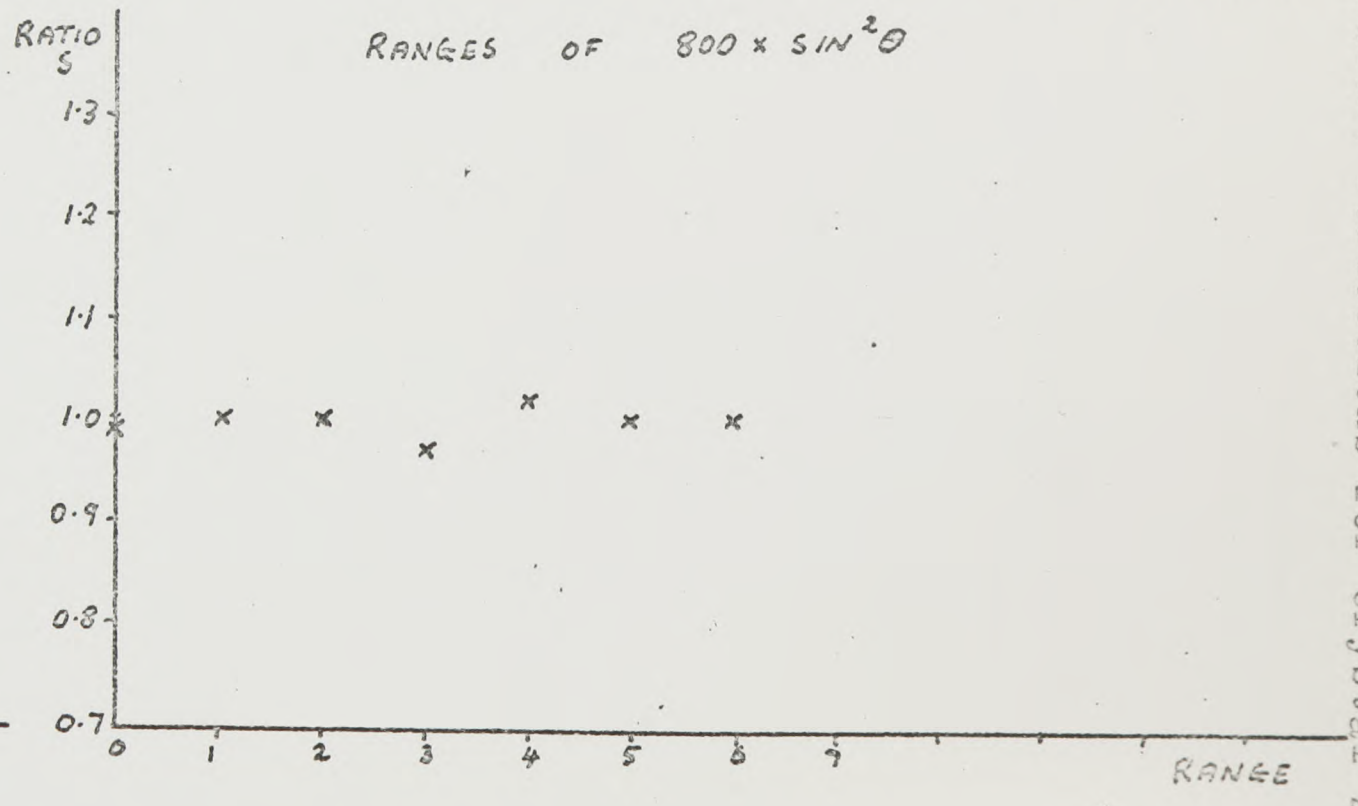


FIGURE 3.62

The agreement between equivalent reflections for crystal 274

estimated from the standard reflections to be 7%; a linear correction with a gradient of 3.90×10^{-5} was applied to the data. By comparison of 98 reflections measured at the beginning and end of the data, this correction was shown to be too high, and a further linear correction varying between 1.0 and 0.986 was applied to the data.

The intensities of the $(hk\bar{l})$ reflections were scaled by the constant factor 0.9925; the overall agreement between equivalent reflections then being:

	No. of refl. pairs	S	R
Centric data	194	1.0059	7.66%
Acentric data	523	0.9957	11.46%
Overall	717	0.9989	10.29%

The plots of S are shown in Figure 3.62.

Crystal to Crystal Scaling

The data sets were scaled on to the set from crystal 272. The numbers of overlapping reflections between the data sets were:

272/273	198
272/274	73

After six cycles of refinement the crystal scale factors converged to:

Crystal number	Scale factor
272	1.0
273	1.135
274	1.184

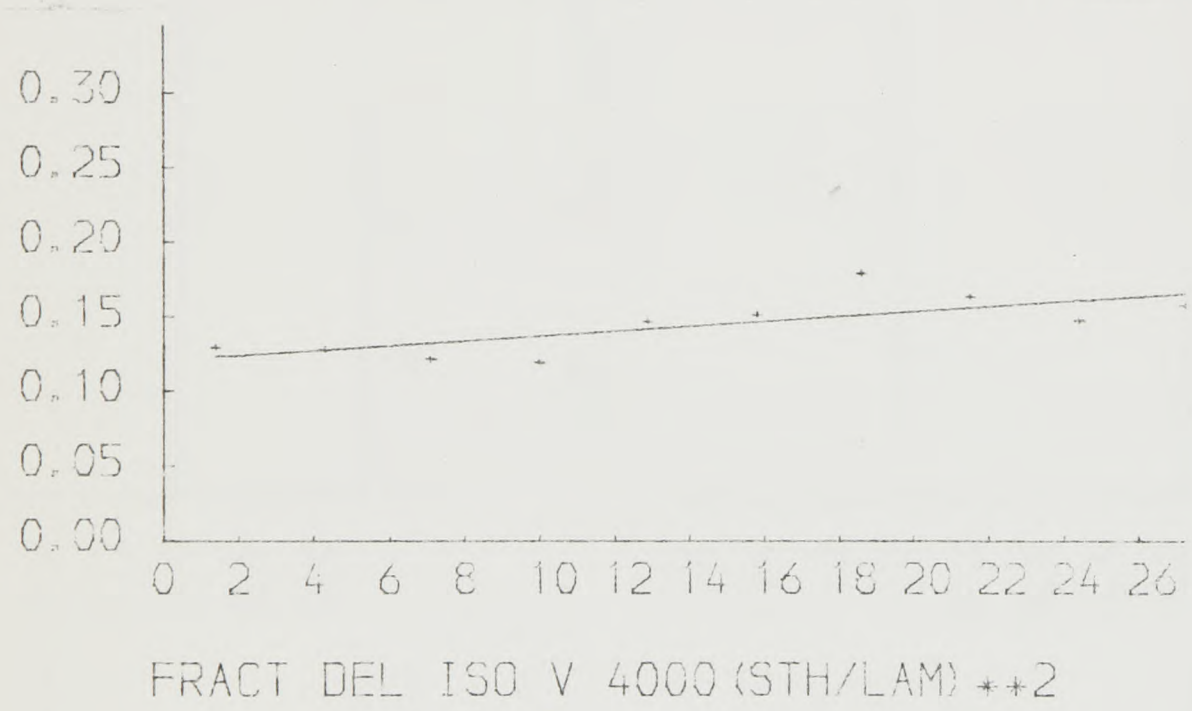
The merged data set comprised 4275 independent reflections with a merging R factor of 9.95%.

FIGURE 3.63

The plots of $\Sigma F_P^2 / \Sigma F_{PH}^2$ for the pipsyl derivative.

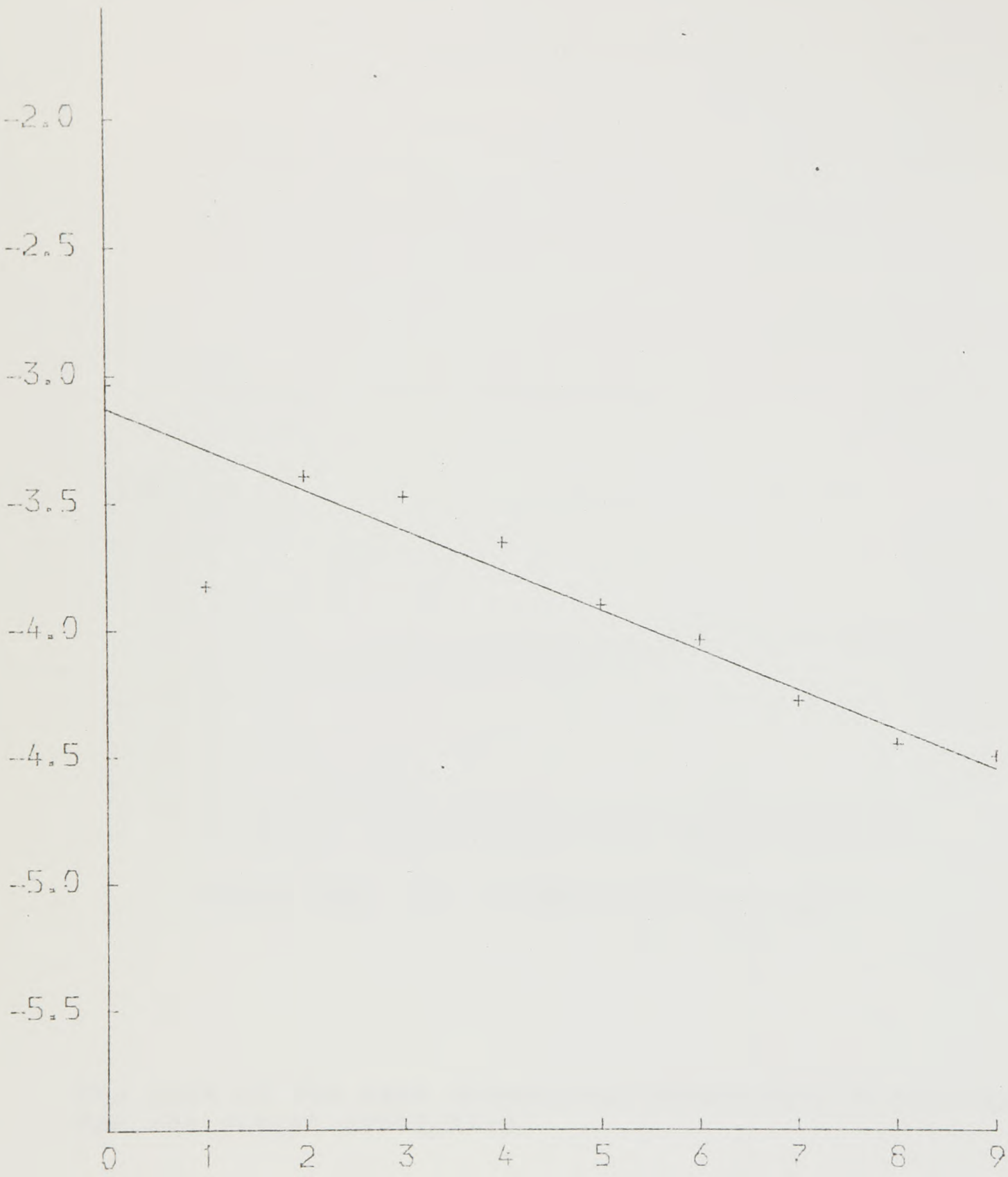


FIGURE 3.64



The plot of the mean fractional isomorphous difference for the pipsyl derivative.

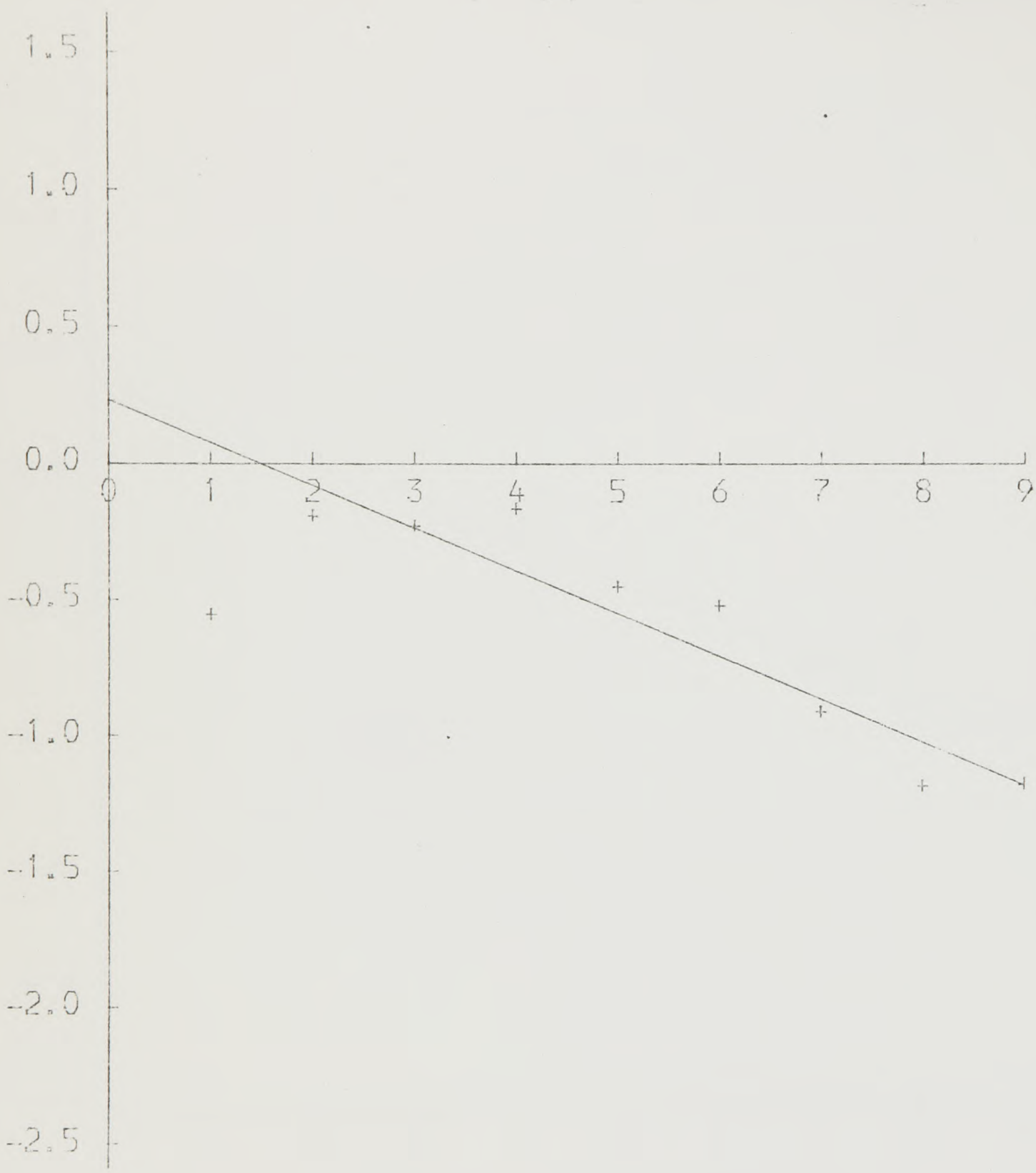
FIGURE 3.65



PIPSYL OV DER WILSON PLOT

The Wilson plot for the pipsyl derivative.

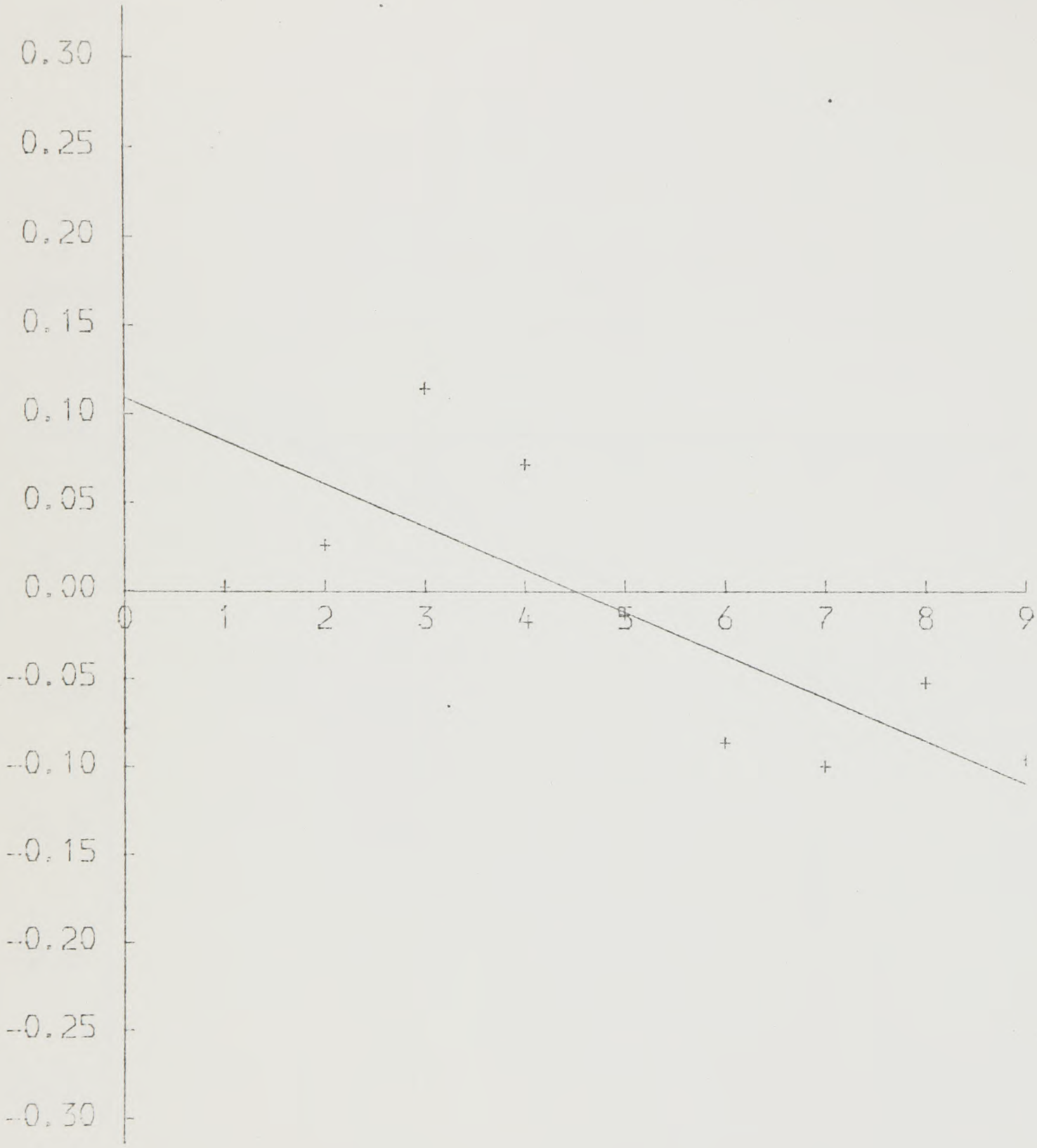
FIGURE 3.66



PIPSYL OV H A WILSON PLOT

The Heavy Atom Wilson plot for the pipsyl derivative.

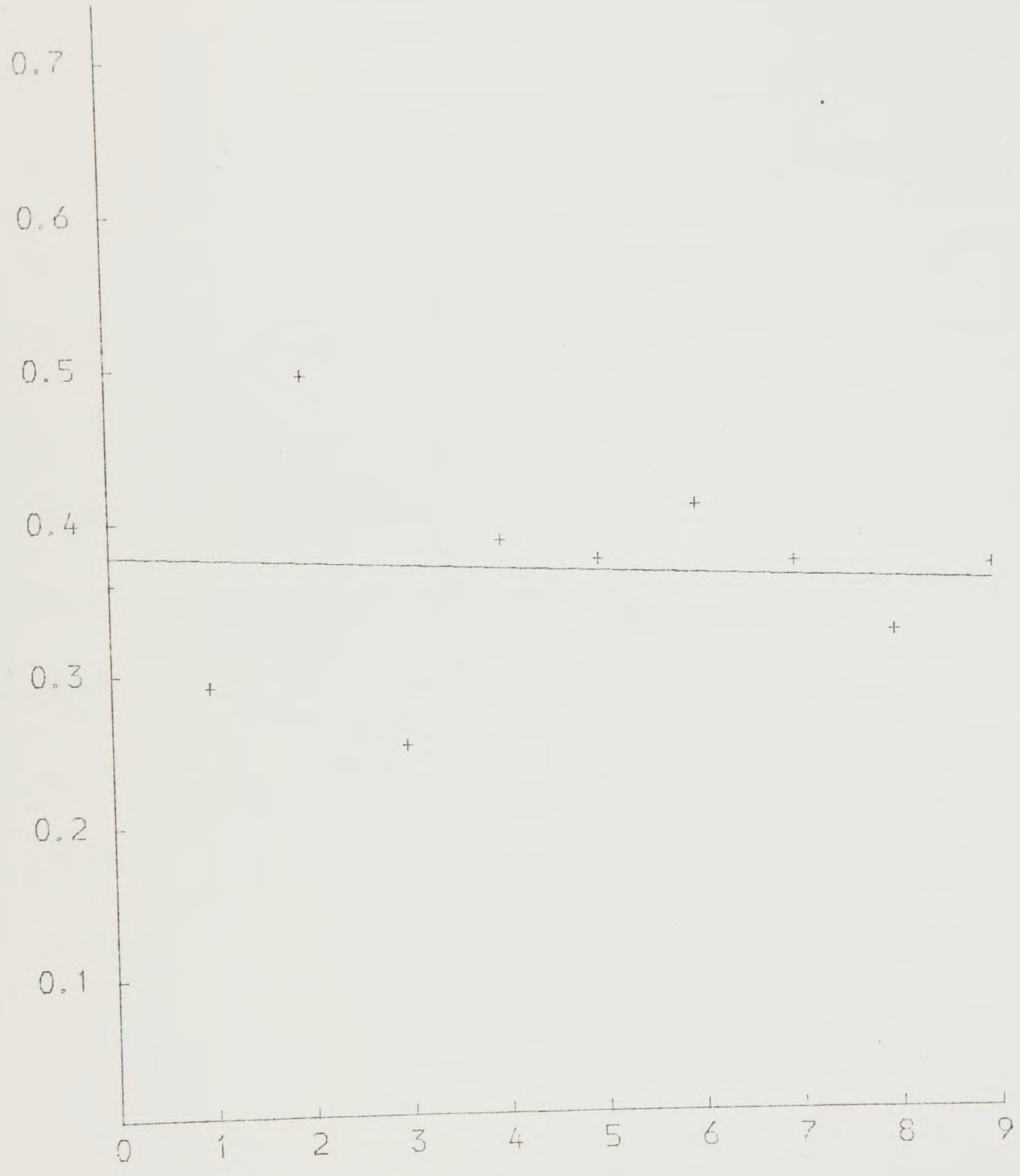
FIGURE 3.67



PIPSYL OV COM WILSON PLOT

The Comparative Wilson plot for the pipsyl derivative.

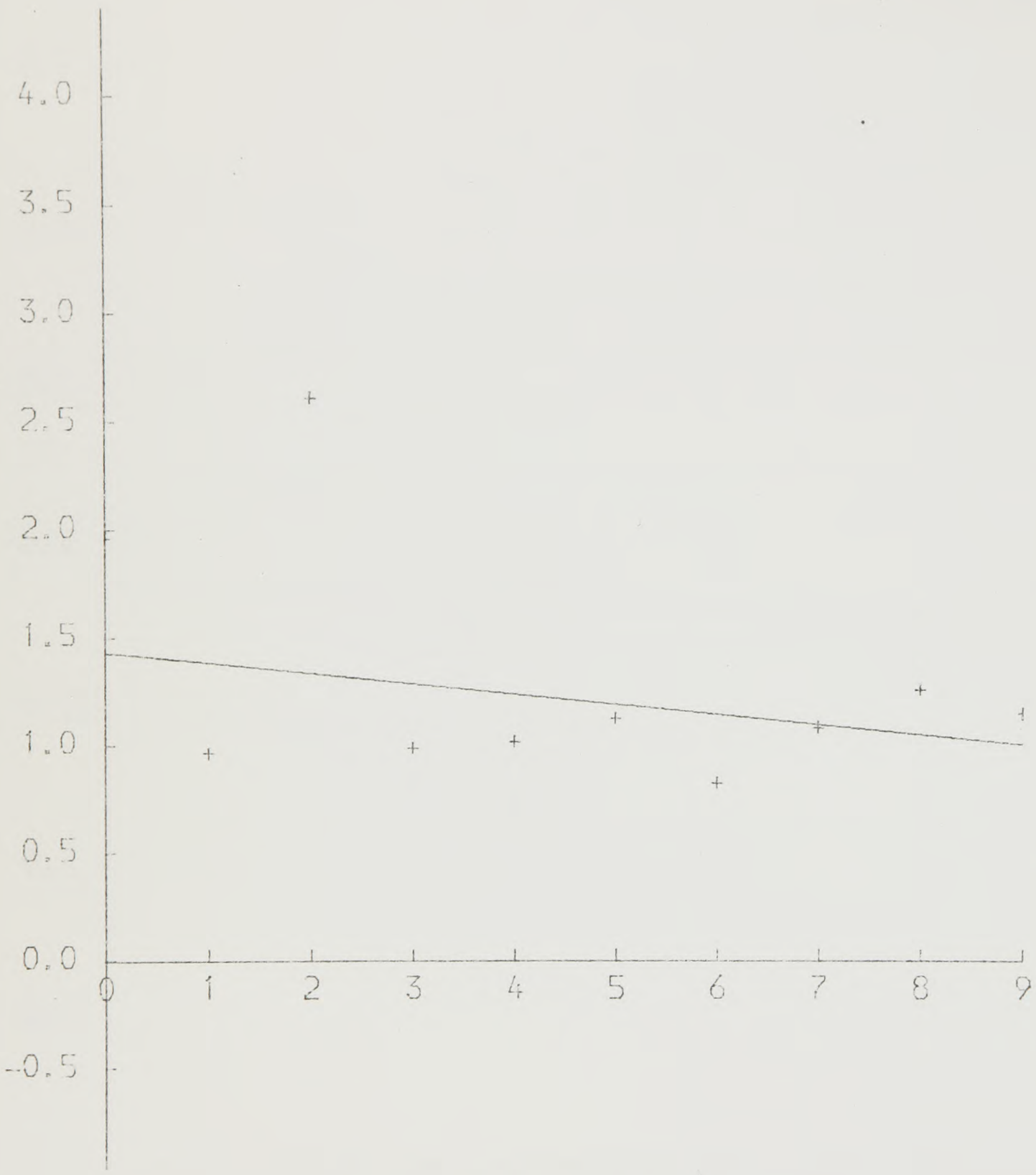
FIGURE 3.68



PIPSYL OVERALL CRICK PLOT

The Crick-Magdoff plot for the pipsyl derivative.

FIGURE 3.69



PIPSYL RATIO CRICK PLOT

The Crick-Magdoff ratio plot for the pipsyl derivative.

TABLE 3.16

Pipsyl derivative crystals - Theoretical and observed fractional change in intensity

Mean $\sin^2\theta/\lambda^2$	Centric terms		Acentric Terms	
	Theoretical	Observed	Theoretical	Observed
0	0.17917	0.37688	0.12669	0.19185
0.00077	0.17981	0.28505	0.12714	0.29525
0.00154	0.18045	0.63972	0.12760	0.24455
0.00231	0.18109	0.24984	0.12805	0.25225
0.00309	0.18174	0.39151	0.12851	0.38344
0.00386	0.18239	0.40573	0.12897	0.35963
0.00463	0.18304	0.35099	0.12943	0.42489
0.00540	0.18370	0.39188	0.12989	0.36132
0.00617	0.18436	0.37839	0.13036	0.30097
0.00694	0.18502	0.39058	0.13083	0.34188

Derivative to Native Scaling

A scale factor varying with $4 \sin^2\theta/\lambda^2$ was applied to the derivative intensities to scale them on to the native data set. This scale factor was:

$$1.6408 - 12.743 \times (4 \sin^2\theta/\lambda^2)$$

The plots of the ratio $\sum F_p^2 / \sum F_{pH}^2$ after scaling are shown in Figure 3.63; the overall ratio was 0.9952. There were 2638 pairs of native and derivative reflections, with a mean isomorphous difference of 30.4 and mean fractional isomorphous difference of 14.97%. The variation of the mean fractional isomorphous difference is shown in Figure 3.64.

The mean empirical k value was 2.24, however, since the anomalous scattering of iodine is small, F_{HLE} coefficients have little meaning, and so none were calculated.

The standard, heavy atom, and comparative Wilson Plots are shown in Figures 3.65, 3.66, 3.67. The heavy atom plot gave a temperature factor of 101.3 and an absolute scale factor of 0.8.

The Crick-Magdoff plot is shown in Figure 3.68, and the ratio plot in Figure 3.69. In Table 3.16 the observed fractional changes in intensity are compared with the theoretical values computed assuming one iodine binding site per monomer.

Difference Patterson and Difference Fourier Sytheses

No iodine binding sites could be found from difference Patterson or difference Fourier syntheses.

The data from these crystals were weak, and, therefore, the isomorphous differences were poorly measured, which

probably accounts for this result.

3.2.12 Conclusion

In order to have a soluble difference Patterson in this space group there must be only one or two major heavy atom binding sites, otherwise the difference Patterson becomes impossibly complicated. However, with a protein the size of phosphorylase the isomorphous differences corresponding to one or two heavy atom binding sites will be small. The diffraction data must, therefore, be measured very accurately using the best possible crystals. The platinum derivative has shown that the heavy atom site can be found given good data. Unfortunately, the uranium and pipsyl derivative crystals are normally cracked thus making the collection of good data difficult.

As a next step, the uranium derivative data should probably be re-collected to a greater degree of accuracy. If this proves to be impracticable the most hopeful source of new derivatives would lie in a further search for co-crystallised derivatives where the crystal quality is more certain. Heavy atoms bound to the pyridoxal phosphate, or the IMP may yield such derivatives. The fact that the platinum derivative has a single site is very encouraging. Good quality heavy atom derivatives with relatively few binding sites can therefore be produced, and so the structure must be soluble by conventional methods.

Recently good quality single derivative electron density maps have been produced of phosphoglycerate kinase (Evans (1973)) and pre-albumin (Geisow, M.J. (1973), private communication). Such maps require accurate measurements of the anomalous scatter-

ing component in the derivative structure factors. With better measurements of the anomalous scattering from the platinum crystal, obtained by at least two measurements of each Bijvoet reflection, it may be feasible to calculate a single derivative map of phosphorylase. Even if the phase information obtained from such data was inadequate to produce a native protein map, it would still be very useful in the search for further heavy atom derivatives.

IV THE DEVELOPMENT OF A ROTATION CAMERA

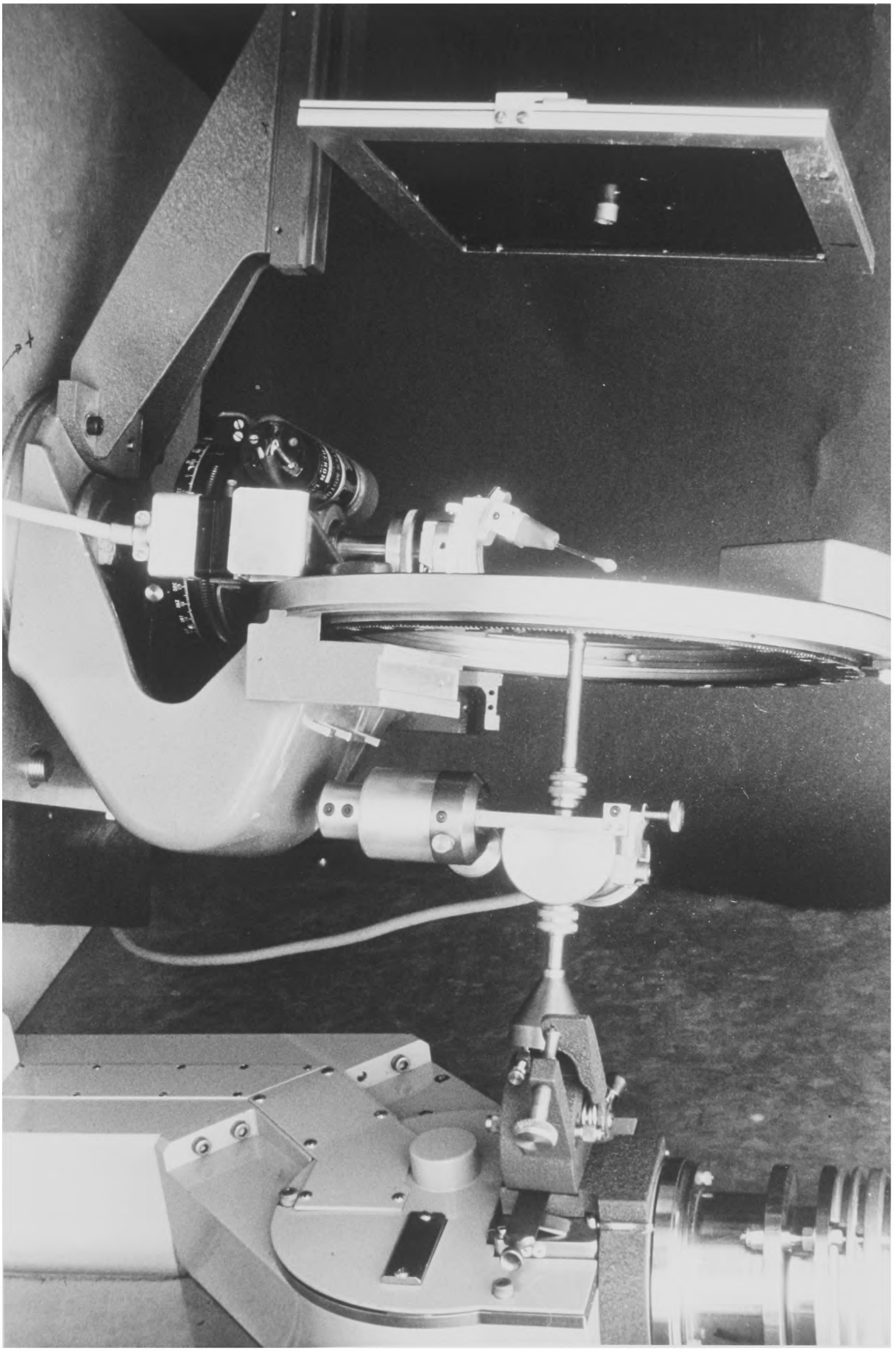
4.1 Introduction

As proteins with larger unit cells are investigated crystallographically, it becomes increasingly important to collect the diffraction data by the most efficient means available. Since, for a crystal with a large unit cell, a large number of reciprocal lattice points are in approximately their reflecting positions simultaneously it should, in principle, be possible to measure these reflections simultaneously. Multiple counter diffractometers (Arndt et al (1964); Evans (1973)) have been developed which can measure up to five reflections quasi-simultaneously. However, the most efficient method of measuring simultaneous reflections is screenless photography where all the reflections which occur simultaneously are recorded, subject only to a maximum Bragg angle defined by the size of the film.

Arndt (1968) has compared diffractometer and screenless photographic methods of data collection and has shown that for large unit cells (particularly those with axes greater than 100Å) screenless photography is more efficient than diffractometer methods. Xong et al (1968) have shown that the screenless precession method is somewhat more efficient than the rotation method. However, the screenless precession method has a disadvantage in that for some reflections the Lorentz-Polarization factor becomes very large and changes rapidly, even over the area of one diffraction spot. The photographs are also extremely complex and cannot be indexed by eye.

It is in principle possible to collect all the diffraction

FIGURE 4.1



The overall view of the rotation camera with the film cassette fitted.

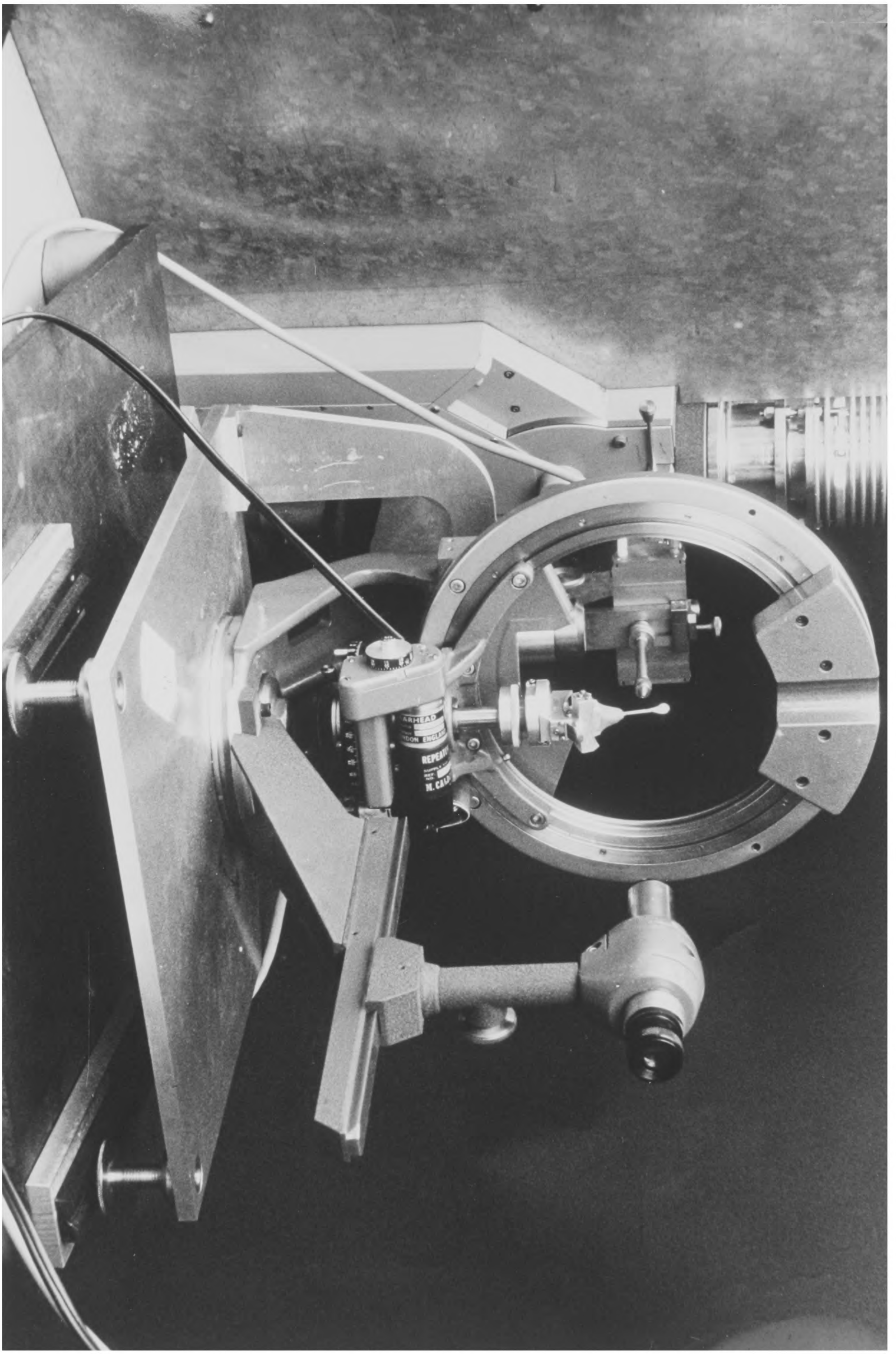
data on one film by rotating the crystal through 180°. However, the resulting diffraction pattern would have a very large number of overlapping reflections, and therefore would be impossible to measure. Arndt (1968) showed that to avoid overlapping reflections completely the crystal rotation must be restricted to d_{min}/a, where d_{min} is the minimum spacing to which reflections are to be measured, and a is the longest unit cell axis. If we consider the case of tetragonal phosphorylase b crystals with data collected to 3Å resolution.

$$\frac{d_{min}}{a} = \frac{3.0}{128} \text{ rad.}$$

$$= 0.024 \text{ rad} = 1^{\circ}24'$$

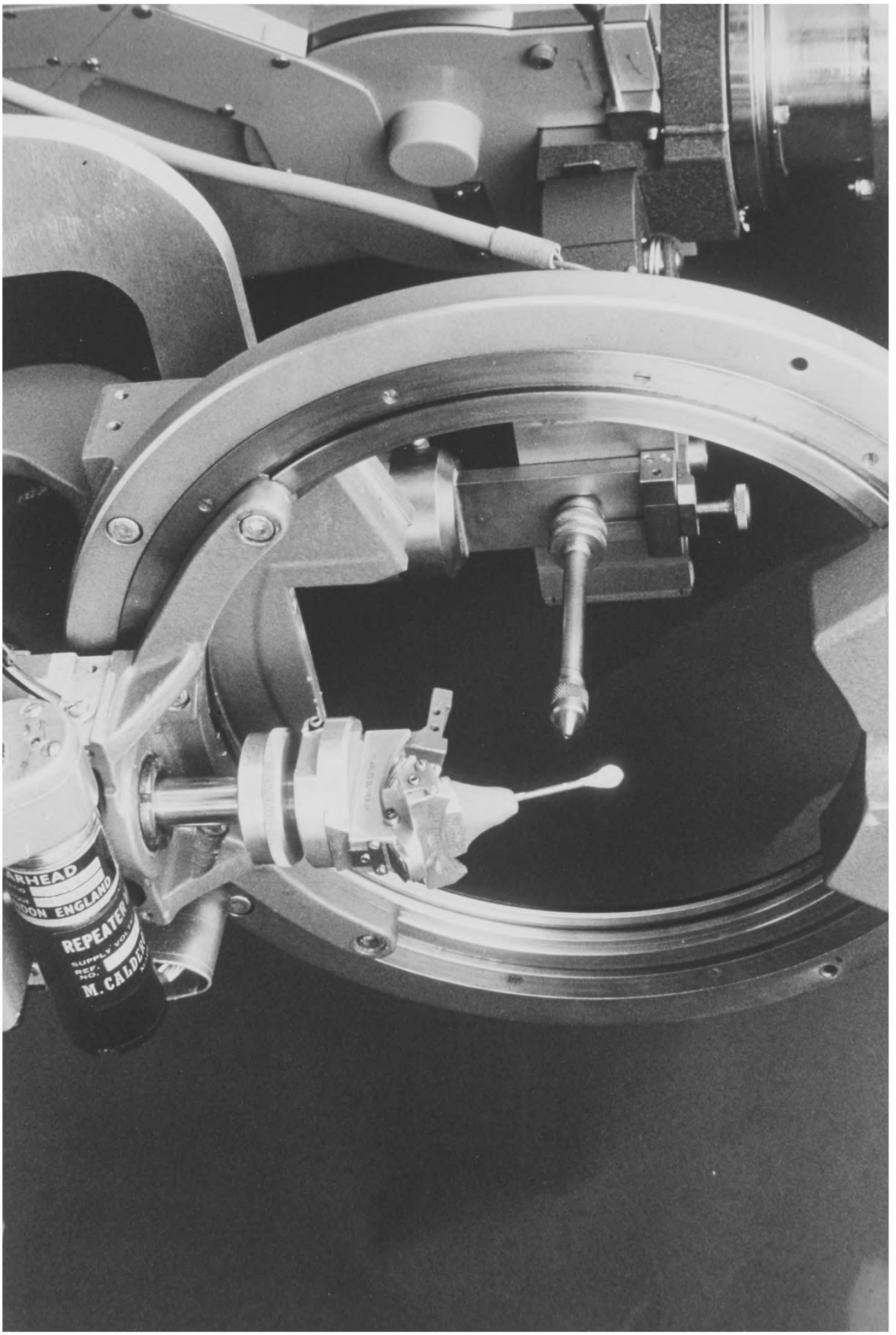
In a c* mount on a rotation camera (c* parallel to the rotation axis), a total rotation of 45° would be required to collect the data set with 4 equivalent reflections. Thus if the rotation were restricted to 1° 24' per film, 32 films would be required; allowing 2 hours exposure per film would result in a total data collection time of 64 hours. To 3Å resolution there are approximately 18,500 unique reflections, and with a 5 counter diffractometer approximately 150 per hour may be measured. Thus, if only two equivalent reflections were measured, the data collection time on such a diffractometer would be approximately 246 hours. This crude estimate shows that there is a considerable improvement in data collection time using a rotation camera. When the extra consideration of radiation damage, which would necessitate a change of crystal every 20 hours is taken into account, the improvement becomes even more considerable.

FIGURE 4.2



The overall view of the rotation camera with the telescope fitted.

FIGURE 4.3



The goniometer, stepping motor and collimator on the rotation camera.

With the advent of high speed computers and automatic densitometers (Arndt et al (1968); Abrahamsson (1966)), it has been possible to automate the measurement of reflection intensities from photographs, thereby making photographic data collection a viable proposition.

A rotation camera was built in this laboratory by Mr. M. Pickford some time ago, to a design by Dr. D.I. Brown. The electronic equipment which controls the crystal rotation was designed and built by Mr. J. Marsh. In this chapter a description of the camera and an account of the development of computer programmes to process the films taken on it will be given. (Unfortunately the development of the film processing system has been held up for approximately two years because of a fault in the Photoscan P1000 Microdensitometer which is used for scanning the films.)

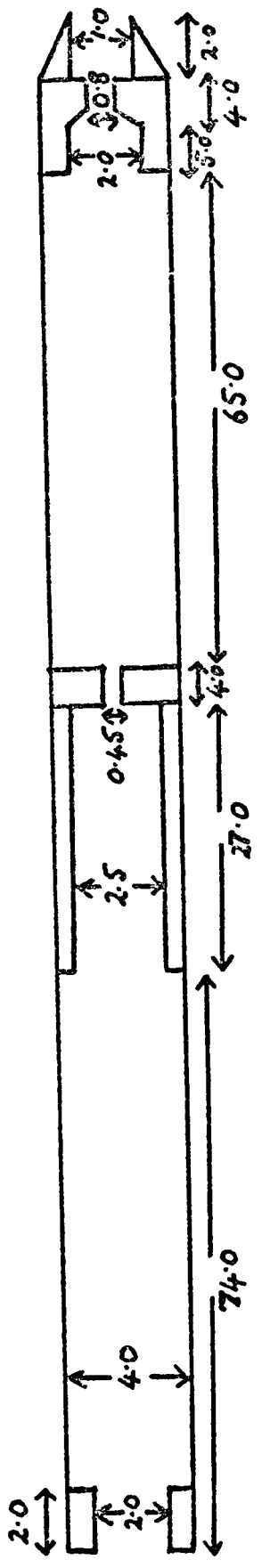
4.2 The Camera

Figures 4.1 and 4.2 give overall views of the camera. It is, in principle, a very simple device, the only movement being rotation about one axis. The rotation axis is normal to the x-ray beam and the reflections are recorded on a flat film.

The goniometer was constructed from two circles of a Hilger and Watts 4 circle diffractometer. The rotation axis (ϕ axis) is driven by a stepping motor which is clearly seen in Figure 4.3. The χ circle may be rotated by hand so that the rotation axis may be vertical or horizontal. Positive rotation is defined as being a clockwise movement when looking on to the camera from above.

The film cassette is mounted on a bracket which in turn is

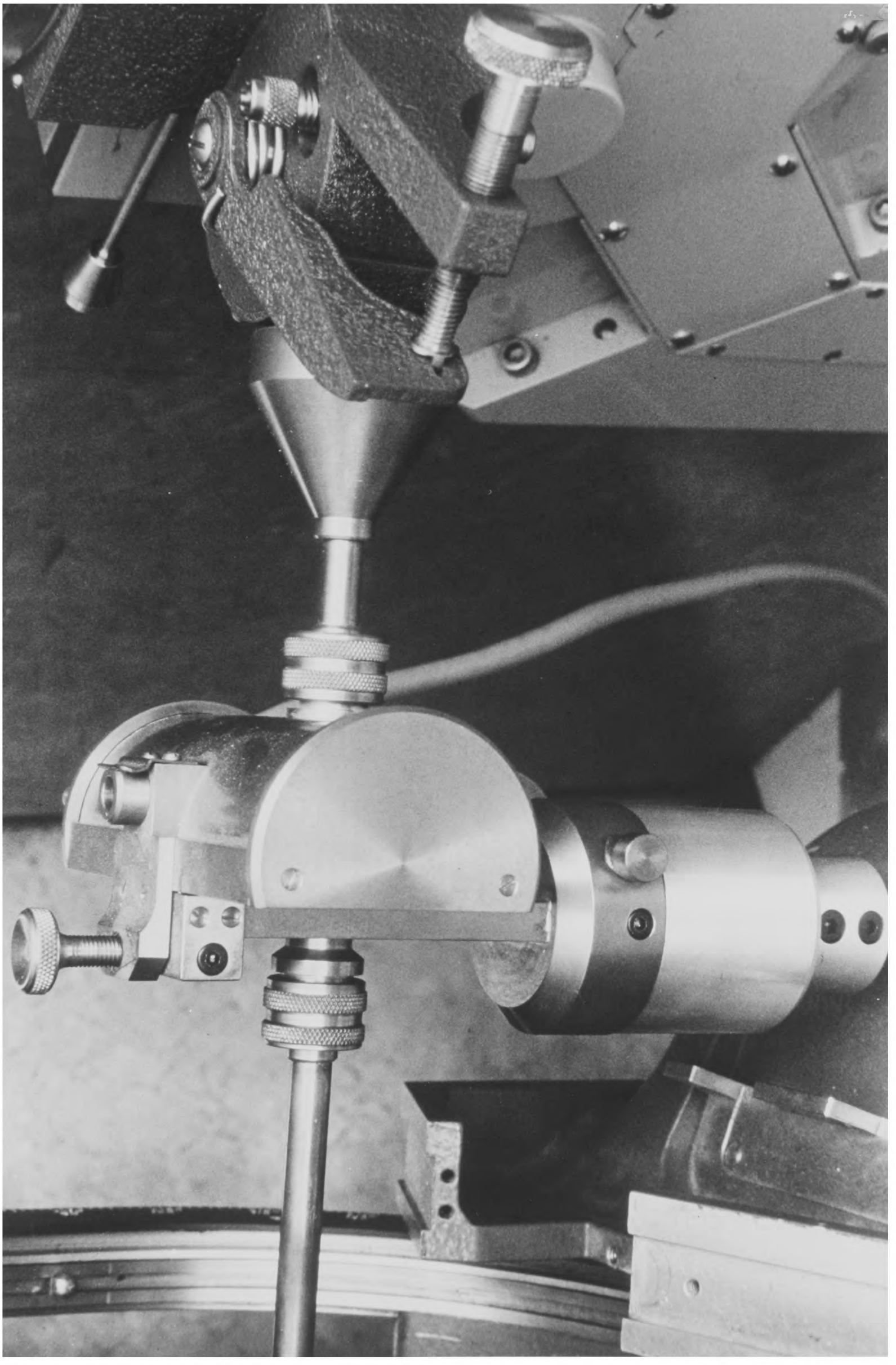
FIGURE 4.4



NOT TO SCALE. DIMENSIONS IN MM.

A schematic view of the rotation camera collimator.

FIGURE 4.5



The collimator and shutter assembly on the rotation camera.

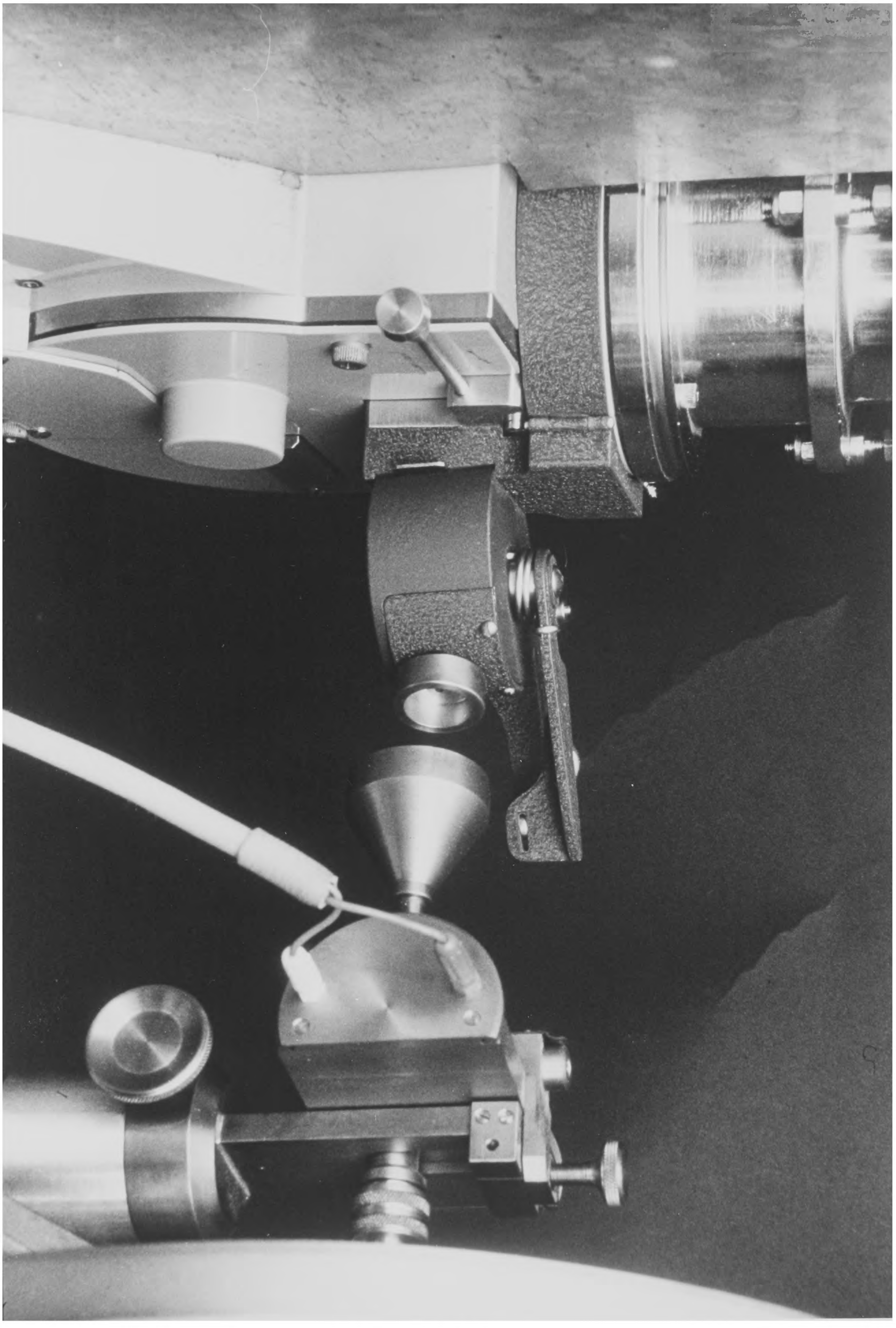


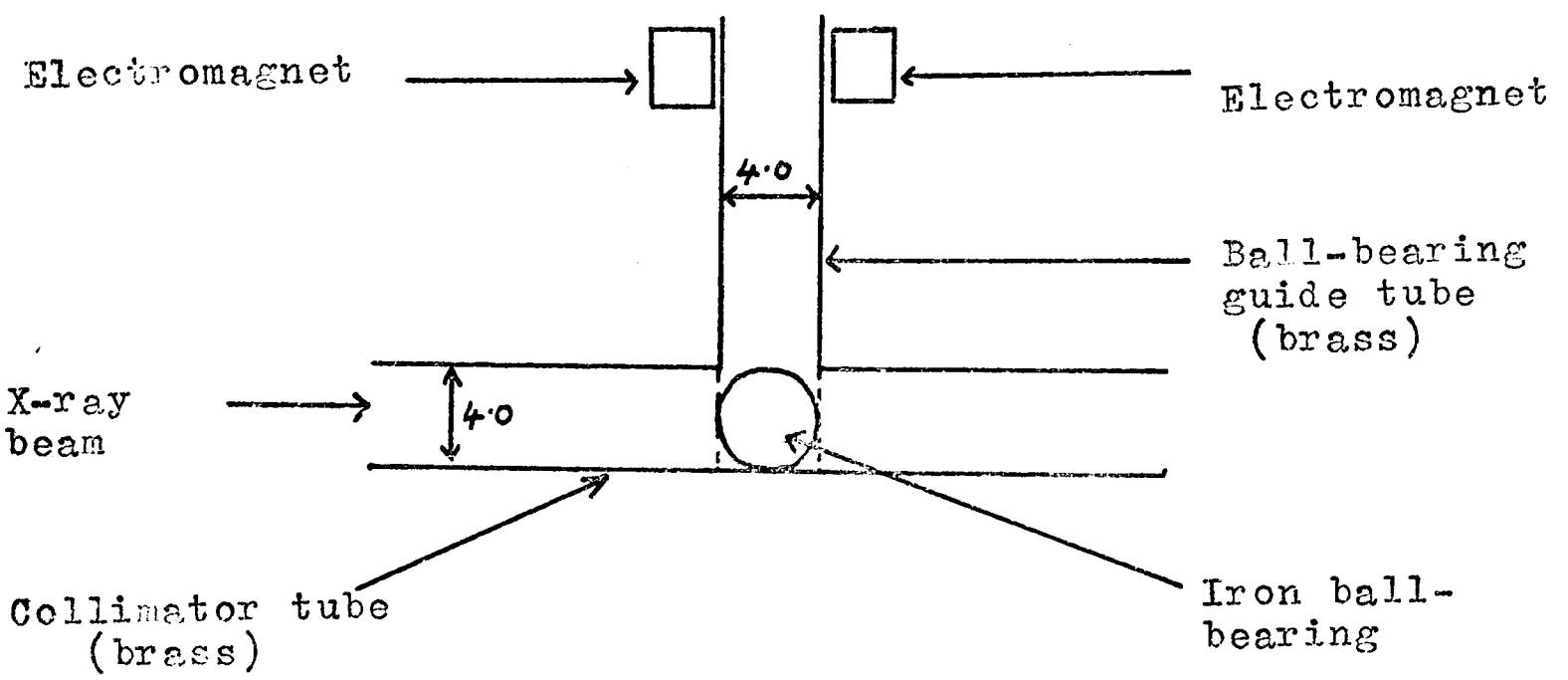
FIGURE 4.6

The rotation camera shutter assembly and the monochromator.

mounted on a slide; the system was designed so that the crystal to film distance could be set at any value between approximately 5 cm. and 45 cm. Originally, the backstop was held in front of the cassette on a mylar sheet supported by another bracket. However, the mylar was found to absorb the diffracted x-rays to a significant extent and was therefore removed. The backstop is now fixed directly on to the cassette as shown in Figure 4.1. The cassette holder may be replaced by a telescope (Figure 4.2) to aid in setting up crystals. The cassette slide may be rotated and translated to bring it parallel to the camera axis.

With screenless photography the collimation of the x-ray beam is very critical since any scattering arising from the collimator will serve to increase the general background level on the film. The collimator was designed to allow all points on the crystal to "see" the whole focal spot of the x-ray source, whilst avoiding, as far as possible, any radiation scattered within the collimator reaching the film. The collimator was originally designed with three apertures, the central one being the limiting one. However, the background on the photographs taken with this collimator was found to be too high, and therefore the final aperture was re-designed. The current collimator design, arrived at after some experimentation, is shown in Figure 4.4. The collimator may be rotated about a vertical axis and raised and lowered so that it may be aligned to point at the centre of the χ circle which is the absolute reference point of the camera. An automatic shutter mechanism is built into the collimator; the outside appearance of this may be seen in Figures 4.5 and 4.6, and a schematic view in Figure 4.7. This

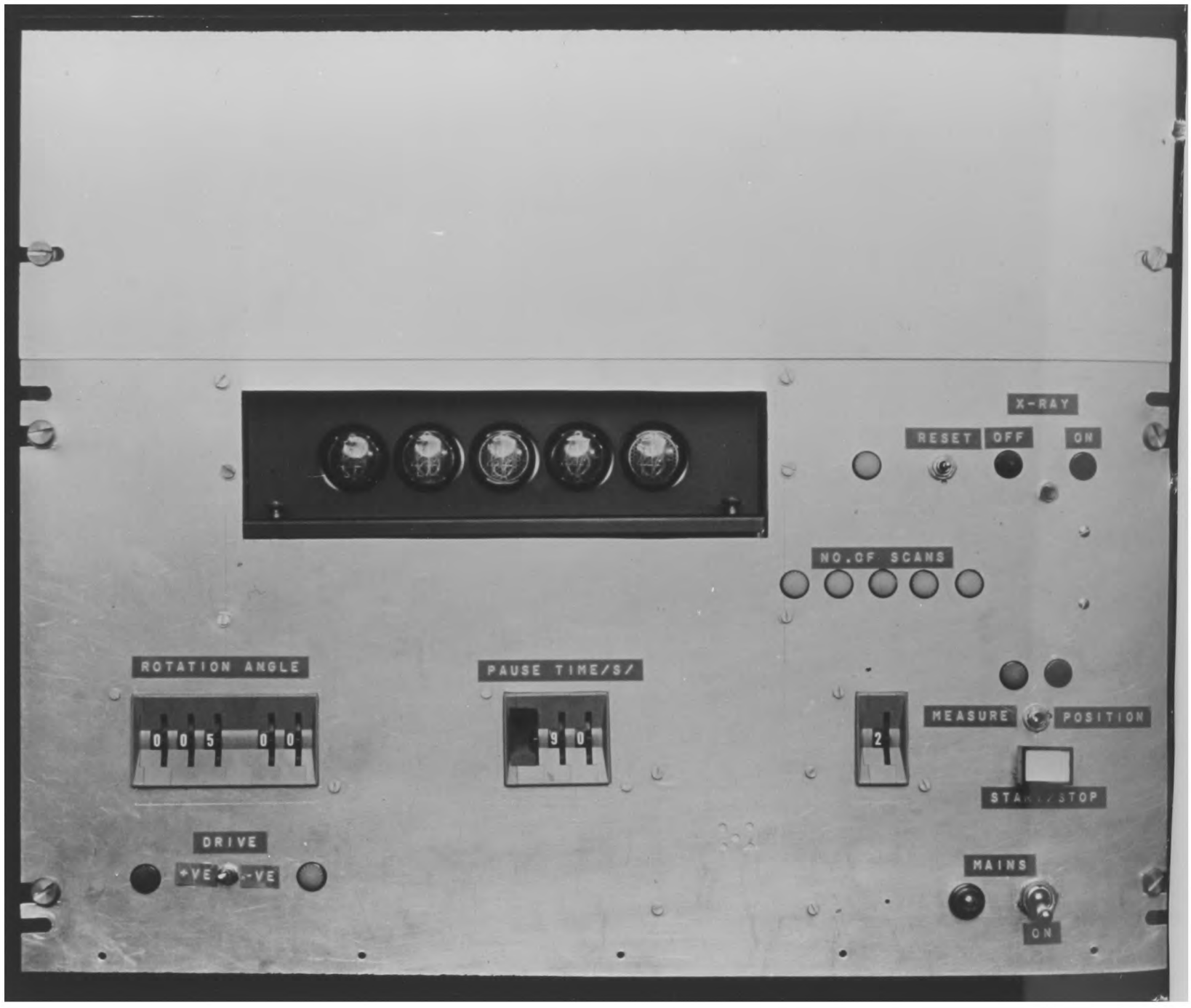
FIGURE 4.7



Not to scale. Dimensions in mm.

A schematic view of the rotation camera shutter assembly.

FIGURE 4.8



The rotation camera contol unit.

mechanism comprises a vertical tube which intersects the collimator, and a ball-bearing which can slide up and down the vertical tube. Normally, the ball-bearing lies at the bottom of the tube, thereby cutting off the x-rays. However, at a signal from the camera control unit an electromagnet in the shutter unit is energised and lifts the ball-bearing out of the path of the x-ray beam.

The goniometer is mounted on a base and secured with a single nut about which it can be rotated for alignment purposes. The collimator is fixed rigidly to the camera base. Recently, an adjustable platform has been made by Mr. M. Pickford to carry the camera base. This platform has rotational and translational movements controlled by screw-threads, and is very useful for making small adjustments when aligning the camera in the X-ray beam.

The camera control unit is shown in Figure 4.8; it allows the camera to be operated in two modes, while recording the current position of the ϕ axis to the nearest 0.01^{o}:

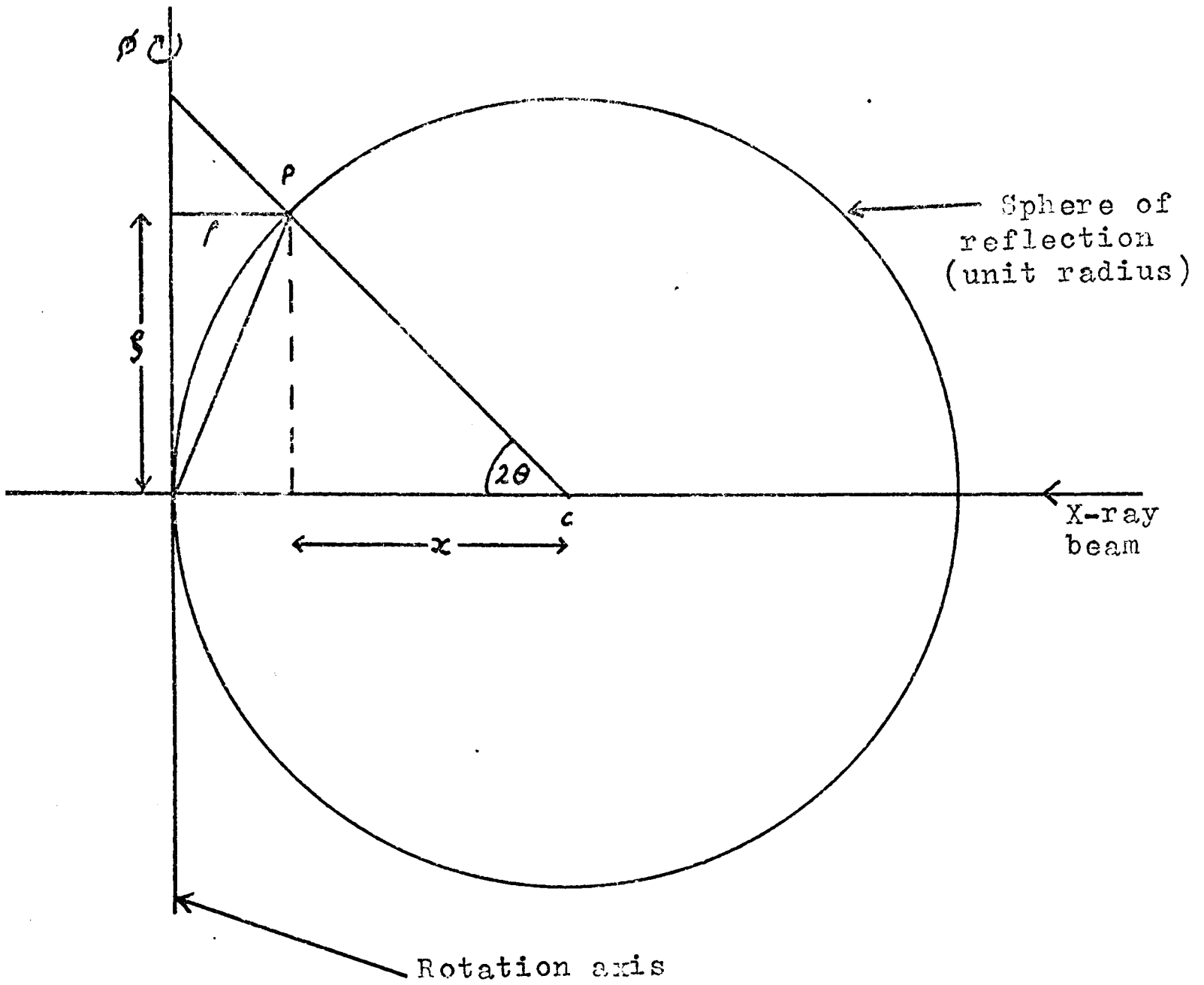
(a) Position mode.

In this mode the ϕ axis is driven continuously in either direction through a preset angle without opening the x-ray shutter.

(b) Measure mode.

When the "START" button is pressed the shutter is opened and after a preset time interval, the ϕ axis is stepped through 0.01^{o}. After a second such time interval, the axis is moved through another 0.01^{o}. This cycle is repeated until the axis has moved through a preset overall angle. The pause time may be varied in 1 second intervals from 1 to 99 seconds.

FIGURE 4.9



C represents the position of the crystal

The section through the rotation axis and the sphere of reflection.

In addition to these two facilities there is a shutter override switch which allows the shutter to be opened without any movement of the ϕ axis. This facility is useful for taking still crystal setting photographs.

A graphite monochromator has been built in the laboratory based on a design by Dr. P.B. Sigler; this monochromator can be seen mounted on an Elliott Rotating Anode x-ray generator in Figures 4.1, 4.5, and 4.6. The camera has been used in conjunction with this monochromator which tends to reduce the amount of background scattering on the films, but also reduces the x-ray beam intensity, compared with nickel filtered radiation.

4.3 Outline of Reflection Geometry

Figure 4.9 shows a section through the rotation axis and sphere of reflection. The reciprocal lattice point, P, will give rise to a reflection when the rotation angle, ϕ, is such that P lies on the sphere of reflection. From this diagram it is obvious that there is a "blind region" near the rotation axis within which reciprocal lattice points will never cut the sphere of reflection. The radius, ρ, of the blind region is a function of the distance, ζ, up the rotation axis. From the diagram:

$$\rho = (1-x)$$

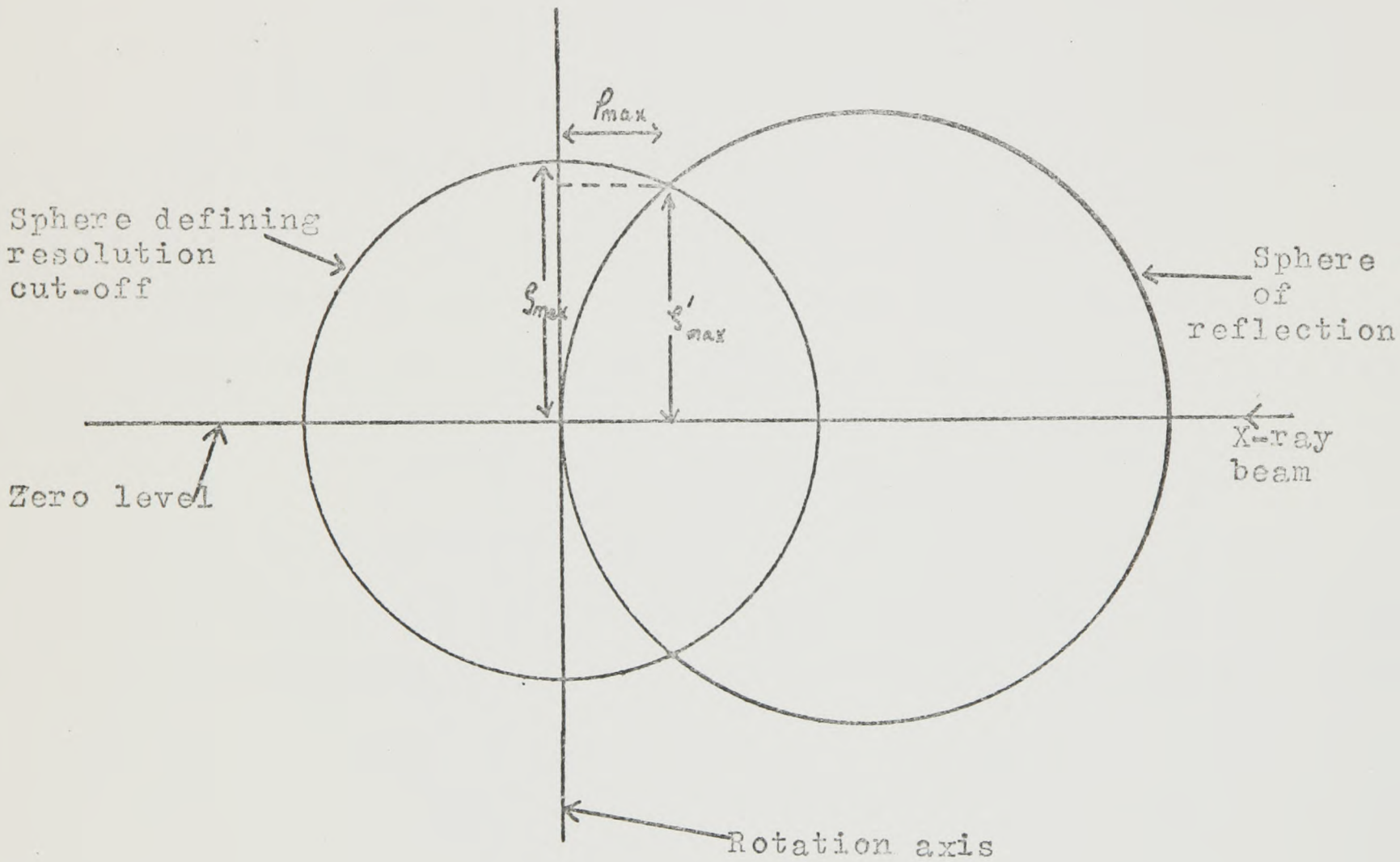
and $$x^2 + \zeta^2 = 1$$

$$\therefore \quad x = (1-\zeta^2)^{\frac{1}{2}}$$

$$\therefore \quad \underline{\rho = 1 - (1-\zeta^2)^{\frac{1}{2}}} \qquad 4.1$$

The volume of the blind region to a given resolution limit may be calculated, and from that the fraction of the total reflection set which is inaccessible estimated. If the data extend to

FIGURE 4.10



The blind region with a resolution cut-off.

a lattice spacing, R Å, the maximum value of ζ is given by

$$\zeta_{max} = \frac{\lambda}{R} \qquad \text{where } \lambda \text{ is the wavelength in Å}$$

The resolution cut-off may be represented by a sphere of radius ζ_{max} as shown in Figure 4.10.

From Figure 4.10:

$$\zeta_{max}^{1\,2} + \rho_{max}^{2} = \zeta_{max}^{2} \qquad 4.2$$

Equation 4.1 gives:

$$\rho_{max} = 1 - (1 - \zeta_{max}^{1\,2})^{\frac{1}{2}}$$

$$\rho_{max}^{2} = 1 + (1 - \zeta_{max}^{1\,2}) - 2(1 - \zeta_{max}^{1\,2})^{\frac{1}{2}}$$

Substitution in equation 4.2 gives:

$$\zeta_{max}^{1\,2} + 1 + (1 - \zeta_{max}^{1\,2}) - 2(1 - \zeta_{max}^{1\,2})^{\frac{1}{2}} = \zeta_{max}^{2}$$

$$\therefore \qquad 2(1 - \zeta_{max}^{1\,2})^{\frac{1}{2}} = 2 - \zeta_{max}^{2}$$

$$\therefore \qquad \underline{\zeta_{max}^{1\,2} = \left[1 - \frac{(2-\zeta_{max}^{2})^{2}}{4}\right]} \qquad 4.3$$

The volume of the blind region above the zero level is, of course, the same as the volume below the zero level. Two integrals are needed to give the volume of the blind region above the zero level; these integrals are valid in separate regions defined by the conditions:

1. $0 \leqslant \zeta \leqslant \zeta_{max}^{1}$
2. $\zeta_{max}^{1} \leqslant \zeta \leqslant \zeta_{max}$

<u>1st Integral</u>:

A volume element in this region is defined by:

$$\delta V_1 = \pi \rho^2 \delta\zeta$$

Using equation 4.1:

$$\delta V_1 = \pi[1 + (1 - \zeta^2) - 2(1 - \zeta^2)^{\frac{1}{2}}]\delta\zeta$$

$\therefore$ The total volume of the region is given by:

$$V_1 = \pi \int_0^{\zeta_{max}^1} [2 - \zeta^2 - 2(1 - \zeta^2)^{\frac{1}{2}}]\delta\zeta$$

This integral evaluates to:

$$V_1 = \pi\{\zeta_{max}^1[2 - \tfrac{1}{3}(\zeta_{max}^1)^2] - \tfrac{1}{2}\sin[2 \sin^{-1}(\zeta_{max}^1)] - \sin^{-1}(\zeta_{max}^1)\} \qquad 4.4$$

2nd Integral

This region is simply the section of a sphere. The volume element is:

$$\delta V_2 = \pi \rho^2 \delta\zeta$$

where $\rho^2 + \zeta^2 = \zeta_{max}^2$

$$\therefore \quad \delta V_2 = \pi(\zeta_{max}^2 - \zeta^2)\delta\zeta$$

$$\therefore \quad V_2 = \pi \int_{\zeta_{max}^1}^{\zeta_{max}} (\zeta_{max}^2 - \zeta^2)\delta\zeta$$

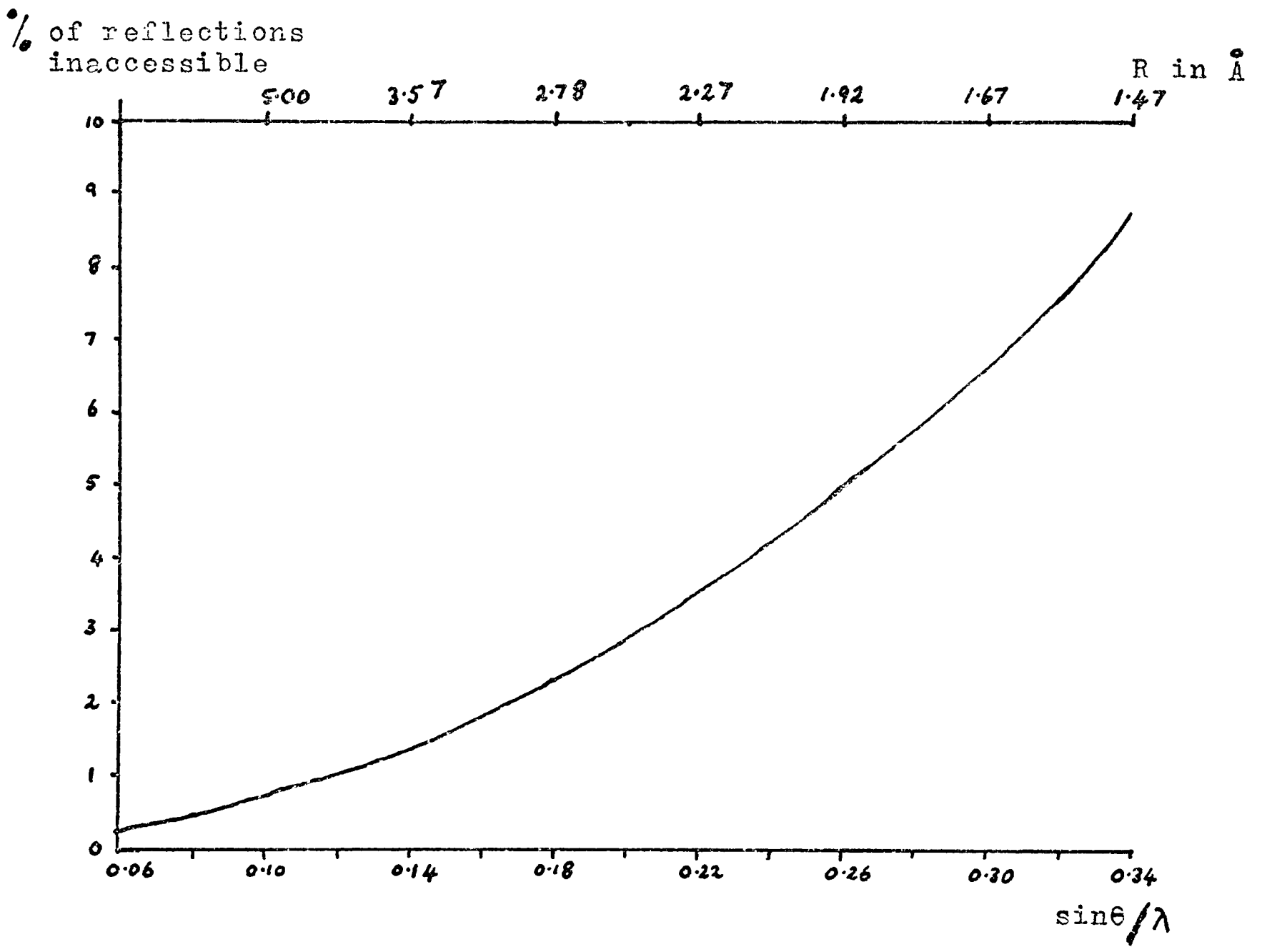
$$\therefore \quad V_2 = \pi\{\tfrac{2}{3}\zeta_{max}^3 + \tfrac{1}{3}\zeta_{max}^{1\,3} - \zeta_{max}^2 \zeta_{max}^1\} \qquad 4.5$$

The volume of the blind region, V_B, is thus given by:

$$V_B = 2(V_1 + V_2)$$

Equations 4.4 and 4.5 then give:

FIGURE 4.11



The variation of the volume of the blind region with $\sin\theta/\lambda$ and lattice spacing, R, in Å.

$$V_B = 2\pi\{\tfrac{2}{3}\zeta_{max}^{3} + 2\zeta_{max}^{1} - \zeta_{max}^{2}\zeta_{max}^{1} - \tfrac{1}{2}\sin[2\sin^{-1}(\zeta_{max}^{1})] - \sin^{-1}(\zeta_{max}^{1})\} \qquad 4.6$$

Equations 4.3 and 4.6 can thus be used to calculate the volume of the blind region.

The volume, V_s, of the sphere of reflection is given by:

$$V_s = \tfrac{4}{3}\pi\zeta_{max}^{3}$$

The fraction, f, of the data set which is inaccessible because of the blind region is given by:

$$f = \frac{V_B}{V_s}$$

A computer programme was written to calculate f for various values of the lattice spacing, R, assuming copper Kα radiation. The plot of f versus sin θ/λ and R is shown in Figure 4.11. It may be seen that the blind region remains small unless very high resolution data is required. It is, of course, possible to collect most of the data in the blind region by rotating the crystal about another axis. However, in view of the relatively small number of reflections which are lost, this may be unnecessary. The above equations are only approximately true since the assumption that reciprocal lattice points are discrete points is not true. Each reciprocal lattice point has a finite size which is dependent on the crystal size and mosaic spread, and the beam divergence and dispersion. This will result in some reflections close to the edge of the blind region being only half recorded.

However, the general conclusions remain the same.

The Lorentz factor for normal beam rotation photographs is given by:

$$L = \frac{1}{(\sin^2 2\theta - \zeta^2)^{\frac{1}{2}}} \qquad \text{(Buerger (1940))}$$

Figure 4.9 shows that on the edge of the blind region:

$$\zeta = \sin 2\theta$$

and therefore the Lorentz factor becomes infinite. Inside the blind region:

$$\zeta > \sin 2\theta$$

and therefore the Lorentz factor becomes imaginary.

Assuming an unpolarized primary x-ray beam, the polarization factor is:

$$P = \frac{1 + \cos^2 2\theta}{2}$$

The combined LP factor is thus:

$$LP = \frac{1 + \cos^2 2\theta}{2(\sin^2 2\theta - \zeta^2)^{\frac{1}{2}}} \qquad 4.7$$

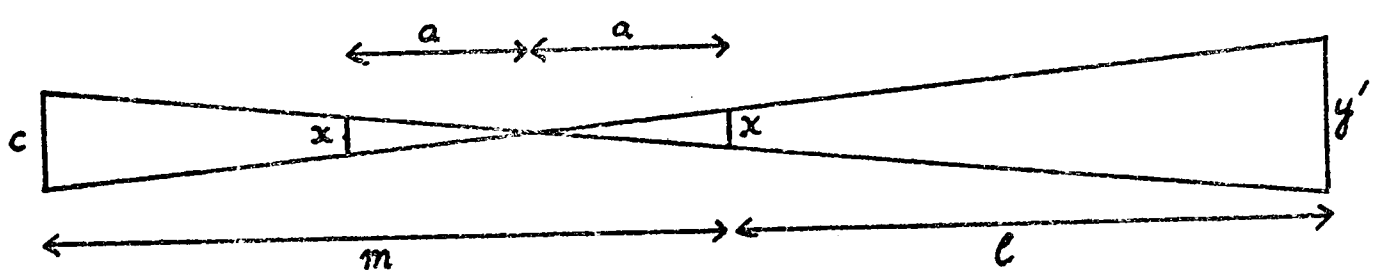
4.4 Spot Sizes and Resolution

The size of the reflection recorded on the film is dependent on three factors:

1. The sizes of the crystal and defining aperture, length of collimator, and crystal to film distance.
2. Wavelength spread in the beam.
3. Mosaic spread in the crystal.

The first is the most important, and is illustrated in Figure

FIGURE 4.12



Where:

x is crystal size

C is the defining aperture size

y is the spot size due to these factors

ℓ is the crystal to film distance

m is the defining aperture to crystal distance

The geometrical factors contributing to spot size.

4.12. From this diagram:

$$\frac{x}{a} = \frac{y'}{(\ell+a)}$$

$$\frac{x}{a} = \frac{c}{(m-a)}$$

Eliminating a from these equations:

$$y' = x(1 + \ell/m) + \ell\, c/m \qquad 4.8$$

The contribution due to the wavelength spread in the x-ray beam is:

$$y'' = 2\,\ell.\delta\theta \qquad 4.9$$

where $\delta\theta = \frac{\delta\lambda}{2d\,\cos\theta}$ (Banner (1972))

Finally, the contribution due to the mosaic spread is:

$$y''' = 2\,\ell.M\,\sin\theta \qquad \text{(Banner (1972))} \qquad 4.10$$

where M is the mosaic spread in radians.

With a flat film on a rotation camera the effective crystal to film distance, ℓ', varies with the Bragg Angle according to the equation

$$\ell' = \frac{\ell}{\cos 2\theta}$$

Equations 4.8, 4.9 and 4.10 should thus be modified accordingly. The total spot size, y, is then given by:

$$y = y' + y'' + y'''$$

The minimum angular separation of reflections, $\Delta_{2\theta}$, is given by

$$\Delta_{2\theta} = 2\delta\theta \qquad 4.11$$

where $\delta\theta = \frac{\Delta d^*}{2\cos\theta}$ (Banner (1972))

Therefore, the minimum spatial separation of reflections, S, is given by:

$$S = \ell'.\Delta_{2\theta} \qquad 4.12$$

The condition for reflections to be resolved on the film is:

$$S > y$$

Using this condition, and the equations 4.8, 4.9, 4.10, 4.11 and 4.12, the largest acceptable crystal size may be determined.

Typical values for the various parameters would be:

ℓ = 100 mm
m = 85 mm
c = 0.45 mm

If we consider collecting 3.5Å data on a tetragonal phosphorylase b crystal, the other parameters would be:

$\Delta d^* = c^* = 0.0133$ rlu.
M $\sim$ 0.005 rad.

For 3.5Å resolution data $\cos 2\theta = 0.9078$

$\therefore \ \ell' = 110$ mm.

$\therefore \ \underline{y' = 2.3x + 0.58 \text{ mm.}}$

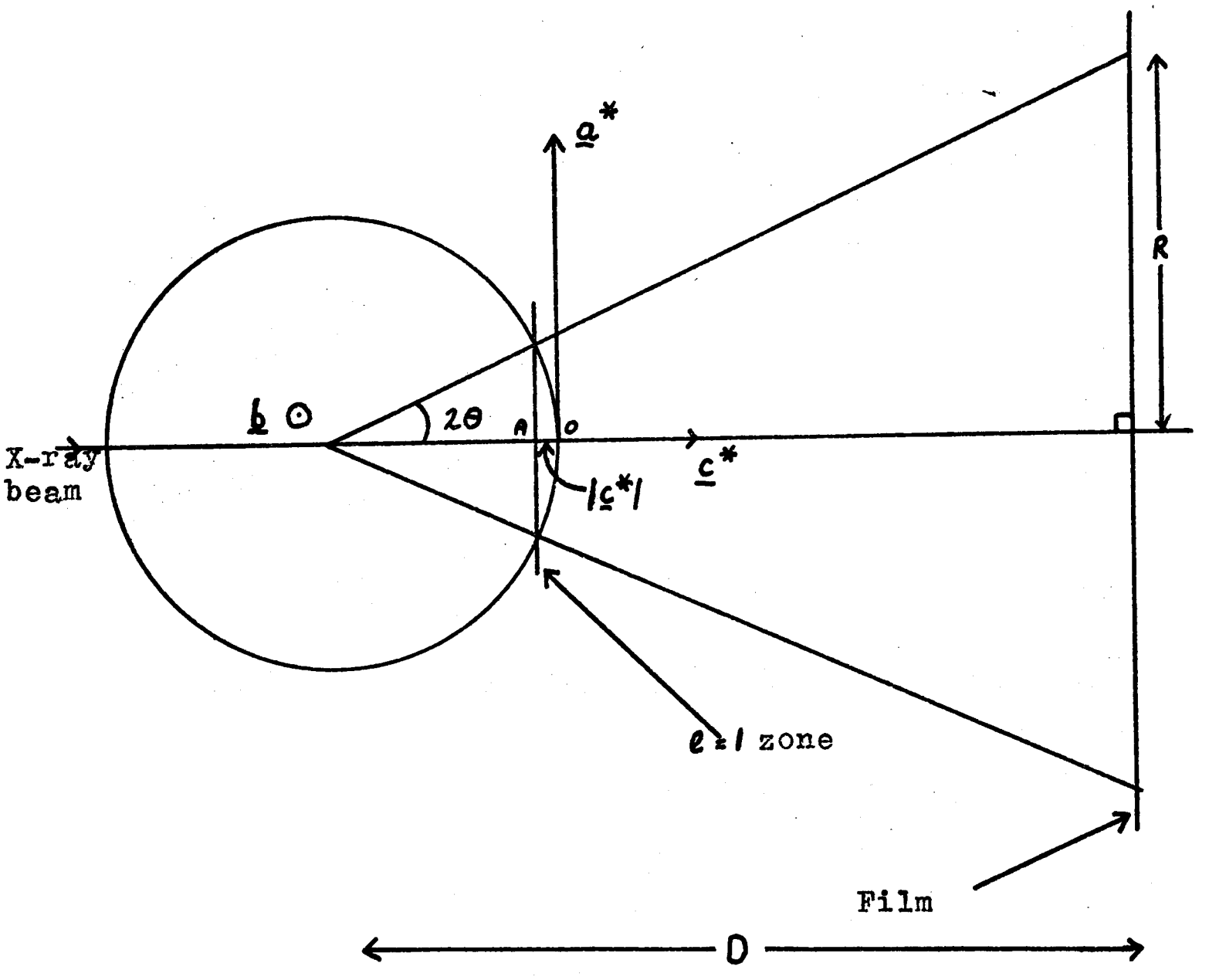
$\delta\lambda$ is the wavelength difference between the copper $K\alpha_1$ and $K\alpha_2$ lines; i.e. $\delta\lambda = 0.00382$Å

$\therefore \ \underline{y'' = 0.12 \text{ mm}}$

$\underline{y''' = 0.24 \text{ mm}}$

$\therefore \ \underline{y = 2.3x + 0.94 \text{ mm}}$

FIGURE 4.13



The still photograph of a perfectly set crystal.

The spot separation, S, is then:

$$S = 1.5 \text{ mm}$$

Applying the resolution condition:

$$2.3x + 0.94 < 1.5$$

$$\therefore \quad 2.3x < 0.6$$

$$\therefore \quad x < 0.3 \text{ mm}$$

The maximum crystal size therefore appears to be 0.3 mm. However, these calculations are only very approximate, and therefor an empirical check on the crystal size should be made.

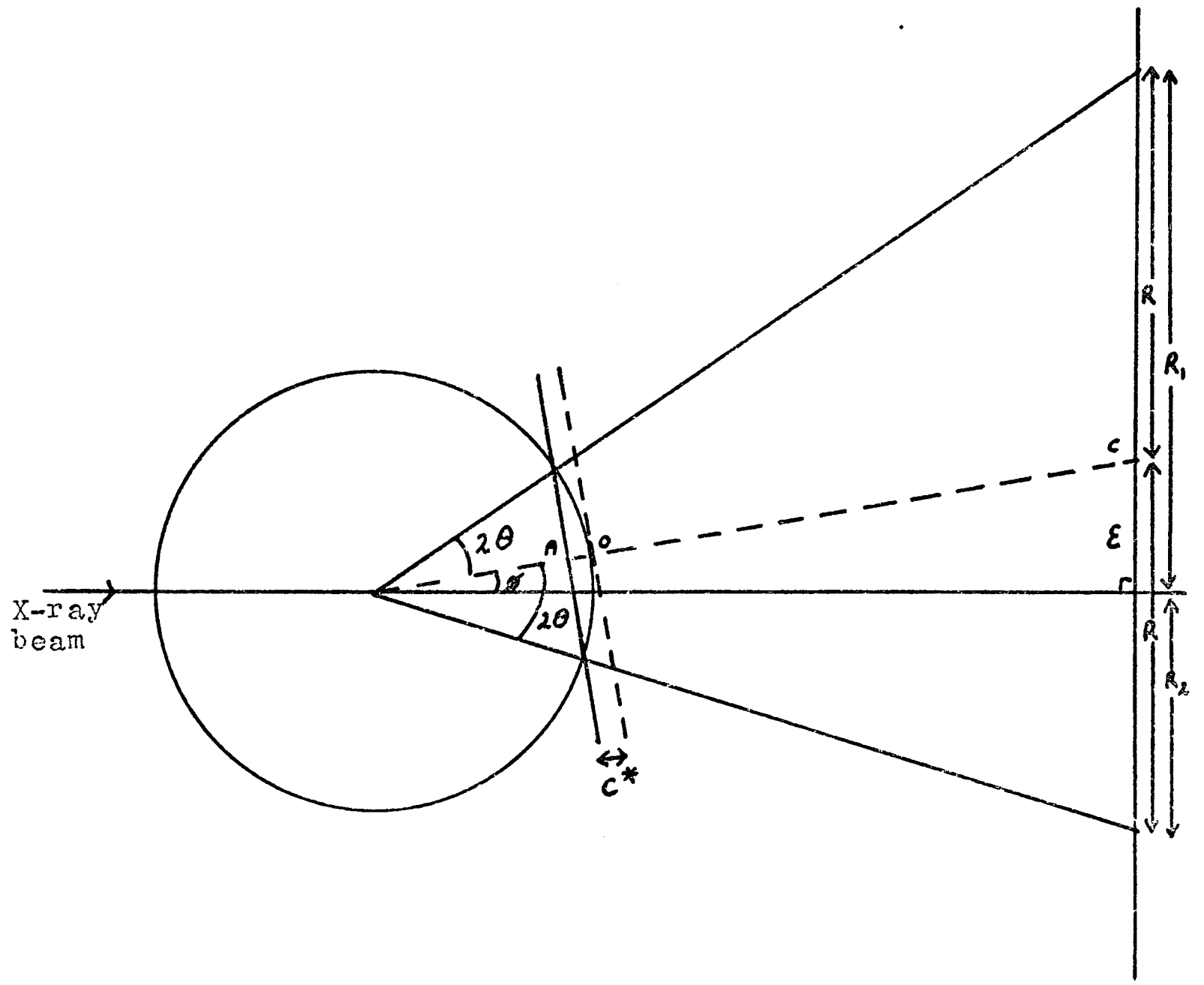
4.5 Crystal Alignment

The data processing programmes have been written for the case where a real crystal axis is parallel to the rotation axis. In this condition two reciprocal lattice axes are in the plane of the incident x-ray beam. If the crystal axes are orthogonal, or if this real axis is the unique axis in a monoclinic space group, the crystal may be aligned on the camera by a series of still photographs as described below.

Using still photographs the crystal can be set so that the incident x-ray beam is parallel to a real lattice axis, and hence, if the axes satisfy the conditions given above, the rotation axis is perpendicular to a second real lattice axis. These zone axis photographs are identical to the still setting photographs taken on precession cameras.

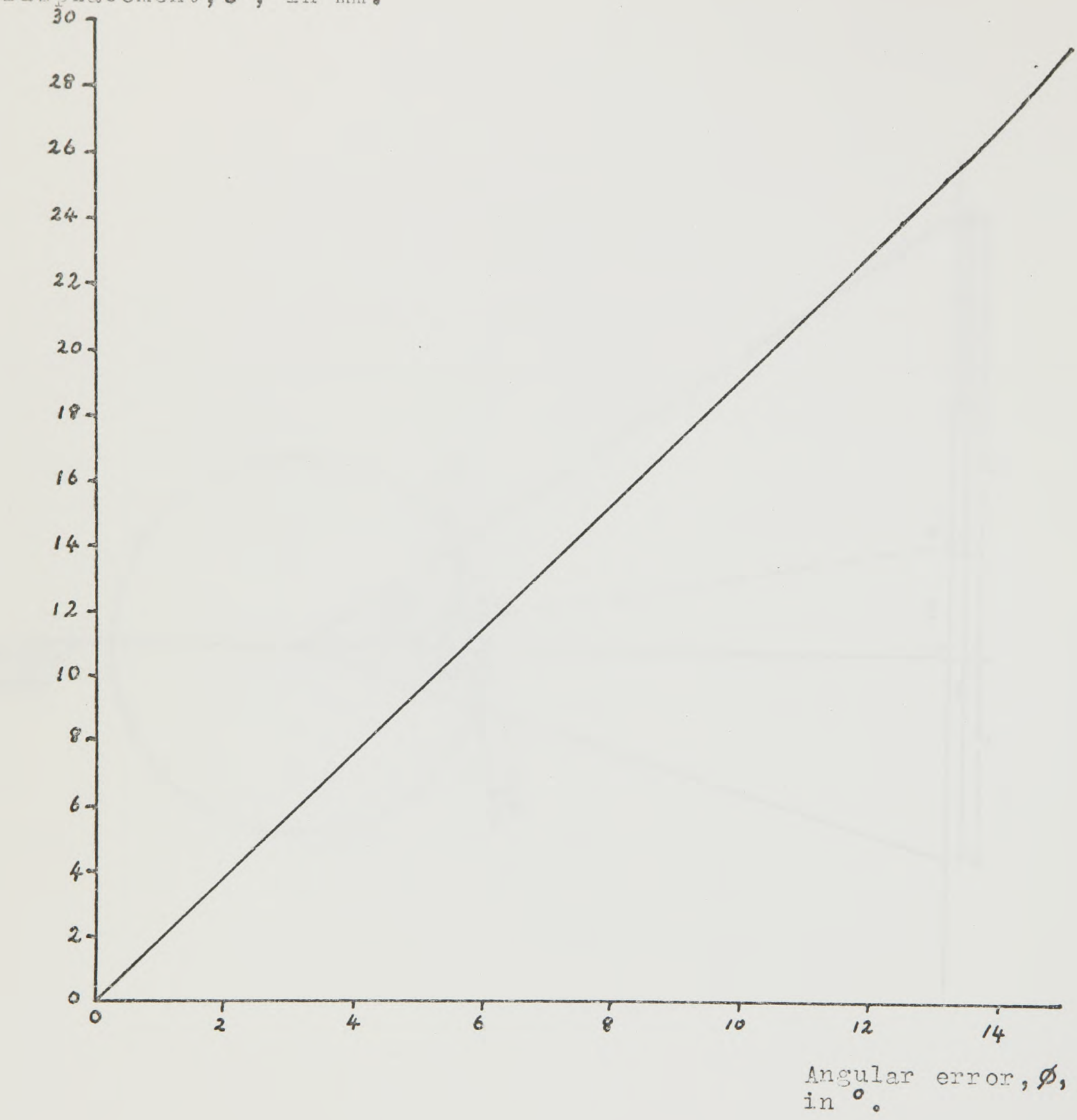
Consider a crystal with orthogonal axes, mounted about the b axis with the c* axis parallel to the incident x-ray beam. The still photograph comprises a series of circles corresponding to l = 1,2,3...etc., and centred on the position of the straight

FIGURE 4.14



The still photograph of a crystal mis-set by ϕ°.

FIGURE 4.15



The angular correction curve for a lysozyme crystal in orientation 2 with c^* approximately anti-parallel to the X-ray beam. The crystal to film distance has been set at 100 mm. for this curve.

through beam. The geometrical representation is shown in Figure 4.13. The radius, R, of the l = 1 zone circle is given by:

$$R = D \tan 2\theta$$

and the value of θ is given by:

$$\cos 2\theta = (1-c^*) \qquad 4.13$$

Suppose now the crystal is mis-set by a small angle, ϕ; this situation is shown in Figure 4.14. The centre, C, of the l=1 circle is displaced a distance, ε, from the position of the direct beam. From the diagram:

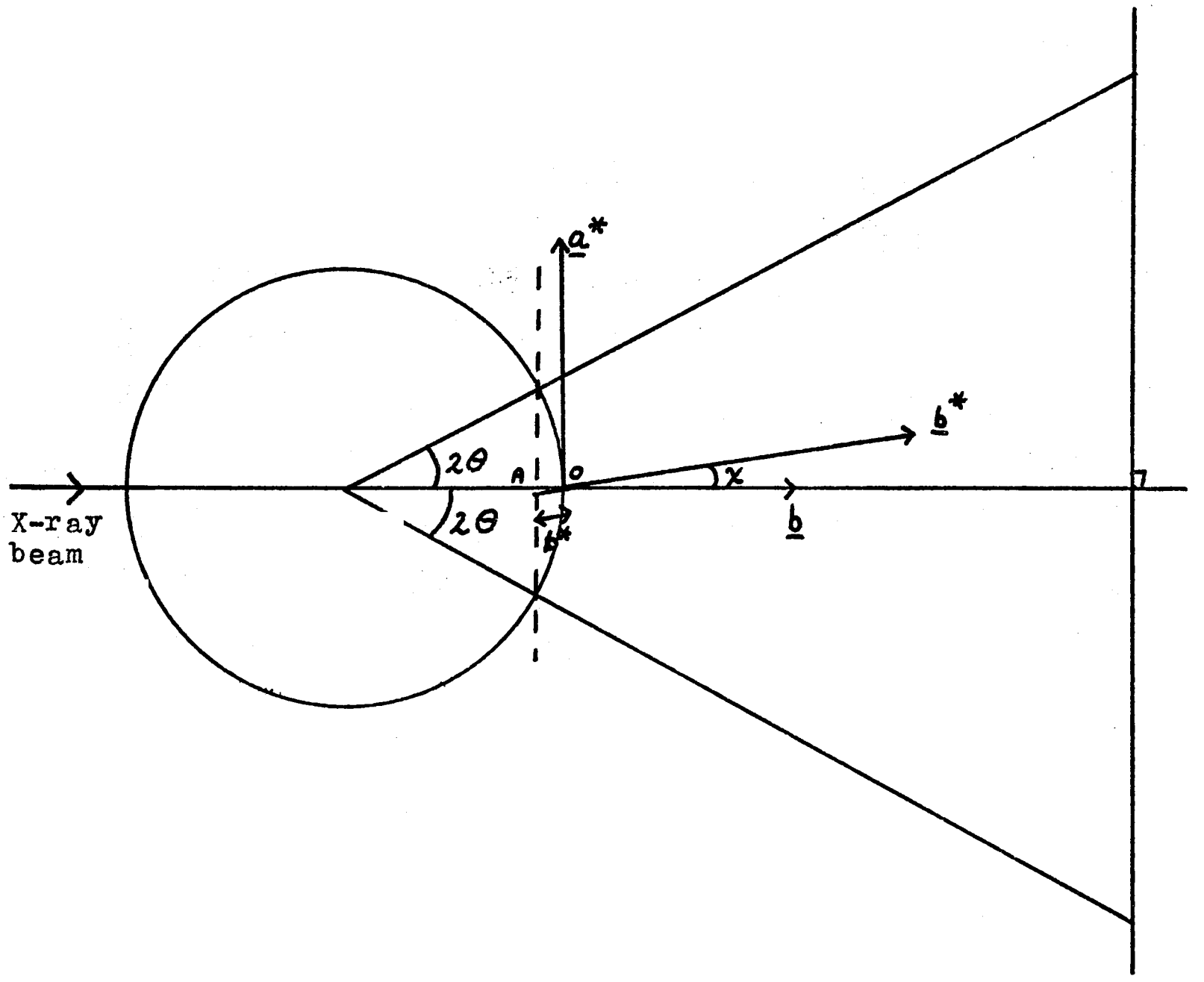
$$R_1 = D \tan (2\theta + \phi)$$
$$R_2 = D \tan (2\theta - \phi)$$

also

$$R_1 = R + \varepsilon \quad \text{and} \quad R_2 = R - \varepsilon$$
$$\therefore \quad R_1 - R_2 = 2\varepsilon$$
$$\therefore \quad \varepsilon = \tfrac{1}{2}(R_1 - R_2)$$
$$\therefore \quad \varepsilon = \frac{D}{2}[\tan (2\theta + \phi) - \tan(2\theta - \phi)] \qquad 4.14$$

If a plot of ε versus ϕ is constructed, the angular error, ϕ, corresponding to a measured error, ε, on the film may be readily found. The plot of ε versus ϕ is almost linear for relatively small values of ϕ as shown in Figure 4.15. Using correction curves such as Figure 4.15, the goniometer arcs can be set so that the crystal is rotating about a real lattice axis, and the position of the x-ray beam relative to the reciprocal lattice axes found. With this setting up method the goniometer arcs may be adjusted to within 15' of arc of their ideal positions. This is sufficiently accurate for the data processing programmes.

FIGURE 4.16



The still photograph of a perfectly set crystal with non-orthoganal axes.

The value of θ used in equation 4.14 derives from equation 4.13 and depends on which reciprocal axis is parallel to the x-ray beam, with a* and b* respectively parallel to the beam, equation 4.13 becomes:

$$\cos 2\theta = (1 - a^*) \qquad 4.13(a)$$

$$\cos 2\theta = (1 - b^*) \qquad 4.13(b)$$

If the two crystal axes in the plane of the incident x-ray beam are not orthogonal, the typical representation of perfectly set still photographs is shown in Figure 4.16. From the diagram the distance AO is given by:

$$AO = b^* \cos \chi$$

where χ is the angle between the $\underline{b}$ and $\underline{b}^*$ axes.

But $\underline{b} \cdot \underline{b}^* = \lambda$

and $b \cdot b^* = b \cdot b^* \cos\chi = \lambda$

$$\therefore \quad \cos\chi = \frac{\lambda}{bb^*}$$

$$\therefore \quad AO = \lambda/b.$$

$$\cos 2\theta = (1-AO)$$

$$\therefore \cos 2\theta = (1-\lambda/b) \qquad 4.15$$

Equation 4.15 is the more general form of equation 4.13(b); there are similar equations corresponding to equations 4.13 and 4.13(a). Equation 4.14 remains the same whether or not the axes are orthogonal.

A typical method of setting up a crystal would be as follows. The crystal is mounted on the goniometer head so that a real lattice axis is approximately parallel to a goniometer arc. Still photographs are then taken with this arc parallel to the

x-ray beam. Angular corrections are found from this photograph which allow adjustments to be made to the goniometer head arc, and the rotation axis to bring the real lattice axis parallel to the incident x-ray beam. The crystal is then rotated until the third real lattice axis is parallel to the x-ray beam, and the second goniometer head arc is adjusted from measurements taken from a second still photograph. As a final check a still photograph superimposed upon one taken with the crystal rotated through 180° may be taken. If the goniometer head arc is perfectly set, the two circles from these two exposures should be concentric. This check should be repeated for the other goniometer arc.

This alignment procedure has been suitable for all the crystals so far examined on the camera.

4.6 Lysozyme Photographs

It was decided to use a crystal of hen egg-white lysozyme as a test crystal for the camera since these crystals diffract strongly, and three-dimensional diffractometer data were available for them. The space group of these crystals is $P4_32_12$, and the unit cell dimensions are:

$$a = b = 79.1\text{Å} \quad c = 37.9\text{Å}$$

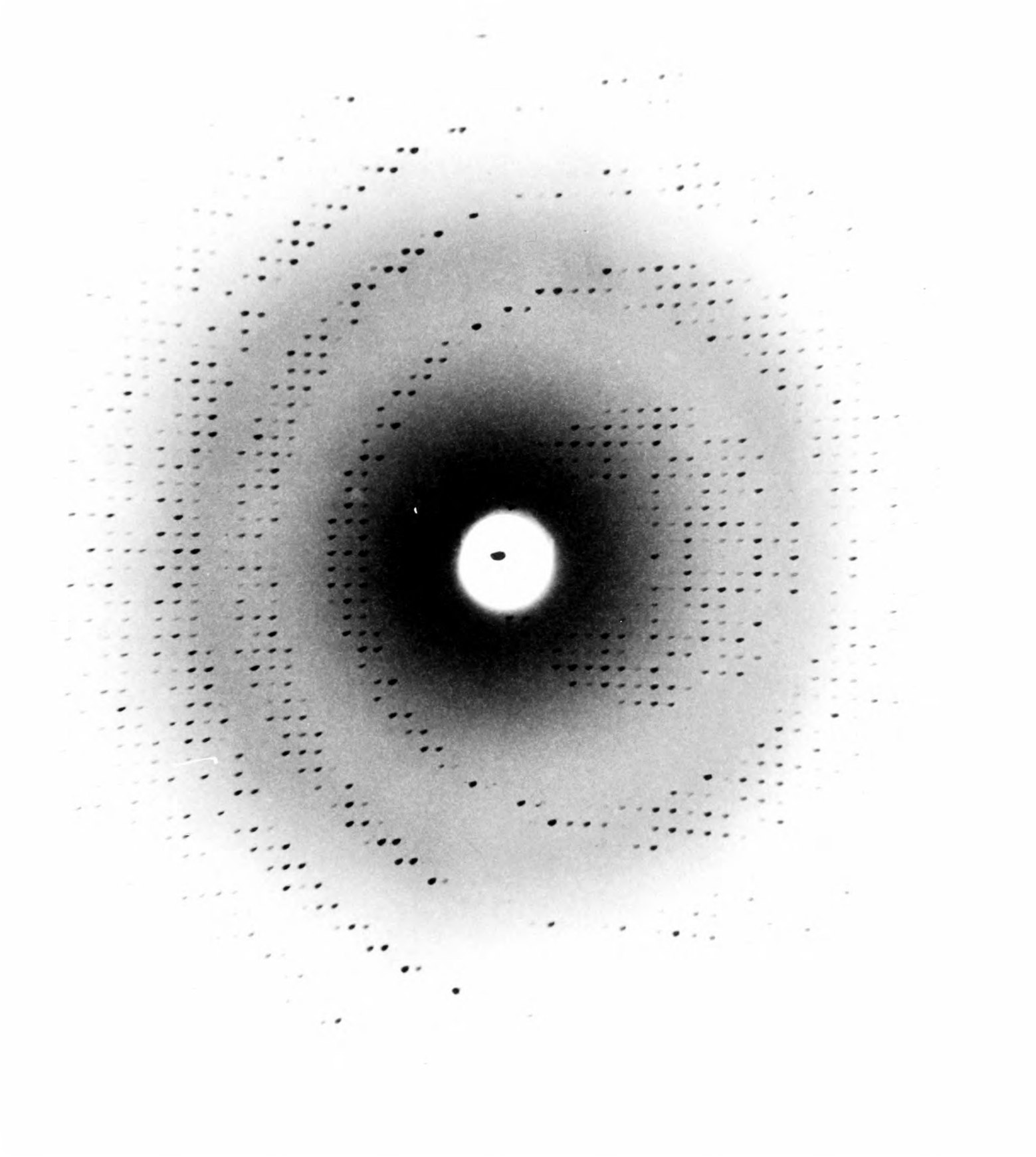
The various elements of the camera were first aligned with respect to the centre of the χ circle. A small metal tube, approximately 5 mm in length and 1 mm internal diameter, was mounted on a goniometer head which in turn was mounted on the camera. By viewing the tube through the telescope and rotating it about the χ and rotation axes, the tube was positioned about the centre of the rotation axis and in the centre of the χ circle

and perpendicular to it. The whole goniometer was then rotated on the base plate about the central securing bolt, which may be seen beneath the stepping motor in Figure 4.2, until the limiting aperture of the collimator was co-linear with the telescope and tube. The collimator itself was then rotated until all three apertures were co-linear with the telescope and tube. If necessary the collimator height was adjusted at this stage. Finally, the slide carrying the telescope, and subsequently the film holder, was adjusted so that it too was colinear with the other camera elements. The camera was then aligned on a Rotating Anode X-ray Generator so that the x-ray beam passed down the centre of the collimator and through the centre of the χ circle.

A lysozyme crystal was mounted in a quartz capillary tube with the b axis parallel to the axis of the tube. The crystal was then aligned on the camera, using the procedure outlined in the previous section, so that the b axis was parallel to the rotation axis. The zero angle of the rotation axis was defined as the position where the c* axis was anti-parallel to the x-ray beam.

Tests were then carried out to determine the amount of any "back-lash" in the rotation axis gearing. A still photograph was taken at $\phi = 0^{\circ}$, and then the axis rotated $+5^{\circ}$ and -5° before another still photograph taken superimposed on the first. The l=1 circle on the photograph was split slightly indicating a mis-setting of approximately 15' between the two "zero" positions. A similar photograph was taken, but this time the zero position was approached from the negative side for each still photograph. In this case there was no evidence of any splitting between the two l=1 circles. This result appeared to indicate that the

FIGURE 4.17



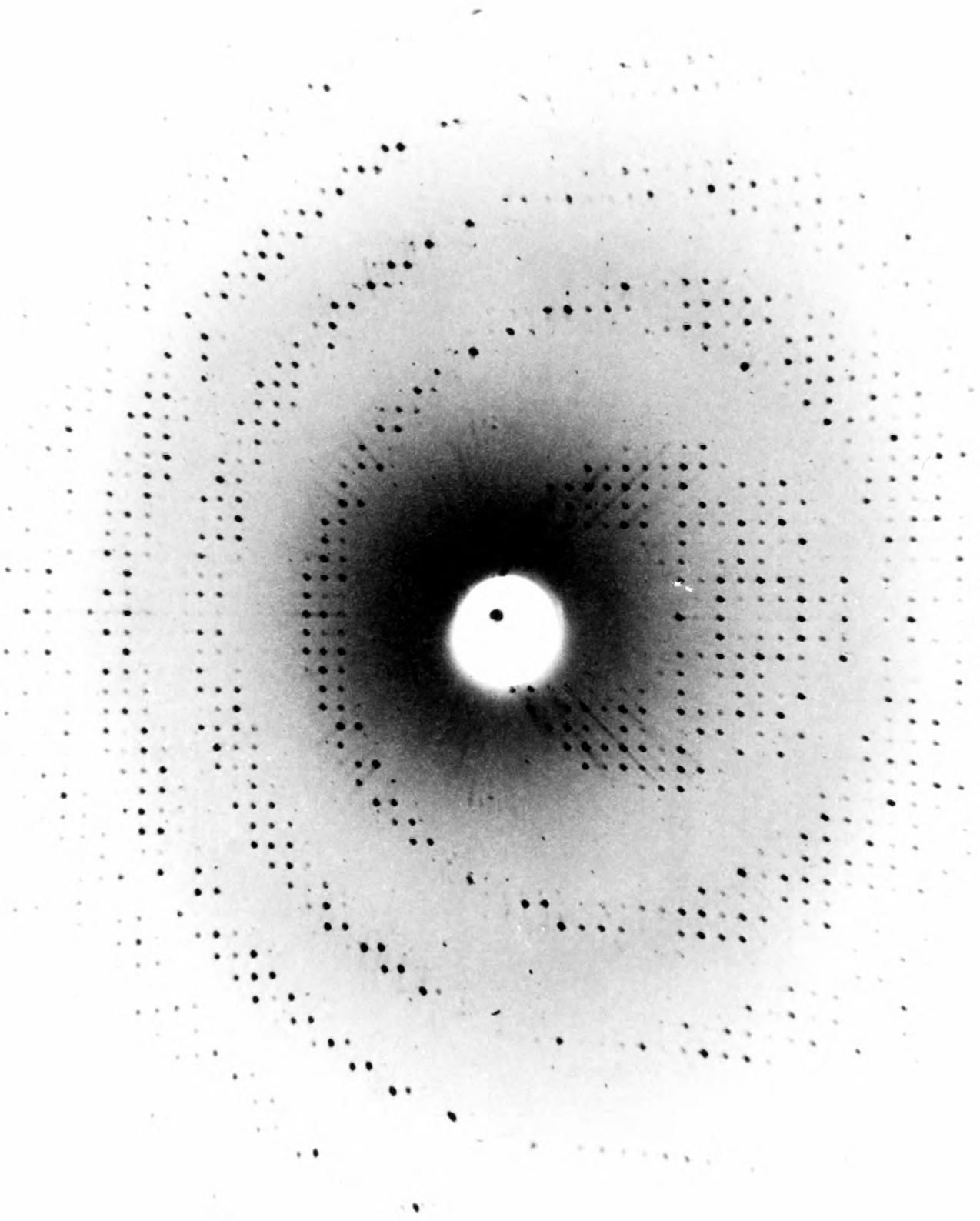
A rotation photograph of lysozyme in orientation 2 in the range 5° to 10°. A monochromator was used to filter the radiation.

back-lash could be kept to a tolerable level if the rotation axis was brought to any position in the positive direction. The fact that there is back-lash in the gearing does, of course, mean that the absolute position of the rotation axis at any one time is not known precisely. However, this should not be a serious drawback since it will not affect the positions of reflections on the films.

A computer programme was used to predict the position of the reflections on a film for a given rotation range (see next section). It was determined that for lysozyme crystals, in this setting, rotation ranges of 5^{o} gave a relatively large number (approx. 600) of reflections on each of the films, but with very few (less than 10) overlapping reflections. Data was considered to a lattice spacing of 3.5Å.

The graphite monochromator was fitted to the rotating anode generator and adjusted to give the copper Kα line. Using this monochromatic radiation a series of rotation photographs was taken of the lysozyme crystal using Ilford Industrial G x-ray film. 5^{o} rotation ranges were used starting from 0^{o} and moving in a positive direction. The x-ray generator was operated at 40 kV., 50 mA., and a 90 sec. pause time used. A typical photograph is shown in Figure 4.17. A strong ring at a lattice spacing of approximately 4Å was observed in each photograph. This ring was later found to be due to the quartz capillary tube in which the crystal was mounted. It is not observed in precession photographs due to the presence of the layer-line screen which prevents this scattering from reaching the film. In future, crystals should be mounted in glass capillary tubes which do not

FIGURE 4.18



A rotation photograph of a lysozyme crystal in orientation 2 in the range 5° to 10°, using nickel filtered radiation.

give rise to this ring.

On each rotation photograph the position of the direct beam was marked by removing the back-stop and opening the x-ray shutter for two or three seconds. This position was needed for the processing of the films which is described in the next section.

In all, the crystal was rotated through 45^{o} so that 9 photographs were taken.

The monochromator was then removed from the x-ray generator, and a 0.022 mm nickel filter placed in the incident x-ray beam. Several more 5^{o} rotation photographs were taken using this nickel filtered radiation; a typical example is shown in Figure 4.18. The spot shapes were better, and the intensities higher with this nickel filtered radiation, than with the radiation from the monochromator. This may indicate that the monochromator had not been aligned to give its optimum output, or that it inherently produces a weaker beam with an asymmetric cross-section.

Further testing of the camera was suspended at this point until progress had been made with the computer programmes needed to process the film data.

4.7 Film Processing

Before processing, the information on a film must be reduced to a digital form. This is achieved using a densitometer which measures the optical density at discrete points over the film. The densitometer used in this laboratory is a Photoscan P1000 manufactured by Optronics Inc. It is a drum-type densitometer and estimates the optical density from the transmittance of a light beam through the film. The film may be scanned on 50μ, 100μ or 200μ rasters, and the optical density is recorded on a scale from 0 to 255, where 255 corresponds to an optical

density of 2 or 3 O.D. units dependent on the choice of the operator. It is normally used on the O.D. 2 range. A similar instrument to this has been evaluated by Nockolds and Kretsinger (1970). They found that the densitometer was linear up to a value of O.D. 1.9 on Ilford Industrial G x-ray film with the 200μ raster. Integrated intensities were reproducible to a precision of ± 1%. The densitometer in this laboratory is an off-line device and outputs the optical density readings on to magnetic tape; one magnetic tape record corresponds to a strip of optical density readings across the film.

The integrated intensity for a reflection on a film is obtained by summing the O.D. readings within a small region containing the reflection, and subtracting from this sum the estimate of the background intensity in the region. This process obviously requires the use of a digital computer. It was decided to use the Ferranti Argus 500 computer in the laboratory to process the film data; this computer has been described in section 3.2.9 "Data Processing". The advantages of using this computer are:

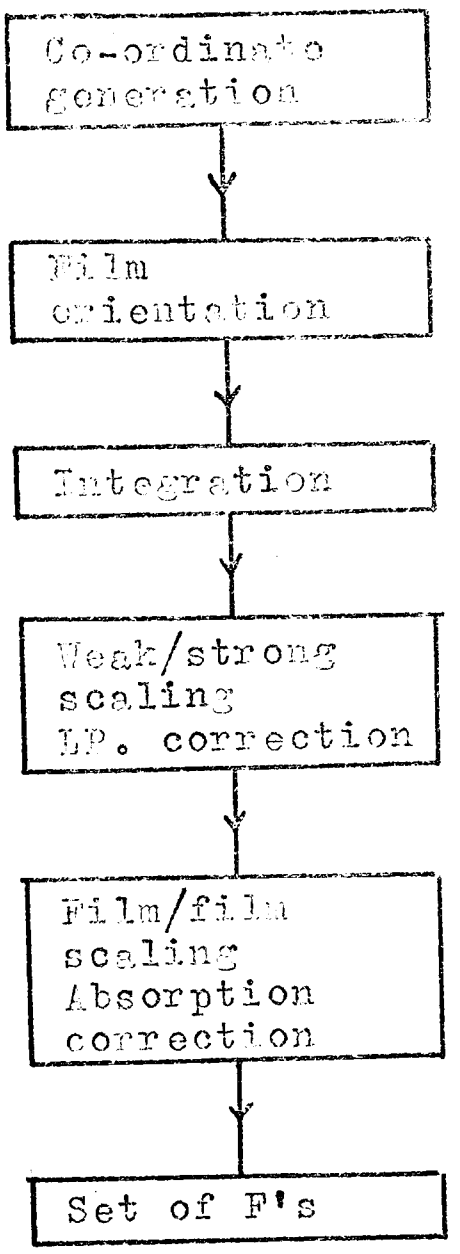
1. The "hands-on" approach is useful when developing the system.

2. It has an on-line cathode ray tube which is very useful for film orientation; which will be described later.

Unfortunately the relatively small amount of core store available (12K words) makes the programming more difficult. The programmes are written in a combination of FORTRAN and the Argus Assembly Language, "APRIL".

The main difficulty in processing rotation photographs

FIGURE 4.19



The scheme of data processing for rotation photographs.

lies in indexing the reflections on a film, or, conversely, in predicting the exact coordinates of the reflections on a film given an imperfect crystal and camera setting. The approach adopted in this case has been to generate the coordinates of the reflections on a film assuming a perfect crystal setting, and then to derive empirical correction factors (i.e. an orientation matrix) which, when applied to these coordinates, will generate the true film coordinates of the reflections. This process must be capable of predicting the reflection positions with an error of at most 2 raster units (0.2 mm with the 100μ raster) in either direction.

In some ways this approach may be compared to the graphical method of indexing rotation photographs using Bernal Charts (see Buerger (1942)). These charts are constructed assuming perfect crystal and camera settings. The photographs are then laid on top of the charts and the reflections indexed by eye; any mis-setting which results in disparities between the charts and the photographs is allowed for mentally.

Subsequent programmes are then required to:

1 Calculate the integrated intensities.

2 Scale together weak and strong films of the same rotation range, and apply the LP correction.

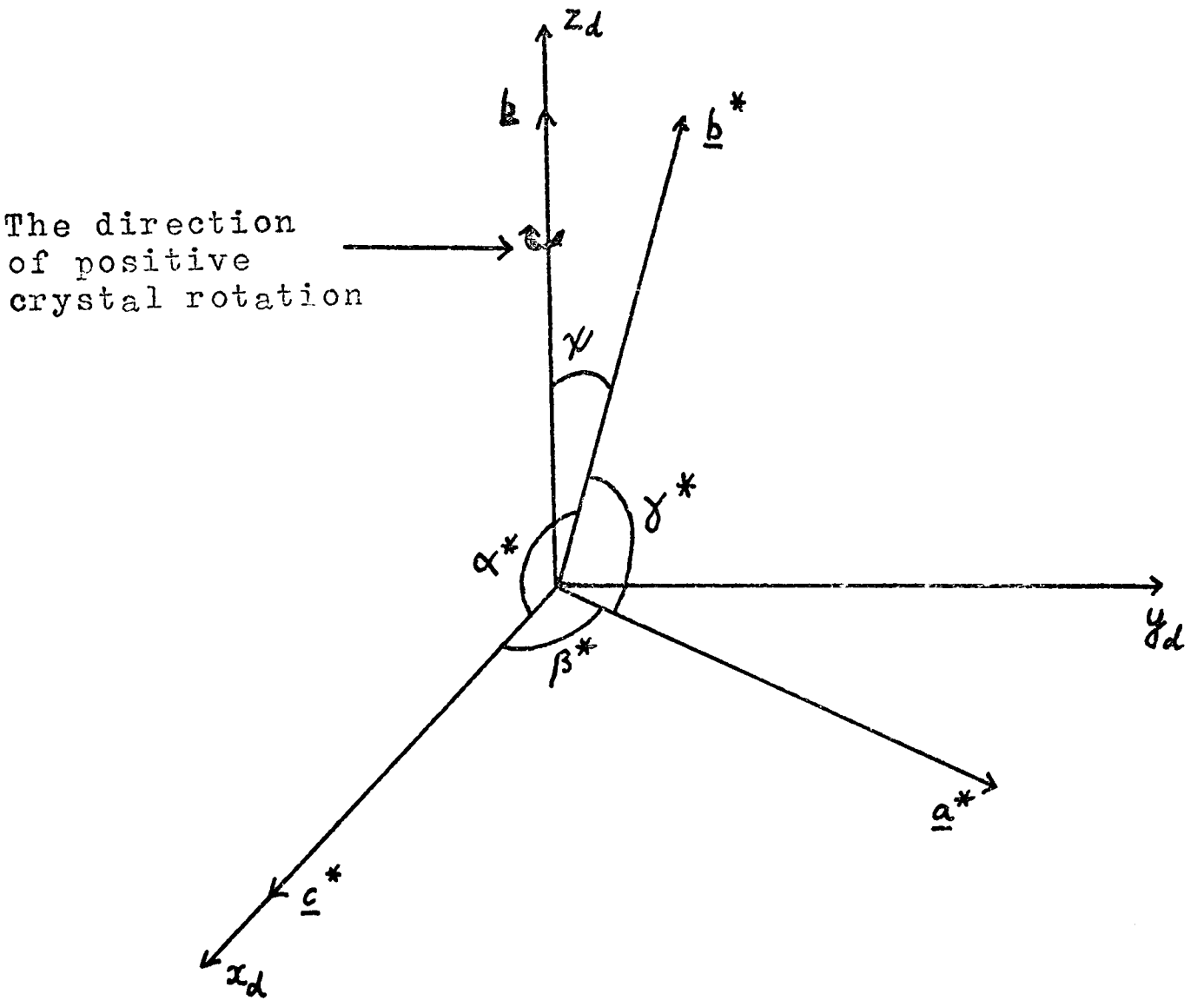
3 Scale together films of different rotation ranges, and, if necessary, apply an absorption correction.

The general outline of the data processing is shown schematically in Figure 4.19.

(a) Coordinate generation

The method used to calculate which reflections occur on

FIGURE 4.20



The relationship between the orthoganol system x_d, y_d, z_d and the crystal axes in orientation 2.

a film demands that a real crystal axis is parallel to the rotation axis. It is, in principle, possible to calculate reflection coordinates for a perfectly general crystal setting, but the limitations imposed by the small storage capacity, and relatively slow speed of the Argus computer make this impracticable.

In order to derive the necessary equations we will consider the crystal to be rotating about the b axis ; the zero rotation angle is defined at the position where the c* axis is anti-parallel to the x-ray beam. By permuting the axes cyclically, the equations for the other two settings can be generated from the equations given below.

We require an orthoganol axial system (x_d, y_d, z_d) which rotates with the crystal; the relationship between this axial system and the crystal axes is shown in Figure 4.20. z_d is the rotation axis. The projections of the crystal axes on the orthogonal coordinate system are:

$$x_{d_{a^*}} = a^* \cos\beta^* \qquad x_{d_{b^*}} = b^* \cos\alpha^* \qquad x_{d_{c^*}} = c^*$$

$$y_{d_{a^*}} = a^* \sin\beta^* \qquad y_{d_{b^*}} = \frac{b^*}{\sin\beta^*}(\cos\gamma^* - \cos\alpha^*\cos\beta^*) \qquad y_{d_{c^*}} = 0$$

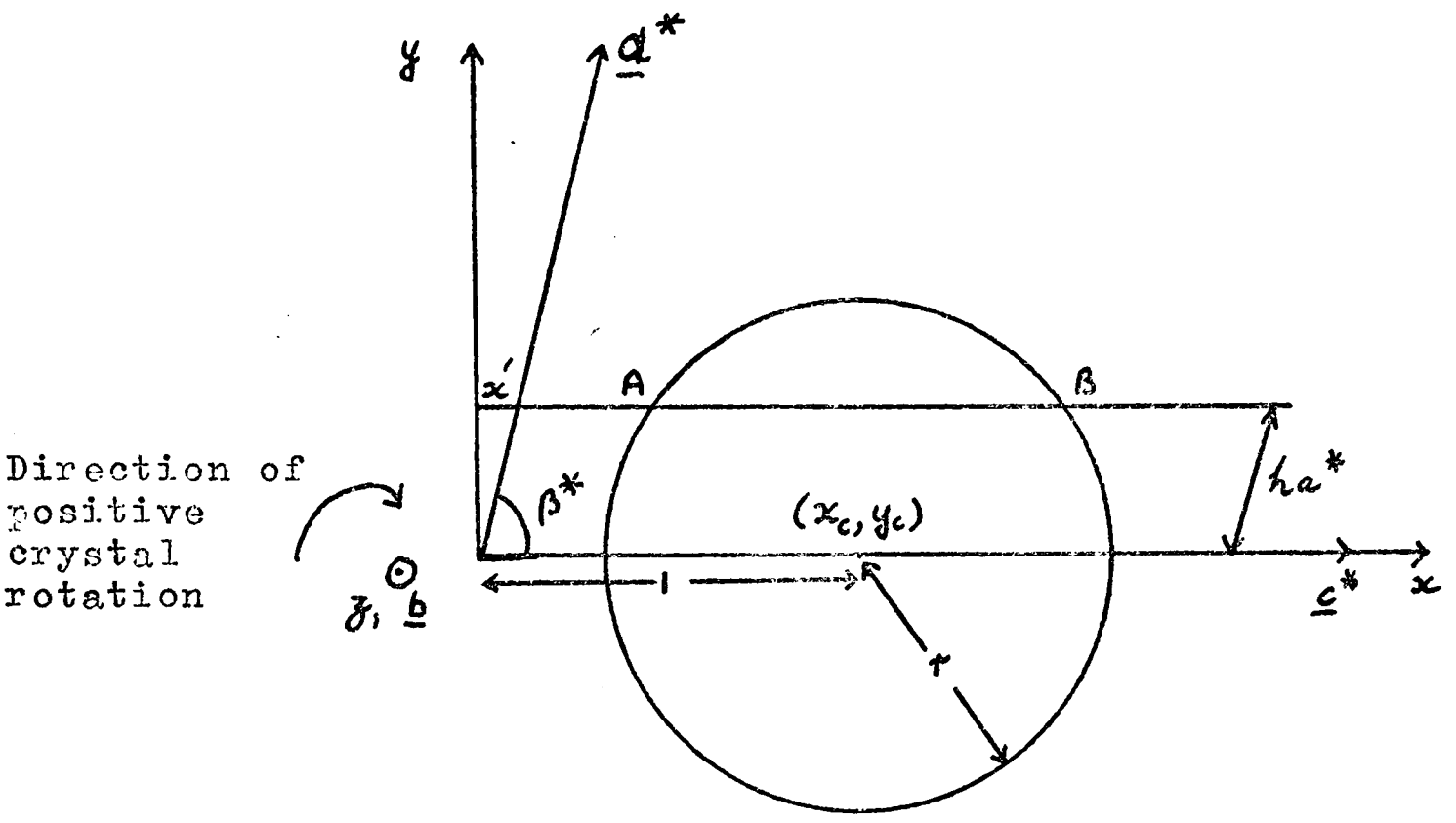
$$z_{d_{a^*}} = 0 \qquad z_{d_{b^*}} = b^* \cos\psi \qquad z_{d_{c^*}} = 0$$

where ψ is the angle between b and b* i.e.:

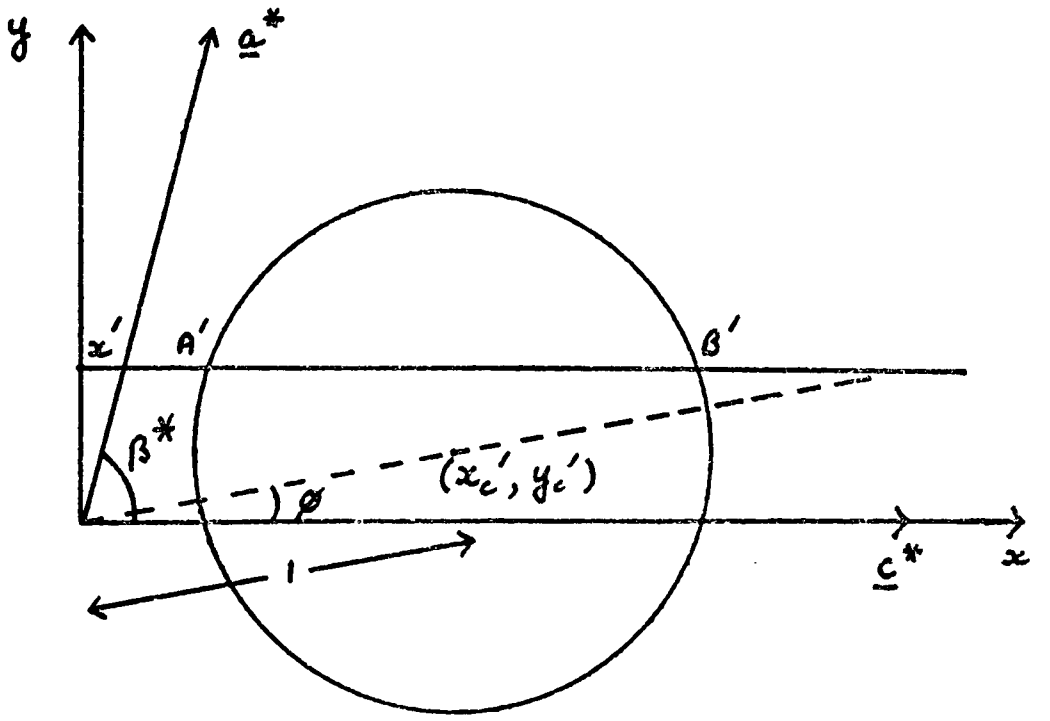
$$\cos\psi = \frac{\lambda}{b.b^*}$$

The reciprocal lattice point defined by the indices (hkl) thus has coordinates in the orthogonal system given by:

FIGURE 4.21



a) An upper reciprocal lattice level at zero rotation.



b) The upper level shown in (a) at a positive rotation of ϕ^{o}.

$$x_d = h\,x_{d_{a*}} + k\,x_{d_{b*}} + l\,x_{d_{c*}}$$

$$y_d = h\,y_{d_{a*}} + k\,y_{d_{b*}} + l\,y_{d_{c*}}$$

$$z_d = h\,z_{d_{a*}} + k\,z_{d_{b*}} + l\,z_{d_{c*}}$$

Figure 4.21(a) shows the position of the crystal axes and sphere of reflection at zero crystal rotation ($\phi = 0$) for an upper level; i.e. k is non-zero. (xyz) is a stationary orthogonal coordinate system.

The radius, r, of the circle of reflection is given by:

$$r^2 = 1 - (kb^* \cos\psi)^2 \qquad 4.16$$

and the centre of the circle is at the point (x_c, y_c). Consider now the line AB which corresponds to a particular value of h; the equation of the line is:

$$y = ha^* \sin\beta^* \qquad 4.17$$

The x coordinates of the points A and B where the line cuts the circle may be found by solving the equation of the line (4.17) simultaneously with the equation of the circle which is:

$$(x-x_c)^2 + (y-y_c)^2 = r^2 \qquad 4.18$$

where r is given by equation 4.16.

Substitution of 4.17 in 4.18 results in expressions for the x coordinates:

$$x_A = x_c - \sqrt{r^2 - (h_{a*}\sin\beta^* - y_c)^2} \qquad 4.19$$

$$x_B = x_c + \sqrt{r^2 - (h_{a*}\sin\beta^* - y_c)^2} \qquad 4.20$$

The presence of the square-root signs results in three possibilities:

i. If $r^2 > (ha^*\sin\beta^* - yc)^2$, the line will cut the circle at two discrete points.

ii. If $r^2 = (ha^* \sin\beta^* - yc)^2$, the line will cut the circle at only one point $(x_A = x_B)$

iii. If $r^2 < (ha^* \sin\beta^* - yc)^2$, the line will not cut the circle

The coordinates of A and B may be related to the reciprocal lattice system by the equations:

$$\left.\begin{aligned} x_A^* &= x_A - x' \\ x_B^* &= x_B - x' \end{aligned}\right\} \qquad 4.21$$

where: $x' = ha^* \cos\beta^*$

From these values, the l indices corresponding to the points A and B are readily found from the expressions;

$$l_A = \frac{x_A^*}{C^*} ; \qquad l_B = \frac{x_B^*}{C^*} \qquad 4.22$$

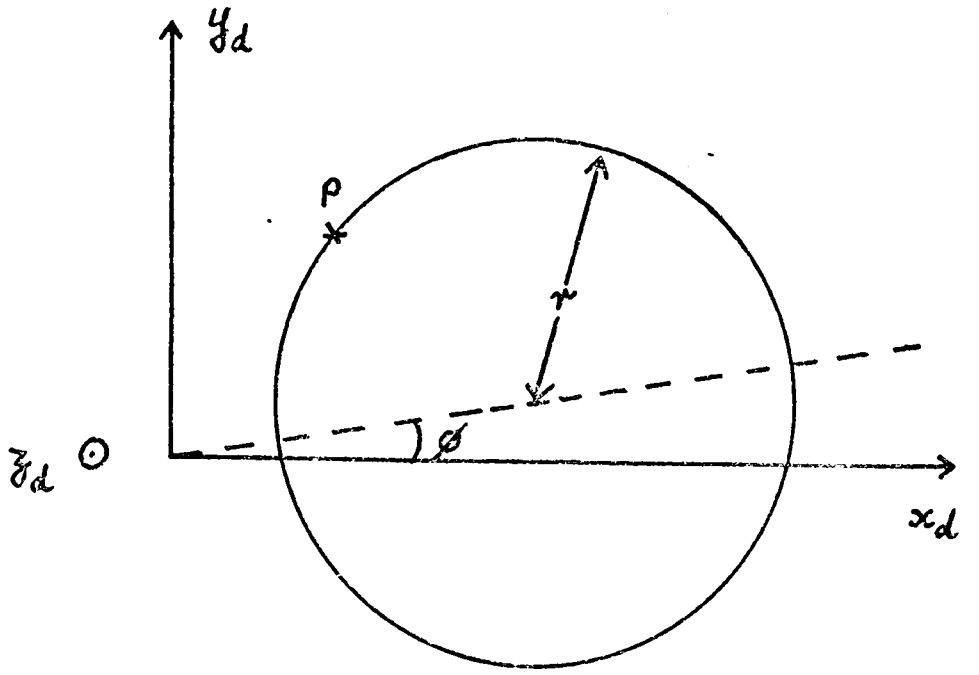
Consider now that the crystal has rotated through a positive angle ϕ. This is shown in Figure 4.21(b), though, in this figure the reflecting circle has been rotated instead of the crystal. By definition, the distance from the origin of the coordinate system to the centre of the circle is unity. The coordinates of the centre of the circle (x_c, y_c) are, therefore, given by:

$$\left.\begin{aligned} x_c &= \cos\phi \\ y_c &= \sin\phi \end{aligned}\right\} \qquad 4.23$$

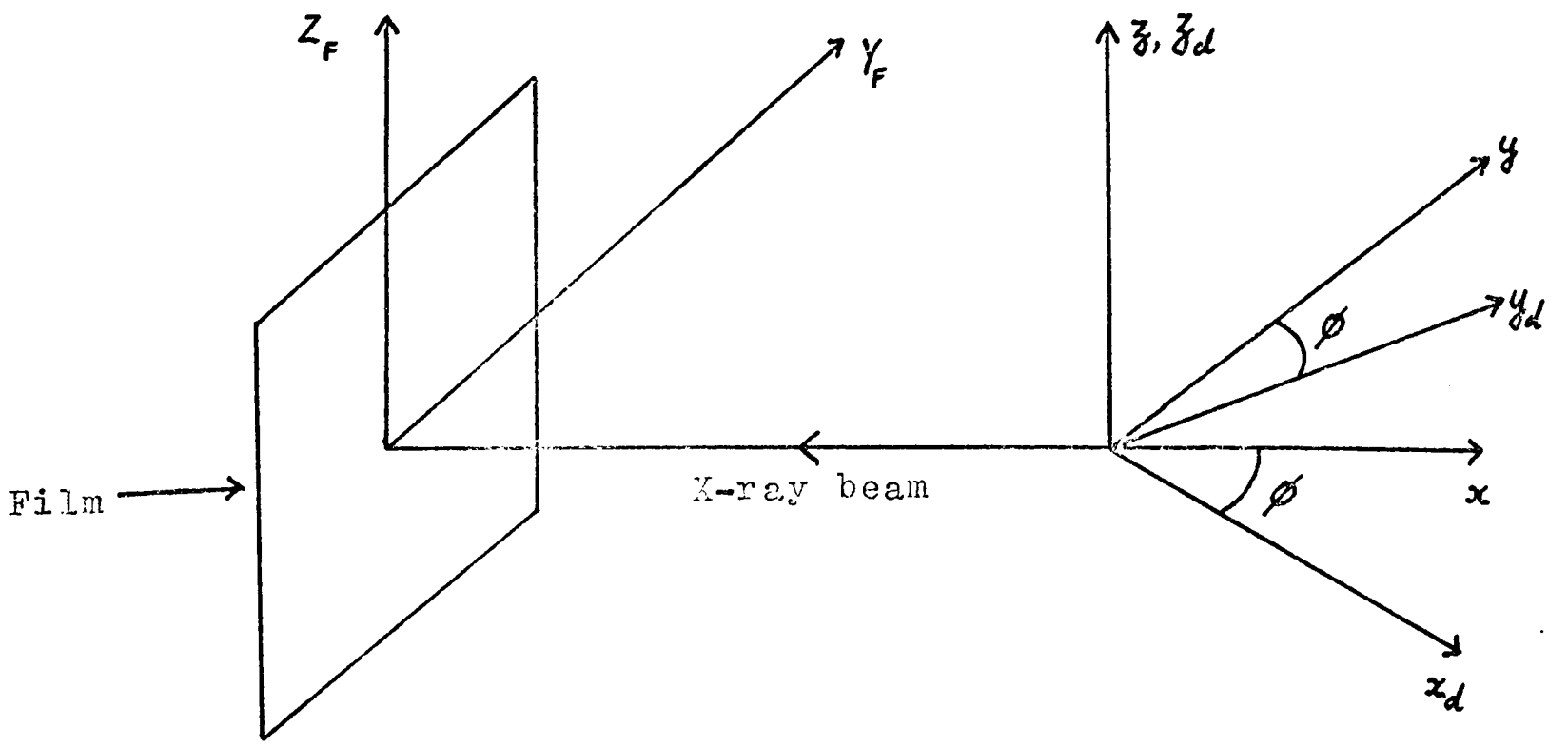
In this case, the line:

$$y = ha^* \sin\beta^* \qquad (4.17)$$

FIGURE 4.22



a) The reciprocal lattice point, P, cutting the sphere of reflection at a rotation angle of ϕ^o.



b) The relationship between the film and crystal co-ordinate systems.

cuts the circle at the points A' and B'. By using the equations 4.18 to 4.22 the l indices, l'_A, l'_B, of these points can be found.

The points between A and A', and B and B' will thus cut the sphere during the rotation from 0 to ϕ^o, and it is therefore possible that reflections with indices:

$$h \quad k \quad l'_A \leqslant l \leqslant l_A$$

$$\text{and} \quad h \quad k \quad l'_B \leqslant l \leqslant l_B$$

will occur on the film.

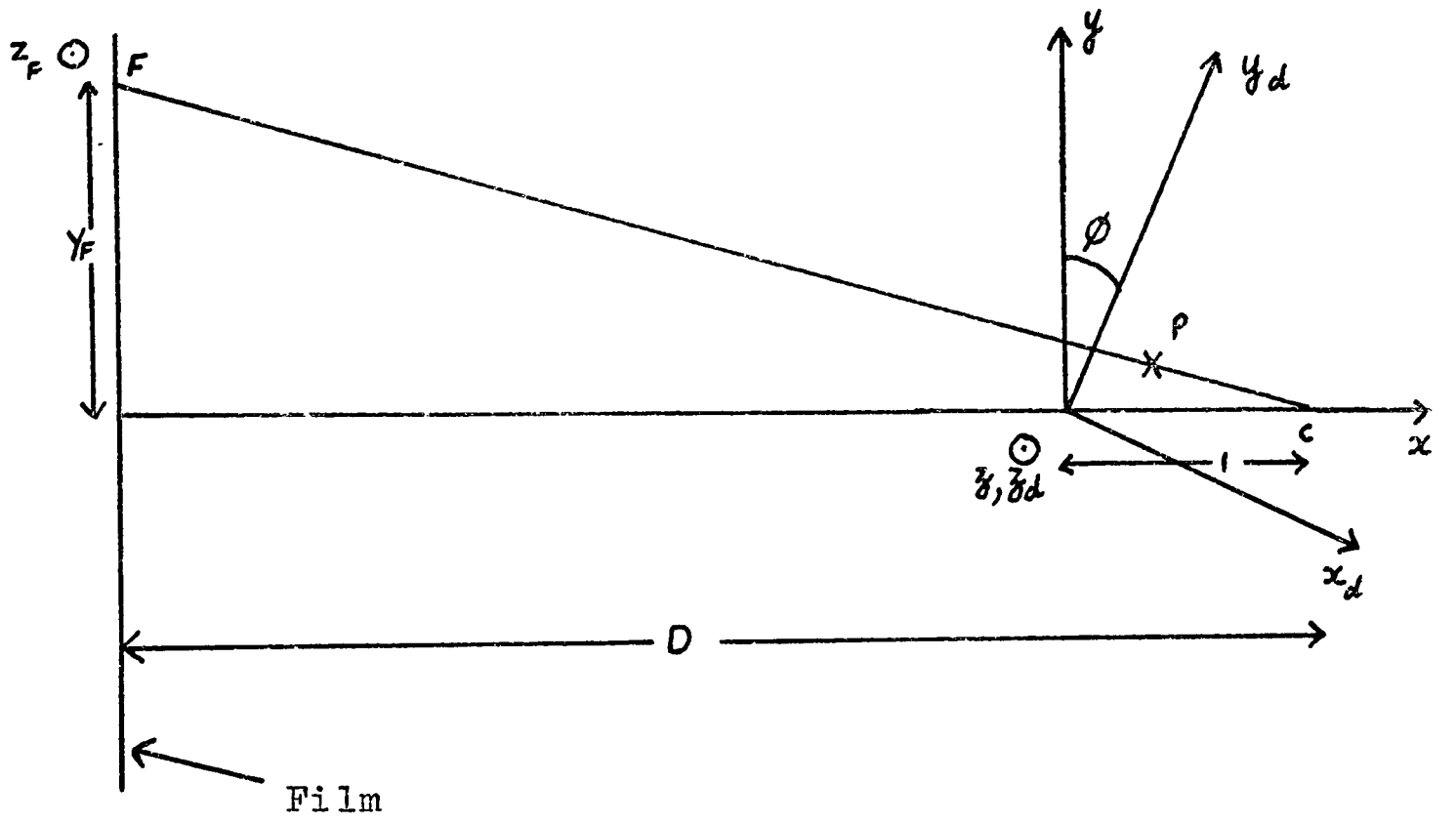
By extending this approach to cover all the combinations of h and k for a particular crystal it is possible to find the regions of reciprocal space which will give rise to reflections for a given rotation of the crystal. The mathematics is general for all rotation ranges not necessarily starting at zero. In this way only those reciprocal lattice points which will give rise to reflections in a given rotation range need be considered in greater detail. This leads to a great saving in computing time.

The next step in the process is to generate the coordinates of the reflections on the film. In order to do this, the precise angle at which each reflection occurs has to be calculated. Consider a reciprocal lattice point, P, with coordinates (x_d, y_d, z_d) which cuts the sphere of reflection at a rotation angle, ϕ; the situation is shown in Figure 4.22(a). Since the point P lies on the sphere of reflection, which is centred on $(\cos\phi, \sin\phi, 0)$, $(x_d\ y_d\ z_d)$must satisfy the equation for the sphere, i.e.:

$$(x_d - \cos\phi)^2 + (y_d - \sin\phi)^2 + z_d{}^2 = 1$$

$$\therefore \quad x_d{}^2 + y_d{}^2 + z_d{}^2 + (\sin^2\phi + \cos^2\phi) - 2x_d \cos\phi - 2y_d \sin\phi = 1$$

FIGURE 4.23



C represents the position of the crystal

D is the crystal to film distance

The reciprocal lattice point, P, giving rise to a reflection at the point, (Y_F, Z_F), on the film.

Putting $d^2 = x_d^2 + y_d^2 + z_d^2$ gives

$$2x_d \cos\phi + 2y_d \sin\phi - d^2 = 0$$

This equation may be solved in terms of $\tan\frac{\phi}{2}$ the solution being:

$$\tan\frac{\phi}{2} = \frac{2y_d \pm \sqrt{4y_d^2 + 4x_d^2 - d^4}}{2x_d + d^2} \qquad 4.24$$

Equation 4.24 gives two real values for ϕ corresponding to the two rotation angles at which the point P lies on the sphere; only one of these values will be in the rotation range under consideration.

To find the coordinates of the reflection on the film we define a coordinate system (Y_F, Z_F) on the film as shown in Figure 4.22(b). The reflection geometry is shown in Figure 4.23. The relationship between the coordinate systems (x,y,z) and $(x_d y_d z_d)$ is:

$$\left.\begin{aligned} x &= x_d \cos\phi + y_d \sin\phi \\ y &= y_d \cos\phi - x_d \sin\phi \\ z &= z_d \end{aligned}\right\} \qquad 4.25$$

Equations 4.25 then give the coordinates of P,(xyz), in this coordinate system. Figure 4.23 shows that:

$$\frac{Y_F}{D} = \frac{y}{1-x}$$

∴ From equations 4.25:

$$Y_F = \frac{D(y_d \cos\phi - x_d \sin\phi)}{(1 - x_d \cos\phi - y_d \sin\phi)} \qquad 4.26$$

Also from 4.23:

$$\frac{Z_F}{z_d} = \frac{FC}{PC}$$

$$\therefore \quad \frac{Z_F}{z_d} = \sqrt{\frac{D^2 + Y_F^2}{1-z_d^2}}$$

$$\therefore \quad Z_F = z_d\sqrt{\frac{D^2 + Y_F^2}{1-z_d^2}} \qquad 4.27$$

Equations 4.26 and 4.27 then give the coordinates of the reflection on the film. This approach is based on an earlier approach to the problem by Dr. M. Dobler.

When coordinates of all the reflections present on a film have been calculated, they can be sorted on Y_F and Z_F and checked for overlapping reflections.

A programme (JM1/MT/D) has been written for the Argus computer and uses this approach to generate all the reflections which occur on a film for a given setting and rotation range, and within given resolution limits. The programme generates all the reflections on the film and then checks them for overlaps; the minimum allowed spacing between reflections is an input parameter to the programme. If the rotation angle at which a reflection occurs lies close to the beginning of the rotation range, a flag associated with the reflection is set to 1; if the angle lies close to the end of the range, the flag is set to 2. Normally the flag has the value 0. The range over which the flags are set is an input parameter to the programme. Reflections which occur at the beginning or end of a rotation range will probably be only

partially recorded on the film; the remaining parts of these reflections will be recorded on films of neighbouring rotation ranges. It is hoped that the separate parts of such a reflection from different films can be summed to give the total reflection intensity. This, however, will have to be thoroughly tested. The programme outputs the reflection coordinates on to magnetic tape in the form:

$$h\ k\ l \quad Y_F \times 10 \quad Z_F \times 10 \quad \text{FLAG}$$

where Y_F and Z_F are in mm. relative to the position on the film of the direct beam.

Tests using the rotation photographs of the lysozyme crystal have shown that this programme is capable of predicting the reflection coordinates to an accuracy of approximately 1 mm. in each direction. This is not sufficiently accurate for the integration programme, and so corrections must be applied to these coordinates in order to generate the true reflection coordinates.

b) Film Orientation:

This procedure relies on being able to generate the correction factors to be applied to all the reflections on one film from a knowledge of the true and theoretical positions of a small number of reflections on the film. Various types of correction factor had been tried before a suitable method was found.

Using equations 4.25, 4.26 and 4.27 it is possible to calculate x_d, y_d, and z_d from Y_F and Z_F using the value of ϕ given by the coordinate generation programme. An attempt was made to index reflections using these calculated values of x_d, y_d and

z_d, but it proved unsuccessful, due to the relatively large differences between the true and theoretical values of Y_F and Z_F. However, the indices of the reflections could be found from the output of the coordinate generation programme, and x_d, y_d, z_d related to (hkl) by a 3 x 3 matrix; i.e.

$$\begin{pmatrix} x_d \\ y_d \\ z_d \end{pmatrix} = \begin{pmatrix} a & b & c \\ d & e & f \\ g & i & j \end{pmatrix} \times \begin{pmatrix} h \\ k \\ l \end{pmatrix}$$

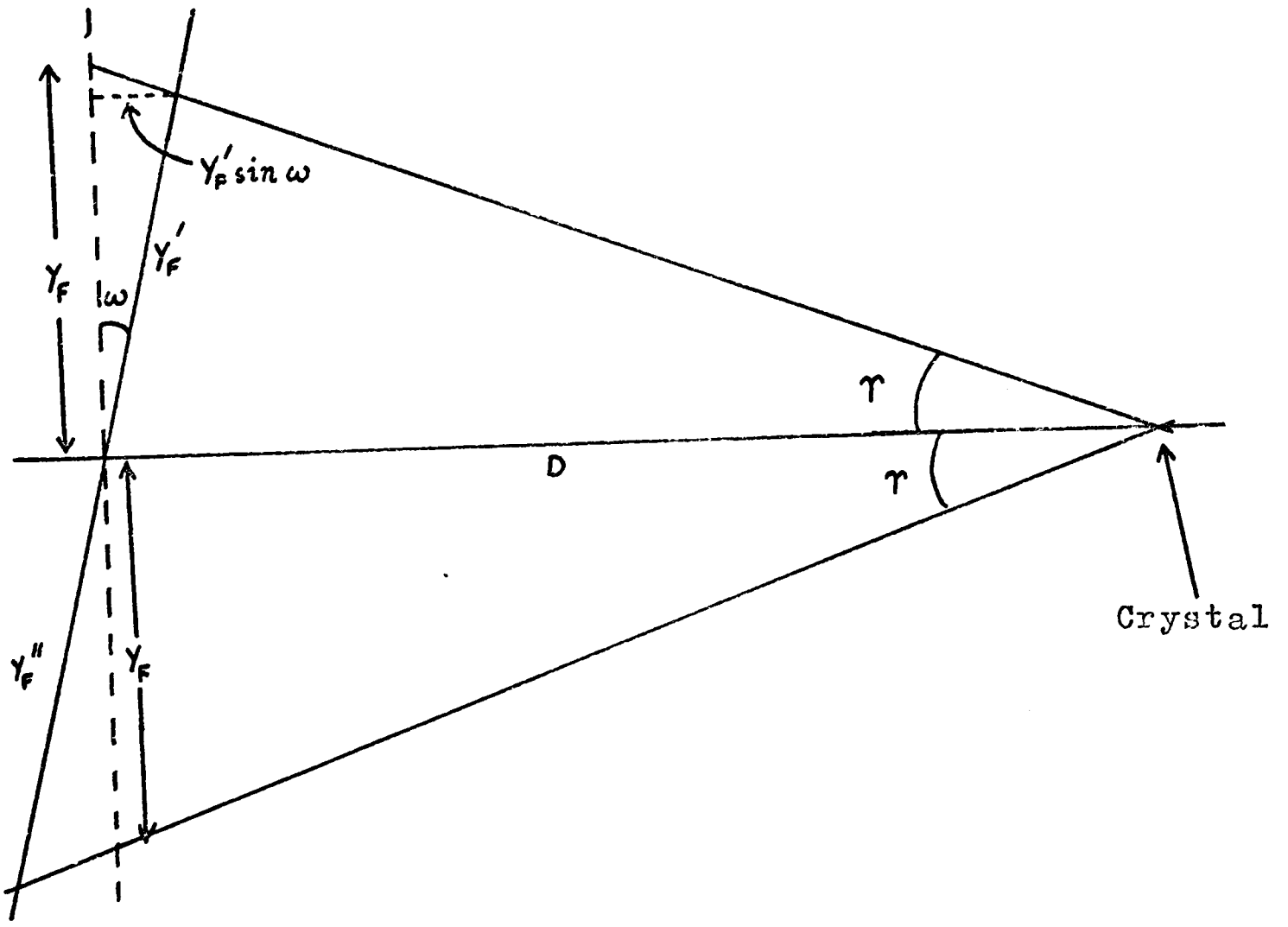
where ideally $a = x_{d_{a^*}}$ etc.

If the true $(x_d y_d z_d)$ are known for at least three reflections of known indices it is possible to calculate the coefficients a - j; this is equivalent to the calculation of a setting matrix on a diffractometer. It was hoped that by calculating such a setting matrix from a few reflections on a film, the matrix could then be used to generate the true positions of all the reflections on the film. This approach, however, proved to be unsatisfactory since it could predict some reflection coordinates to an accuracy of only 3 or 4 raster units. (0.3 - 0.4 mm).

A more empirical approach, in which correction factors are applied to the theoretical reflection positions, has proved satisfactory. This approach relies on the assumption that all the errors in the crystal setting and camera geometry can be assumed to lie in the film mounting. These errors are:

1. Displacement of the film in the Y_F Z_F plane
   This will result in additive correction factors being applied to the theoretical reflection positions.

FIGURE 4.24



The effect on a reflection of the film's being tilted about a vertical axis by an angle ω.

2. Imprecise crystal to film distance, which will result in multiplicative correction factors.

3. Rotation of the film in the $Y_F Z_F$ plane. This will result in the need to apply a rotation matrix to the theoretical positions.

4. Film not perpendicular to the incident X-ray beam. This situation is shown in Figure 4.24 from which it may be seen that:

$$Y_F = Y_F' \cos\omega + Y_F' \sin\omega \tan 2\gamma$$

$$Y_F = Y_F' \cos\omega(1 + \tan\omega \tan 2\gamma)$$

$$\therefore \quad Y_F' = \frac{Y_F}{\cos\omega(1+\tan\omega\tan 2\gamma)}$$

Setting $A = 1/\cos\omega$ and $B = \tan\omega$

$$Y_F' = \frac{A\, Y_F}{(1+B\tan 2\gamma)}$$

Assuming ω is small:

$$Y_F' = A\, Y_F(1-B\tan 2\gamma)$$

But $\tan 2\gamma = Y_F/D$

$$\therefore \quad Y_F' = A\, Y_F(1-\frac{B}{D}Y_F)$$

$$\therefore \quad Y_F' = AY_F - CY_F^2 \quad \text{where } C = \frac{AB}{D}$$

By a similar argument:

$$Y_F'' = -(AY_F + CY_F'^2)$$

Similar corrections will apply to Z_F if the film is tilted about an axis parallel to the y axis.

These four types of error may, therefore,be accommodated by the use of a quadratic polynomial in the predicted reflection coordinates. The true reflection coordinates, Y_C and Z_C, are given by expressions of the form:

$$\left.\begin{aligned} Y_C &= a\,Y_F^2 + b\,Y_F Z_F + c\,Z_F^2 + d\,Y_F + e\,Z_F + f \\ Z_C &= g\,Y_F^2 + i\,Y_F Z_F + j\,Z_F^2 + m\,Y_F + n\,Z_F + p \end{aligned}\right\} \quad 4.28$$

where a - p are constants for a given film. These constants may be found if the Y_C, Z_C, Y_F and Z_F are known for a minimum of six reflections. If these values are known for more than six reflections, a least-squares approach may be used to calculate the constants. In general, the equations 4.28 cannot be solved exactly if the coordinates of more than six reflections are used- there will be small errors, ε_y and ε_z, where ε_y and ε_z are given by

$$\varepsilon_y = Y_C - (a\,Y_F^2 + b\,Y_F Z_F + c\,Z_F^2 + d\,Y_F + e\,Z_F + f)$$

$$\varepsilon_z = Z_C - (g\,Y_F^2 + i\,Y_F Z_F + j\,Z_F^2 + m\,Y_F + n\,Z_F + p)$$

If there are n reflections for which $Y_C Z_C$ and $Y_F Z_F$ pairs are known, the sums, E_y and E_z of the squares of the errors are given by:

$$E_y = (\varepsilon_y^2)_1 + (\varepsilon_y^2)_2 + \ldots\ldots + (\varepsilon_y^2)_n$$

$$E_z = (\varepsilon_z^2)_1 + (\varepsilon_z^2)_2 + \ldots\ldots + (\varepsilon_z^2)_n$$

The best values of the constants a to p are given by partially differentiating E_y and E_z with respect to each constant in turn and setting the differentials to zero. The results of this process may be written in matrix form as:

$$\begin{pmatrix} Y_{C_1} & Z_{C_1} \\ Y_{C_2} & Z_{C_2} \\ \vdots & \vdots \\ Y_{C_n} & Z_{C_n} \end{pmatrix} - \begin{pmatrix} Y_{F_1}^2 & Y_{F_1} Z_{F_1} & Z_{F_1}^2 & Y_{F_1} & Z_{F_1} & 1 \\ Y_{F_2}^2 & Y_{F_2} Z_{F_2} & Z_{F_2}^2 & Y_{F_2} & Z_{F_2} & 1 \\ \vdots & \vdots & \vdots & \vdots & \vdots & \vdots \\ Y_{F_n}^2 & Y_{F_n} Z_{F_n} & Z_{F_n}^2 & Y_{F_n} & Z_{F_n} & 1 \end{pmatrix} \begin{pmatrix} a & g \\ b & i \\ c & j \\ d & m \\ e & n \\ f & p \end{pmatrix} = 0$$

$$\text{i.e.} \quad \underset{\sim}{Y_C} - \underset{\sim}{Y_F} \cdot \underset{\sim}{Q} = 0$$

$$\therefore \quad \underset{\sim}{Y_C} = \underset{\sim}{Y_F} \cdot \underset{\sim}{Q} \qquad 4.29$$

where $\underset{\sim}{Q}$ is the orientation matrix.

Pre-multiplying both sides of equation 4.29 by the transpose of $\underset{\sim}{Y_F}$, $\underset{\sim}{Y_F}^T$, gives:

$$\underset{\sim}{Y_F}^T \cdot \underset{\sim}{Y_C} = \underset{\sim}{Y_F}^T \cdot \underset{\sim}{Y_F} \cdot \underset{\sim}{Q}$$

$\underset{\sim}{Y_F}^T \cdot \underset{\sim}{Y_F}$ is a 6 x 6 matrix, and $\underset{\sim}{Y_F}^T \cdot \underset{\sim}{Y_C}$ a 6 x 2 matrix.

$$\text{let} \quad \underset{\sim}{G} = \underset{\sim}{Y_F}^T \cdot \underset{\sim}{Y_F}$$

$$\text{and} \quad \underset{\sim}{\mu} = \underset{\sim}{Y_F}^T \cdot \underset{\sim}{Y_C}$$

$$\therefore \quad \underset{\sim}{\mu} = \underset{\sim}{G} \cdot \underset{\sim}{Q}$$

Pre-multiplying each side of this equation by the inverse of $\underset{\sim}{G}$ gives the orientation matrix:

$$\underset{\sim}{G}^{-1} \cdot \underset{\sim}{\mu} = \underset{\sim}{G}^{-1} \cdot \underset{\sim}{G} \cdot \underset{\sim}{Q}$$

$$\therefore \quad \underset{\sim}{Q} = \underset{\sim}{G}^{-1} \cdot \underset{\sim}{\mu} \qquad 4.29$$

The elements of $\mathcal{G}$ are given by:

$$\mathcal{G} = \begin{pmatrix} Y_{F_1}^2 & Y_{F_2}^2 & \ldots. & Y_{F_n}^2 \\ Y_{F_1}Z_{F_1} & Y_{F_2}Z_{F_2} & \ldots. & Y_{F_n}Z_{F_n} \\ Z_{F_1}^2 & Z_{F_2}^2 & \ldots. & Z_{F_n}^2 \\ Y_{F_1} & Y_{F_2} & \ldots. & Y_{F_n} \\ Z_{F_1} & Z_{F_2} & \ldots. & Z_{F_n} \\ 1 & 1 & & 1 \end{pmatrix} \times \begin{pmatrix} Y_{F_1}^2 & Y_{F_1}Z_{F_1} & Z_{F_1}^2 & Y_{F_1} & Z_{F_1} & 1 \\ Y_{F_2}^2 & Y_{F_2}Z_{F_2} & Z_{F_2}^2 & Y_{F_2} & Z_{F_2} & 1 \\ . & & & & & \\ . & & & & & \\ . & & & & & \\ Y_{F_n}^2 & Y_{F_n}Z_{F_n} & Z_{F_n}^2 & Y_{F_n} & Z_{F_n} & 1 \end{pmatrix}$$

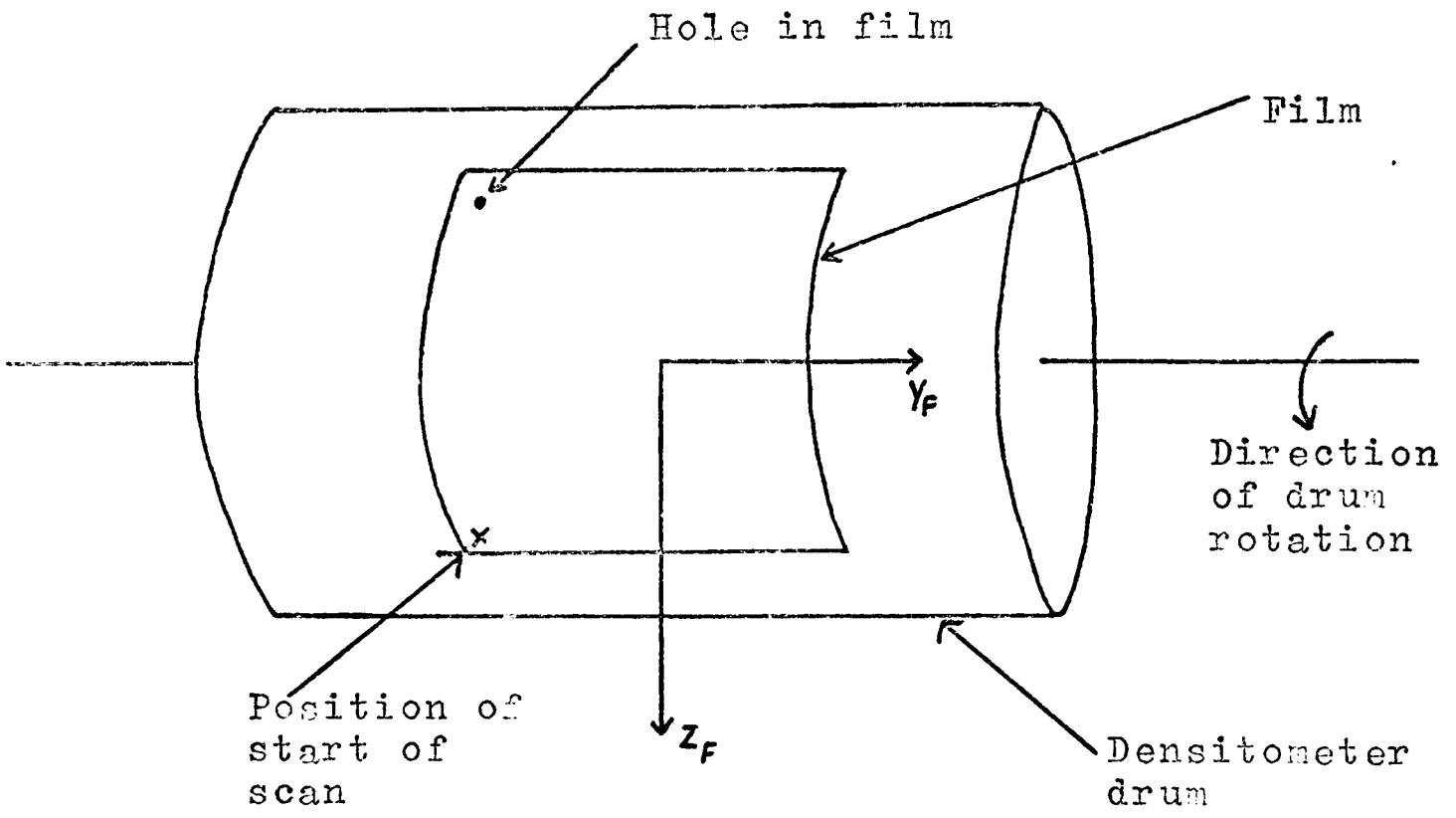
$$\therefore \quad \mathcal{G} = \begin{pmatrix} \sum Y_{F_i}^4 & \sum Y_{F_i}^3 Z_{F_i} & \sum Y_{F_i}^2 Z_{F_i}^2 & \sum Y_{F_i}^3 & \sum Y_{F_i}^2 Z_{F_i} & \sum Y_{F_i}^2 \\ \sum Y_{F_i}^3 Z_{F_i} & \sum Y_{F_i}^2 Z_{F_i}^2 & \sum Y_{F_i} Z_{F_i}^3 & \sum Y_{F_i}^2 Z_{F_i} & \sum Y_{F_i} Z_{F_i}^2 & \sum Y_{F_i} Z_{F_i} \\ \sum Y_{F_i}^2 Z_{F_i}^2 & \sum Y_{F_i} Z_{F_i}^3 & \sum Z_{F_i}^4 & \sum Y_{F_i} Z_{F_i}^2 & \sum Z_{F_i}^3 & \sum Z_{F_i}^2 \\ \sum Y_{F_i}^3 & \sum Y_{F_i}^2 Z_{F_i} & \sum Y_{F_i} Z_{F_i}^2 & \sum Y_{F_i}^2 & \sum Y_{F_i} Z_{F_i} & \sum Y_{F_i} \\ \sum Y_{F_i}^2 Z_{F_i} & \sum Y_{F_i} Z_{F_i}^2 & \sum Z_{F_i}^3 & \sum Y_{F_i} Z_{F_i} & \sum Z_{F_i}^2 & \sum Z_{F_i} \\ \sum Y_{F_i}^2 & \sum Y_{F_i} Z_{F_i} & \sum Z_{F_i}^2 & \sum Y_{F_i} & \sum Z_{F_i} & n \end{pmatrix}$$

where the summations cover values of i from 1 to n; the elements of $\mathcal{U}$ are given by

$$\mathcal{U} = \begin{pmatrix} Y_{F_1}^2 & Y_{F_2}^2 & \ldots. & Y_{F_n}^2 \\ Y_{F_1}Z_{F_1} & Y_{F_2}Z_{F_2} & \ldots. & Y_{F_n}Z_{F_n} \\ Z_{F_1}^2 & Z_{F_2}^2 & \ldots. & Z_{F_n}^2 \\ Y_{F_1} & Y_{F_2} & \ldots. & Y_{F_n} \\ Z_{F_1} & Z_{F_2} & \ldots. & Z_{F_n} \\ 1 & 1 & & 1 \end{pmatrix} \times \begin{pmatrix} Y_{C_1} & Z_{C_1} \\ Y_{C_2} & Z_{C_2} \\ . & \\ . & \\ . & \\ Y_{C_n} & Z_{C_n} \end{pmatrix}$$

$$= \begin{pmatrix} \sum Y_{F_i}^2 Y_{C_i} & \sum Y_{F_i}^2 Z_{C_i} \\ \sum Y_{F_i} Z_{F_i} Y_{C_i} & \sum Y_{F_i} Z_{F_i} Z_{C_i} \\ \sum Z_{F_i}^2 Y_{C_i} & \sum Z_{F_i}^2 Z_{C_i} \\ \sum Y_{F_i} Y_{C_i} & \sum Y_{F_i} Z_{C_i} \\ \sum Z_{F_i} Y_{C_i} & \sum Z_{F_i} Z_{C_i} \\ \sum Y_{C_i} & \sum Z_{C_i} \end{pmatrix}$$

FIGURE 4.25



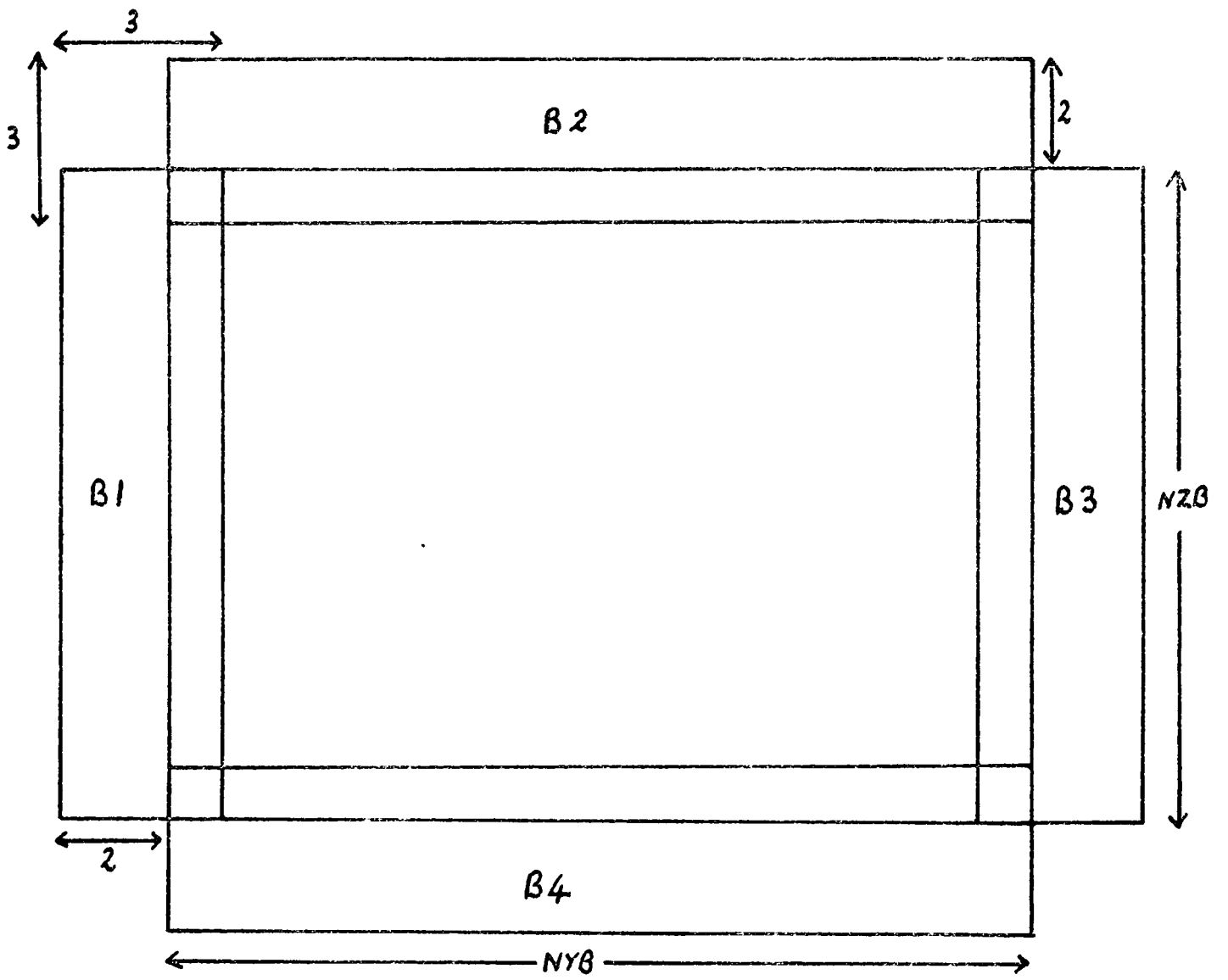
The orientation of the film on the densitometer drum.

A programme (JM4/MT/E) has been written which generates the orientation matrix Q using the mathematics given above.

This programme requires the digital image of the film on magnetic tape produced by the densitometer. Before it is scanned, the film is placed in a frame mounted on graph paper and a small hole punched in the corner corresponding to negative Y_F and Z_F; the coordinates of this hole are fixed in the frame system. The coordinates of the spot on the film corresponding to the direct beam are then noted. Several reflections (a minimum of 6 and maximum of 20) are then chosen for centering; their coordinates on the film are noted and their predicted coordinates found from the programme JM1/MT/D. The film is then scanned by placing it on the densitometer drum as shown in Figure 4.25.

The programme JM4/MT/E reads through the densitometer tape until it finds the hole, which is the only region of zero, or very nearly zero, optical density. Since the coordinates of the hole on the film are known, the programme can then find the reflections specified. The areas of the film surrounding each of these reflections are displayed as a number field on the computer CRT display. The operator then centres the reflection on the CRT by interacting with the programme via an on-line keyboard. During this process the operator may also estimate the optimum box size for integration. When all the chosen reflections have been centred the programme calculates the orientation matrix Q, from the correct reflection coordinates in raster units, and the predicted positions in mm. Finally, the matrix is checked against the reflections displayed. Using this approach it is possible to predict reflection positions with an error of, at worst, 2 raster units.

FIGURE 4.26



The dimensions are in raster units.

The form of the peak and background integration boxes used in the Integration programme.

A further programme, JM21, then applies the orientation matrix to all the reflections predicted by JM1/MT/D. The reflections are then resorted and checked again for overlaps. The coordinates of the reflections are now given in raster units, i.e. the units defined by the densitometer. The magnetic tape produced by JM21 is read directly by the integration programme.

C) Reflection Integration;

In this procedure, the optical density measurements over the area of the reflection are summed and an estimate of the background, taken from an area surrounding the reflection, is made. The integration and background boxes are shown in Figure 4.26.

The integration box size is an input parameter to the programme (JM5/B), and the background sampling areas B1, B2, B3, B4 form a "picture frame" around the reflection. A more flexible approach to background sampling may prove to be necessary; this approach was chosen because of its simplicity. The four background measurements are scaled so that they have the same effective area, and then the mean found. If one or more measurements differ by more than a given fraction (normally 0.1) of the mean from the mean, the reflection is monitored. The total background measurement is then scaled so that it has the same effective area as the peak measurement, and the integrated intensity found by subtracting the scaled background from the peak measurement. If the integration box contains more than a given number of optical density readings higher than a set figure (normally more than 3 measurements greater than 254) the reflection is considered to be too strong to measure

and the reflection is monitored. There is also a facility for setting reflections with intensities less than a set figure to zero. The programme outputs the intensity data to magnetic tape in the form:

h k l Y_F Z_F Rotation angle Intensity FLAG (B1 B2 B3 B4) flag from JM1/MT/D

where FLAG = 0 normally

= 1 when reflection is too strong to measure

= -1 when backgrounds unequal; in this case, the four background measurements are also output in positions B1-B4.

The magnetic tape is then ready to be used in further data processing.

D) Subsequent Processing

The programmes to take the data beyond the stage of integrated intensities have not yet been written. However, an outline of the methods by which the processing might be achieved will now be given.

Assuming two or three film packs are to be used with the rotation camera, a method of weak to strong film scaling will be required. Matthews et al (1972) have shown that the intensity of a reflection is not a linear function of the measured optical density, instead it is given to a good approximation, by an equation of the form:

$$I = D + BD^2$$

where I is the reflection intensity.

D is the integrated background subtracted density

B is a constant.

Matthews et al give the expressions for the constant, B, and the film to film scale factor. Scaling based on this approach would appear to be necessary for films from the rotation camera. The LP correction may also be applied in the weak to strong film scaling programme.

Absorption correction is a more difficult problem. If the crystal is smaller than the incident x-ray beam in every direction, an absorption curve may be measured on a diffractometer. The absorption correction would then follow the method of North et al (1968). Alternatively, if the crystal is larger than the beam, an absorption curve may be estimated by the variation in the intensity of the direct beam (suitably attenuated) at the film as the crystal is rotated. A third method, which also provides a method of scaling film data from different rotation ranges together, would require a precession photograph of the zero level projected down the rotation axis. This precession photograph would then have reflections in common with each of the rotation ranges which could be used to scale the films together and correct for absorption at the same time. Unfortunately, there may be relatively few overlapping reflections which may result in imprecise scaling.

The most straight-forward method of scaling films together is to arrange that neighbouring films have fully measured reflections in common which can be used to give film to film scale factors. However, this method of collecting data is very inefficient since the regions of overlap between films would have to be very large (probably of the order of 1^{o}) in order to give a sufficiently large number of common reflections.

The number of films required to collect a given data set would, therefore, be increased markedly. Other possible methods of film to film scaling will, therefore, be considered.

If rotation photographs are taken mounted about a second axis, the overlapping reflections between the two sets of reflections can be used to provide scaling information. A fourth possible approach relies on Wilson statistics (Wilson (1949)), which show that the mean intensity is given by:

$$\langle I \rangle = \sum_{j=1}^{N} f_j^2$$

where N is the number of atoms in the unit cell, and f_j is the atomic scattering factor of the jth atom. This theory assumes that the average is taken over a sufficiently large number of reflections for which $\sin\theta > \lambda/a$ where a is the shortest unit cell dimension, and that the molecule comprises atoms of approximately the same scattering power all in random positions Using this theory, the scale factors between films could be chosen so that the average intensity on each film was the same. This approach would obviously need careful testing before use.

Once the films have been scaled together, the reflections which are partially measured on neighbouring films can be summed to give the total reflection intensity. Again the procedure should be thoroughly checked, particularly in view of the large amount of "back-lash" in the camera gearing.

Film to film scaling etc. are probably better carried out on the 1906A computer where the large core store makes handling large numbers of reflections easier than it is on the Argus computer.

4.8 First Results

The four programmes written so far have been used to measure the intensities of the lysozyme photograph of the range 0^{o} to 5^{o}. There were 658 reflections on the film to a lattice spacing of 3.5Å. The photograph was scanned on the densitometer using the 100 μ raster with the O.D range set at 0 to 2. Using an integrating box of 15 units along Y_F and 13 units along Z_F, 4 reflections were rejected as being too close together to measure. The integrated intensities of the remaining 654 reflections were measured. Of these reflections, 51 were too intense by virtue of having more than 3 optical density measurements greater than 254 within the integration box, and 10 had one or more background measurements which differred by more than 10% from the mean of the four.

The agreement between Friedel equivalent reflections on the film (hkl & $h\bar{k}l$) was calculated for well measured reflections which occurred in the centre of the rotation range, and for which both equivalent reflections had measured intensities greater than zero. 244 reflection pairs were used to calculate an R factor defined by:

$$R = \frac{\sum |I(hkl) - I(h\bar{k}l)|}{\sum \langle I \rangle}$$

The R factor was 12.4%. However, the intensities of 5 reflections were found to differ markedly from the intensities of their equivalents. These reflections were examined on the film and one of each pair was found to be a partially measured reflection not monitored by the coordinate generation programme. This situation obviously arose from a crystal mis-setting such

that it was not rotating precisely about the b axis. When the 5 pairs of reflections were omitted from the R-factor calculation the value of the R factor fell to 9.1%. This figure is comparable with the R factor of the best native Ppb 6Å data set (crystal 206) measured on a diffractometer. Here the R factor was 8.65%.

From this result it would seem that the regions of the rotation range over which the end flag is set should be set rather wide so that reflections which are partially measured because of crystal mis-setting may be monitored. The results from this film are encouraging and show that the camera and processing system is capable of measuring reflection intensities to a sufficiently high precision.

Although, as outlined above, there are several areas in which further development is necessary, these studies on the rotation camera have laid the foundations for a system of data collection which makes high resolution data collection on a protein as large as phosphorylase a feasible proposition.

V CONCLUDING REMARKS

The results obtained so far on phosphorylase b are encouraging. It has been established that isomorphous derivatives can be found for such a large asymmetric unit, and, moreover, the heavy atom sites can be located provided the structure amplitudes are determined to a relatively high accuracy.

Two native electron density maps have been computed using the two sets of native phase angles determined from the platinum derivative. The two sets correspond to the two possible 'hands' of the anomalous contribution (see section 3.2.12(b)). As discussed in section 3.2.12(b), the mean figure of merit was 49.6% for both sets of phase angles, and so very little reliance should be placed on either map. However, there are features in each map which can be interpreted in terms of protein structure; e.g. rods of 'electron density' with approximately the correct diameters for α-helices. There is also a degree of connectivity in each map which is encouraging. No attempt has been made to define the molecular boundary, although there are regions of very low electron density which could be solvent. There should be high contrast between the protein and solvent regions because of the low salt content of the mother liquor. There is 'electron density' on the two-fold axis in each map which is somewhat discouraging. It has not been possible to decide which map is more "protein-like", and so decide on the correct hand for the anomalous scattering data.

While it is most unlikely that either of these maps represents the electron density of the protein, it is encouraging that they do have some protein-like features. They do suggest

that if another isomorphous derivative could be found, the resulting phase angles would be sufficiently accurate to yield an interpretable protein electron density map. Alternatively, it appears that sufficiently accurate phase angles could be calculated given more accurate measurements of the anomalous scattering from the platinum derivative. Ideally, the anomalous scattering contributions should be measured with an accuracy such that the F_{HLE} coefficients calculated from them may be refined to give R factors less than 40% (see section 3.2.12(b)).

The key to the phosphorylase structure determination lies in accurately measured reflection intensities. Indeed, this would appear to be the key to the determination of the crystal structure of any molecule with a molecular weight in this region, where the isomorphous and anomalous intensity changes, due to the introduction of heavy atoms into the structure, are relatively small.

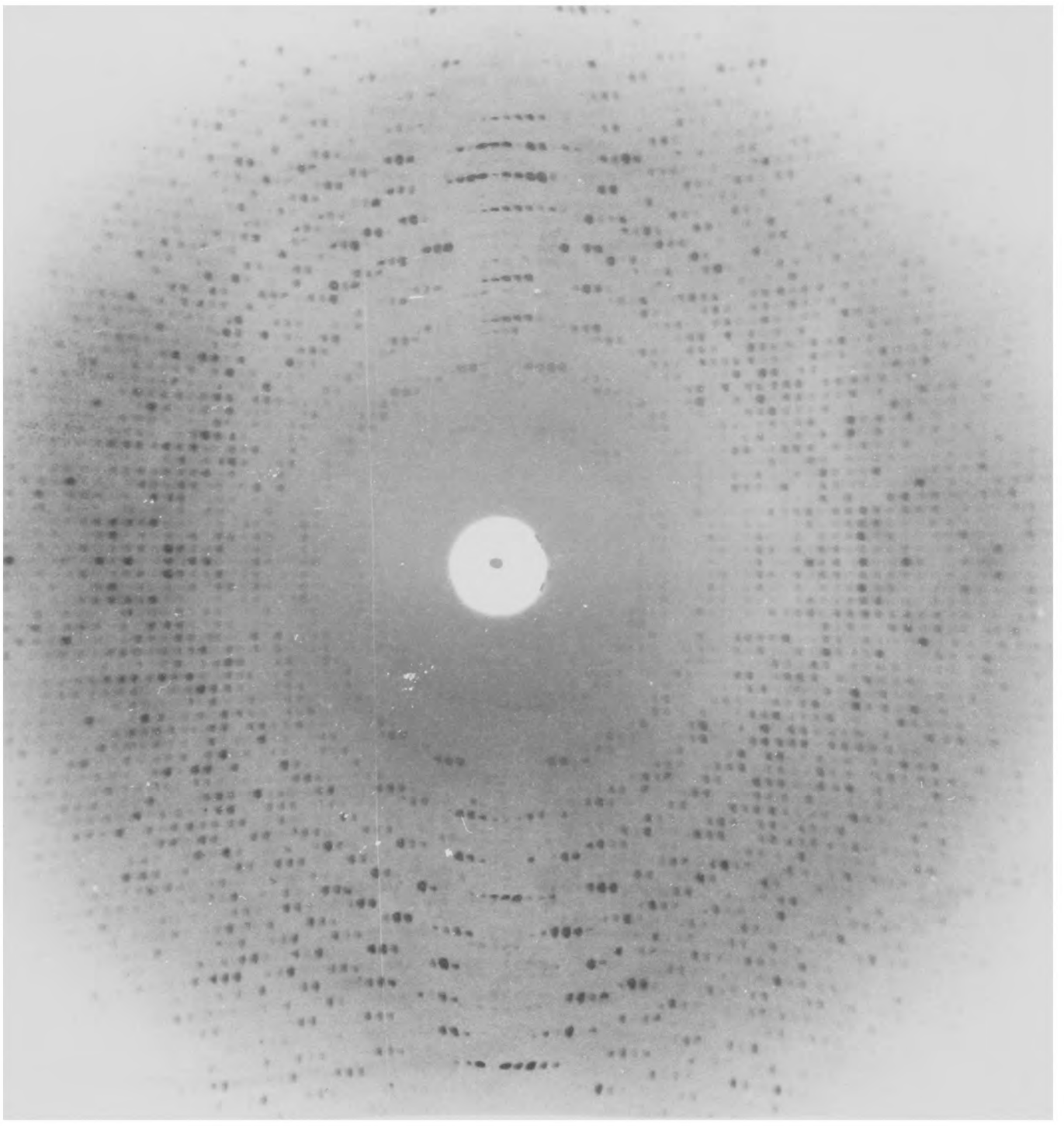
Experience with the tetragonal Ppb crystals has shown that the most useful diffractometer has been the four-circle machine. This is a very reliable machine which can be relatively quickly set up for data collection. It will tolerate larger and slightly less well-formed crystals than multiple-counter diffractometers where reflection resolution is more critical. This ability to use large crystals is very welcome when the scattering is weak due to a large unit cell. Unfortunately the four-circle diffractometer is a relatively slow data collection device, and hence several crystals must be used if the radiation damage is to be kept to an acceptable level.

In an attempt to measure a complete 6Å data set on one

crystal, some data were collected on the five counter linear diffractometer. With this machine the total data collection time should have been of the order of 30 hours. However, at these relatively low Bragg angles the diffractometer required frequent re-adjustment and could not be left to run automatically for periods of more than approximately 20 minutes. In some regions of the data set the diffractometer had to be re-adjusted to measure the individual reflections within a "quasi-simultaneous" group. As a result of this, the total time required to collect the 6Å data set was of the order of four days despite operating the diffractometer for 14 or 15 hours per day. Once initiated, radiation damage on these crystals appears to proceed even in the absence of x-rays with the result that the radiation damage on these data sets was unacceptably high (approximately 30%), even though the irradiation time was only of the order of 30 hours.

Some initial experiments to determine the usefulness, or otherwise, of the five counter, five-circle diffractometer for collecting Ppb data have been carried out. In order to measure reflections in adjacent levels of a c* mount simultaneously, it was necessary to set the crystal to counter distance to 714 mm. Spot resolution becomes a problem at such large distances and, in order to overcome this, the source to crystal distance was increased to approximately 30 cm., and a crystal of less than 1 mm in the largest dimension used. The resultant intensities at the counters were somewhat smaller than those on the four-circle. Any crystal splitting was critical since it served to increase the spot size and hence increased the

FIGURE 5.1



A rotation photograph of a Ppb tetragonal crystal in orientation 3 (c* parallel to the rotation axis) in the range 0° to 2°.

difficulty of reflection resolution. These problems could possibly be reduced by measuring reflections in alternate levels simultaneously, the counter distance could then be reduced to 357 mm. This is equivalent to reducing the axial length of the mounting axis to half of its true value; the effective axial length would then be 58Å. Unfortunately, this length is somewhat smaller than the optimum for giving quasi-simultaneous reflections in the flat-cone setting. This experience indicates that the five counter, five circle diffractometer is not the ideal machine on which to collect Ppb data. The machine also has a relatively lengthy setting-up procedure which mitigates against its use when radiation damage considerations demand that a crystal is changed after approximately 40 hours exposure.

Both the very large number of reflections and the comparative weakness of the intensities point to the use of the rotation camera for the collection of Ppb data to resolutions greater than 6Å. The relative efficiency of the camera compared to a diffractometer has been outlined in section 4.1. With a tetragonal Ppb crystal mounted about the c axis on the rotation camera, a rotation of 2^{o} from a* anti-parallel to the x-ray beam results in 2503 reflections to a lattice spacing of 3.5Å. A photograph of this rotation range is shown in Figure 5.1; the total exposure time for this photograph was 5.5 hours. The rotation range is somewhat high hence the large number of closely spaced reflections. However, this photograph does indicate that the camera is capable of measuring phosphorylase data to this resolution.

When the development of the software associated with the

camera has been carried out as outlined in Chapter 4, the system should be capable of collecting Ppb data to a resolution of at least 3Å. Use of the rotation camera should, therefore, lead to an electron density map of phosphorylase b from which an atomic model of the molecular structure can be built.

APPENDIX

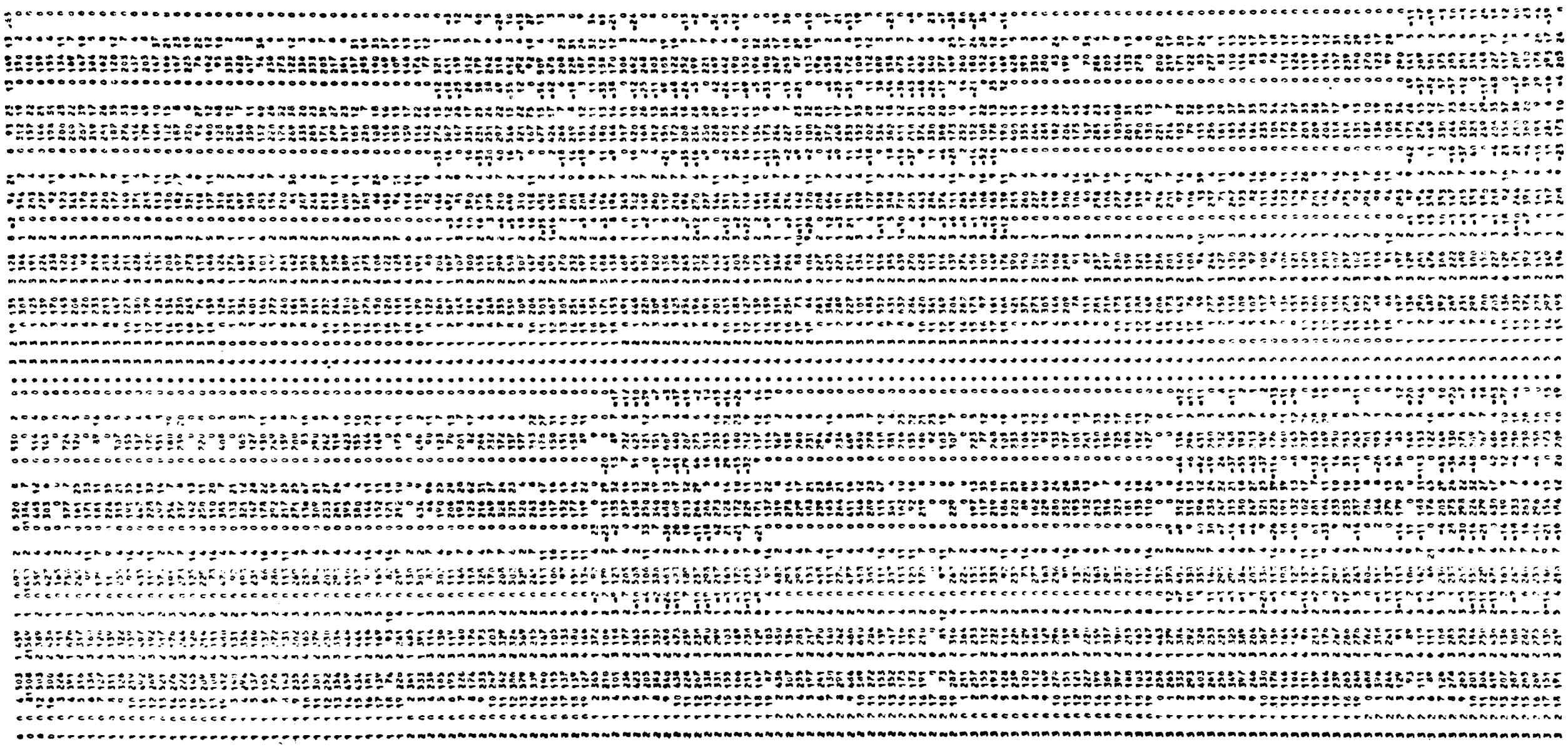
LIST OF STRUCTURE AMPLITUDES

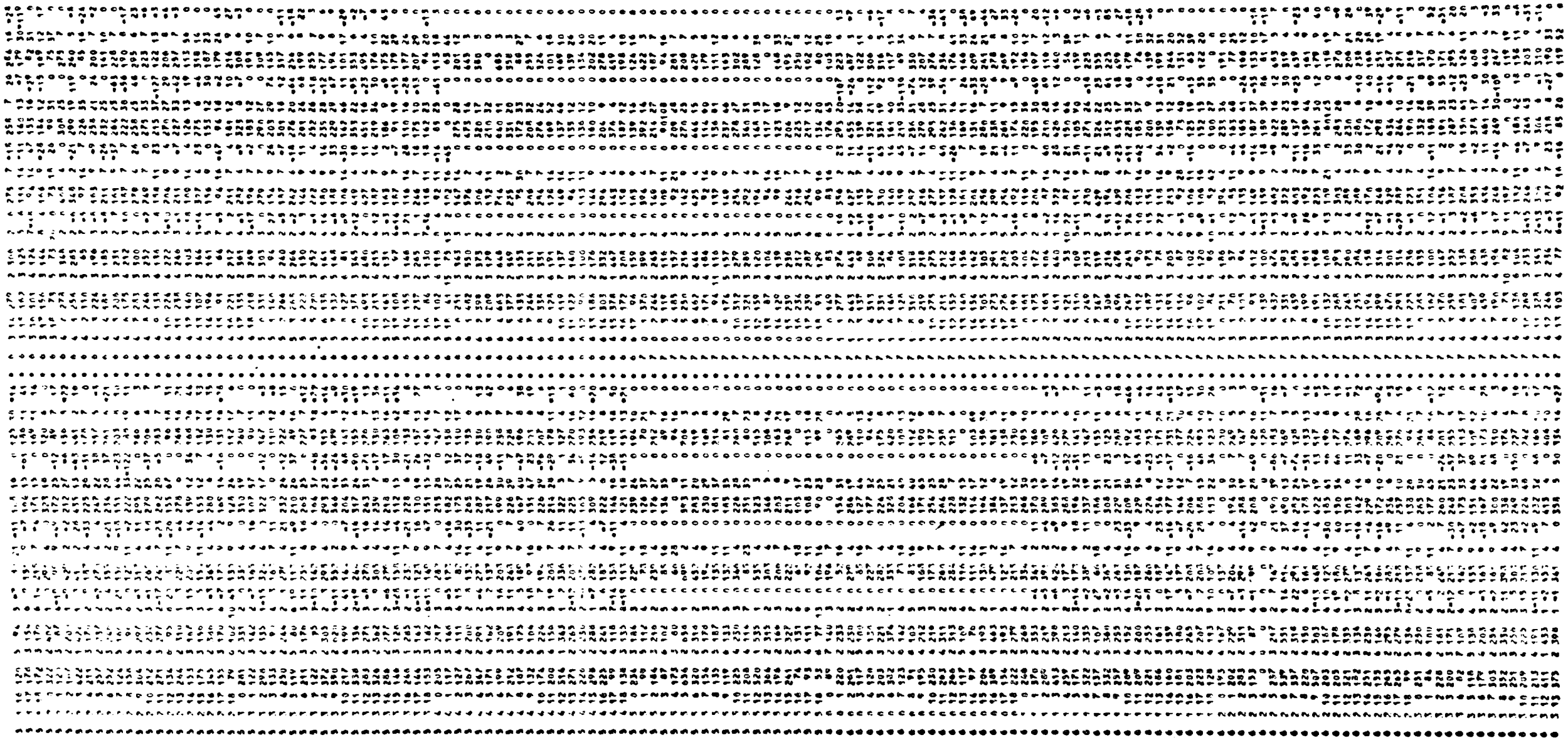
The order of the numbers in this list is

h k l	F_p σ_p	$F_{pH}\sigma_{pH}\Delta_{anom}$	$F_{pH}\sigma_{pH}\Delta_{anom}$	$F_{pH}\sigma_{pH}\Delta_{anom}$	$F_{pH}\sigma_{pH}\Delta_{anom}$
		Mercury derivative	Platinum derivative	Uranium derivative	Pipsyl derivative

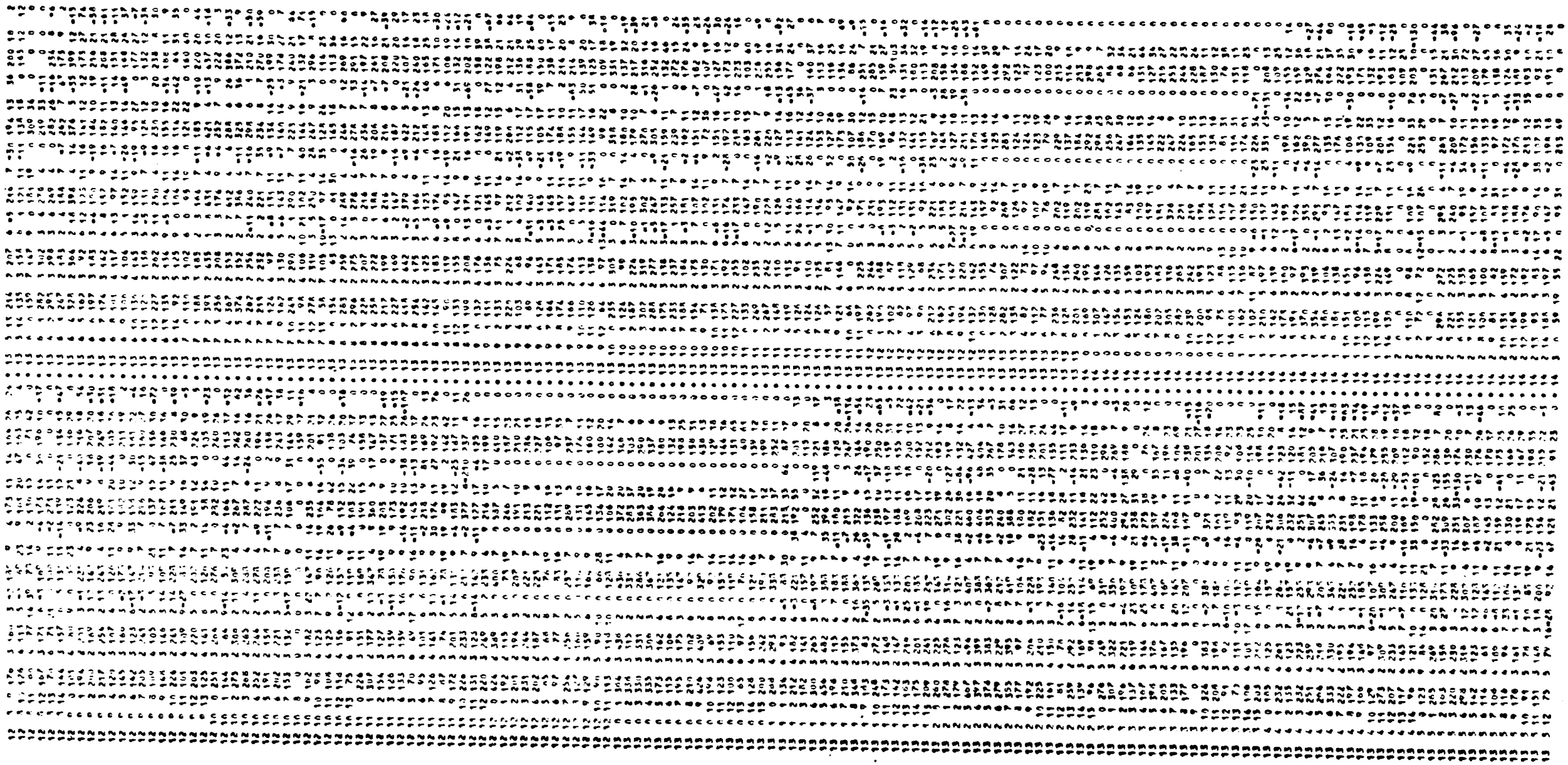
The anomalous difference, Δ_{anom}, is given by:

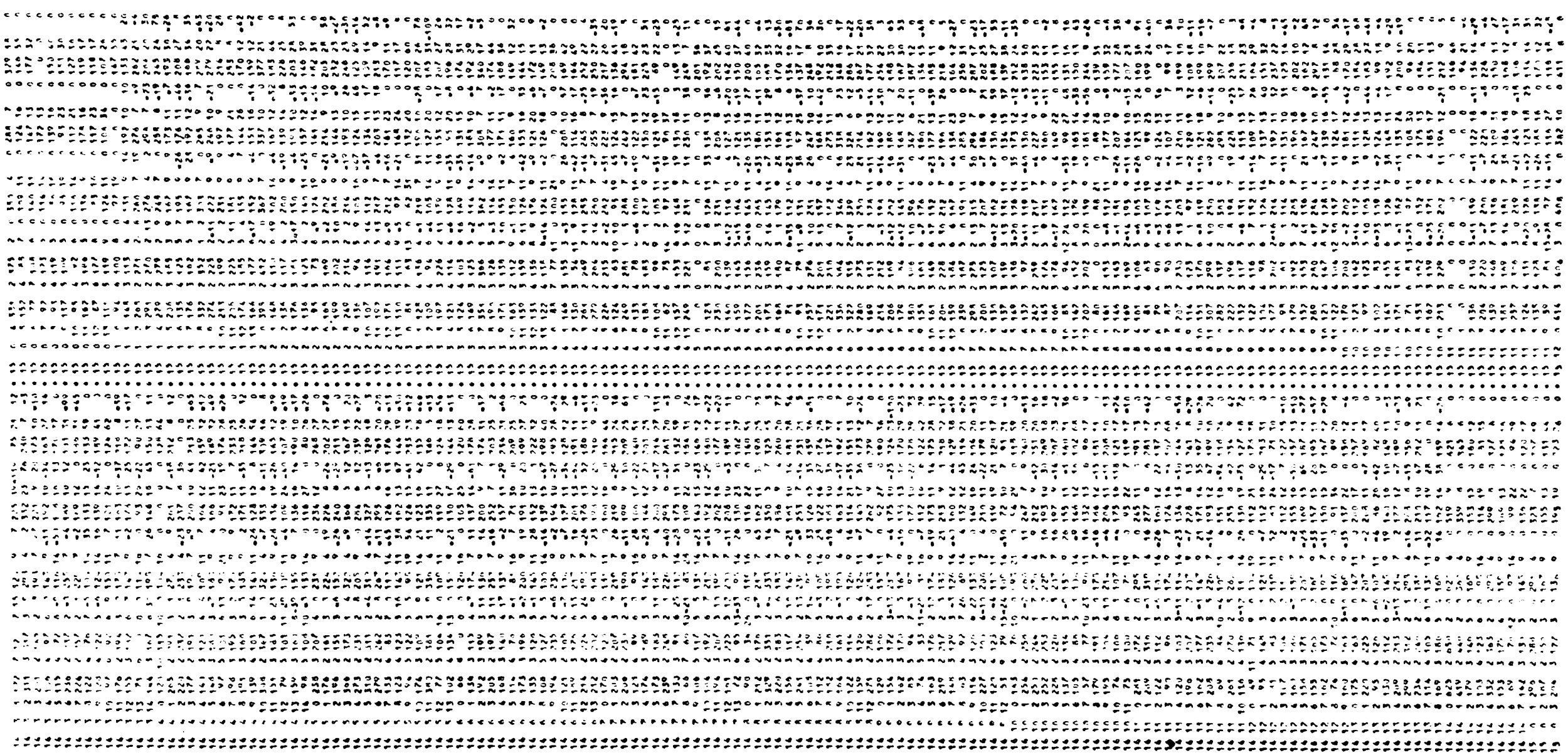
$$\Delta_{anom} = F_{pH}(hkl) - F_{pH}(hk\bar{l})$$

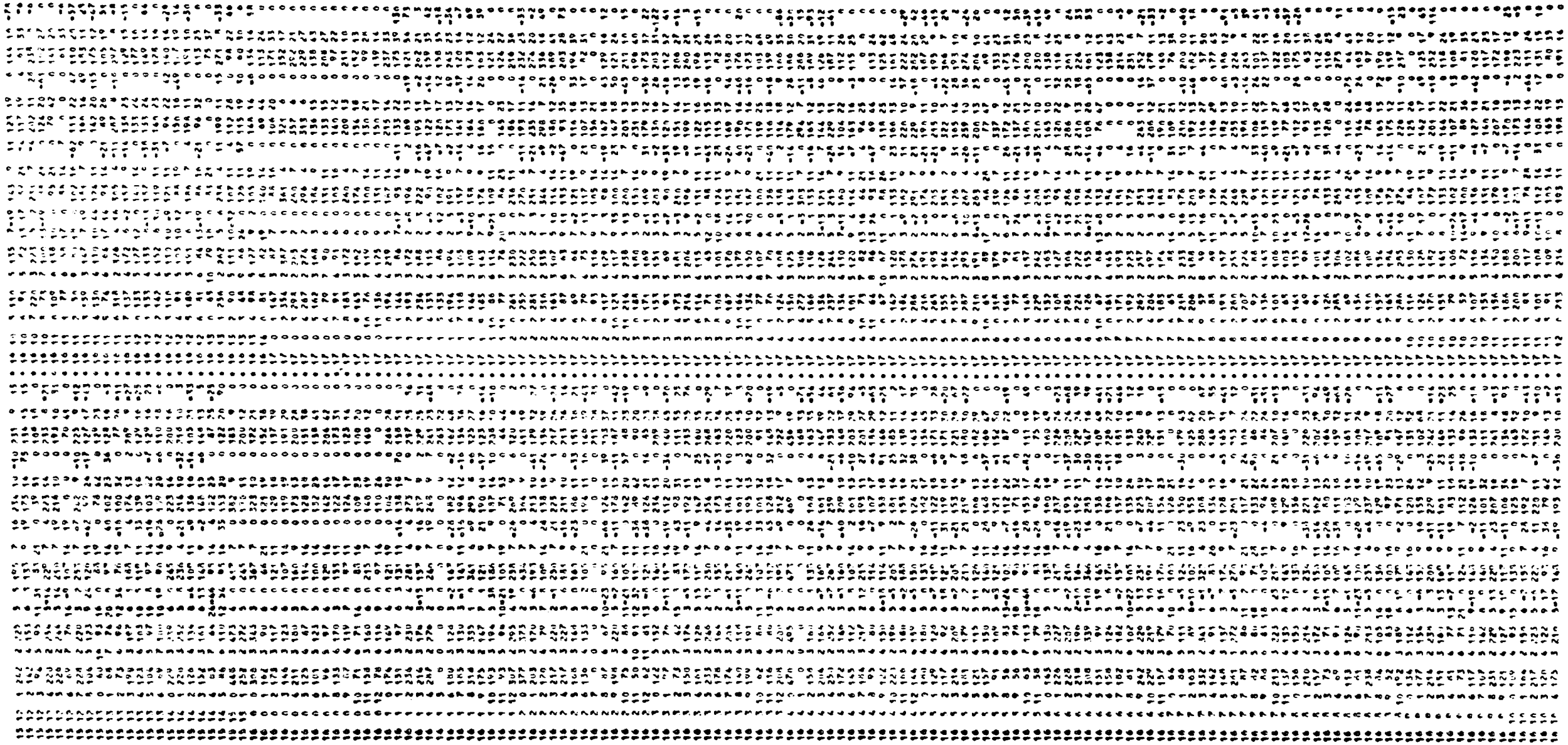


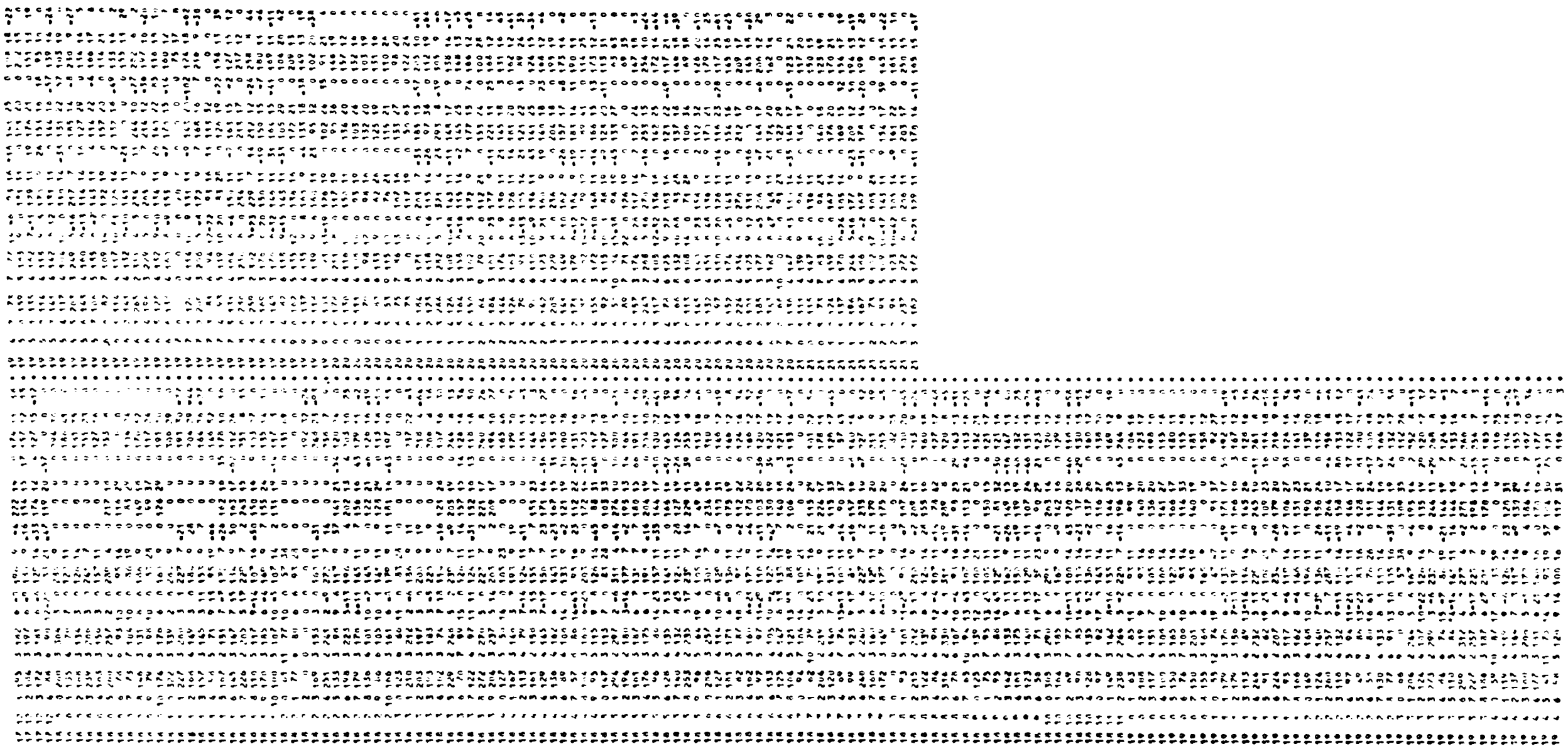












REFERENCES

Abrahamson, S. (1966) J.Sci.Instr., 43, 931

Adams, M.J. (1968) D.Phil. Thesis, Oxford University.

Arndt, U.W. (1968) Acta Cryst., B24, 1355

Arndt, U.W., Crowther, R.A. and Mallett, J.F.W. (1968) J. Phys.E; Sci.Instrum. i, 510

Arndt, U.W., North, A.C.T. and Phillips, D.C. (1964) J.Sci. Instr., 41, 421

Arndt, U.W. and Phillips, D.C. (1961) Acta Cryst., 14, 807.

Arndt, U.W., and Willis, B.T.M. (1966) "Single Crystal Diffractometry", Cambridge University Press.

Arnone, A., Bier, C.J., Cotton, F.A., Day, V.W., Hagen, E.E. Jr., Richardson, D.C., Richardson, J.S. and Yonath, A. (1971) J.B.C., 246, 2302

Auramoic-Zikie, O., Smillie, L.B. and Madsen, N.B. (1970) J.B.C., 245, 1558.

Banner, D.W. (1972) D.Phil. Thesis, Oxford University

Battell, M.L., Smillie, L.B. and Madsen, N.B. (1968) J.B.C., 243, 6202

Bennick, A.B., Campbell, I.D., Dwek, R.A., Price, N.C., Radda, G.K., and Salmon, A.G. (1971) Nature, 234, 140.

Bernal, J.D. and Crowfoot, D. (1934) Nature, 133, 794.

Bijvoet, J.M. (1954) Nature, 173, 188.

Black, W.J. and Wang, J.H. (1968) J.B.C., 216, 113.

Blake, C.C.F., Evans, P.R.E., and Skopes, R.K. (1972) Nature New Biology, 235, 195.

Blake, C.C.F., Koenig, D.F., Mair, G.A., North, A.C.T., Phillips, D.C. and Sarma, V.R. (1965) Nature, 206, 757.

Blow, D.M. and Crick, F.H.C. (1959) Acta.Cryst., 12, 794.

Bragg, W.L. (1913) Proc. Cambridge Phil.Soc., 17, 43

Britensky, M.W. and German, R.E. (1973) Prog. in Biophysics and Molecular Biology, 26, 409

Brown, D.H. and Cori, C.F. (1961) "The Enzymes" Vol.V, p.207.

Buckley, H.E. (1951) "Crystal Growth", Wiley, New York.

Buehner, M., Ford, G.C., Moras, D., Olsen, K.W. and Rossmann, M.G. (1973), In press.

Buerger, M.J. (1940) P.N.A.S., 26, 637.

Buerger, M.J. (1942) "X-ray Crystallography", Wiley, New York.

Bühner, M. (1972) At the Protein Crystallography Workshop, Alpbäch, Austria, March 1972.

Bunn, C.W. (1933) Proc. Roy. Soc., A141, 567

Bunn, C.W. (1961) "Chemical Crystallography", 2nd Ed., Oxford University Press

Bunn, C.W., Moews, P.C. and Baumber, M.E. (1971) Proc.Roy.Soc., B178, 245.

Chignell, D.A., Gratzer, W.B. and Valentine, R.C. (1968) Biochemistry, 7, 1082.

Childress, C.C. and Sacktor, B. (1970) J.B.C., 245, 2927.

Cohen, P. (1972) B.J., 130, 5P

Crick, F.H.C. and Magdoff, B.S. (1956) Acta Cryst., 9, 901

Damjanovich, S., Sanner, T. and Phil, A. (1967) European Jour. Biochem., 1, 347

Dickerson, R.E., Kendrew, J.C. and Strandberg, B.E. (1961) Acta Cryst., 14, 1188.

Dodson, E. and Vijayan, M. (1971) Acta Cryst. B27, 2402

Dwek, R.A., and Radda, G.K. (1972) Mosbach Symposium on protein-protein interactions

Eagles, P.A.M., Iqbal, M., Johnson, L.N., Mosley, J. and Wilson, K.S. (1972) J.M.B., 71, 803.

Eagles, P.A.M. and Johnson, L.N. (1972) J.M.B., 64, 693.

Evans, P.R. (1973) D.Phil. Thesis, Oxford University.

Feldman, K., Ziesel, H. and Helmreich, E. (1972) P.N.A.S., 69, 2278

Fischer, E.H., Cohen, P., Fosset, M., Muir, L.W. and Saari, J.C. (1971), 2nd Symposium on Metabolic Interconversion of Enzymes; Springer-Velag. 67.

Fischer, E.M. and Krebs, E.G. (1962) In "Methods in Enzymology", Vol.5, p.369, Academic Press, New York.

Fischer, E.H., Pocker, A. and Saari, J.C. (1970) Essays in Biochemistry, Vol.6.

Freer, S.T., Kraut, J., Robertus, J.D., Wright, H.T. and Xong, N.H. (1970) Biochemistry, 9, 1997.

Graves, D.J., Fischer, E.H. and Krebs, E.G. (1960) J.B.C., 235, 805.

Graves, D.J. and Wang, J.H. (1972) "The Enzymes", Vol.V, p.207

Green, A.A. and Cori, G.T. (1943) J.B.C., 151, 21.

Green, D.W., Ingram, V.M. and Perutz, M.F. (1954) Proc.Roy.Soc., A225, 287

Hamilton, W.C., Rollet, J.S. and Sparks, R.A. (1965) Acta Cryst., 18, 129.

Hanes, C.S., and Maskell, E.J. (1942) B.J., 36, 76

Harker, D. (1956) Acta Cryst., 9, 1.

Hart, R.G. (1961) Acta Cryst., 14, 1194

Hedrick, J.L. (1966) A.B.B., 114, 216

Henry, N.F.M., Lipson, H. and Wooster, W.A. (1960) "The Interpretation of X-Ray Diffraction Photographs", 2nd Ed., Macmillan & Co. Ltd.

Hestrin, S. (1949) J.B.C., 179, 943.

Howells, E.R., Phillips, D.C. and Rogers, D. (1950) Acta Cryst., 3, 210

Illingworth, B., Jansz, H.S., Brown, T.H. and Cori, C.F. (1958) P.N.A.S., 44, 1180.

James, R.W. (1948) Acta Cryst., 1, 132.

Johnson, G.F. and Graves, D.J. (1966) Biochemistry, 5, 2906

Kendrew, J.C., Dickerson, R.E., Strandberg, B.E., Hart, R.G., Davies, D.R., Phillips, D.C. and Shore, V.C. (1960) Nature, 185, 422

Koshland, D.E., Nemethy, G. and Filmer, D. (1966) Biochemistry, 5, 365.

Krebs, E.G., De Lange, R.J., Kemp, R.G., and Riley, W.D. (1966) Pharmac. Rev., 18, 673.

Krebs, E.G. and Fischer, E.H. (1955) J.B.C., 216, 113

Krebs, E.G. and Fischer, E.H. (1956) B.B.A., 20, 150

Krebs, E.G., Graves, D.J. and Fischer, E.H. (1959) J.B.C. 234, 2867.

Krebs, E.G., Love, D.S., Bratvold, G.E., Frayser, K.A., Meyer, W.L., and Fischer, E.H. (1964) Biochemistry, 3, 1022

Kraut, J., Strahs, G. and Freer, S.T. (1962) P.N.A.S., 48, 1417

Larner, J., Villar-Palasi, C. and Richman, D.J. (1960) A.B.B., 86, 56.

Lipson, H. and Cochran, W. (1966) "The Crystalline State" Vol.III, "The Determination of Crystal Structures"; G. Bell & Sons Ltd.

Luzzatti, V. (1955) Acta Cryst., 8, 795

Madsen, N.B. and Cori, C.F. (1956) J.B.C., 233, 1055

Madsen, N.B., Honikel, H.O. and James, M.N.G. (1971) Second International Symposium in Metabolic Interconversion of Enzymes; pub. Springer-Velag.

Matthews, B.W. (1966a) Acta Cryst., 20, 82

Matthews, B.W. (1966b) Acta Cryst., 20, 230

Matthews, B.W. (1968) J.M.B., 33, 491

Matthews, B.W., Klopfenstein, C.E. and Colman, P.M. (1972) J. Phys. E., Sci.Instrum., 5, 353

Monod, J., Changeux, J-P. and Jacob, F. (1963) J.M.B., 6, 306

Monod, J., Wyman, J. and Changeux, J-P. (1965) J.M.B., 12, 88

Nockolds, C.E. and Kretsinger, R.H. (1970) J. Phys. E., Sci. Instrum. 3, 842.

Nolan, C., Novoa, W.B., Krebs, E.G. and Fischer, E.H. (1964) Biochemistry, 3, 542.

North, A.C.T. (1965) Acta Cryst., 18, 212

North, A.C.T. and Phillips, D.C. (1969) Prog. in Biophys. and Mol.Biol., 19, 1

North, A.C.T., Phillips, D.C., and Matthews, F.S. (1968) Acta Cryst., A24, 351

Phillips, D.C. (1964) J.Sci.Instrum., 41, 123

Phillips, D.C. (1966) Advances in Research by Diffraction Methods, 2, 75

Puchwein, P.G., Kratky, O., Golker, C.F. and Helmreich, E. (1970) Biochemistry, 9, 4691

Rossmann, M.G. (1961) Acta Cryst., 14, 383

Rossmann, M.G. and Blow, D.M. (1962) Acta Cryst., 15, 24

Watson, H.C., Shotton, D.M., Cox, J.M. and Muirhead, H. (1970) Nature, 225, 806

Wilson, A.J.C. (1942) Nature, 150, 152

Wilson, A.J.C. (1949) Acta Cryst., 2, 318

Wilson, A.J.C. (1950) Acta Cryst., 3, 397

Woolfson, M.M. (1970) "An Introduction to X-ray Crystallography" Cambridge University Press.

Wyckoff, H.W., Hardman, K.D., Allewell, N.M., Inagami, T., Tsernoglou, D., Johnson, L.N. and Richards, F.M. (1967) J.B.C., 242, 3984

Xong, N. and Freer, S.T. (1971) Acta Cryst., B27, 2380

Xong, N., Kraut, J., Seely, O., Freer, S.T. and Wright C.S. (1968) Acta Cryst. B24, 289.